Bearing Currents in Inverter-Fed AC-Motors

Vom Fachbereich 18
Elektrotechnik und Informationstechnik
der Technischen Universitaet Darmstadt
zur Erlangung des akademischen Grades
einer Doktor-Ingenieurin (Dr.-Ing.)
genehmigte Dissertation
von
Dipl.-Ing.

Annette Muetze

geboren am 02. Februar 1974
in Singen/Hohentwiel

Referent:	Prof. Dr.-Ing. habil. A. Binder
Korreferent:	Prof. Dr.-Ing. A. G. Jack
Tag der Einreichung:	28. 10. 2003
Tag der muendlichen Pruefung:	23. 01. 2004

D 17
Darmstaedter Dissertation

To those who never had the chance
to get the education they wanted.

Do not be anxious about anything,
but in everything
by prayer and petition, with thanksgiving,
present your requests to God.

Philippians 4.6

Contents

Table of Contents iii

Abstract v

Objectives vi

Zusammenfassung [in German] vii

Aufgabenstellung [in German] viii

Acknowledgements ix

Motivation 1

1 Physics of Bearing Currents 3
- 1.1 "Classical" Bearing Currents . . . 3
- 1.2 Capacitive and Ohmic Behavior of a Roller Bearing . . . 5
- 1.3 System Voltages . . . 6
- 1.4 Motor Capacitances and Bearing Voltage Ratio . . . 8
- 1.5 Additional Bearing Currents at Inverter-Supply . . . 10

2 Research Program 15
- 2.1 Overview . . . 15
- 2.2 Drive Configurations . . . 22
- 2.3 Tests for Bearing Damage Assessment . . . 27

3 Measurement Techniques 29
- 3.1 Introduction . . . 29
- 3.2 Motor Setup . . . 29
- 3.3 Motor Preparation for Bearing Current Assessment . . . 30
- 3.4 Quantification of the Measurement Results . . . 34
- 3.5 Measurement of Motor Capacitances and Bearing Voltage Ratios . . . 37

4 Ground and Bearing Currents in Industrial Drive Systems 41
- 4.1 Measurements at Line-Operation . . . 41

4.2 Determination of Different Types of Bearing Currents 42
4.3 Influence of Motor Size 45
4.4 Influence of Motor Speed and Bearing Temperature 46
4.5 Influence of Motor-Inverter-Combination 50
4.6 Influence of Switching Frequency 55
4.7 Influence of Shielded versus Unshielded Motor Cable 56
4.8 Influence of Motor Cable Length 59
4.9 Influence of Stator Grounding Configuration with Rotor not Grounded . . 61
4.10 Influence of Parasitic Current Path via Grounded Rotor 63
4.11 Calculated Apparent Bearing Current Densities 67

5 Influence of Mitigation Techniques on Bearing Currents 71
5.1 Review of Mitigation Techniques 71
5.2 Basic Function of Filters 74
5.3 Influence of Filters 77
5.4 Influence of Insulated Bearings 86
5.5 Influence of Hybrid Bearings 91

6 Tests for Bearing Damage Assessment 93
6.1 Setup 93
6.2 Results of Bearing Inspection 98

7 Modeling of Bearing Currents 107
7.1 The Bearing as an Electrical Impedance 107
7.2 High-Frequency Behavior of Motors 110
7.3 Motor Capacitances and Bearing Voltage Ratios 112
7.4 EDM-Bearing Currents 121
7.5 Generation of High-Frequency Ground Currents 132
7.6 Calculation of Common Mode Ring Flux 145
7.7 Circulating Bearing Currents 153

8 Practical Rules for Bearing Current Assessment 169

9 Conclusions 175

Symbols and Abbreviations 183

A Test Objects 195
A.1 Three-phase Motors 195
A.2 Inverters 198
A.3 Motor Cables 201
A.4 Inverter-Output Filters 202
A.5 Grease 207

B Measuring Instruments 209

C Calculated *Hertz*'ian Contact Areas 211

D Calculated Minimum Thicknesses of the Lubrication Films 215

E Common Mode and Bearing Voltage Waveforms 219

F Ground Current Waveforms 227

G Line-to-line and Line-to-earth Voltage Waveforms 229

Bibliography 245

Abstract

Modern fast switching IGBT-inverters (*I*nsulated *G*ate *B*ipolar *T*ransistors) allow high dynamic operation of variable speed drives while leading at the same time to energy savings. However, due to the steep voltage surges, bearings may suffer from inverter-induced bearing currents. These bearing currents may destroy bearings - depending on the system - within short time of operation.

So far, research has focused on the physical explanation of the different bearing current phenomena. Here, a thorough analysis of the qualitative and quantitative influence of different parameters under exactly the same conditions on motors from less than 1 kW up to 500 kW rated power was carried out within the frame of a research project. The system parameters studied are motor size, motor speed and bearing temperature, design of motor and inverter (components from different manufacturers), motor cable type and motor cable length, filter operation and operation with use of insulated bearings and with use of hybrid bearings. The results obtained show that the significance of the different bearing current phenomena vary with different motor sizes and grounding configurations. As a consequence, mitigation techniques applied to reduce or eliminate the bearing currents have to be chosen for different drive systems selectively.

In addition, a series of tests for bearing damage assessment was carried out to obtain a better understanding of the mechanisms of damage of the bearing. Despite manifold investigations, the phenomena of the generation of corrugation cannot be explained with today's understanding. However, the deterioration of the bearing grease was found to correlate with the stress on the bearings. A parameter "W" that is proportional to an energy was introduced to quantify the stress.

Furthermore, models that are based on the design parameters are proposed to give physical explanations for the measured correlations of the parameters of a drive system and their impact on the bearing current phenomena. The models identify the parameters that are sensitive for the occurrence and the magnitude of the bearing current phenomena.

However, detailed modeling may not always be applicable with practical applications in the field. Here, many parameters may be unknown. Therefore, a flowchart to estimate the endangerment due to inverter-induced bearing currents is proposed, where detailed

knowledge of the different design parameters is not available. This flowchart might serve as a tool for engineers to assess the endangerment of a drive system due to inverter-induced bearing currents. The flowchart also summarizes possible mitigation techniques to prevent bearing damage.

Objectives

The research project should identify the parameters of an adjustable drive system that are relevant for occurrence of inverter-induced bearing currents and deepen the understanding of the different mechanisms of bearing current generation and flow.

Reasonable solutions to prevent bearing damage due to inverter-induced bearing currents should be evaluated.

This should be done by a systematic study of the influence of the different parameters of a variable speed drive system such as motor size, motor speed and bearing temperature, design of motor and inverter, inverter control, motor cable type and motor cable length. Different mitigation techniques based on commercially available components such as inverter-output filters, insulated bearings and hybrid bearings should be investigated.

Better understanding of the mechanisms of damage in the bearing should be obtained through a series of long term tests for bearing damage assessment. The tests also should give a limit value to evaluate the risk of endangerment of a bearing through a given bearing current.

Models should be given to explain the correlations found in the measurements and to allow prediction of the occurrence of inverter-induced bearing currents for a given drive system.

Zusammenfassung

Moderne, schnell schaltende IGBT-Umrichter (*I*nsulated *G*ate *B*ipolar *T*ransistors) ermoeglichen einen hochdynamischen Betrieb drehzahlveraenderbarer Antriebe bei gleichzeitiger Verringerung der umrichterbedingten Zusatzverluste. Aufgrund der steilen Spannungsflanken koennen die Lager der angeschlossenen Motoren jedoch unter umrichterbedingten Lagerstroemen leiden. Solche Lagerstroeme koennen Lager - abhaengig vom jeweiligen System - innerhalb relativ kurzer Zeit zerstoeren.

Die bisher durchgefuehrte Forschung konzentrierte sich vor allem auf die physikalische Erklaerung der verschiedenen Lagerstromphaenomene. Im Rahmen eines Forschungsprojekts wurde an Motoren von weniger als 1 kW bis zu 500 kW Nennleistung - unter stets gleichen Versuchsbedingungen - der qualitative und quantitative Einfluss der verschiedenen Systemparameter auf die Lagerstromphaenomene untersucht. Die untersuchten Systemparameter sind Motorbaugroesse, Motordrehzahl und Lagertemperatur, Motor- und Umrichterauslegung (Komponenten verschiedener Hersteller), Motorkabeltyp und -laenge, Einsatz von Umrichterausgangsfiltern, sowie von stromisolierten Lagern und von Hybridlagern. Die Ergebnisse zeigen, dass die Bedeutung der verschiedenen Lagerstromphaenomene mit unterschiedlicher Motorbaugroesse und Erdungskonfiguration variiert. Folglich muessen die unterschiedlichen Abhilfemassnahmen, mit denen solche Lagerstroeme reduziert oder eliminiert werden koennen, individuell ausgewaehlt werden.

Ferner wurde eine Serie von Dauerversuchen durchgefuehrt, die besseres Verstaendnis des Schadensmechanismus ermoeglichen sollte. Die Riffelbildung in den Laufbahnen der Lager kann jedoch trotz vielfaeltiger Untersuchungen mit dem heutigen Verstaendnis nicht erklaert werden. Allerdings wurde herausgefunden, dass die Alterung des Lagerfetts mit der Lagerbelastung korreliert. Der Parameter "W", der proportional einer Energie ist, wurde eingefuehrt, um die Lagerbelastung zu quantifizieren.

Desweiteren werden Modelle, die auf den Auslegungsdaten der Komponenten des Antriebs basieren, vorgeschlagen. Diese Modelle geben physikalische Erklaerungen fuer die gemessenen Zusammenhaenge zwischen den Parametern eines drehzahlveraenderbaren Antriebs und ihrem Einfluss auf die unterschiedlichen Lagerstromphaenomene. Diese Modelle identifizieren die empfindlichen Parameter fuer das Auftreten und die Amplitude der unterschiedlichen Lagerstroeme.

Bei praktischer Anwendung im Feld ist detaillierte Modellbildung nicht immer moeglich, da dort ggf. viele Parameter unbekannt sind. Deshalb wird ein Flussdiagramm als Hilfsmittel zur Einschaetzung der Gefaehrdung der Lager des angeschlossenen Motors durch umrichterbedingte Lagerstroeme vorgeschlagen, wenn die genauen Auslegungsparameter der Komponenten des Antriebs nicht bekannt sind. Die verschiedenen Abhilfemassnahmen zur Verhinderung von Lagerschaedigung sind in diesem Flussdiagramm zusammengefasst.

Aufgabenstellung

Ziel des Projekts war, die Parameter zu identifizieren, die fuer das Auftreten von umrichterbedingten Lagerstroemen relevant sind, und das Verstaendnis der verschiedenen Mechanismen von Lagerstromentstehung und -fluss zu vertiefen.

Technisch vernuenftige Loesungen, um Lagerschaedigung durch umrichterbedingte Lagerstroeme zu verhindern, sollten evaluiert werden.

Diese Ziele sollten durch systematische Untersuchung verschiedener, ausgewaehlter Einflussparameter eines drehzahlvariablen Antriebssystems wie Motorbaugroesse, Motordrehzahl und Lagertemperatur, unterschiedliche Ausfuehrungsformen von Motor und Umrichter, unterschiedliche Umrichteransteuertechniken, sowie Typ und Laenge des Motorkabels erreicht werden. Ausserdem sollte die Untersuchung verschiedene, kommerziell erhaeltliche Abhilfemassnahmen wie Umrichterausgangsfilter und stromisolierte, sowie Hybridlager einschliessen.

Besseres Verstaendnis des Schadensmechanismus im Lager sollte durch eine Reihe von Langzeitversuchen erhalten werden. Diese Tests sollten auch einen Grenzwert zur Bewertung der Gefaehrdung des Lagers durch einen gegebenen Lagerstrom ermitteln.

Modelle, die die in den Messungen beobachteten Zusammenhaenge erklaeren und Vorhersagen ueber das Auftreten umrichterbedingter Lagerstroeme bei einem gegebenen Antriebssystem ermoeglichen, sollten gefunden werden.

Acknowledgements

This research was carried out during the years 2000 to 2003 while I was working as research assistant at the Institute of Electrical Energy Conversion at Technische Universitaet Darmstadt.

In many ways, it was like a ship that embarks into the sea in order to reach another harbor: There might be the captain at the controls, but it is the whole crew that makes the journey a successful one. I am deeply indebted to all the people that contributed to this work.

Especially, I would like to thank my supervisor, Professor Dr.-Ing. habil. Andreas Binder, the head of the institute, for giving me the opportunity to carry out this work, for sharing his enormous expertise, for his guidance and his support along the journey.

I would also like to express my deepest gratitude to Professor Alan G. Jack for taking on the role as second reader and for giving me the freedom to embark on this journey while staying available at the shore.

The research involved a lot of measurements that had not been possible without the strong support of the mechanical and electrical workshop of the institute. I am deeply grateful for the support of the part of the crew in the workshops! Especially, I would like to thank Mr. Schmidt for sharing his experience when I had to design the preparation of all the test motors, as well as to Mr. Fehringer for changing innumerable bearings.

I am also very thankful to Dr.-Ing. Rudolf Pfeiffer for his help in carrying out the practical work in the laboratory, and to my colleagues at the institute for their contribution to the pleasure I could have along the journey.

I also wish to thank the members of the committee that accompanied the project. These are (in alphabetical order) ABB, AEG Electric Motors Lafert GmbH, Antriebssysteme Faurndau, ATB Antriebstechnik AG, Baumueller Nuremberg GmbH, Danfoss GmbH, Heidelberger Druckmaschinen AG, Oswald Elektromotoren GmbH, Schaffner EMV GmbH, Siemens AG, SKF GmbH, VEM Motors GmbH Wernigerode and Winergy AG. Without their support in providing the numerous test objects, practical work as well as valuable feedback on the results and share of their experiences the project could not have been performed. Special thanks go to Dr. Auinger and Dr. Zwanziger for heading the committee.

Financial support by the “Arbeitsgemeinschaft industrielle Forschung e.V.” (AiF) is also deeply acknowledged.

Harbor came into sight with the results obtained, but putting them down on paper was needed for the final arrival. I am deeply grateful to my patient proofreaders (in alphabetical order) Dr. Herbert De Gersem, Prof. Rolf Schaefer and Dipl.-Ing. Anita Stanik.

Finally, I am deeply indebted to my family and my friends for their love, patience and support. The ship had never reached its harbor without their encouragements.

Annette Muetze

Motivation

The variety of variable speed drive systems using fast switching IGBT-inverters (*I*nsulated *G*ate *B*ipolar *T*ransistors) available at the market of drive applications increases drastically. Conventional, line-operated drive systems have low losses, low noise and smooth torque, yet, they run at constant speed. Inverter-operated drive systems allow variable speed and therefore energy saving for variable speed operation when compared with conventional drive systems. However, at low switching frequencies, these drive systems suffer from additional losses for rated motor speed, additional noise and torque ripples and have poor dynamic performance. Motor operation with higher switching frequencies can reduce the additional losses, additional noise and torque ripples and increase the drive dynamics. Due to the fast switching, new phenomena have come up that had not been of influence before, but now come into effect. Fast switching IGBT-inverter operated motors are submitted to increased winding stress, increased EMI-problems (*E*lectro-*M*agnetic *I*nterference) as well as additional ground and bearing currents.

The phenomena of inverter-induced bearing currents have been investigated since almost 10 years [1], [2]. The results presented are based on specific investigations with either small or large motors with power ratings $P_\mathrm{r} = (1...15)$ kW, respectively $P_\mathrm{r} \geq 150$ kW. Only one research lab reported on investigations done on motors with power ratings $P_\mathrm{r} = (30...70)$ kW and $P_\mathrm{r} = 355$ kW [3], [4], [5]. Different mitigation techniques to eliminate inverter-induced bearing currents have been proposed.

The studies reported were done using different measurement techniques and test setups, rendering forthright comparison of the qualitative and quantitative results difficult.

Further systematic studies of the influence and the significance of different parameters of an adjustable drive system on the bearing current phenomena had been necessary. The studies had to include a systematical experimental survey of different selected mitigation techniques to evaluate their effectiveness for different types of bearing currents. This should be done under exactly the same conditions, using identical measurement techniques for all test setups.

The “apparent bearing current density” has been the common measure to evaluate the endangerment of the bearing due to “classical” bearing currents of line-fed motors [6], [7], [8], [9], [10]. The transfer of this method to the phenomena of inverter-induced

bearing currents has been questionable, because of the different nature of these currents. A series of tests to assess bearing damage had been necessary to obtain more knowledge about the mechanisms of damage to the bearings due to inverter-induced bearing currents.

The research carried out should allow identification of the endangerment of a given adjustable drive system due to inverter-induced bearing currents in advance of occurring damage. On one hand, this model should be simple to be applicable in the field, where many parameters of the drive might be unknown. On the other hand, it should provide the physical understanding of the correlations stated and allow more complex investigation of the system where the parameters needed are available.

Chapter 1

Physics of Bearing Currents

1.1 "Classical" Bearing Currents

The phenomenon of bearing currents of line-operated electrical machines, also referred to as "classical" bearing currents, has been known for decades and was investigated thoroughly [11], [12], [13], [14], [15], [16].

These currents are a parasitic effect and are mainly caused by magnetic asymmetries in the machine. These asymmetries are the reason for a parasitic ac magnetic flux linkage in the loop "stator housing - drive-end bearing - motor shaft - non drive-end bearing" that induces a voltage in this loop. Thus, the ac shaft voltage v_{sh} can be measured between the two ends of the shaft as part of this loop (Fig. 1.1).

The induced voltage may cause a circulating bearing current in the above mentioned loop. Current may only flow if the induced voltage surpasses a certain threshold to bridge the insulating lubrication film of the bearing. The threshold for this current to occur is typically $v_{\mathrm{sh,rms}} \approx 350$ mV, respectively $\hat{v}_{\mathrm{sh}} \approx 500$ mV (Fig. 1.2) [17]. European and American standards give limits of $\hat{v}_{\mathrm{sh}} \approx 500$ mV [18], respectively $\hat{v}_{\mathrm{sh}} \approx 1$ V [19] for the shaft voltage at line-operation to be not dangerous with low-voltage motors.

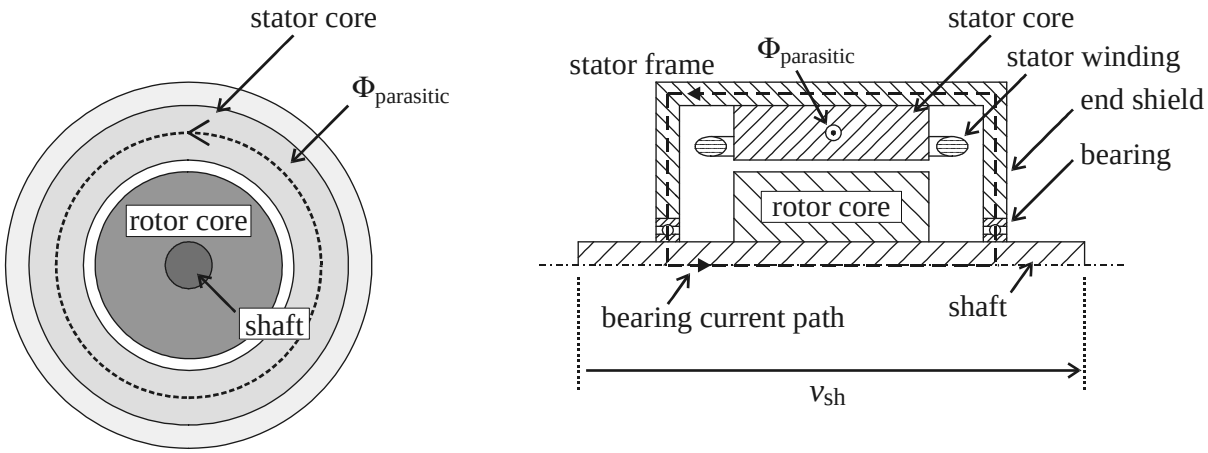

Figure 1.1: Bearing currents due to magnetic asymmetries at line-operation

With increasing motor size, these "classical" bearing currents are more likely to occur, because the parasitic flux linkage increases. Line-operated induction machines with two poles show the biggest flux per pole for a certain shaft height thus also creating the biggest parasitic flux linkage. They are therefore the most critical type of machine concerning bearing currents within a certain shaft height.

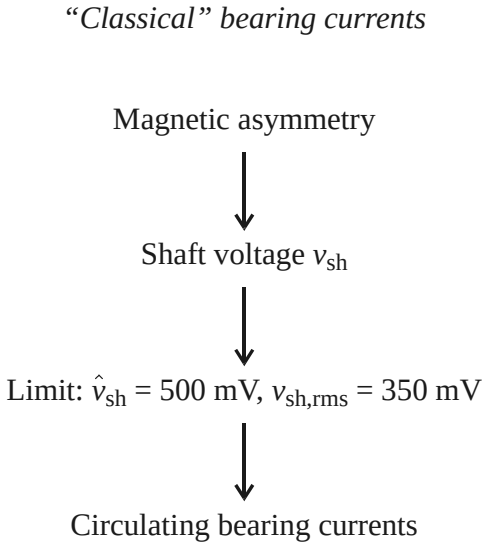

Figure 1.2: Bearing currents of line-operated electrical machines

By insulating e.g. the non-drive end bearing, this circulating bearing current can be suppressed. Generally, motors of sizes beyond shaft height 500 mm are investigated during the final tests after manufacturing by measuring the shaft voltage v_{sh} to decide if such an additional adaptation is necessary. Large machines (typically $P_r \geq 1$ MW) are equipped with counter-measures like insulated bearings as standard design.

The shaft voltage due to magnetic asymmetries varies with stator voltage and motor utilization. Following literature [16], with induction motors, v_{sh} reaches its maximum at approximately 70% of the rated stator voltage and typical saturation degree of the magnetic circuit. A lot of literature on this subject is available, of which a good summary is also given e.g. in [16].

The "classical", circulating type bearing currents are of inductive nature. Other types of bearing currents due to electrostatic charging (e.g. because of steam brushing turbine blades) and due to external voltage on the rotor windings (e.g. as a result of static excitation equipment or asymmetries of the voltage source or rotor winding insulation) have also been reported for large synchronous generators [12], [13], [15].

These types of bearing currents are not in the focus of the work presented. However, some corresponding measurements were made. None of the investigated motors showed "classical" bearing currents, and the measured shaft voltages v_{sh} were much below the critical level (→ Section 4.1, p. 41).

When machines are operated by an inverter, different types of bearing currents may occur. *This research focuses on inverter-induced bearing currents.*

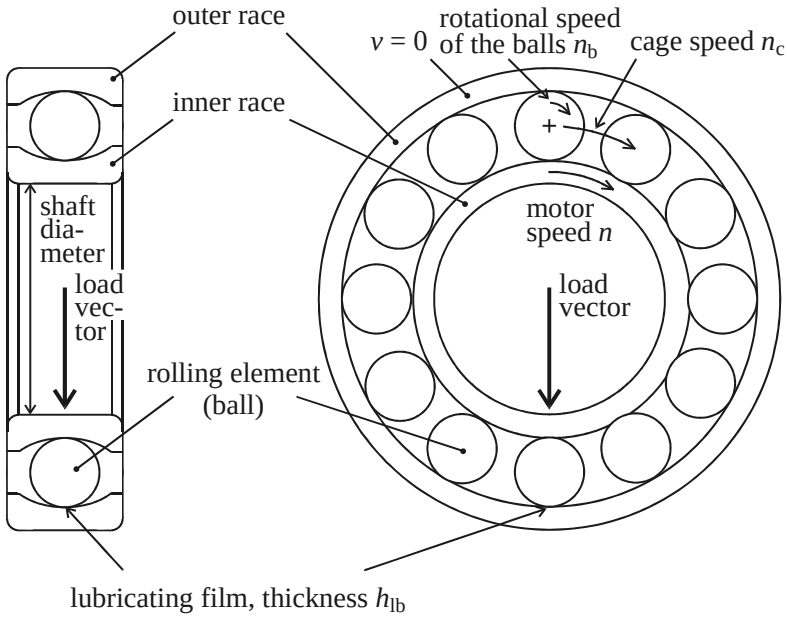

Figure 1.3: Sketch of a ball bearing

1.2 Capacitive and Ohmic Behavior of a Roller Bearing

Fig. 1.3 shows a sketch of a ball bearing, consisting of the inner and outer bearing races and the rolling elements (here: balls). The load vector and the rotational speed of the different elements are also shown. Such a bearing is a complex, non-linear impedance in the equivalent circuit of the motor. It is described in detail in Section 7.1 (p. 107).

From a simplified point of view, two ranges of operation can be distinguished that are important for understanding of the mechanisms of additional bearing currents at inverter-supply:

▶ At standstill and low motor speed (typically $n \leq 100$ /min), the lubrication film in the load zone of the bearing is only some nm thick. If voltage is applied across this distance, it can be easily bridged by conducting electrons due to the tunnel effect of quantum mechanics. In this range, the bearing acts as an *ohmic resistance*.

▶ At elevated motor speed (typically $n > 100$ /min), due to hydrodynamic effects, the lubricating film of the bearing is more than 100 times thicker than at standstill, typically (0.1...2) μm. This lubricating film has insulating properties, and the bearing acts as a *capacitor* (→ Section 7.1, p. 107).

1.3 System Voltages

Fig. 1.4 shows the different voltages of a three phase drive system (Fig. 1.4a) and an induction or PM machine (Fig. 1.4b). In detail, the voltages are denoted as follows:

► *Line-to-ground voltage* v_{Lg}:
The line-to-ground voltage (or: "line-to-earth voltage") is the difference of potential between an individual phase and the ground. Hence, a three phase system contains the three line-to-ground voltages v_{ug}, v_{vg} and v_{wg}. In this thesis, this voltage refers to the voltage measured between the terminal of the individual phases of the inverter or motor and the grounding connection of the inverter or motor respectively.

At inverter-operation, the line-to-ground voltage changes with the switching frequency ("chopping frequency") of the switching elements of the inverter f_c.

► *Line-to-line voltage* v_{LL}:
The line-to-line voltage is the difference of potential between two phases of a multi phase system. Hence, a three phase system contains the three line-to-line voltages v_{uv}, v_{vw} and v_{wu}. Here, this voltage refers to the voltage measured at the terminals.

At inverter-operation, this voltage changes with *two times* the switching frequency of the switching elements of the inverter f_{c}.

► *Line-to-neutral voltage* v_{LY}:
The line-to-neutral voltage denotes the difference of potential between an individual phase terminal and the neutral point of the phase connections (e.g. star point in a Y-connected system). Hence, a three phase system contains the three line-to-neutral voltages v_{uY}, v_{vY} and v_{wY}.

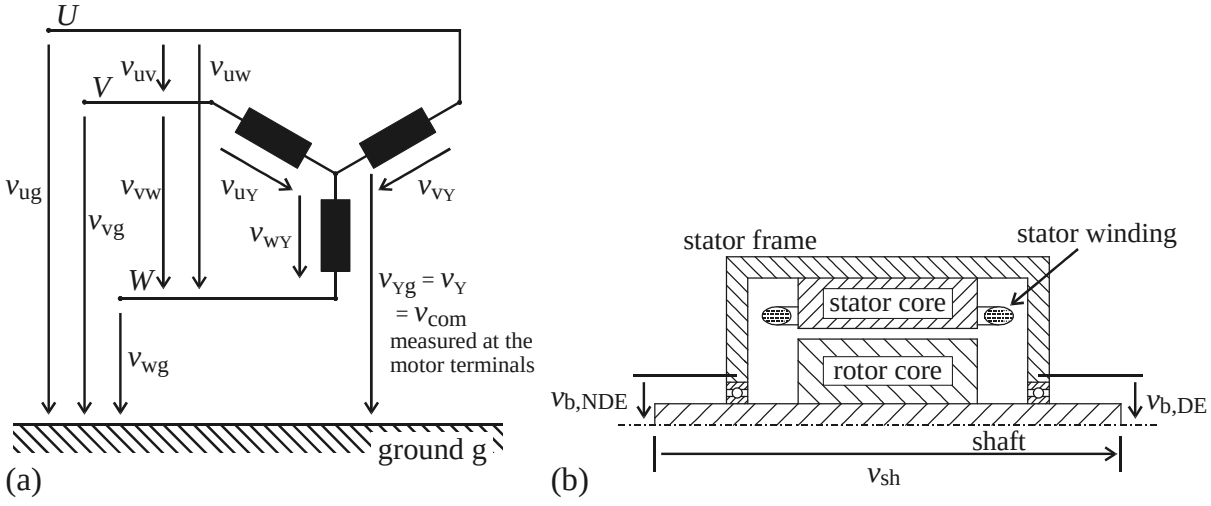

Figure 1.4: Definition of system voltages

At inverter-operation, the line-to-neutral voltage changes with the switching frequency of the switching elements of the inverter f_c.

► *Common mode voltage* v_{com}:
The common mode voltage (in literature, the common mode voltage is also often denoted v_0) is defined by the arithmetic mean of the line-to-ground voltages as given by (1.1).

$$v_{com} = \frac{v_{ug} + v_{vg} + v_{wg}}{3} \tag{1.1}$$

At inverter-operation, the common mode voltage changes with *three times* the switching frequency of the switching elements of the inverter f_c.

► *Neutral-to-ground voltage* v_{Yg}:
The neutral-to-ground voltage is the difference of potential between the neutral point of the phase connections (e.g. star point in a Y-connected system) and the grounding connection. In this thesis, it is simply denoted v_Y.

At inverter-operation, this voltage also changes with *three times* the switching frequency of the switching elements of the inverter f_c.

► *Bearing voltage* v_b:
The difference of potential between inner and outer race of a bearing is called bearing voltage. At a standard machine with two ends - drive end DE and non drive end NDE - two bearing voltages are defined, $v_{b,DE}$ and $v_{b,NDE}$. At inverter-operation, when the common mode voltage contains high frequency components, and an intact lubricating film when the bearing acts as a capacitor, the bearing voltage mirrors the common mode voltage at the motor terminals by a capacitive voltage divider (→ Section 1.4).

► *Shaft voltage* v_{sh}:
The shaft voltage of a machine is measured between the two ends of the shaft of a machine.

1.4 Motor Capacitances and Bearing Voltage Ratio

The capacitances of electrical machines are usually not of influence at line-operation. They come into effect, when the machine is submitted to a common voltage that contains high frequency components (→ Section 7.2, p. 110). The five most important capacitances are given by the following parts of a machine (Fig. 1.5):

▶ *Stator winding-to-frame capacitance* C_{wf}:
The stator winding-to-frame capacitance C_{wf} is the capacitance between stator winding at high voltage and stator iron at grounded potential. The different voltage levels are separated by electrical insulation between the winding copper and the stator iron stack. In this thesis, C_{wf} is defined as the stator winding-to-frame capacitance *per phase*.

▶ *Phase-to-phase capacitances* C_{ph}:
The phase-to-phase capacitances C_{ph} are formed mainly by the winding parts of the different phases U, V and W in the winding overhang, where they are separated only by special insulating paper, the so-called "phase-separation".

▶ *Stator winding-to-rotor capacitance* C_{wr}:
The stator winding-to-rotor capacitance C_{wr} is given by the gap distance between rotor surface and stator winding, being separated by winding insulation, slot wedges and air gap. In this thesis, C_{wr} is defined as the stator winding-to-rotor capacitance *for all three phases in parallel*.

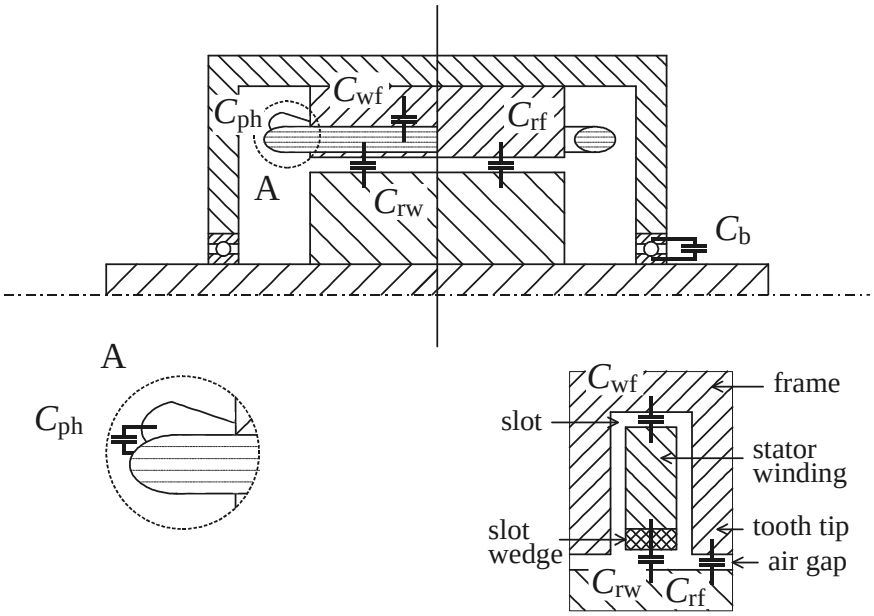

Figure 1.5: Main capacitances of an induction or PM synchronous machine that are import at high frequencies

▶ *Rotor-to-frame capacitance* C_{rf}:
The rotor-to-frame capacitance C_{rf} is mainly determined by the rotor surface and the stator iron stack surface at the air-gap, mainly the stator tooth tips.

▶ *Bearing capacitance* C_{b}:
At intact lubrication film, meaning that the lubrication film has insulating properties, the bearing acts as a capacitor with the capacitance C_{b}.

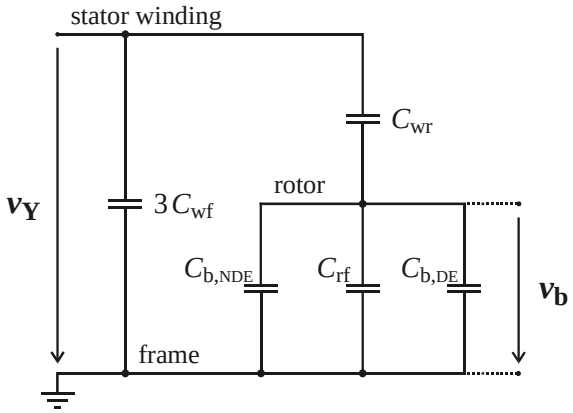

Figure 1.6: Equivalent circuit of the main capacitances of an induction or PM synchronous machine that are important at high frequencies

At intact lubrication film of the bearing, which insulates the rotor from the stator iron, the stator winding-to-rotor, rotor-to-frame and bearing capacitances C_{wr}, C_{rf} and $C_{\mathrm{b,NDE}} \approx C_{\mathrm{b,DE}} \approx C_{\mathrm{b}}$ form a capacitive voltage divider (Fig. 1.6). The high frequency common mode voltage at the motor terminals v_{Y} is mirrored over the bearing by this voltage divider, causing the bearing voltage v_{b}.

The ratio between bearing voltage v_{b} and common mode voltage at the motor terminals v_{Y} is defined as *B*earing *V*oltage *R*atio, short "BVR" (1.2).

$$\mathrm{BVR} = \frac{\text{bearing voltage}}{\text{stator winding common mode voltage}} = \frac{v_{\mathrm{b}}}{v_{\mathrm{Y}}} = \frac{C_{\mathrm{wr}}}{C_{\mathrm{wr}} + C_{\mathrm{rf}} + 2C_{\mathrm{b}}} \tag{1.2}$$

1.5 Additional Bearing Currents at Inverter-Supply

The phenomena of additional bearing currents in variable speed drive systems due to fast switching IGBT-inverters have been reported by various authors since almost 10 years [1], [2], [3], [4], [5], [17], [20], [21], [22], [23], [24], [25].

The origin of these bearing currents is the common mode voltage v_{com}, which is the voltage in the zero phase-sequence system of the feeding inverter (→ Section 1.3). The rise-times t_{r} of the IGBTs are short, typically t_{r} = several 100 ns, leading to high dv/dt = (2...10) kV/μs. The high frequency components of this voltage interact with capacitances of the machine as discussed above (→ Section 1.4).

Four types of inverter-induced bearing currents can be distinguished. The first two are related to the influence of the common mode voltage v_{com} on the bearing voltage v_{b}, the last two are caused by ground currents that result from the interaction of the common mode voltage v_{com} with high dv/dt and the capacitance between stator winding and motor frame C_{wf} (Fig. 1.7):

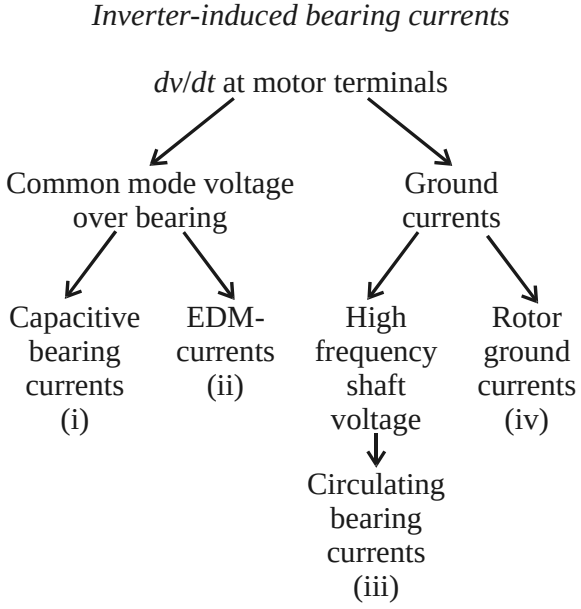

Figure 1.7: Bearing currents of inverter-operated electrical machines

(i) *Capacitive bearing currents*:

The common mode voltage v_{com} at the stator windings causes - due to the voltage divider of the capacitances of the machine - a voltage drop v_{b} across the bearing between inner and outer race.

At low bearing temperature ($\vartheta_{\mathrm{b}} \approx 25°\mathrm{C}$) and motor speed $n \geq 100$ /min the lubricating insulating film and the balls and races of the bearing form a capacitance (→ Section 1.3). The dv/dt over the bearing causes along with the bearing capacitance C_{b} small capacitive bearing currents in the range of $\hat{i}_{\mathrm{b}}$ = (5...10) mA (1.3), (Fig. 1.8).

$$i_{\mathrm{b}} = C_{\mathrm{b}} \cdot \frac{dv_{\mathrm{b}}}{dt} \tag{1.3}$$

At bearing temperatures typical for load operation, $\vartheta_{\mathrm{b}} \approx (70...90)°\mathrm{C}$, and low motor speed, $n \leq 100$ /min, the lubrication film of the bearing may be bridged by metallic contact and has no longer insulating properties. Then, the bearing is an ohmic resistance. The voltage causes small bearing currents with amplitudes $\hat{i}_{\mathrm{b}} \leq 200$ mA.

According to the present standard of knowledge, this type of bearing current is *not harmful to the bearing* as it is too small. *This type of bearing currents is not discussed any further*, because of the much smaller amplitude when compared with the other types of bearing currents.

(ii) *Electrostatic discharge currents*:

At intact lubrication film, the bearing voltage v_b mirrors the common mode voltage at the stator terminals v_Y (bearing temperature $\vartheta_b \approx 25°C$, motor speed $n \geq 100$ /min) via the capacitive voltage divider BVR (*B*earing *V*oltage *R*atio), as it was described before (→ Section 1.4). Hence, the bearing voltage v_b is determined via the BVR by the common mode voltage of the stator windings v_Y (1.4).

$$v_b = v_Y \cdot \mathrm{BVR} = v_Y \cdot \frac{C_{wr}}{C_{wr} + C_{rf} + 2C_b} \tag{1.4}$$

The electrically loaded lubrication film between balls and running surface breaks down when the threshold voltage of the film is surpassed ($v_{b,th} \approx$ (5...30) V at bearing temperature $\vartheta_b \approx 20°C$). The lubrication film discharges, causing an EDM-current pulse (*E*lectric *D*ischarge *M*achining). These breakdowns occur statistically distributed [5], [23].

At bearing temperature typical for load operation, $\vartheta_b \approx$ (70...90)°C, the bearing no longer mirrors v_Y. The lubrication film repeatedly builds up voltage and discharges at $v_b \approx$ (5...15) V, which is a lower value than at bearing temperature $\vartheta_b \approx 20°C$ (Fig. 1.9).

The breakdown of the lubrication film is influenced by metallic particles due to wear in the grease. Therefore, shaft voltage pulses occurring at moments when only few particles pass the load zone of the bearing film, may be held by the film. Larger duration of these voltages is not possible, as the statistical metallic wear will lead to break down. Therefore, for short time bearing voltages v_b up to $\hat{v}_b = 30$ V are possible, whereas with dc or ac 50/60 Hz only about $\hat{v}_b = 0.5$ V are observed. Due to large dv/dt with fast switching IGBT-inverters voltage buildup $\hat{v}_b \approx 30$ V is possible.

Peak amplitudes are $\hat{i}_b \approx$ (0.5...3) A. This effect is harmful especially for small motors. The theoretical discussion of this type of bearing current is content of Section 7.4 (p. 121).

(iii) *Circulating bearing currents*:

The high dv/dt at the motor terminals causes - mainly because of the stator winding-to-frame capacitance C_{wf} - an additional ground current i_g (→ Section 7.2, p. 110). The frequencies of these currents range from $f(i_g) \approx 100$ kHz up to $f(i_g) =$ several MHz.

The ground current i_g excites a circular magnetic flux around the motor shaft. This flux induces a shaft voltage v_{sh} along the shaft of the motor. If v_{sh} is large enough to puncture the lubricating film of the bearing and destroy its insulating properties, it causes a circulating bearing current i_b along the loop "stator frame - non drive end - shaft - drive end". Because this type of bearing current is due to inductive coupling, it mirrors the ground current. It is of differential mode, the bearing currents being of opposite direction in both bearings (Fig. 1.10).

Peak amplitudes of circulating bearing currents vary - depending on the motor size - $\hat{i}_b \approx$ (0.5...20) A (power rating up to $P_r = 500$ kW). More theoretical description of this type of bearing current is given in Section 7.7 (p. 153).

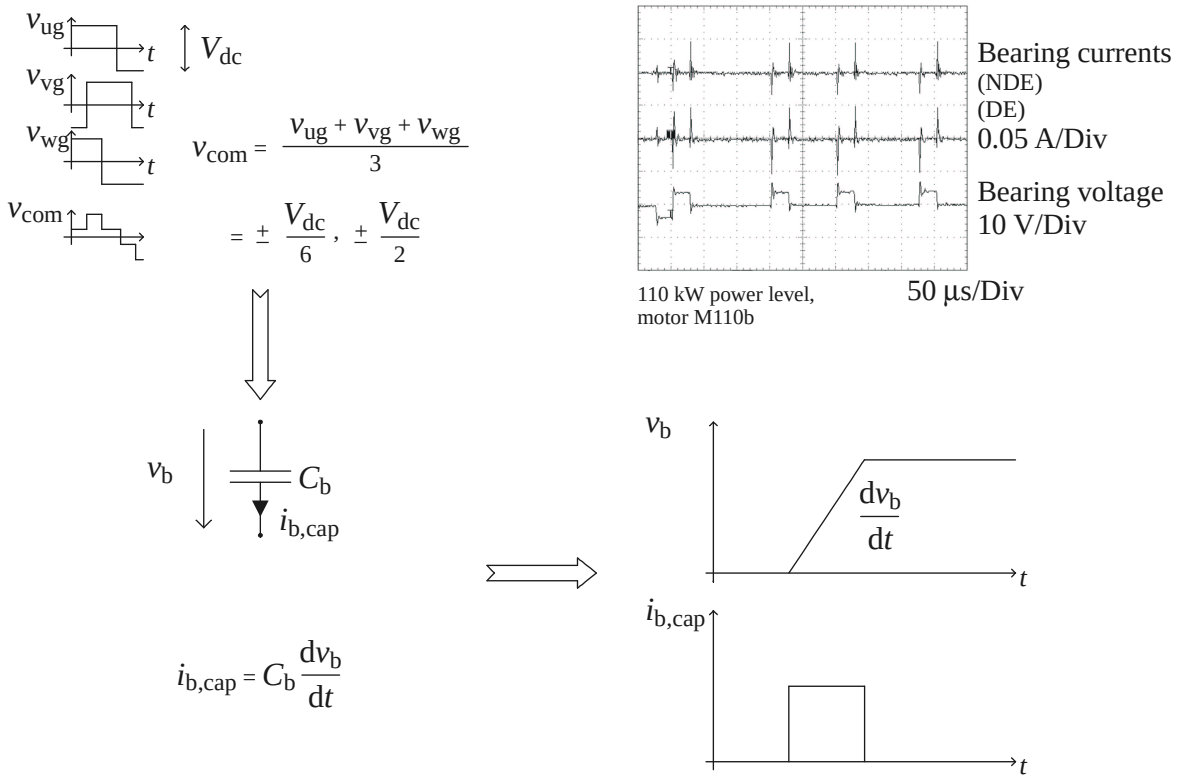

Figure 1.8: Capacitive bearing currents (characterized by small amplitudes of $\hat{i}_b = (5...10)$ mA)

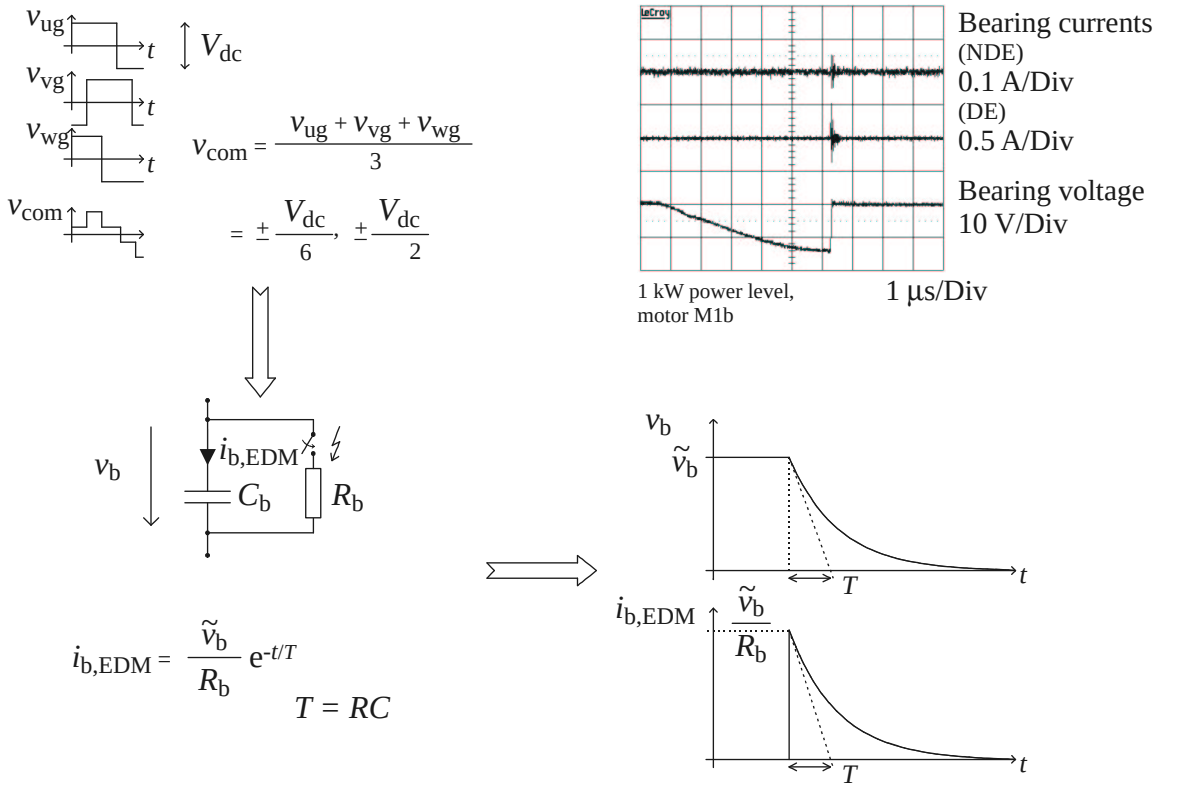

Figure 1.9: EDM-bearing currents (characterized by common mode peak amplitudes of $\hat{i}_b = (0.5...3)$ A and oscillating frequency of several MHz)

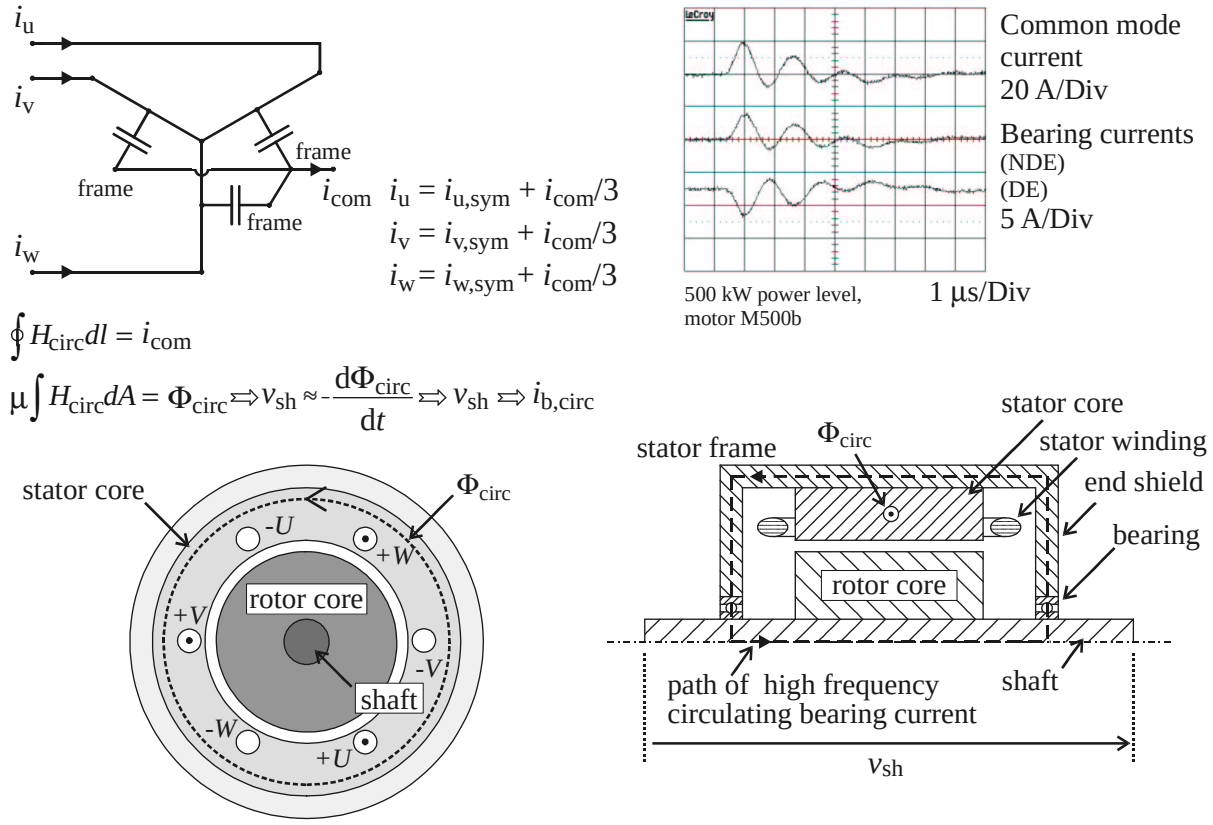

Figure 1.10: High frequency circulating bearing currents (characterized by differential mode, large amplitudes of several A (depending on the motor size) and oscillating frequency of several 100 kHz)

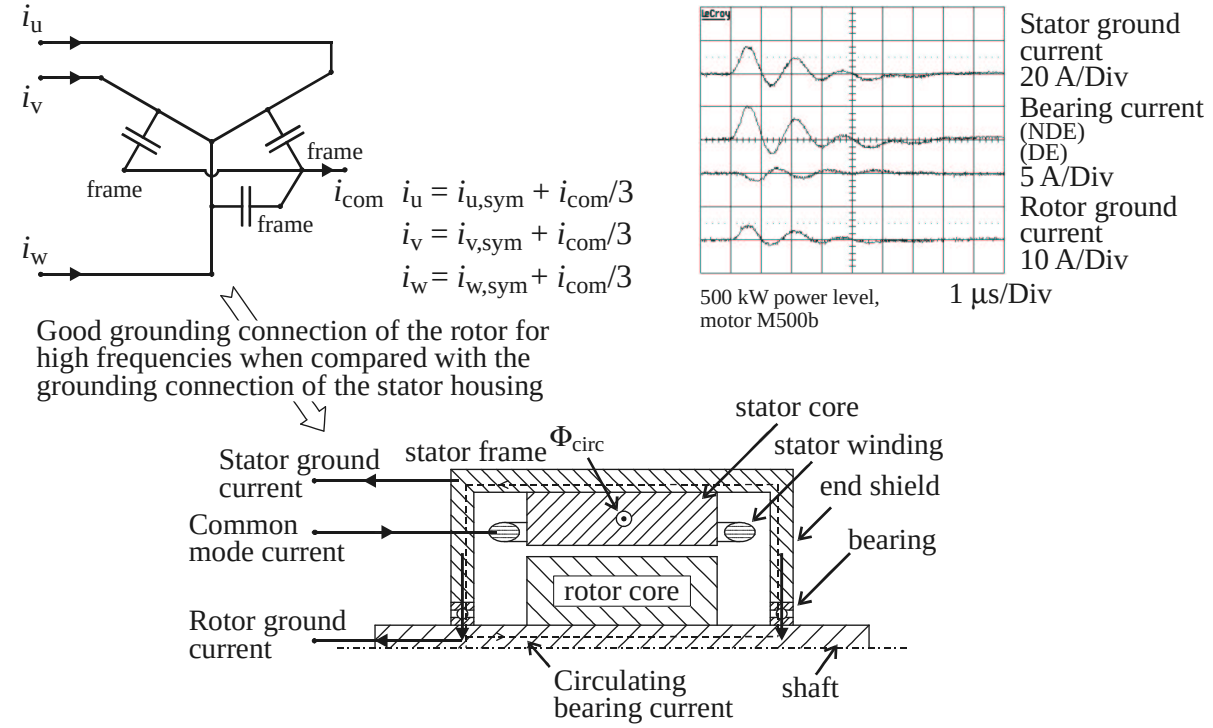

Figure 1.11: Rotor ground currents (characterized by common mode, large amplitudes of several A (depending on the motor size) and oscillating frequency of several 100 kHz)

(iv) *Rotor ground currents*:

If the motor is grounded via the driven load, part of the overall ground current may pass as rotor ground current i_{rg}. Depending on the HF-grounding impedances of stator housing and rotor, i_{rg} may reach considerable magnitudes with increasing motor size. As i_{rg} passes nearly totally via the bearing of the motor and - passing the conductive coupling - via the bearing of the driven load, it can be especially harmful to the bearings and destroy motors in short operation time (Fig. 1.11). Section 7.5 (p. 132) contains the theoretical discussion of this type of bearing current.

1.5.1 Endangerment of the Bearings through Bearing Currents

The bearings of a machine depend on motor size, field of application and conditions of operation and may vary in many aspects between different machines. Therefore, absolute values of bearing currents are not the appropriate measure to evaluate the endangerment of bearings due to bearing currents.

The *Hertz*'ian contact area A_{H} is given by the elastic deformation of the balls or rolls of the bearing under the mechanical pressure in practical operating conditions (→ Appendix C, p. 211). In the context of "classical" bearing currents, the endangerment of bearings due to bearing currents is considered via the "apparent" bearing current density J_b. J_{b} is given by the peak value of the bearing current i_{b}, $\hat{i}_{\mathrm{b}}$, related to the *Hertz*'ian contact area A_{H} (1.5):

$$J_{\mathrm{b}} = \hat{i}_{\mathrm{b}}/A_{\mathrm{H}} \tag{1.5}$$

Experience from the field of dc- and low frequency ac-applications (50 / 60 Hz) has given critical limits of bearing current densities to consider the endangerment of the bearing. Summarizing different reports [6], [7], [8], [9], [10], [26],

▷ bearing current densities $J_{\mathrm{b}} \leq 0.1$ A/mm^2 do not influence bearing life and

▷ bearing current densities $J_{\mathrm{b}} \geq 0.7$ A/mm^2 may significantly reduce bearing life.

One research lab projects bearing life with EDM- and dv/dt-currents by converting historical current density based on a mechanical model of the bearing contact area [27]. According to these authors,

▷ bearing current densities $J_{\mathrm{b}} \leq 0.4$ A/mm^2 do not degrade bearing life,

▷ bearing current densities $J_{\mathrm{b}} \leq (0.6...0.8)$ A/mm^2 do probably not degrade bearing life,

▷ bearing life with bearing current densities $J_{\mathrm{b}} \geq 0.8$ A/mm^2 may be endangered.

Except for this, statements on the mechanism of damage and a limit for *dangerous bearing current density under inverter-supply* had been missing. This led to the setup of a series of tests for bearing damage assessment within the research program. The tests are content of Chapter 6 (p. 93).

Chapter 2

Research Program

2.1 Overview

The following research program for systematical bearing current evaluation in variable speed drive systems mainly with squirrel-cage induction motors was set up:

Several *totally enclosed, fan-cooled, squirrel-cage induction motors* of three different power levels (11 kW / 110 kW / 500 kW) - two motors per power level - from different manufacturers were selected for the studies. In addition to these motors, two outer rotor, inner stator EC-motors (*E*lectronically *C*ommutated permanent magnet motors) for fan applications with 0.8 kW rated power were chosen. Thereby, a certain variation of motor attributes, such as slot geometry, air-gap diameter, shape and size of winding overhang, end-shield geometry and bearing size was achieved (Table 2.1).

Fitting to the studied induction motors, a number of *standard voltage source IGBT-inverters* available on the market, again from different manufacturers, were chosen for motor supply (Table 2.2). All of the inverters for the induction motors have a dc-link voltage of $V_{\mathrm{dc}} = 560$ V. The EC-motors were operated with an EC-controller with a

Power level	Motor	Motor type	Rated power	Number of poles	Shaft height
1 kW	M1a	PM-ECM	0.8 kW	4	63 mm
	M1b	PM-ECM	0.8 kW	4	63 mm
11 kW	M11a	AC-IM	11 kW	4	160 mm
	M11b	AC-IM	11 kW	4	160 mm
110 kW	M110a	AC-IM	110 kW	4	280 mm
	M110b	AC-IM	110 kW	4	280 mm
500 kW	M500a	AC-IM	435 kW	6	400 mm
	M500b	AC-IM	560 kW	2	400 mm

Table 2.1: Selected motors for bearing current investigations, PM-ECM = *P*ermanent *M*agnet *E*lectronically *C*ommutated Motor, AC-IM = *A*luminum *C*age *I*nduction *M*otor

Power level	Inverter	Rated power	Inverter Control	Switching frequency
1 kW	EC1	1.2 kVA	asynchronous PWM	9 kHz (fixed)
11 kW	I11a	18 kVA	asynchronous PWM	(3...14) kHz (fixed)
	I11b	30 kVA	direct torque control (hysteresis control)	(2...3) kHz (average)
	I11c	20 kVA	space vector control with predictive control algorithm	(4.5...7.5) kHz (average)
110 kW	I110a	147 kVA	asynchronous PWM	(3...4.5) kHz (fixed)
	I110b	114 kVA	direct torque control (hysteresis control)	(2...3) kHz (average)
	I110c	118 kVA	voltage vector control with predictive control algorithm	(3...4.5) kHz (average)
500 kW	I500	540 kVA	asynchronous PWM	(1.7...2.5) kHz (fixed)

Table 2.2: Selected inverters for bearing current investigation

dc-link voltage of $V_{dc} = 400$ V. One main difference between the chosen inverters is the type of inverter control pattern of the output voltage (a) asynchronous PWM (*P*ulse *W*idth *M*odulation) with fixed switching frequency, b) direct torque control (hysteresis control) with variable switching frequency, c) space vector control with predictive control algorithm to obtain sinusoidal current and with variable switching frequency. A lot of literature on this subject is available. A good overview is given e.g. in [28] and [29]. The switching frequency f_c of the EC-controller of the 1 kW power level is 9 kHz. The switching frequencies f_c of the switching elements range from 3 kHz to 14 kHz for the 11 kW, 2 kHz to 4.5 kHz for the 110 kW and 1.7 kHz to 2.5 kHz for the 500 kW power level. Another significant difference are the IGBT-switching elements that produce different voltage waveforms and dv/dt at the inverter output (→ Appendix G, p. 229).

For each of the power levels 11 kW, 110 kW and 500 kW, unshielded and shielded *motor cables* of different lengths ($l_c = 2$ / 10 / 50 / 80 m) were chosen. The EC-motors were supplied with unshielded cable with $l_c = 1$ m (Table 2.3).

Different *inverter-output filters* (dv/dt-filters, dv/dt-reactors, sinusoidal filters, common mode chokes and one common mode filter) were selected, again for each power level 11 kW, 110 kW and 500 kW (Table 2.4). For both power levels 11 kW and 110 kW, one inverter (inverters I11c and I110c) contains an integrated dv/dt-filter at the inverter output. This filter reduces the dv/dt at the inverter output down to $dv/dt < 0.5$ kV/μs.

Power level	Cross sectional area	Cable type	Remark
1 kW	4 x 0.5 mm^2	Y-JZ (unshielded)	
11 kW	4 x 2.5 mm^2	Y-JZ (unshielded)	
	4 x 2.5 mm^2	NY-CY (shielded)	coaxial PE
110 kW	4 x 70 mm^2	NYY-J (unshielded)	
	4 x 70 mm^2	2YSLCY-J (shielded)	alu-tape & braided shield
500 kW	3 x 150 mm^2 + 1 x 70 mm^2	NYY-J (unshielded)	two cables in parallel
	3 x 150 mm^2 + 3 x 25 mm^2	2YSLCY-J (shielded)	two cables in parallel alu-tape & braided shield

Table 2.3: Selected motor cables for bearing current investigation

Power level	Filter	Rated power	Filter type	Remark (→ Figs. 5.1, 5.3, 5.4, p. 75)
11 kW	DVF11a	17 kVA	dv/dt-filter	RLC-combination
	DVF11b	17 kVA	dv/dt-filter	RLC-combination with integrated common mode choke
	SF11a	22 kVA	sinusoidal filter	$L_{\mathrm{ph}} = 2$ mH $C_{\mathrm{LL}} = 2$ μH
	SF11b	22 kVA	sinusoidal filter	$L_{\mathrm{ph}} = 1$ mH $C_{\mathrm{LL}} = 4$ μH
	CMC11a	17 kVA	common mode choke	core material: ferrite
	CMC11b	55 kVA	common mode choke	core material: stainless steel
	CMF11	8 kVA	common mode filter	connection to the dc-link of the inverter
110 kW	DV110a	114 kVA	dv/dt-reactor	$L_{\mathrm{ph}} = 0.092$ mH
	DV110b	118 kVA	dv/dt-reactor	$L_{\mathrm{ph}} = 0.5$ mH
	SF110	118 kVA	sinusoidal filter	$L_{\mathrm{ph}} = 0.5$ mH $C_{\mathrm{LL}} = 0.35$ μH
	CMC110	139 kVA	common mode choke	core material: ferrite
500 kW	DV500	312 kVA	dv/dt-reactor	$L_{\mathrm{ph}} = 0.05$ mH
	SF500	423 kVA	sinusoidal filter	$L_{\mathrm{ph}} = 0.05$ mH $C_{\mathrm{LL}} = 0.24$ μH
	CMC500	159 kVA	common mode choke	core material: stainless steel

Table 2.4: Selected inverter-output filters for bearing current investigation

Furthermore, "*conventional*" as well as *insulated* ("coated") and *hybrid bearings* were studied (Tables 2.5 and 2.6). Conventional rolling bearings with the inner and outer rings as well as the balls made from stainless steel were used for the measurements on the influence of all system parameters other than the type of bearing. Except for motor M500a, all motors are designed for operation with single row, deep grove ball bearings. Motor M500a is operated with ball and cylindrical roller bearings (→ Appendix C, p. 211). Insulated bearings are bearings with all elements made from stainless steel that have an additional insulating layer at outside and end faces of the outer bearing ring. The coat is made from a ceramic material consisting mostly of aluminum oxide (Al_2O_3). Layer thickness is generally (50...250) μm and the coat can sustain dc-voltages of more than $v_{dc} \geq 1000$ V. Hybrid bearings have inner and outer rings made from stainless steel and rolling elements made from ceramics (Silicon Nitride, Si_3N_4).

The bearings of the EC-motors of the 1 kW power level were lubricated with the *standard high impedance bearing grease Asonic* GHY72. All bearings of the motors at the 11 kW, 110 kW and 500 kW power level were lubricated with the *standard high impedance bearing grease Norlith* STM3 (→ Section A.5, p. 207).

The manufacturers of the drive components are summarized in Table 2.7. Note that the different inverters of the 11 kW and 110 kW power level, inverters I11a, I11b and I11c and inverters I110a, I110b and I110c, are from the same manufacturers respectively.

►►► An overview of the selected motors, inverters, cables, filters and bearings is given in Table 2.8. The data of the test objects are given in detail in Appendix A (p. 195).

All measurements were done using the same measurement technique with the motors prepared and set up in the same way to obtain comparable measurement results (→ Chapter 3, p. 29). Bearing currents i_b and stator and rotor ground currents i_g and i_{rg} were measured with high frequency current probes ($f_{cut\text{-}off} = 50$ MHz; → Appendix B, p. 209). For each point of operation, a large number of measurement samples ($N_s \geq 30$) with a time window of 8 ms per sample was taken. Average peak-to-peak (pk-to-pk) current values from the maximum value per sample were used to get statistically reliable results (→ Section 3.4, p. 34).

Bearing temperatures ϑ_b were measured at the outer bearing race, using thermo-couples type J (→ Appendix B, p. 209).

Line-to-line and line-to-earth voltages v_{LL} and v_{Lg} at inverter output and motor terminals, stator winding common mode voltage v_Y as well as bearing and shaft voltages v_b and v_{sh} (→ Section 1.3, p. 6) were measured using high frequency differential voltage probes (→ Appendix B, p. 209).

A detailed description of the measurement techniques is given in Chapter 3 (p. 29).

Power level	Bearing type	Inner race mat.	Outer race mat.	Ball / Roller mat.	Cage mat.	Remark
1 kW	6002	Stainless steel	Stainless steel	Stainless steel	Stainless steel	Deep grove ball bearing, RZ = sealed bearing (non-contact type)
11 kW	6209	Stainless steel	Stainless steel	Stainless steel	Stainless steel	Deep grove ball bearing, C3 = internal clearance greater than normal
	6209	Stainless steel	Stainless steel, Al_2O_3 coat	Stainless steel	Stainless steel	Deep grove ball bearing, C3 = internal clearance greater than normal, thickness of insulating coat = 50 μm
	6209	Stainless steel	Stainless steel	Ceramics (Si_3N_4)	Stainless steel	Deep grove ball bearing, C3 = internal clearance greater than normal
110 kW	6316	Stainless steel	Stainless steel	Stainless steel	Stainless steel	Deep grove ball bearing, C3 = internal clearance greater than normal
	6316	Stainless steel	Stainless steel, Al_2O_3 coat	Stainless steel	Stainless steel	Deep grove ball bearing, C3 = internal clearance greater than normal, thickness of insulating coat = 250 μm
	6316	Stainless steel	Stainless steel	Ceramics (Si_3N_4)	Stainless steel	Deep grove ball bearing, C3 = internal clearance greater than normal
	6317	Stainless steel	Stainless steel	Stainless steel	Stainless steel	Deep grove ball bearing, C3 = internal clearance greater than normal
	6317	Stainless steel	Stainless steel, Al_2O_3 coat	Stainless steel	Stainless steel	Deep grove ball bearing, C3 = internal clearance greater than normal, thickness of insulating coat = 250 μm
	6317	Stainless steel	Stainless steel	Ceramics (Si_3N_4)	Stainless steel	Deep grove ball bearing, C3 = internal clearance greater than normal

Table 2.5: Selected bearings for bearing current investigation at 1 kW, 11 kW and 110 kW power level (mat. = material)

Power level	Bearing type	Inner race mat.	Outer race mat.	Ball / Roller mat.	Cage mat.	Remark
500 kW	NU224e	Stainless steel	Stainless steel	Stainless steel	Stainless steel	Cylindrical roller bearing, C3 = internal clearance greater than normal
	6224	Stainless steel	Stainless steel	Stainless steel	Stainless steel	Deep grove ball bearing, C3 = internal clearance greater than normal
500 kW	6317	Stainless steel	Stainless steel	Stainless steel	Stainless steel	Deep grove ball bearing, C3 = internal clearance greater than normal
	6317	Stainless steel	Stainless steel, Al_2O_3 coat	Stainless steel	Stainless steel	Deep grove ball bearing, C3 = internal clearance greater than normal, thickness of insulating coat = 250 μm

Table 2.6: Selected bearings for bearing current investigation at 500 kW power level (mat. = material)

Motor	Manufacturer	Bearing	Manufacturer	Inverter	Manufacturer	Filter	Manufacturer
M1a	A	6002	H	EC1	A		
M1b	A	6002	H				
M11a	B	6209	I	I11a	L	DVF11a	L
M11b	C	6209	I	I11b	D	DVF11b	M
				I11c	G	SF11a	M
						SF11b	M
						CMC11a	M
						CMC11b	M
						CMF11	M
M110a	D	6316	J	I110a	L	DV110a	D
M110b	E	6316, 6317	J	I110b	D	DV110b	G
				I110c	G	SF110	G
						CMC110	M
						CMC500	M
M500a	F	6224, NU224e	K	I500	F	DV500	M
						SF500	M
M500b	G	6317	J			CMC500	M

Table 2.7: Overview of the manufacturers of the drive components

Power level, motor size	Motor	Inverter	Motor cables, filters and other components
1 kW, 63 mm	-M1a, -M1b	-EC1	- Cables: l_c = 1 m, unshielded
	Conventional bearings		
11 kW, 160 mm	-M11a, -M11b	-I11a, -I11b, -I11c	- Cables: l_c = 2/10/50 m, unshielded / shielded - Filters: dv/dt-filters (DVF11a, DVF11b), sinusoidal filters (SF11a, SF11b), common mode chokes (CMC11a, CMC11b), common mode filter (CMF11)
	Bearings: - Conventional bearings (both motors) - Insulated bearings (motor M11b) - Hybrid bearings (motor M11b)		
110 kW, 280 mm	-M110a, -M110b	-I110a, -I110b, -I110c	- Cables: l_c = 10/50/80 m, unshielded / shielded - Filters: dv/dt-reactors (DV110a, DV110b), sinusoidal filter (SF110), common mode chokes (CMC110, CMC500)
	Bearings: - Conventional bearings (both motors) - Insulated bearings (motor M110b) - Hybrid bearings (motor M110b)		
500 kW, 400 mm	-M500a, -M500b	-I500	- Cables: l_c = 2/10 m, unshielded / shielded - Filters: dv/dt-reactor (DV500), sinusoidal filter (SF500), common mode choke (CMC500)
	Bearings: - Conventional bearings (both motors) - Insulated bearings (motor M500b)		

Table 2.8: Overview of the investigated drive systems, comprising motors, inverters, cables, filters and other components

2.2 Drive Configurations

For all test setups, the *motors, inverters and other components were mounted on electrically insulated test benches*. The motors were connected to the inverter via the selected motor cables for power supply as well as the grounding connection of the motor housing (main setup). The inverter-chassis were grounded to the common ground connection of the laboratory (grounding cable with length l_c = 2 m). The chassis of the EC-controller for operation of the EC-motors was grounded via the 230 V supply cable.

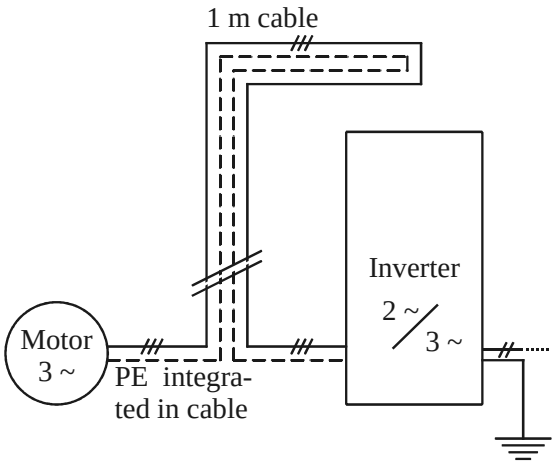

Configuration E1 (”Main setup”)

Figure 2.1: Grounding configuration for bearing current assessment at the 1 kW power level

Four different grounding concepts were chosen (Fig. 2.1 and Fig. 2.2):

▶ Motor grounded via the PE and/or shield of the motor cable to the ground connection of the inverter (configuration E1),

▶ Motor grounded with grounding cable with l_c = 2 m to the common ground connection of the laboratory (configuration E2),

▶ Motor grounded with grounding cable with l_c = 50 m to the common ground connection of the laboratory (configuration E3),

▶ Motor grounded via the PE and/or shield of the motor cable to the ground connection of the inverter and motor shaft grounded with grounding cable with l_c = 2 m to the common ground connection of the laboratory (configuration E4).

The grounding configurations are referred to as $E1_{01}$, $E1_{02}$, $E1_{10}$ and $E1_{50}$ depending on the length of the motor cable. If a shielded cable is used, it is denoted with a star, giving $E1^*_{02}$, $E1^*_{10}$, $E1^*_{50}$ and $E1^*_{80}$ (Table 2.9).

Setup of configuration E1 was used in *all* studies of the different parameters. It is therefore referred to as “main setup”. Other configurations were chosen selectively for further study of the parameter under investigation.

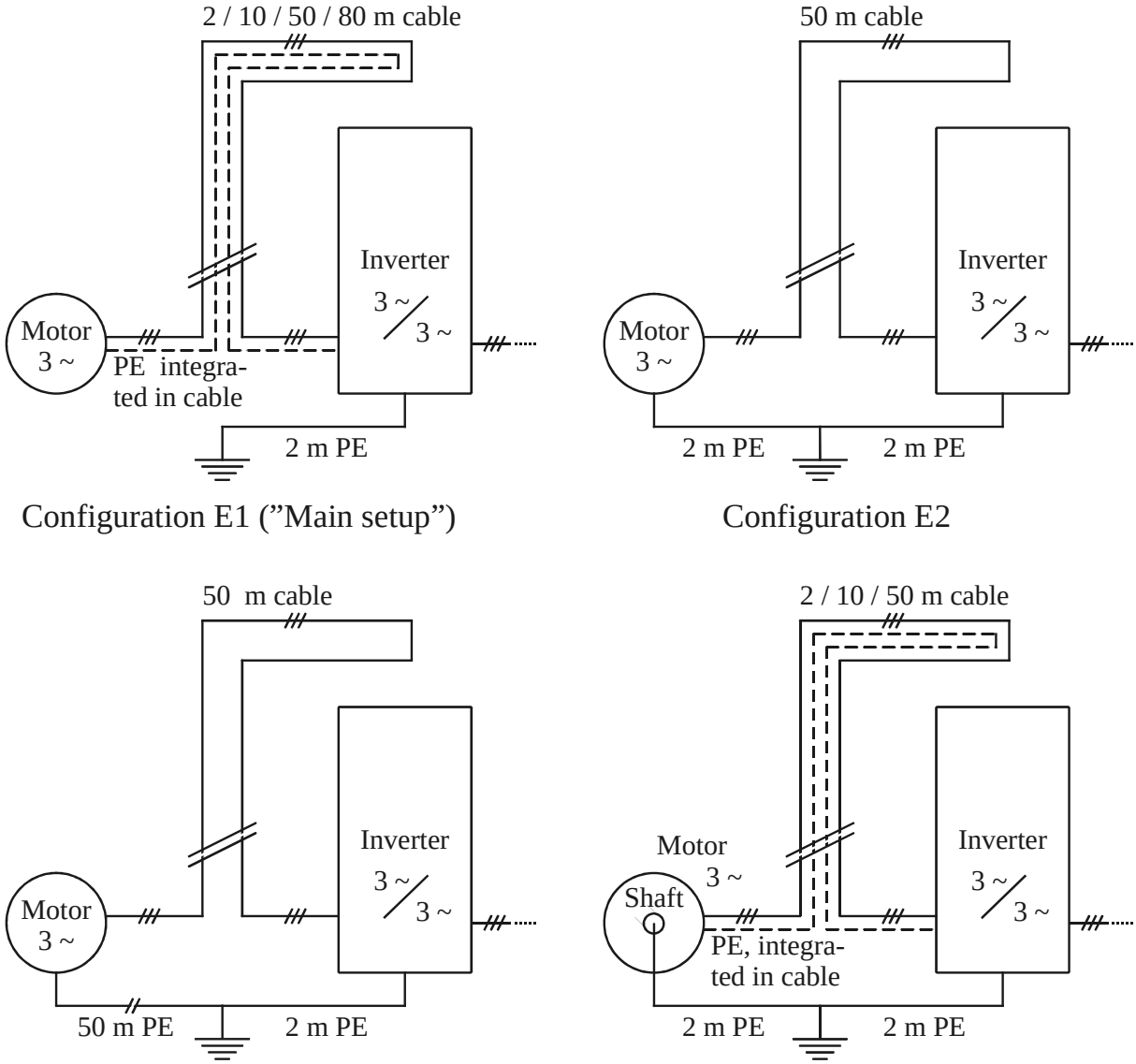

Figure 2.2: Grounding configurations for bearing current assessment at the 11 kW, 110 kW and 500 kW power level

►►► Tables 2.10 and 2.11 give an overview of the investigated drive configurations in terms of motor-inverter-combination, grounding configuration, motor cable type and lengths, operation with use of inverter-output filters and with different types of bearings.

♦ The measurements regarding the influence of the *different motor-inverter-combinations* and the *grounding configurations with rotor not grounded* were done using unshielded cables (Table 4.2).

Configuration	Grounding of the motor
E1	motor grounded via the PE and/or shield of the power cable to the ground connection of the inverter
E2	motor grounded with grounding cable to the common ground connection of the laboratory, $l_c = 2$ m
E3	motor grounded with grounding cable to the common ground connection of the laboratory, $l_c = 50$ m
E4	motor grounded via the PE and/or shield of the power cable to the ground connection of the inverter, motor shaft grounded with grounding cable to the common ground connection of the laboratory, $l_c = 2$ m
Indication of motor cable length	
e.g. $E1_{02}$	$l_c = 2$ m, e.g. grounding configuration E1
e.g. $E1_{10}$	$l_c = 10$ m, e.g. grounding configuration E1
e.g. $E1_{50}$	$l_c = 50$ m, e.g. grounding configuration E1
e.g. $E1_{80}$	$l_c = 80$ m, e.g. grounding configuration E1
Indication of cable type	
e.g. $E1_{10}$	unshielded cable (e.g. grounding configuration E1, $l_c = 10$ m)
e.g. $E1^*_{10}$	shielded cable (e.g. grounding configuration E1, $l_c = 10$ m)

Table 2.9: Notations of grounding configurations

♦ As consequence of the results obtained concerning the influence of different motor-inverter-combinations, for each power level, only *one inverter* was used for the studies of the *influence of cable length and type*, the *impact of inverter-output filters* and of *different types of bearings* (Tables 4.3, 5.2 and 5.4). The influence of these parameters was not studied at the EC-motors.

♦ Measurements on the influence of *cable length and type* were done on *both motors of each power level* 11 kW, 110 kW and 500 kW, using the inverters as shown in Table 4.3 (p. 56).

♦ The influence of *inverter-output filters* was also studied on *both motors of each power level* 11 kW, 110 kW and 500 kW, using the inverters and cables as shown in Table 5.2 (p. 77).

♦ The *type of bearing* was changed on *one motor per power level* 11 kW, 110 kW and 500 kW, using the inverters and cables as shown in Table 5.4 (p. 86).

Power level	Motor	Inverter	Config.	Cable			Filter-op.	Ins./ Hyb. bear.	Table(s)
				length	unsh.	sh.			
1 kW	M1a	EC1	E1	1 m	X				4.2
	M1b	EC1	E1	1 m	X				4.2
11 kW	M11a	I11a	E1	2 m	X		X		4.2, 4.3, 5.2
			E4	2 m	X				4.2
			E1	10 m	X				4.2, 4.3
			E4	10 m	X				4.2
			E1	50 m	X	X			4.2, 4.3
			E2	50 m	X				4.2
			E3	50 m	X				4.2
			E4	50 m	X	X			4.2
		I11b	E1	50 m	X				4.2
			E2	50 m	X				4.2
			E3	50 m	X				4.2
		I11c	E1	50 m	X		X		4.2
			E2	50 m	X				4.2
			E3	50 m	X				4.2
	M11b	I11a	E1	2 m	X		X	X	4.2, 4.3, 5.2, 5.4, 5.5
			E4	2 m	X				4.2
			E1	10 m	X				4.2, 4.3
			E4	10 m	X				4.2
			E1	50 m	X	X			4.2, 4.3
			E2	50 m	X				4.2
			E3	50 m	X				4.2
			E4	50 m	X	X			4.2
		I11b	E1	50 m	X				4.2
			E2	50 m	X				4.2
			E3	50 m	X				4.2
		I11c	E1	50 m	X		X		4.2
			E2	50 m	X				4.2
			E3	50 m	X				4.2

Table 2.10: 1 kW and 11 kW power level - overview of studied investigated configurations (config. = configuration, unsh. = unshielded, sh. = shielded, op. = operation, ins. = insulated, hyb. = hybrid, bear. = bearing)

Power level	Motor	Inverter	Config.	Cable			Filter-op.	Ins./ Hyb. bear.	Table(s)
				length	unsh.	sh.			
110 kW	M110a	I110a	E1	10 m	X	X	X		4.2, 4.3, 5.2
			E4	10 m	X	X	X		4.2
			E1	50 m	X	X			4.2, 4.3
			E2	50 m	X				4.2
			E3	50 m	X				4.2
			E4	50 m	X	X			4.2
		I110b	E1	50 m	X				4.2
			E2	50 m	X				4.2
			E3	50 m	X				4.2
		I110c	E1	50 m	X				4.2
			E2	50 m	X				4.2
			E3	50 m	X				4.2
	M110b	I110a	E1	10 m	X	X	X	X	4.2, 4.3, 5.2, 5.4, 5.5
			E4	10 m	X	X	X		4.2
			E1	50 m	X	X			4.2, 4.3
			E2	50 m	X				4.2
			E3	50 m	X				4.2
			E4	50 m	X	X			4.2
		I110b	E1	50 m	X				4.2
			E2	50 m	X				4.2
			E3	50 m	X				4.2
		I110c	E1	50 m	X				4.2
			E2	50 m	X				4.2
			E3	50 m	X				4.2
500 kW	M500a	I500	E1	2 m	X				4.2, 4.3
			E1	10 m	X	X	X		4.2, 4.3, 5.2
			E4	10 m	X	X			4.2
	M500b	I500	E1	2 m	X			X	4.2, 4.3, 5.4
			E1	10 m	X	X	X		4.2, 4.3, 5.2
			E4	10 m	X	X			4.2

Table 2.11: 110 kW and 500 kW power level - overview of investigated drive configurations (config. = configuration, unsh. = unshielded, sh. = shielded, op. = operation, ins. = insulated, hyb. = hybrid, bear. = bearing)

2.3 Tests for Bearing Damage Assessment

A series of tests for bearing damage assessment was set up in addition to the studies of the influence of the system parameters on the bearing current phenomena. These tests should allow better understanding of the mechanism of damage and give a limit value to evaluate the risk of endangerment of a bearing through a given bearing current.

Therefore, four fan-cooled squirrel cage induction motors with 11 kW rated power - motors M11c, M11d, M11e and M11f - and two suitable voltage-source inverters - inverters I11b and I11d - similar to the motors and inverters used for the research described above were chosen (Table 2.12).

In these tests, the influences of bearing current amplitude $\hat{i}_\mathrm{b}$, "apparent bearing current density" J_b (→ Section 1.5.1, p. 14), inverter switching frequency f_c, inverter control, and time of operation t_op of the motor were investigated.

Detailed description of the tests and discussion of the results is the content of Chapter 6 (p. 93).

<table>
<tr><th>Motors</th><th>Inverters</th><th>Other components</th></tr>
<tr><td>-M11c,
-M11d,
-M11e,
-M11f</td><td rowspan="2">-I11b,
-I11d</td><td rowspan="2">- Shaft brushes to generate rotor ground currents
- Additional capacitances at the motor terminals to increase the rotor ground currents</td></tr>
<tr><td>all motors:
-11 kW power level,
-shaft height 160 mm</td></tr>
<tr><td colspan="3">Conventional bearings</td></tr>
</table>

Table 2.12: Drive components for tests for bearing damage assessment

Chapter 3

Measurement Techniques

3.1 Introduction

Systematical investigations of the influence of different system parameters of a variable speed drive system on the bearing current phenomena need to be done using identical measurement techniques. Therefore, all motors were prepared in the same way and motor setup was identical for all power levels.

Thus, bearing temperatures ϑ_b, bearing currents i_b and bearing voltages v_b on drive-end and non-drive-end, as well as shaft voltages v_{sh} were measured using the same technique for all setups under investigation.

Furthermore, stator ground currents i_g and - if existing - rotor ground currents i_{rg}, stator winding common mode voltages v_Y, as well as dv/dt and voltage waveforms of line-to-line and line-to-earth voltages v_{LL} and v_{Lg} at different points of the operating system were determined similarly for all studied drive configurations.

The data of the high frequency current and voltage probes are given - together with those of the other measuring instruments - in Appendix B (p. 209).

3.2 Motor Setup

All motors were mounted on electrically insulated test benches in order to ensure total ground current flow via the installed grounding connections. This was ensured by one or more grounding cables and / or the shield of the cables that were used.

In the main setup, configuration E1, the motors were connected to the inverter via an unshielded power cable and grounded via the PE of the motor cable. Three other grounding configurations, E2, E3 and E4, were also analyzed, with the motor grounded separately from the inverter or the shaft of the rotor grounded additionally. In all grounding configurations, the inverter-chassis was grounded to the laboratory's common ground connection with a grounding cable with $l_c = 2$ m (→ Chapter 2, p. 15).

The 11 kW, 110 kW and 500 kW motors were operated at no-load with the shaft-mounted fans removed to obtain bearing temperatures ϑ_b typical for load operation. The

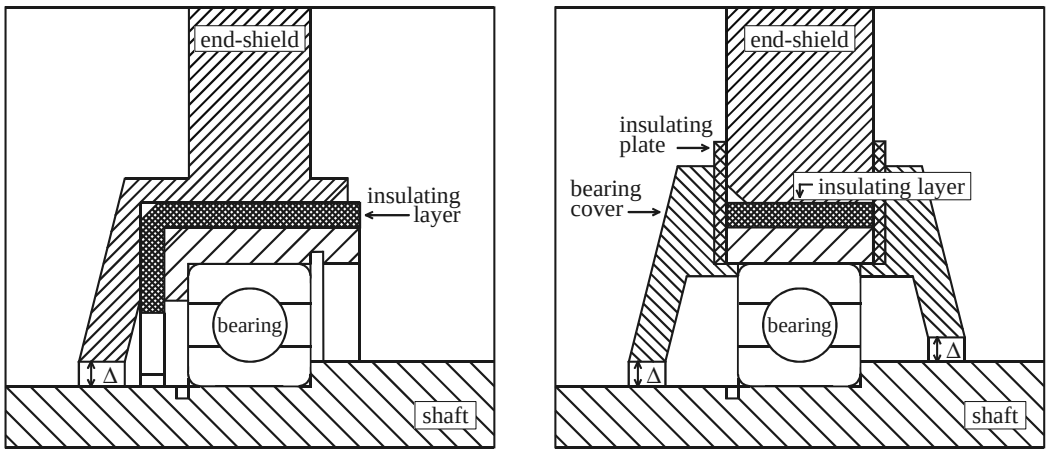

Insulating layer in bearing seats of motors without bearing covers (1 kW / 11 kW power level)

Insulating layer in bearing seats of motors with bearing covers (110 kW / 500 kW power level)

Figure 3.1: Sketch of preparation of the bearing seats for measurement of bearing current; bearing seat insulated towards end-shield

ventilator EC-motors of the 1 kW power level were operated at rated load, due to their special use. The load is given by the fan, thus, it was not necessary to load these motors additionally. The 11 kW, 110 kW and 500 kW motors were heated up by no-load losses to bearing temperatures of $\vartheta_\mathrm{b} \geq 70°\mathrm{C}$, the EC-motors by the load losses to $\vartheta_\mathrm{b} \geq 40°\mathrm{C}$.

The 11 kW, 110 kW and 500 kW motors were operated with rated flux between almost standstill ($n = 15$ /min) and synchronous speed (motors M11a, M11b, M110a, M110b: $n_\mathrm{s} = 1500$ /min, motor M500a: $n_\mathrm{s} = 1000$ /min, motor M500b: $n_\mathrm{s} = 1800$ /min) and with weakened flux up to maximum speed (motors M11a, M11b: $n_\mathrm{max} = 3000$ /min, motors M110a, M110b, M500a: $n_\mathrm{max} = 2000$ /min, motor M500b: $n_\mathrm{max} = 3000$ /min). The 1 kW EC-motors were operated with rated flux between low motor speed, $n = 15$ /min, and $n = 1227$ /min.

3.3 Motor Preparation for Bearing Current Assessment

3.3.1 Measurement of Bearing Currents

The bearing currents i_b should be measured in the same way for all types of bearings studied. Furthermore, the concept should be applicable to all motors of all power levels investigated, and the bearing currents should be measured as close to the bearing as possible. Therefore, an insulating layer was inserted into the end-shields of the motors close to the bearing seat to insulate the bearing from the end-shield. Insulating, temperature resistant plates and sleeves were used to insulate the bearings from the bearing covers

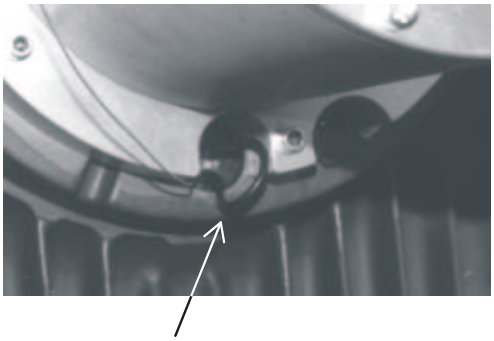

Insulation bridged by copper loop for bearing current measurement
(a)

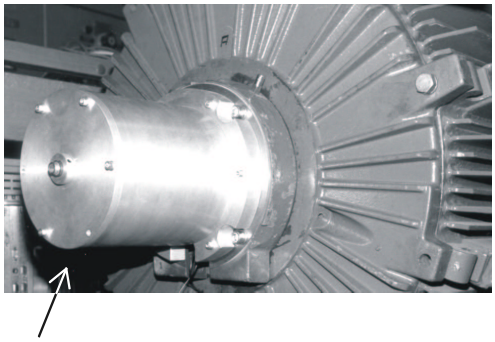

Aluminum cylinder for bearing voltage measurement
(b)

Figure 3.2: Preparation for (a) bearing current and (b) bearing voltage measurement; here 500 kW power level, (a) motor M500a, (b) motor M500b

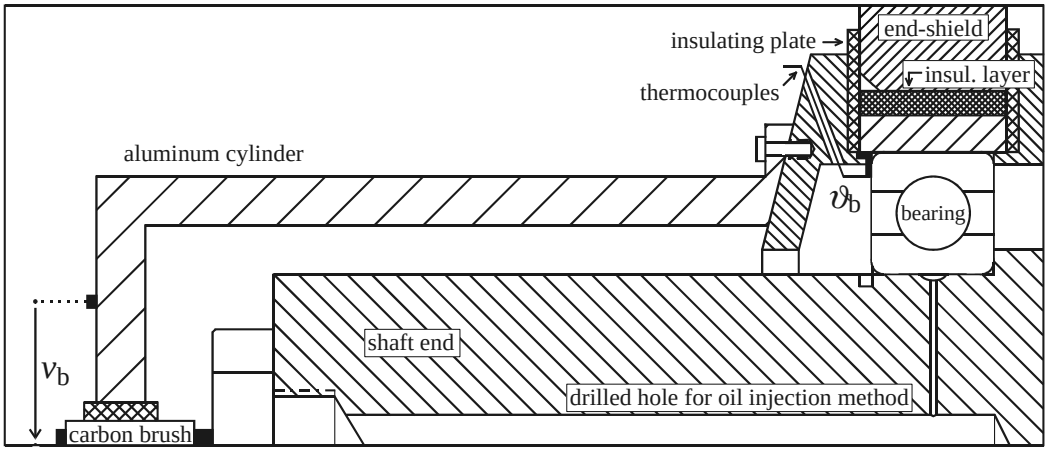

Figure 3.3: Sketch of preparation of the shaft ends for measurement of bearing voltages and application of oil injection method

(Fig. 3.1). The motors of the 1 kW and 11 kW power level had no bearing covers, but only one end-shield on each side. The insulation was bridged by a short copper loop to measure the bearing current.

Influence of the by-passed insulating layer on the measured bearing currents cannot be avoided. However, if the chosen method is the same for all motors, the error will be of systematical nature and the results obtained from measurements can be compared among each other.

To ensure that no current flows from the bearing cover to the rotor[1] via small conductive particles, the diameters of the corresponding openings of the bearing covers[2] were enlarged by 2 mm (Distance Δ in Fig. 3.1).

[1] 11 kW power level: from the end-shield to the rotor
[2] 11 kW power level: end-shields

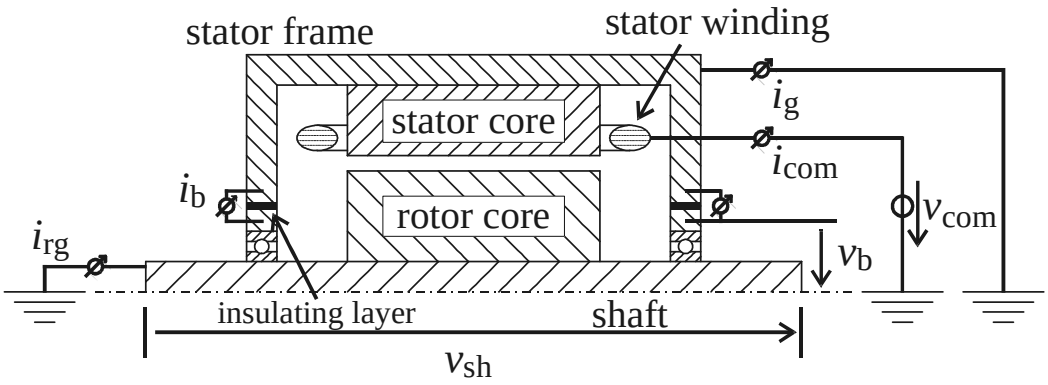

Figure 3.4: Sketch of selected measured electrical quantities

3.3.2 Measurement of Bearing and Shaft Voltages

The environment of an inverter system is subject to a lot of electromagnetic noise. The taps to measure the bearing and shaft voltages v_b and v_{sh} need to be very close together to avoid interference with other signals. For this reason, cylinders from aluminum were manufactured as shown in Fig. 3.3. Using these devices, the electric potential of the outer race of the bearing was accessible at the shaft end, where the potential of the shaft is measured also. This was done frontally, axially to the shaft end with use of carbon brushes and screws with a flat turned head that are axially screwed into the center of the shaft. No cylinders were manufactured for the very small ventilator motors of the 1 kW power level.

3.3.3 Measurement of Bearing Temperatures

The bearing temperature at the inner bearing race cannot be measured without extraordinary expenses. Thus, the temperature at the outer bearing race ϑ_b was measured using Fe-CuNi thermo-couples type J. These thermo-couples were either inserted into a tiny hole in the end-shield very close to the bearing, or soldered on small copper plates that are pressed against the outer race of the bearing (Fig. 3.3).

3.3.4 Removal of Bearings

Both shaft ends of motors M11a, M11b, M11c, M11d, M11e, M11f, M110b and M500b were prepared for bearing removal applying the oil injection method [30], [31]. This method allows bearing removal without doing damage to the bearing (Fig. 3.3).

3.3.5 Measurement of Ground Currents

The *total ground current* i_{com}, also named "common mode current", is the sum of the three phase currents. It flows to the machine through the phase cables and leaves via the grounding connections. In the research program, total ground current flow via the installed grounding connections, i.e. PE of motor cable and/or additional grounding cables, e.g. at the shaft, and/or cable shield, was assured through motor installation on electrically insulated test benches (→ Section 3.2). The ground current can flow back to its source as *stator ground current* i_{g} and as *rotor ground current* i_{rg}. If the rotor of the machine is not grounded, the stator ground current i_{g} equals the common mode current i_{com} (3.1).

$$i_{\mathrm{com}} \;=\; i_{\mathrm{u}} + i_{\mathrm{v}} + i_{\mathrm{w}} \;=\; i_{\mathrm{g}} + i_{\mathrm{rg}} \tag{3.1}$$

With use of an unshielded motor cable, the stator ground currents i_{g} were measured with high-frequency current probes at the motor PE. This current equals the total ground current in grounding configurations E1 to E3, where the rotor was not grounded. In grounding configuration E4 (rotor grounded), the total ground current can be derived from the measured stator and rotor ground currents (3.1).

With use of a shielded motor cable, at the 11 kW power level, the shield of the shielded cable is used as PE conductor. The total ground current i_{com} was measured around the three conductors used for motor supply. This current equals the stator ground current in configurations E1 to E3 (rotor not grounded). In grounding configuration E4 (rotor grounded), the stator ground current can be derived from the measured total ground currents and rotor ground currents.

This method could not be applied to the 110 kW and 500 kW power level, because no current probe with an opening as well as band width large enough for this purpose was available. At the 110 kW and 500 kW power level, with use of a shielded motor cable, i_{g} was measured at the motor PE and the pigtail connection (Fig. 3.5a) of the cable shield. It has to be pointed out that, for reasons of EMI, the pigtail cable grounding connection is *not* recommended for practical applications. In the context of the research presented,

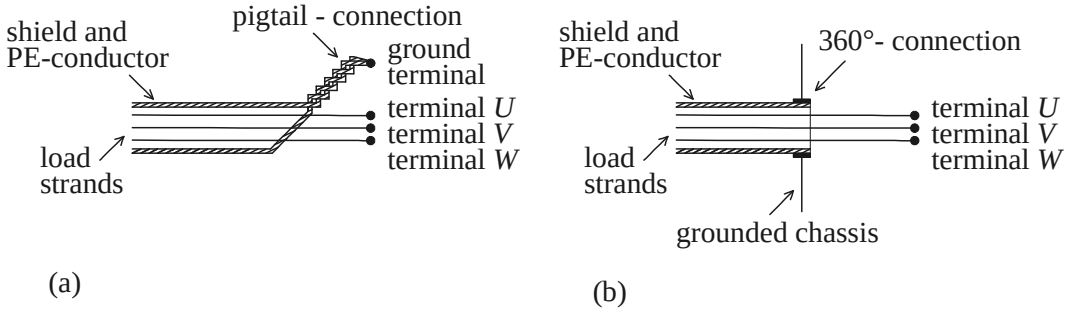

Figure 3.5: (a) Pigtail and (b) 360°-connection of a shielded cable

for comparison, measurements of the bearing currents i_b were done with both the cable shield connected with a pigtail connection (length ≈ 0.2 m) and using a 360°-connection (Fig. 3.5b). No difference was found on the measured bearing currents of any type. The increase in impedance in the zero-sequence system with use of a pigtail connection is of importance for the frequency range of EMI. However, the impact on the magnitude of the ground currents seems negligible (→ Chapter 4, p. 41, and Section 7.5, p. 132).

The rotor ground currents i_{rg} were measured with high-frequency current probes at the grounding cable of the rotor that was used to represent the configuration of a grounded motor shaft in practical applications.

3.4 Quantification of the Measurement Results

3.4.1 Ground and Bearing Currents

The quantification of the measured currents was an important aspect of the research. It is important to obtain statistically reliable results and not to measure a maximum amplitude that only rarely occurs.

The following technique was applied for the measured currents: A large number of measurement samples ($N_s \geq 30$) was taken for each point of operation studied. Sampling time was $t_s = 8$ ms and sampling depth 100 MS/s. The maximum peak-to-peak (pk-to-pk) value occurring within this time window was measured for each sample taken and the average sample value over all samples taken was calculated. These average peak-to-peak current values from the maximum value per sample were used to get statistically reliable results. *Standard deviation was generally below 25%.* An example of the distribution of measured maximum values per sample is given in Table 3.1 and Fig. 3.6.

The high sampling depth was necessary to capture the EDM-currents of several MHz. Time window and sampling size were based on experience. In most cases, no change of the measured maximum amplitudes per sample was found after approximately 10 samples. The higher number of samples was chosen to increase the confidence level. Measurements with sampling size $N_s \geq 100$ were done on a random basis and the results compared with

Current	Average value	Minimum value	Maximum value	Standard deviation
	A pk-to-pk	A pk-to-pk	A pk-to-pk	A pk-to-pk
Common mode current	45.2	33.4	59.7	9.7
Bearing current NDE	2.93	1.53	4.00	0.69
Bearing current DE	2.93	1.51	4.00	0.69

Table 3.1: Example of the distribution of measured maximum values per sample, values of the example of a scope plot of measurement of ground and bearing currents (Fig. 3.6)

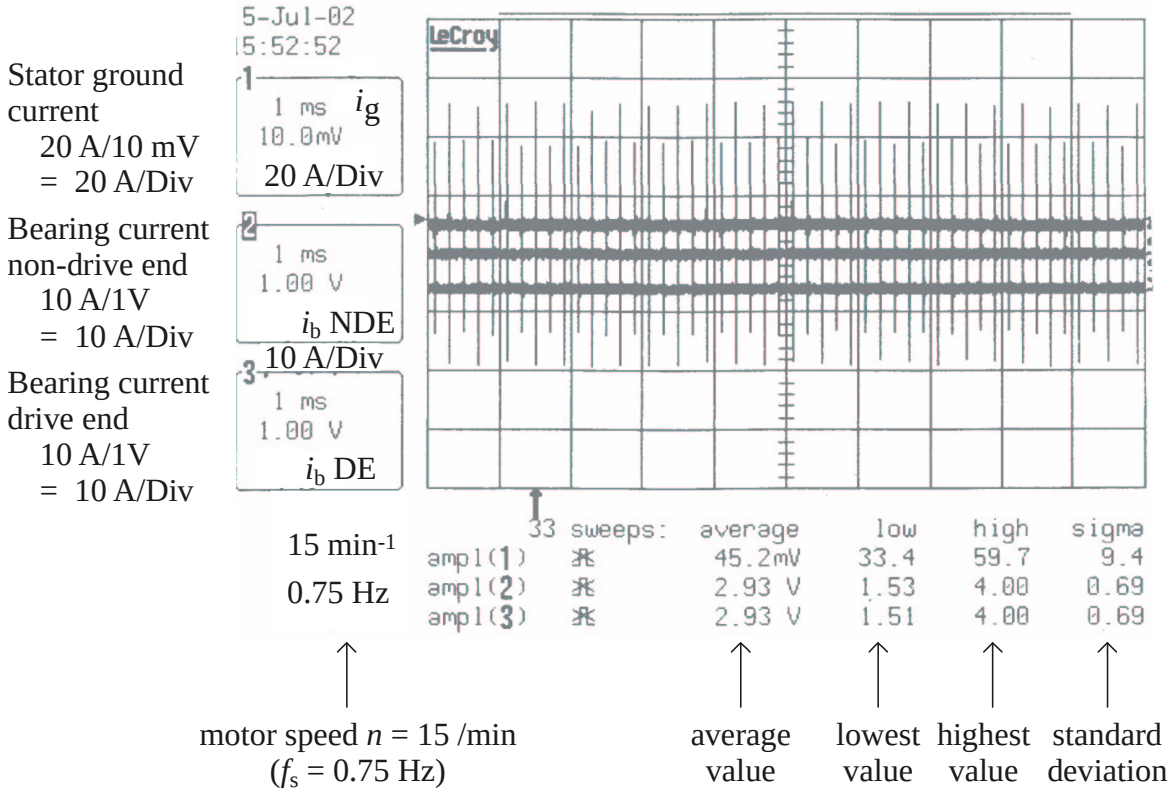

Figure 3.6: Example of a scope plot of measurement of ground and bearing currents, here 500 kW power level, motor M500a and inverter I500, motor speed $n = 15$ /min, configuration $E1_{10}$ ($l_c = 10$ m, unshielded motor cable), $\vartheta_b \approx 70°C$ (Table 3.1)

those obtained for the same point of operation with sampling size $N_s \geq 30$ to verify this statement empirically. If the values of the bearing currents were different in the DE- and NDE-bearing (EDM-currents, superposition of circulating bearing currents and rotor ground currents), the larger value was taken.

The waveforms of the currents were measured and stored on the hard disk of the scope for further analysis. The sampling depth was chosen according to the frequency range concerned. Sampling length of measured ground currents was generally one period of the fundamental operating frequency of the motor. Sampling length of rotor ground and bearing currents was adapted to the waveform of the currents, and plots of discrete occurrences of bearing currents were taken.

3.4.2 Voltages at Different Points of the Operating System

The voltage waveforms at different points of the operating system were also measured with a sampling depth according to the frequency range concerned, and a sampling time of generally one period of the fundamental operating frequency of the motor. The dv/dt and the voltage over-shoot of the different measured voltages were determined manually from these stored traces, using the cursor functions of the scope.

Determination of dv/dt was done according to the international standard IEC 60034-17 [18] where dv/dt is defined as the ratio of the voltage difference between 90 % and 10 % of the final value of the voltage $\hat{v}$ and the rise time t_r (3.2) which is the time interval needed for the voltage rise (3.3) (Fig. 3.7a).

$$t_r = t_{0.9\hat{v}} - t_{0.1\hat{v}} \tag{3.2}$$

$$\frac{dv}{dt} = \frac{0.9\hat{v} - 0.1\hat{v}}{t_{0.9\hat{v}} - t_{0.1\hat{v}}} \tag{3.3}$$

where:

t_r = rise time,
$\hat{v}$ = final value of voltage rise.

Voltage over-shoot was measured as the value of the voltage rise above steady-state value when compared with the steady-state value (3.4) (Fig. 3.7b).

$$\text{over-shoot} = \frac{\hat{v} - v_{\text{steady-state}}}{v_{\text{steady-state}}} \tag{3.4}$$

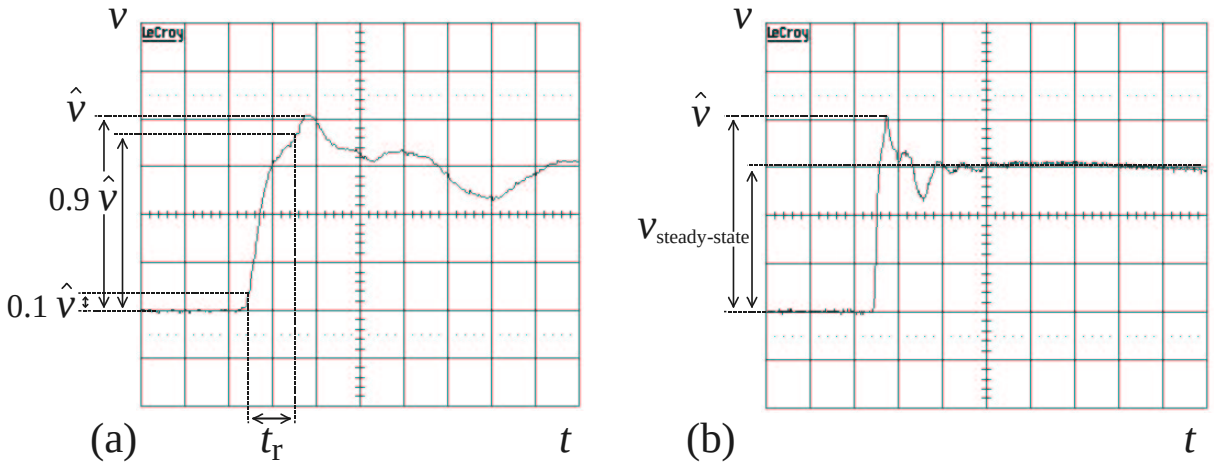

Figure 3.7: Measurement of rise time t_r according to [18] and determination of voltage over-shoot

3.5 Measurement of Motor Capacitances and Bearing Voltage Ratios

3.5.1 Stator Winding-to-frame and Phase-to-phase Capacitances

The stator winding-to-frame capacitance C_{wf} (→ Section 1.4, p. 8) is a fundamental reason for the high frequency ground current as discussed in Section 7.5 (p. 132).

The capacitances C_{wf} of the induction motors were measured along with the phase-to-phase capacitances C_{ph} (→ Section 1.4, p. 8) using a capacitance meter and three different configurations for each motor.

The terminals of the stator windings were shorted for the measurement of the resultant capacitance C_{m1} (Fig. 3.8a) and open-circuited for the resultant capacitances C_{m2} and C_{m3} (Fig. 3.8b). The parallel capacitance between stator winding and rotor C_{wr} is - depending on the motor - between more than ten (11 kW power level) and more than one hundred (500 kW power level) times smaller (→ Section 7.3, p. 112). Therefore, the presence of the rotor is neglected.

$$C_{\mathrm{m1}} = 3C_{\mathrm{wf}} \tag{3.5}$$

$$C_{\mathrm{m2}} = \frac{1}{2}(C_{\mathrm{wf}} + 3C_{\mathrm{ph}}) \tag{3.6}$$

$$C_{\mathrm{m3}} = C_{\mathrm{wf}} + \frac{2C_{\mathrm{wf}}C_{\mathrm{ph}}}{C_{\mathrm{wf}} + C_{\mathrm{ph}}} \tag{3.7}$$

C_{wf} and C_{ph} can be calculated from (3.5) and (3.6), using (3.8) and (3.9). Equation (3.7) can be used for crosscheck.

$$C_{\mathrm{wf}} = \frac{1}{3}C_{\mathrm{m1}} \tag{3.8}$$

$$C_{\mathrm{ph}} = \frac{1}{3}(2C_{\mathrm{m2}} - C_{\mathrm{wf}}) \tag{3.9}$$

The measurement results are given and compared with calculations in Section 7.3 (p. 112).

3.5.2 Rotor-to-frame and Rotor-to-winding Capacitances

The rotor-to-frame and rotor-to-winding capacitances C_{rf} and C_{rw} (→ Section 1.4, p. 8) play an important role on the occurrence of EDM-bearing currents as reasoned in Section 7.4 (p. 121).

At standstill, the metallic contact of the bearings short-circuits the capacitance C_{rf}, because this capacitance is in parallel to the bearings. As the bearing seats of the test motors were insulated for measurement of the bearing currents i_{b} (→ Section 3.3.1, p. 30), it was possible to interrupt this short-circuit by opening the copper loop for bearing current measurement. Then, the capacitances of the insulating layer of the end-shields on DE and NDE-side, $C_{\mathrm{i,DE}}$ and $C_{\mathrm{i,NDE}}$, were in parallel to C_{rf}. By short-circuiting the

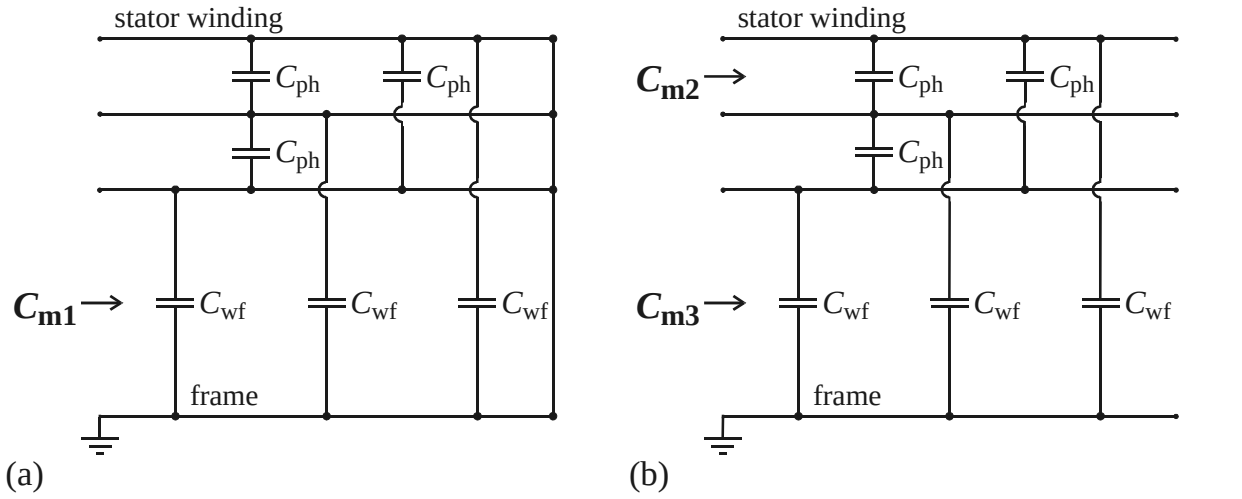

Figure 3.8: Measurement of stator winding-to-frame and phase-to-phase capacitances

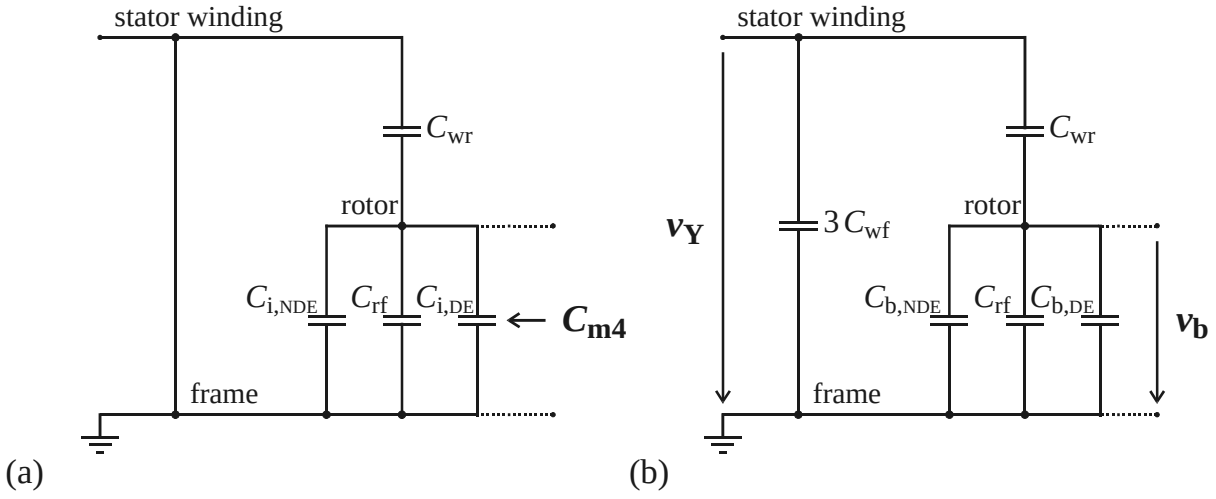

Figure 3.9: Measurement of (a) rotor-to-frame capacitance and (b) bearing voltage ratio

capacitances between stator winding and frame, the sum of $C_{\mathrm{rf}} + C_{\mathrm{wr}}$ could be derived from measurement of the capacitance C_{m4} as shown in Fig. 3.9a (3.10):

$$C_{\mathrm{rf}} + C_{\mathrm{wr}} = C_{\mathrm{m4}} - C_{\mathrm{i,NDE}} - C_{\mathrm{i,DE}} \tag{3.10}$$

It is important to note that the *same results* were obtained *without short-circuiting* the capacitances between stator winding and frame C_{wf}, because C_{wf} is orders of magnitudes larger than C_{wr}. It was not possible to separate the two capacitances with measurements of this rather simple type, because of the ratios of the capacitances. The measurement results are presented along with the calculated values in Section 7.3 (p. 112).

3.5.3 Bearing Voltage Ratios

The BVRs (→ Section 1.4, p. 8) of the test motors were determined by measuring at the same time v_Y and v_b (Fig. 3.9b). The bearing voltage v_b was measured using the aluminum cylinders and carbon brushes as described in Subsection 3.3.2 of this chapter. The stator winding common mode voltage v_Y can be measured between star point and ground connection of the motors if the motor is Y-connected, or with use of an artificial star point. In the work presented, v_Y was measured between motor star point and grounding connection. Out of the test motors, only motor M11b is designed for $V_s = 400$ V Y / $f_s = 50$ Hz. Therefore, motors M11a, M110a, M110b and M500a were operated at $V_s = 400$ V Y / $f_s = 30$ Hz ($\frac{50 \text{ Hz}}{\sqrt{3}} \approx 30$ Hz), motor M500b at $V_s = 400$ V Y, $f_s = 17$ Hz ($\frac{50 \text{ Hz}(400 \text{ V}/690 \text{ V})}{\sqrt{3}} \approx 17$ Hz) for operation with rated flux.

The measured BVRs are given together with the calculated BVRs in Section 7.3 (p. 112). Additional data and waveforms of v_Y and v_b are shown in Appendix E (p. 219).

Chapter 4

Ground and Bearing Currents in Industrial Drive Systems

4.1 Measurements at Line-Operation

In order to see the influence of "classical" bearing currents on the measurement results, bearing currents i_b and shaft voltages v_{sh} at line-operation, rated flux and speed and bearing temperature typical for load operation, $\vartheta_b \approx 70°C$, were measured in advance. This was done for the 11 kW, 110 kW and 500 kW power level. None of the investigated motors features "classical" bearing currents. All measured shaft voltages v_{sh} have uncritical low values that are not able to lead to lubrication film breakdown. Therefore, no bearing current flow through the lubrication film of the bearings was possible.

One research lab reported on flow of "classical" bearing currents initiated by flow of inverter-induced high frequency circulating bearing currents at one large squirrel cage induction motor ($P_r = 355$ kW) [4]. This phenomenon was not observed within the studies carried out in the research presented here.

♦ ***11 kW power level*:** The bearing currents i_b and shaft voltages v_{sh} of motors M11a and M11b at line-operation, rated flux and rated speed and bearing temperature typical for load operation ($V_s = 400$ V, $n = 1500$ /min / $f_s = 50$ Hz, $\vartheta_b \approx 70°C$) were measured. No bearing currents were found. The measured shaft voltages are shown in Fig. 4.1a and Table 4.1.

♦ ***110 kW power level*:** The bearing currents i_b and shaft voltages v_{sh} of motors M110a and M110b at line-operation, rated flux and rated speed and bearing temperature typical for load operation ($V_s = 400$ V, $n = 1500$ /min / $f_s = 50$ Hz, $\vartheta_b \approx 70°C$) were measured. Again, no bearing currents were found. The measured shaft voltages are shown in Fig. 4.1b and Table 4.1.

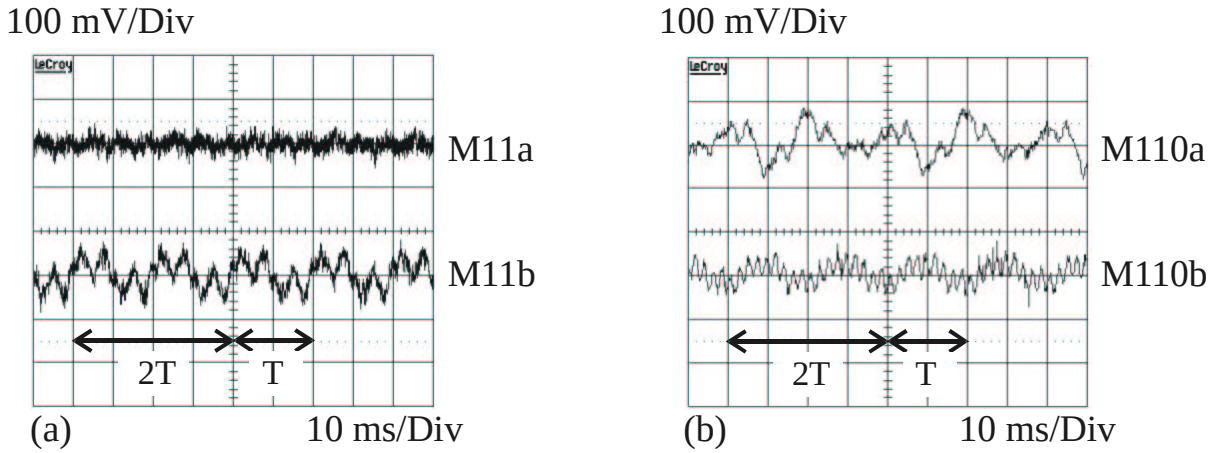

Figure 4.1: Measured shaft voltages of motors (a) M11a, M11b, (b) M110a and M110b at line-operation, $V_s = 400$ V, $n = 1500$ /min / $f_s = 50$ Hz, $\vartheta_b \approx 70°C$, T = cycle time = 20 ms

Motor	$v_{sh,rms}$	Motor	$v_{sh,rms}$
M11a	46 mV	M500a	85 mV
M11b	26 mV	Motors with similar design as M500b	(20...50) mV
M110a	49 mV		
M110b	80 mV		

Table 4.1: Measured shaft voltages at line operation

♦ ***500 kW power level*:** The shaft voltage v_{sh} of motor M500a at line-operation, rated flux and rated speed ($V_s = 400$ V, $n = 1000$ /min / $f_s = 50$ Hz) was measured in the test floor of the manufacturer. The shaft voltage v_{sh} of motor M500b at line-operation was not measured. Motors of a similar design of the same manufacturer show very low shaft voltage (Table 4.1).

4.2 Determination of Different Types of Bearing Currents

Stator ground current i_g, rotor ground current i_{rg}, and bearing currents i_b at drive-end and non-drive-end were measured with high frequency, low inductance current probes (→ Chapter 3, p. 29). The type of bearing current can be distinguished from the waveform of the measured current. Due to the different frequency ranges, EDM- and circulating bearing currents can be identified from the bearing current measured in one of the bearings. However, measurement of the bearing current in the other bearing and of the stator ground current strongly improves unambiguousness of the measurements and offers illustration of the correlation of the parameters. Therefore, in more than 90 % of the studies, all three currents, i_g and i_b on drive-end and non-drive-end, were measured.

♦ ***EDM-bearing currents*:** The EDM-bearing current flow occurs when the bearing voltage v_b suddenly breaks down. These events are triggered by the breakdown of the lubrication film, that occurs with a statistical influence of metallic wear within the lubricating film. Therefore, EDM-bearing currents need not necessarily occur with a switching incident of the stator phase voltages. When a break down occurs in one bearing, the second bearing that discharges via the other bearing shows also current, however, this current is much smaller. Measured EDM-bearing currents have oscillating frequencies of several MHz (Fig. 4.2a, Fig. 4.2b, Fig. 4.3b and Fig. 5.20 of Section 5.4, p. 86).

♦ ***Circulating bearing currents*:** Circulating bearing currents are of differential mode. Therefore, they have opposite sign in DE and NDE bearing. As the circulating bearing current is driven by a shaft voltage that is induced by the flux linkage of the ground current, the shape of the current waveform resembles closely to the waveform of the stator ground current. These currents have oscillating frequencies of several 100 kHz (Fig. 4.3a, Fig. 4.4a and Fig. 5.5a, Fig. 5.6a of Section 5.3, p. 77).

♦ ***Rotor ground currents*:** A grounding connection between rotor and ground has to exist for rotor ground currents to occur. The rotor ground currents in both bearings have equal sign and the same waveform as the stator ground current. Hence, the oscillating frequency is also several 100 kHz. No EDM-bearing currents occur any more when rotor ground currents flow, because the lubrication film of the bearing has no longer insulating properties. The rotor ground currents are superimposed to the existing circulating bearing currents. Therefore, the amplitude of the bearing current is larger in the NDE-bearing than in the DE-bearing (Fig. 4.4b, Fig. 4.5a, Fig. 4.5b).

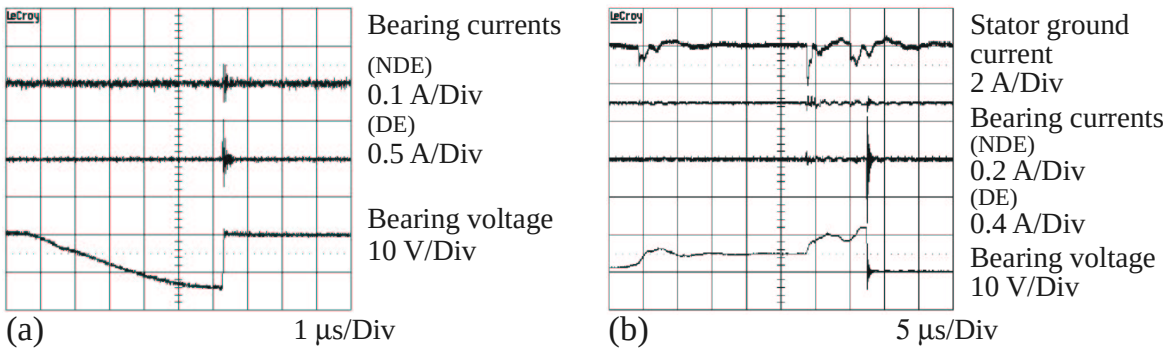

Figure 4.2: Example of measured EDM-bearing currents, here 1 kW and 11 kW power level: (a) permanent magnet motor M1a and EC-controller EC1, motor speed $n = 1000$ /min, configuration $E1_{01}$ ($l_c = 1$ m, unshielded motor cable), $\vartheta_b \approx 30°C$ (b) induction motor M11a and inverter I11a, motor speed $n = 1500$ /min, configuration $E1_{50}$ ($l_c = 50$ m, unshielded motor cable), $\vartheta_b \approx 30°C$

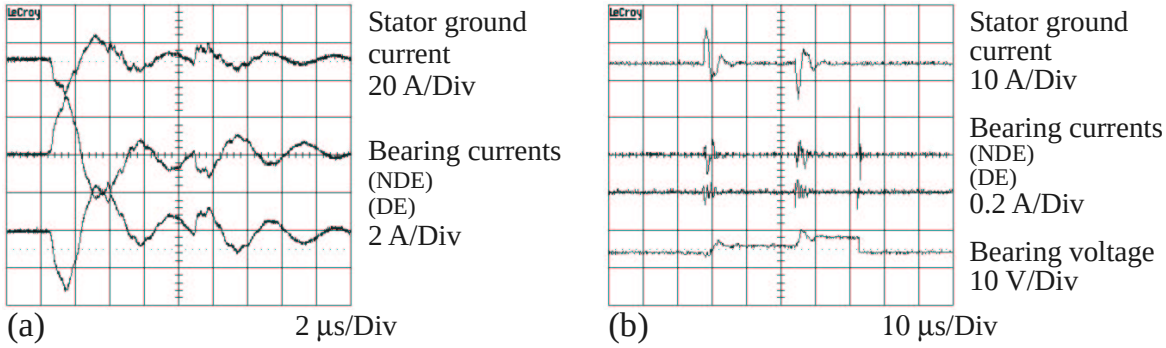

Figure 4.3: Example of measured circulating and EDM-bearing currents, here 110 kW power level: motor M110b, configuration $E1_{10}$ ($l_c = 10$ m, unshielded motor cable), $\vartheta_b \approx 70°C$, (a) circulating bearing current, inverter I110a, motor speed $n = 15$ /min, (b) EDM-bearing current inverter I110b, motor speed $n = 1500$ /min

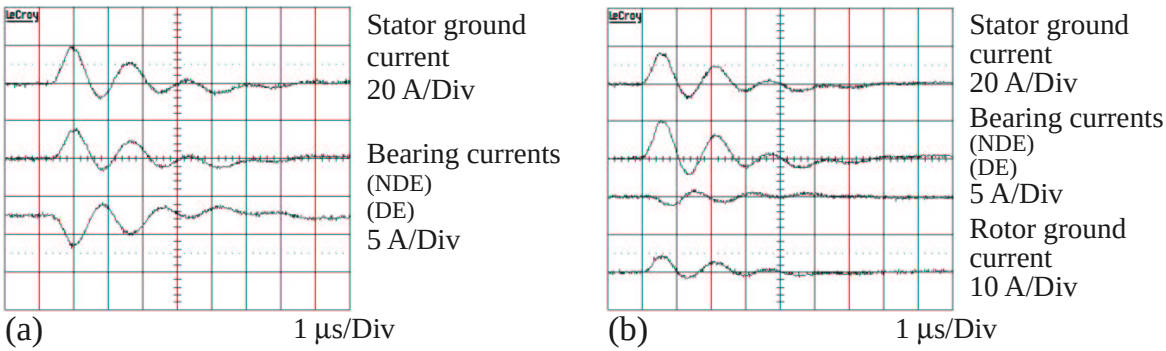

Figure 4.4: Example of measured circulating bearing currents and rotor ground currents, here 500 kW power level: induction motor M500b and inverter I500, motor speed $n = 15$ /min, $\vartheta_b \approx 70°C$ (a) configuration $E1_{10}$ ($l_c = 10$ m, unshielded motor cable), (b) configuration $E4_{10}$ ($l_c = 10$ m, unshielded motor cable, grounded rotor)

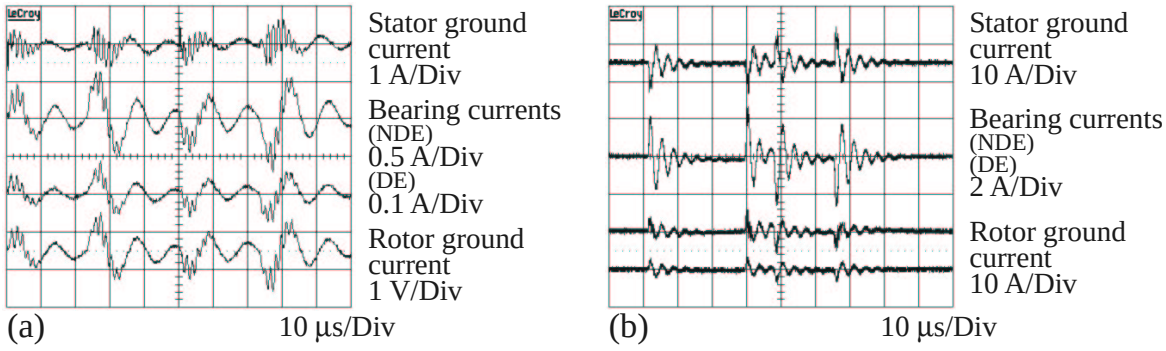

Figure 4.5: Example of measured rotor ground currents, here 11 kW and 110 kW power level: configuration $E4_{50}$ ($l_c = 50$ m, unshielded motor cable, grounded rotor), $\vartheta_b \approx 70°C$ (a) induction motor M11b and inverter I11b, motor speed $n = 15$ /min, (b) induction motor M110b and inverter I110a, motor speed $n = 1500$ /min

4.3 Influence of Motor Size

The results on the influence of motor size, motor speed n and bearing temperature ϑ_b on the bearing current phenomena obtained are *true for all motor-inverter-combinations per power level* (→ Section 4.5), *with use of both shielded and unshielded motor cable* (→ Section 4.7), *for all motor cable lengths investigated* (→ Section 4.8) and *for all stator grounding configurations* under consideration (→ Section 4.9). Therefore, for each power level, one figure is given exemplarily showing the values of the measured bearing currents i_b as function of motor speed n and bearing temperature ϑ_b for one selected motor-inverter-combination.

In this section, only the nature of the bearing currents is discussed. Section 4.4 deals with the influence of motor speed n and bearing temperature ϑ_b on the bearing currents i_b within the investigated ranges (→ Section 3.2, p. 29), that can also be seen from these figures.

Motor size has a significant influence on the nature of the bearing currents and on the magnitudes of bearing and ground currents.

♦ ***1 kW power level*:** The *very small motors* show small capacitive common mode currents and larger EDM-currents over the whole speed and temperature range. The amplitudes depend on motor speed n and bearing temperature ϑ_b (Section 4.4). The maximum peak-to-peak value is 1.3 A with the bearings at ambient temperature, $\vartheta_b \leq 20°C$, directly after motor start and 0.3 A after several time of operation at full load (Fig. 4.6). Circulating currents do not occur.

The stator ground current i_g was measured at several points of operation. The maximum peak-to-peak value was 2.5 A. Note that the motor cable is very short, $l_c = 1$ m. It is $l_c = 50$ m (11 kW, 110 kW power level), respectively $l_c = 10$ m (500 kW power level) long at the studies at the other power levels that are presented in this section. Therefore, the stator ground current i_g of the motors of this power level is relatively large (→ Section 4.8).

♦ ***11 kW power level*:** The *small motors* of the 11 kW power level show similar behavior as the motors of the 1 kW power level: Small capacitive common mode currents and larger EDM-currents occur over the whole speed and temperature range. Likewise, the values depend on motor speed n and bearing temperature ϑ_b (→ Section 4.4). With bearing temperature typical for load operation, $\vartheta_b \approx 70°C$, the peak-to-peak value of the bearing current i_b is less than 1 A (Fig. 4.7). The peak-to-peak value of the stator ground current i_g is (4...5) A. It is about constant for different bearing temperatures ϑ_b and motor speed n.

Circulating currents are only observed for motor M11b at very low motor speed, $n = 15$ /min, and elevated bearing temperature, $\vartheta_b \approx 70°C$, shortly after change of motor speed.

♦ ***110 kW power level*:** The behavior of the *larger motors* is different: Both circulating and EDM-bearing currents occur, depending on motor speed n and bearing temperature ϑ_b. The *circulating currents are dominating*, with maximum peak-to-peak values $i_b \approx (3...5)$ A at low motor speed ($n = 15$ /min) and bearing temperature $\vartheta_b \approx 70°C$ (Fig. 4.8). The peak-to-peak value of the stator ground current i_g is $i_g \approx (25...30)$ A. It is about 5 times larger than at the 11 kW power level.

♦ ***500 kW power level*:** With the *large motors*, no EDM-bearing currents, but only distinctive circulating bearing currents with peak-to-peak values $i_b \approx (15...30)$ A pk-to-pk occur at bearing temperature $\vartheta_b \approx 70°C$ over the whole speed range of the motors (Fig. 4.9). The peak-to-peak value of the stator ground current i_g is $i_g \approx 50$ A. It is about twice as large as at the 110 kW power level, and ten times as large as at the 11 kW power level.

Motor size has a significant influence on the nature of the bearing currents and on the magnitude of the bearing and ground currents.
For small motors, only EDM-bearing currents occur.
With large motors, distinctive circulating bearing currents are observed.

4.4 Influence of Motor Speed and Bearing Temperature

The results presented in this section are again *true for all motor-inverter-combinations per power level* (→ Section 4.5), *with use of both shielded and unshielded motor cable* (→ Section 4.7), *for all motor cable lengths investigated* (→ Section 4.8) and *for all stator grounding configurations* under consideration (→ Section 4.9). Therefore, the influence of motor speed n and bearing temperature ϑ_b on the bearing currents i_b is discussed on the basis of the figures of the previous section 4.3 (Fig. 4.6, Fig. 4.7, Fig. 4.8, Fig. 4.9).

♦ ***1 kW and 11 kW power level*:** At *low motor speed* - due to partially metallic contact in the bearings - *common mode capacitive currents* occur in both bearings (DE- and NDE-side) of the motor, but no EDM-currents. At *elevated motor speed*, when the lubrication film - due to hydrodynamic effects - is thick enough to allow voltage buildup across the film, the *EDM-bearing currents* appear when the electric breakdown occurs. The minimum motor speed n for *EDM-bearing currents* to occur depends on the bearing temperature ϑ_b. It increases with increasing bearing temperature ϑ_b from $n \approx 100$ /min at $\vartheta_b \approx 25°C$ to $n \approx 750$ /min at $\vartheta_b \approx 70°C$.

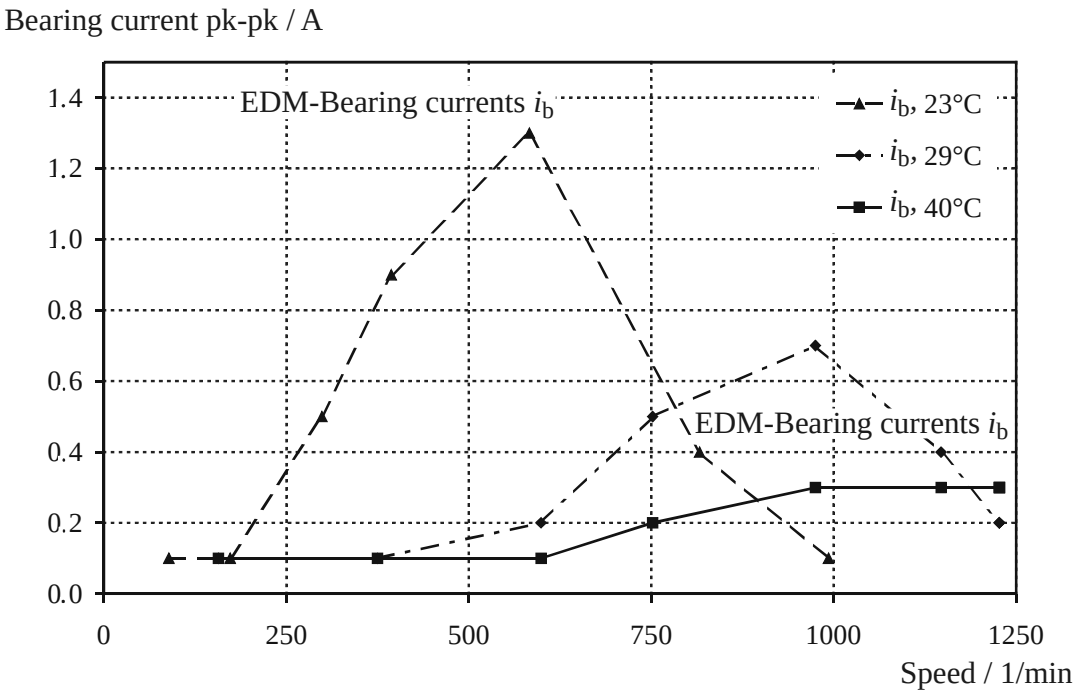

Figure 4.6: 1 kW power level - Measured influence of *motor speed and bearing temperature* on bearing currents, permanent magnet motor M1a and EC-controller EC1, configuration $E1_{01}$ ($l_c = 1$ m, unshielded motor cable)

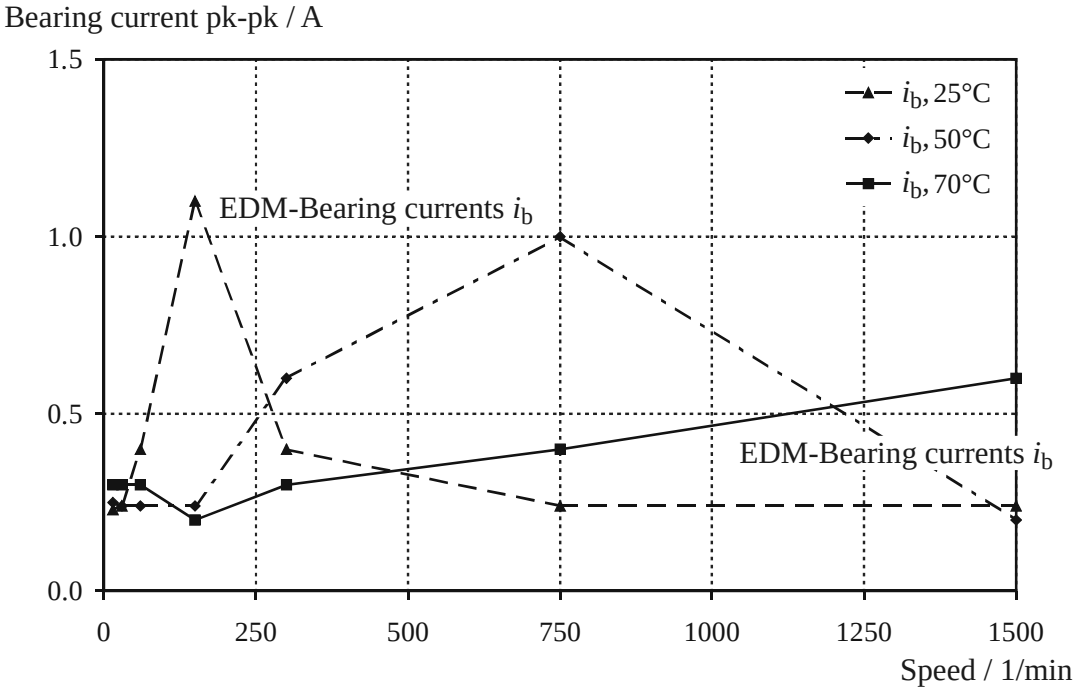

Figure 4.7: 11 kW power level - Measured influence of *motor speed and bearing temperature* on bearing currents, induction motor M11a and inverter I11a, configuration $E1_{50}$ ($l_c = 50$ m, unshielded motor cable)

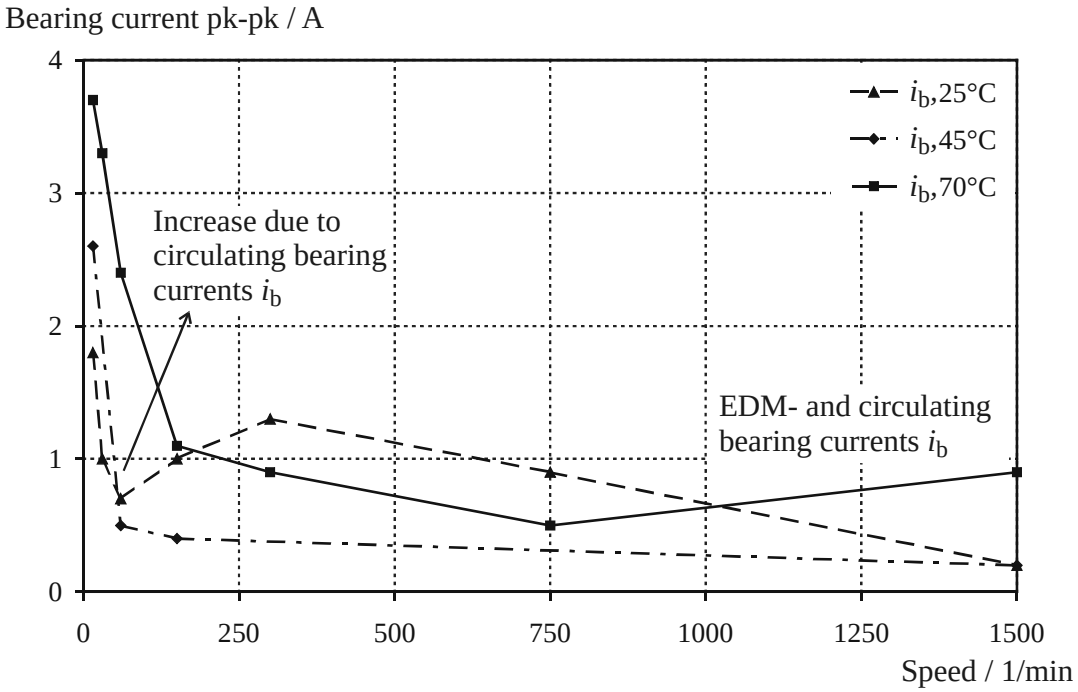

Figure 4.8: 110 kw power level - Measured influence of *motor speed and bearing temperature* on bearing currents, induction motor M110b and inverter I110b, configuration $E1_{50}$ ($l_c = 50$ m, unshielded motor cable)

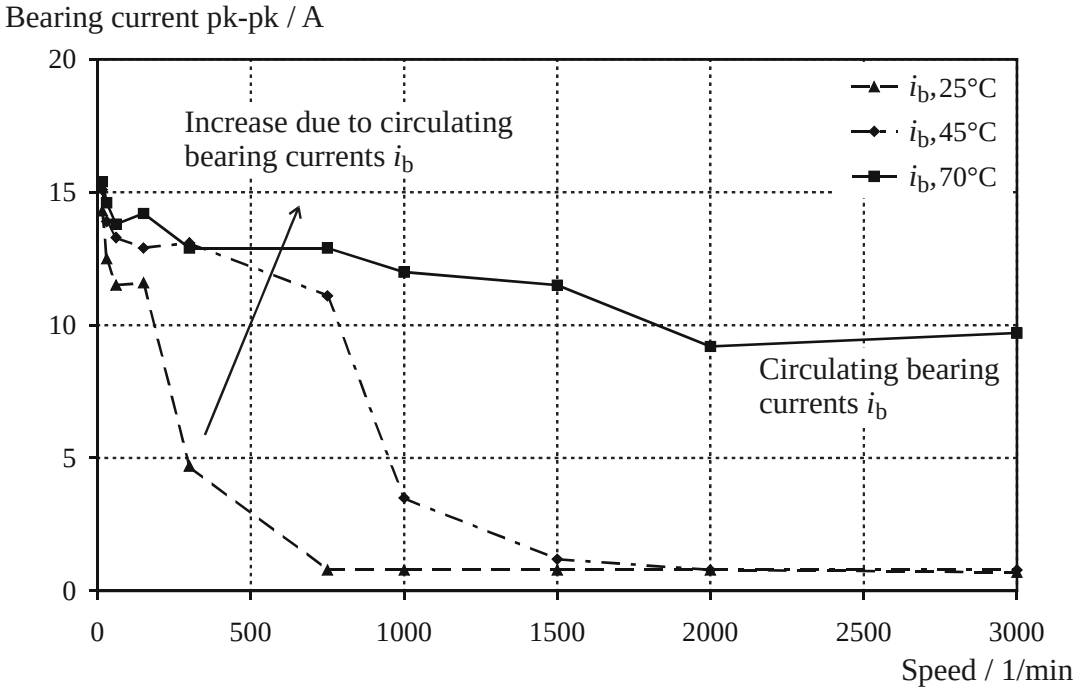

Figure 4.9: 500 kW power level - Measured influence of *motor speed and bearing temperature* on bearing currents, induction motor M500b and inverter I500, configuration $E1_{10}$ ($l_c = 10$ m, unshielded motor cable)

For a given bearing temperature ϑ_b, a maximum of EDM-current magnitude exists at a certain motor speed n. With increasing bearing temperature ϑ_b, the value of this maximum is reduced and the maximum is shifted to higher motor speed n. Furthermore, the bearing voltage v_b no longer mirrors the stator common mode voltage v_Y, but the lubricating film repeatedly builds up voltage and discharges (Fig. 4.6).

♦ ***110 kW power level*:** At the 110 kW power level, the influence of motor speed n and bearing temperature ϑ_b on the bearing currents is different than at the smaller power levels, as circulating bearing currents dominate at the 110 kW power level. These currents increase with decreasing motor speed n and increasing bearing temperature ϑ_b. Thus, the largest circulating bearing currents occur at low motor speed, $n = 15$ /min, and bearing temperature typical for load operation, $\vartheta_b \approx 70°C$. Some EDM-currents appear also. With bearing temperature $\vartheta_b \approx 70°C$, EDM-currents occur in addition to the circulating bearing currents at high motor speed ($n = 1500$ /min). For bearing temperatures $\vartheta_b \approx 25°C$ and $\vartheta_b \approx 50°C$, only EDM-currents exist at this motor speed. The limits for EDM-currents to occur in addition to circulating bearing currents and for the circulating bearing currents to vanish are shifted to higher motor speed n with increasing bearing temperature ϑ_b (Fig. 4.8).

♦ ***500 kW power level*:** At this power level, some EDM-currents appear, but large circulating bearing currents occurring over the whole speed range of the motors at $\vartheta_b \approx 70°C$ and with more than 10 times larger amplitudes are dominating. These bearing currents are increasing with increasing bearing temperature ϑ_b and decreasing motor speed n. For bearing temperatures $\vartheta_b \approx 25°C$ and $\vartheta_b \approx 50°C$, EDM-currents occur at one motor, motor M500b, at motor speed $n \geq 750$ /min ($\vartheta_b \approx 25°C$). Again, with increasing bearing temperature ϑ_b the limit for EDM-current to occur is shifted to higher motor speed n. With motor M500a, no EDM-currents exist at all - even at lower bearing temperatures. Measured peak-to-peak values of EDM-currents are only about $i_b \approx 1$ A as at the lower power levels. Hence, EDM-currents are much smaller than the dominating circulating bearing currents. The influence of motor speed n and bearing temperature ϑ_b on the bearing currents at this power level is in line with the results obtained at the other power levels (Fig. 4.9).

Motor speed and bearing temperature influence mainly the magnitude of the bearing currents at each power level.
For small motors with EDM-currents, a maximum current value exists at a certain motor speed for a given bearing temperature. With increasing bearing temperature, it is reduced and shifted to higher motor speed.
For large motors, the circulating bearing currents reach maximum values at low motor speed and elevated bearing temperature (maximum studied bearing temperature $\vartheta_b \approx 70°C$).

4.5 Influence of Motor-Inverter-Combination

The influence of the motor-inverter-combination on stator ground and bearing currents i_g and i_b was investigated using the main setup, configuration E1, and unshielded motor cable. Motor cable length was $l_c = 1$ m at the 1 kW and 50 m at the 11 kW, 110 kW and 500 kW power level (Table 4.2).

Power level	Motor cable type and length
1 kW	unshielded cable, $l_c = 1$ m (configuration $E1_{01}$)
11 kW	unshielded cable, $l_c = 50$ m (configuration $E1_{50}$)
110 kW	unshielded cable, $l_c = 50$ m (configuration $E1_{50}$)
500 kW	unshielded cable, $l_c = 50$ m (configuration $E1_{10}$)

Table 4.2: Use of unshielded motor cable for the investigation of the influence of *motor-inverter-combination* and *grounding configuration*

Comparative figures show the values of the measured stator ground and bearing currents i_g and i_b for bearing temperature $\vartheta_b \approx 70°C$ for different motor-inverter-combinations at selected speed level (Fig. 4.12, Fig. 4.14, Fig. 4.16). Measured values of bearing currents i_g as function of motor speed n and bearing temperature ϑ_b for motor-inverter-combinations other than shown in Section 4.3 are given in this section (Fig. 4.10, Fig. 4.15).

♦ ***1 kW power level*:** *Significant difference* exists neither between the amplitudes of the measured bearing currents, nor between the influence of motor speed n and bearing temperature ϑ_b on the bearing currents of the two motors of this power level, motors M1a and M1b (Fig. 4.10).

♦ ***11 kW power level*:** The magnitude of the bearing currents of motor M11a are lower than those of motor M11b (maximum peak-to-peak value 1.3 A versus 2.5 A). The influence of motor speed n and bearing temperature ϑ_b remains unchanged (Fig. 4.7, Fig. 4.11). For *small motors, the EDM-bearing currents are the same for all studied motor-inverter-combinations*, even if the control of the inverters is different. The control of the inverter influences the magnitude of the stator ground current i_g, yet, the EDM-bearing currents i_b remain unaffected (Fig. 4.12).

♦ ***110 kW power level*:** At low motor speed n, where circulating bearing currents are distinctive, motor M110b has about 25 % higher stator ground and bearing currents than motor M110a. The influence of motor speed n and bearing temperature ϑ_b is the

same. At this power level, the inverter output-filter of inverter I110c was bypassed for additional measurements in order to separate the influence of the filter from the control parameters of the inverter (Fig. 4.8, Fig. 4.13). The *differences between the two motors* are *not significant*. *No influence of the inverter* on the bearing currents exists for *high motor speed* (EDM-currents and some small circulating currents), even if the control of the inverters is different. At *low motor speed* (circulating bearing currents), *no significant influence* on the bearing currents exists, *as long as the inverter does not contain protective elements (e.g. dv/dt-filter) at the output* (Fig. 4.14). The influence of the filter is discussed in detail in Section 5.3 (p. 77).

♦ ***500 kW power level*:** At this power level, in contrast to the results at the smaller power levels, a difference between the results obtained for the two motors exists: For the same test setup, the *stator ground current* i_g of motor M500a is *about 40 % larger* than that of motor M500b, causing a *(30...50) % larger circulating bearing current* i_b of motor M500a. Furthermore, even with bearing temperature $\vartheta_b \approx 25°C$, only circulating bearing currents occur up to maximum motor speed $n = 2000$ /min (Fig. 4.9, Fig. 4.15, Fig. 4.16). The two motors of this power level have different numbers of poles. The rotor of motor M500a, which has six poles, is heavier than the rotor of motor M500b with two poles, which leads to a larger *Hertz*'ian contact area (→ Appendix C, p. 211). Therefore, the *apparent bearing current density* J_b is about the *same in both motors* (Section 4.11).

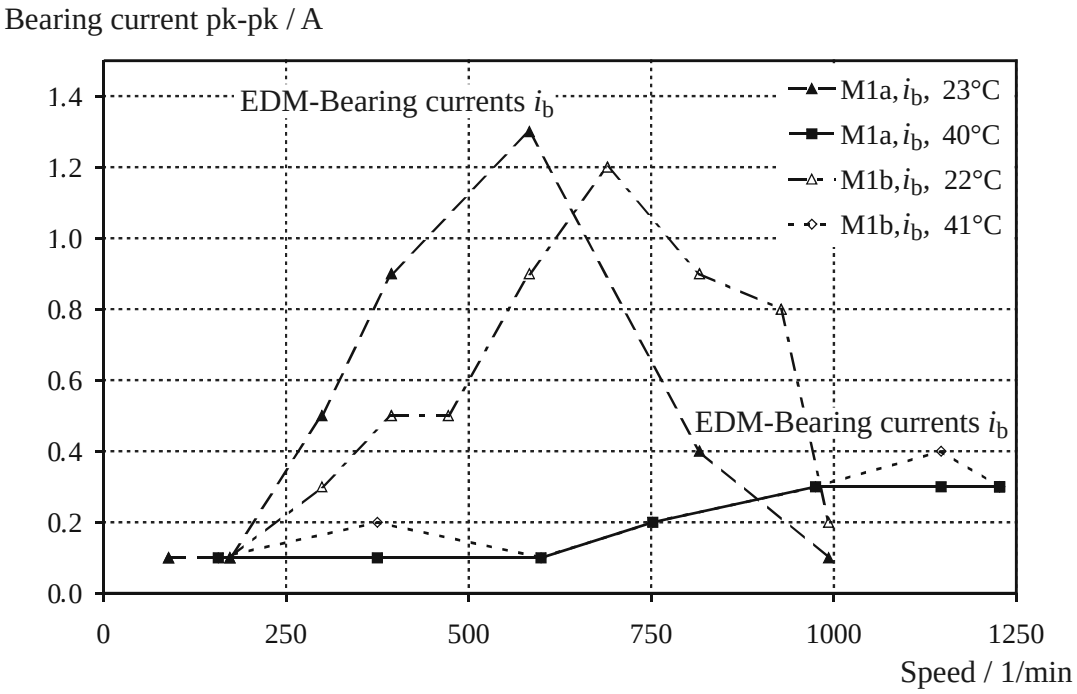

Figure 4.10: 1 kW power level - Measured influence of *motor speed and bearing temperature* on bearing currents, permanent magnet motors M1a and M1b and EC-controller EC1, configuration $E1_{01}$ ($l_c = 1$ m, unshielded motor cable)

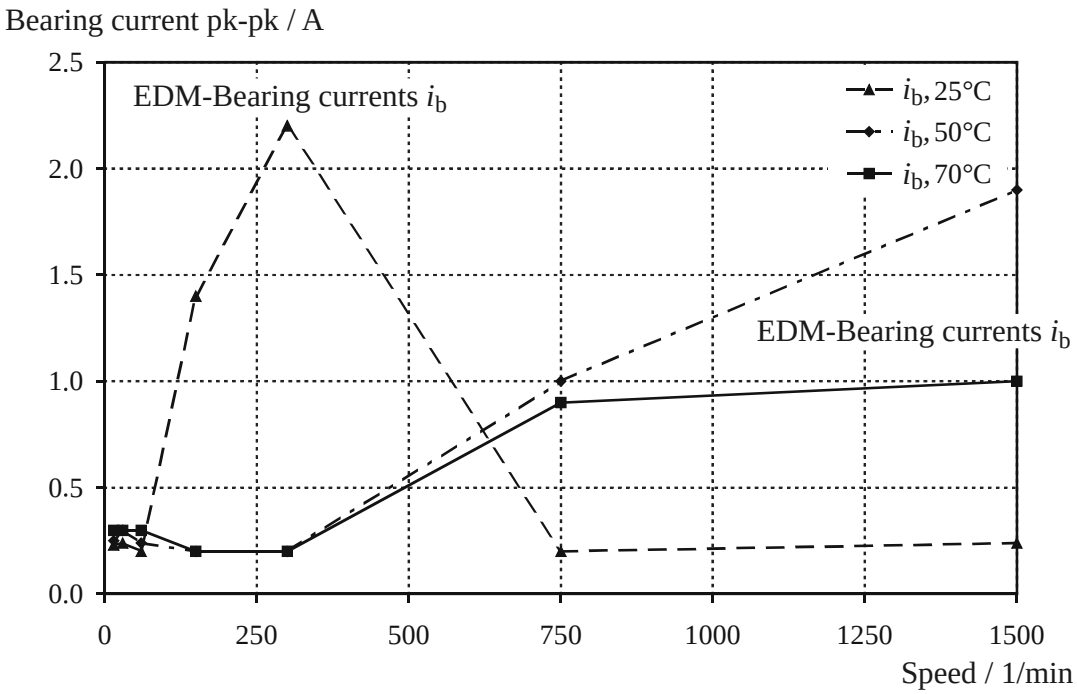

Figure 4.11: 11 kW power level - Measured influence of *motor speed and bearing temperature* on bearing currents, induction motor M11b and inverter I11a, configuration $E1_{50}$ ($l_c = 50$ m, unshielded motor cable)

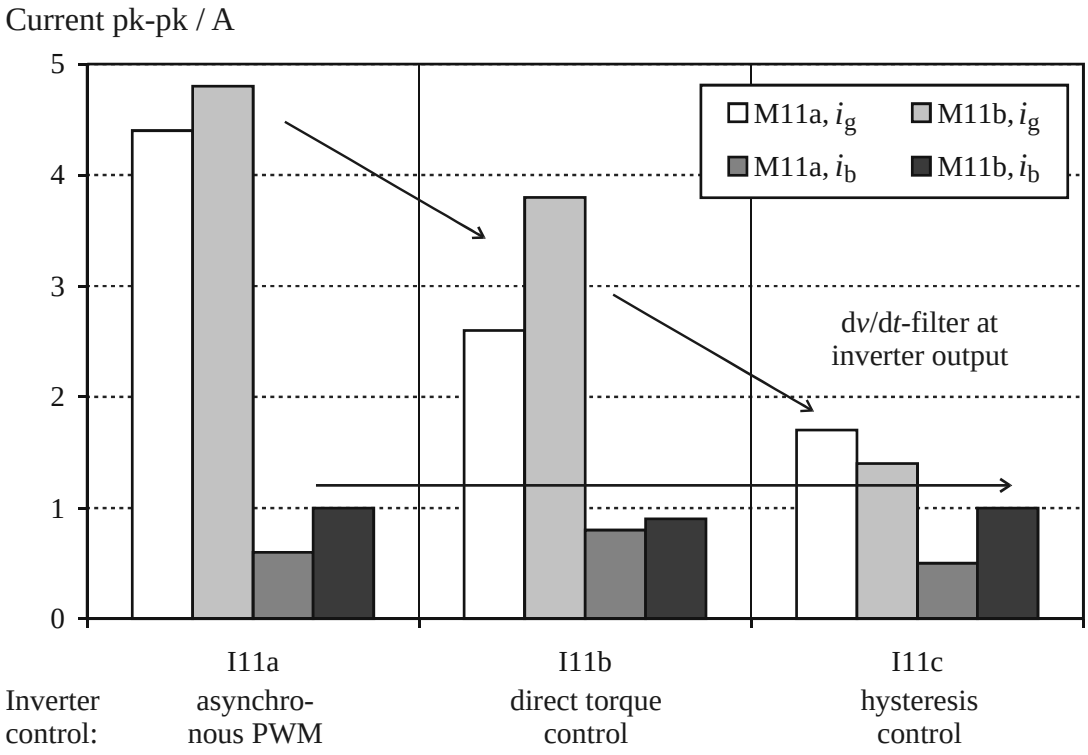

Figure 4.12: 11 kW power level - Measured influence of *motor-inverter-combination* on stator ground and bearing currents, induction motors M11a and M11b, configuration $E1_{50}$ ($l_c = 50$ m, unshielded motor cable), motor speed $n = 1500$ /min, $\vartheta_b \approx 70°C$

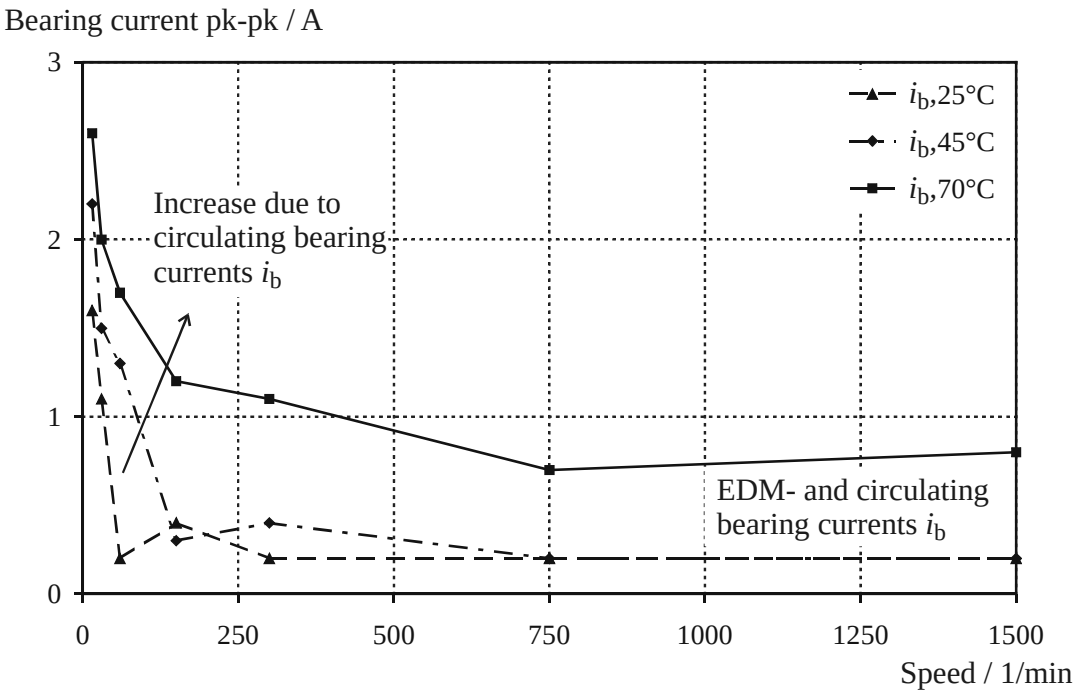

Figure 4.13: 110 kw power level - Measured influence of *motor speed and bearing temperature* on bearing currents, induction motor M110a and inverter I110b, configuration $E1_{50}$ ($l_c = 50$ m, unshielded motor cable)

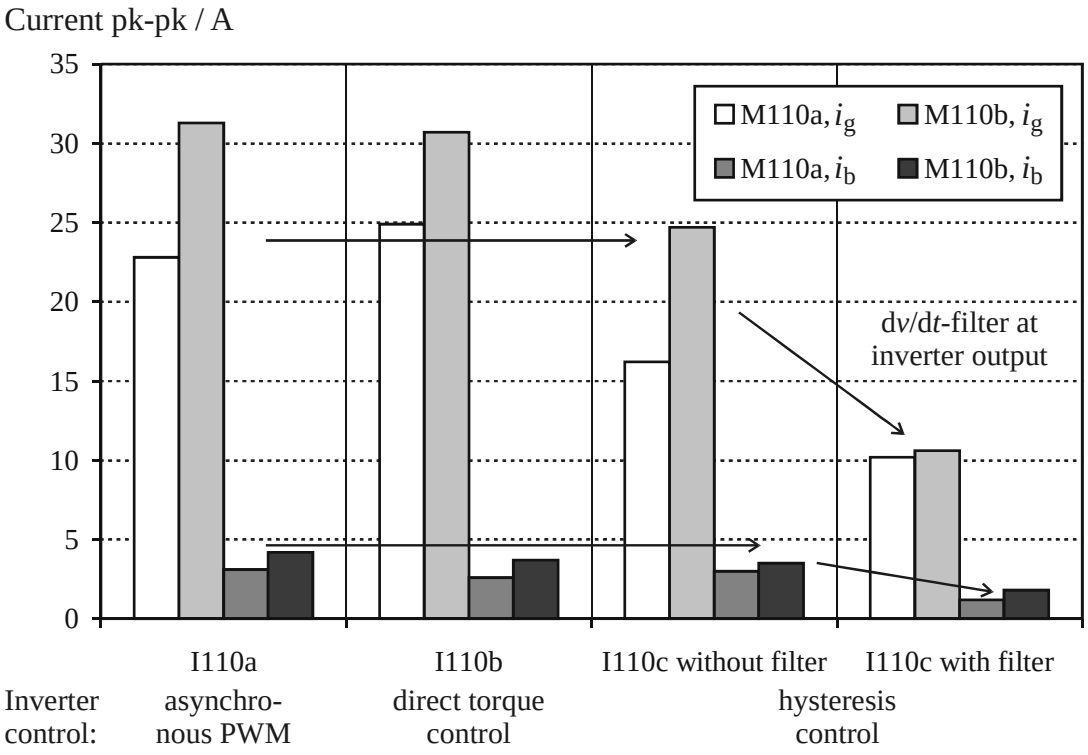

Figure 4.14: 110 kW power level - Measured influence of *motor-inverter-combination* on stator ground and bearing currents, induction motors M110a and M110b, configuration $E1_{50}$ ($l_c = 50$ m, unshielded motor cable), motor speed $n = 15$ /min, $\vartheta_b \approx 70°C$

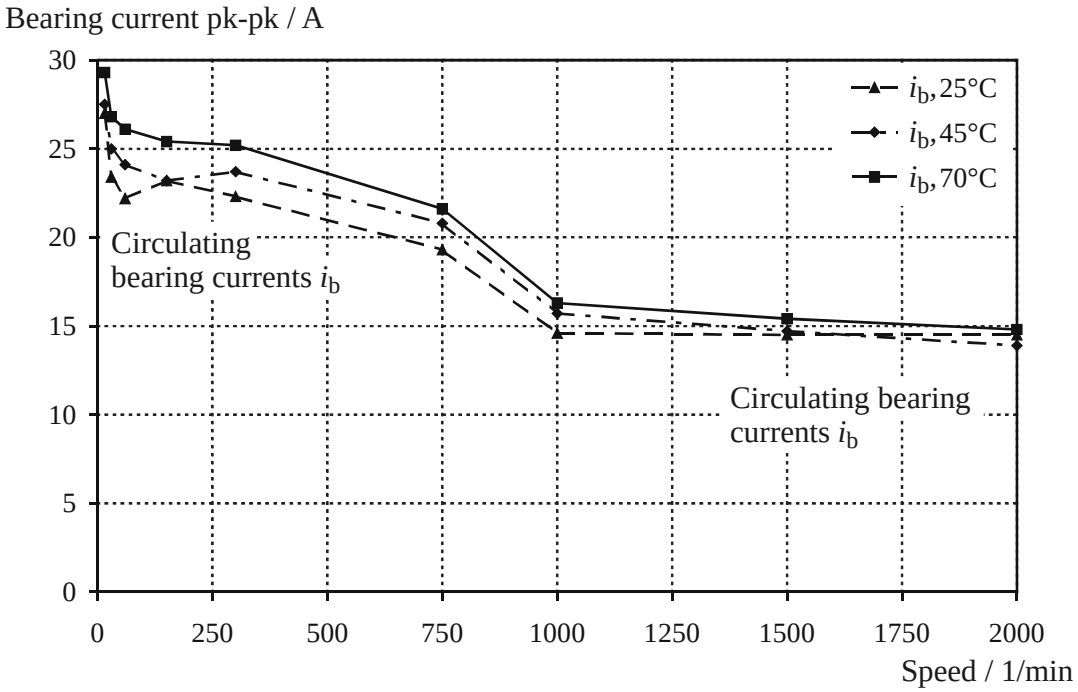

Figure 4.15: 500 kW power level - Measured influence of *motor speed and bearing temperature* on bearing currents, induction motor M500a and inverter I500, configuration $E1_{10}$ ($l_c = 10$ m, unshielded motor cable)

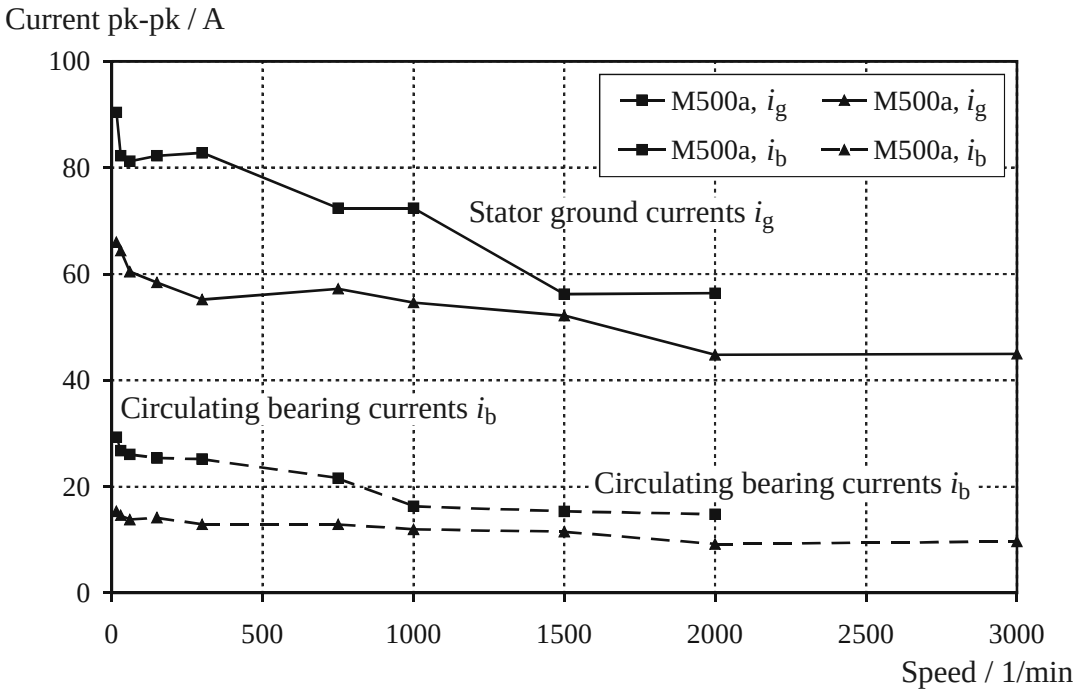

Figure 4.16: 500 kW power level - Measured influence of *motor-inverter-combination* and speed on stator ground and bearing currents, induction motors M500a and M500b and inverter I500, configuration $E1_{10}$ ($l_c = 10$ m, unshielded motor cable), $\vartheta_b \approx 70°C$

For a given power level, the results concerning the nature of the bearing currents and the influence of motor speed and bearing temperature on the bearing currents, are valid for all studied motor-inverter-combinations.
Only, if the inverter contains an additional output filter to reduce the dv/dt, circulating bearing currents of large motors may be reduced down to more than 50 %.

4.6 Influence of Switching Frequency

The influence of the switching frequency f_c of the switching elements of the feeding inverter on the stator ground and bearing currents i_g and i_b in a given motor-inverter-combination was analyzed at the 11 kW and 110 kW power level (Fig. 4.17). The time between two switching instants varies with the switching frequency f_c. Therefore, the stator ground current i_g may change when the motor is operated with another switching frequency f_c (→ Section 7.5, p. 132). This is obvious at the increase of the stator ground current i_g at the 11 kW power level. The magnitudes of the *EDM-bearing currents are not influenced* by the switching frequency f_c, those of the *circulating bearing currents remain almost unaffected*, when compared with the influence of the other system parameters described before.

For a given configuration, the switching frequency does not significantly influence the amplitude of the bearing currents.

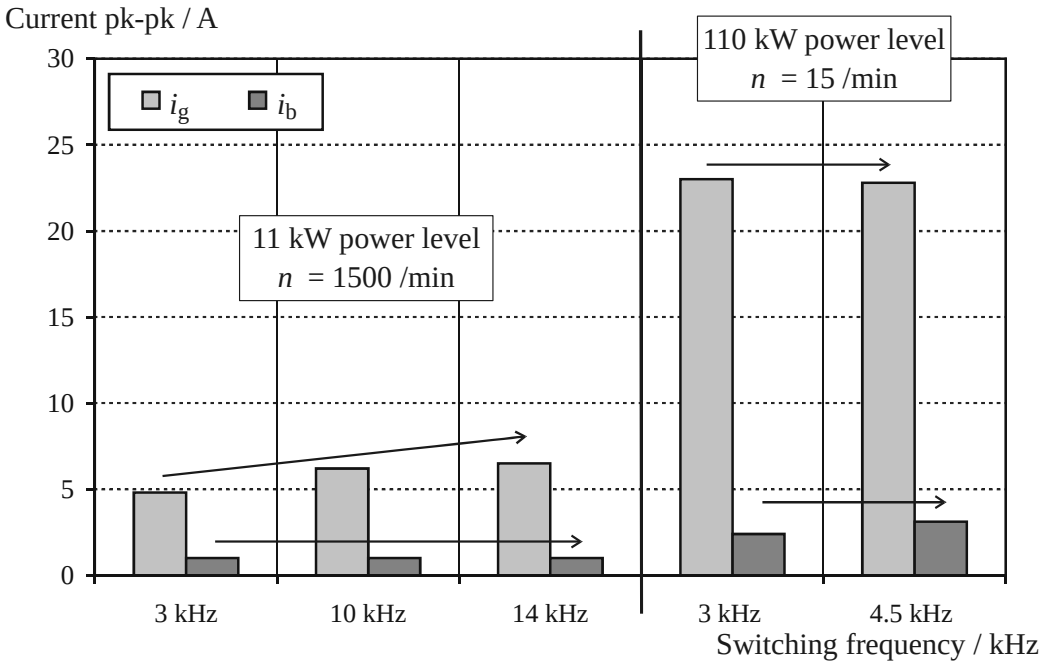

Figure 4.17: Measured influence of the *switching frequency* on stator ground and bearing currents, induction motors M11b and M110a and inverters I11a and I110a respectively, configuration $E1_{50}$ (l_c = 50 m, unshielded motor cable), $\vartheta_b \approx 70°C$

4.7 Influence of Shielded versus Unshielded Motor Cable

The influence of motor operation with use of shielded instead of unshielded motor cable was investigated at the 11 kW, 110 kW and 500 kW power level in the main configuration with motor cables of different lengths l_c (Table 4.3).

Power level	Inverter	Motor cable type and length
11 kW	I11a	unshielded cable, l_c = 2/10/50 m (configurations $E1_{02}$, $E1_{10}$, $E1_{50}$)
		shielded cable, l_c = 50 m (configuration $E1^*_{50}$)
110 kW	I110a	unshielded cable, l_c = 10/50 m (configurations $E1_{10}$, $E1_{50}$)
		shielded cable, l_c = 10/50 m (configurations $E1^*_{10}$, $E1^*_{50}$)
500 kW	I500	unshielded cable, l_c = 10 m (configuration $E1_{10}$)
		shielded cable, l_c = 2/10 m (configurations $E1^*_{02}$, $E1^*_{10}$)

Table 4.3: *Types and lengths of studied motor cables* and respective motor-inverter-combinations, (E1/E1* = unshielded/shielded cable respectively)

Comparative figures show the values of the measured stator ground and bearing currents i_g and i_b for bearing temperature $\vartheta_b \approx 70°C$ for use of shielded and unshielded motor cable of different lengths l_c at selected speed level (Fig. 4.18, Fig. 4.19, Fig. 4.20). This section discusses only the influence of the motor cable type - shielded versus unshielded motor cable. The discussion of the influence of the motor cable length l_c is content of the following Section 4.8.

♦ ***11 kW power level*:** *The same results* as shown in Fig. 4.11 (Section 4.5) are obtained *when the motor is supplied with shielded motor cable*. In the case of shielded motor cable, the stator ground currents i_g increase about 30 % when compared with use of the unshielded motor cable. However, for *the small motors* of this power level, *the bearing currents of EDM-type remain the same* with use of *shielded and unshielded motor cable* (Fig. 4.18).

♦ ***110 kW power level*:** The stator ground currents i_g increase both with l_c = 50 m and with l_c = 10 m by (20...40) % if the shielded instead of the unshielded motor cable is used. However, the *increase of the distinctive circulating bearing currents at low motor speed is negligible* (Fig. 4.19). At elevated motor speed, e.g. n = 1500 /min, the

higher stator ground currents i_g induce bearing currents of circulating type with maximum peak-to-peak values of (2...3) A. The EDM-bearing currents vanish. This results in *flatter curves* of the bearing currents i_b as function of motor speed n and bearing temperature ϑ_b when *shielded instead of unshielded motor cable* is used (Fig. 4.22). However, as the dominating circulating bearing currents occur at low motor speed, this increase in the amplitude of the bearing currents at elevated motor speed n is of minor importance.

♦ ***500 kW power level*:** The influence of the type of motor cable on the stator ground and bearing currents i_g and i_b is very similar to the one at the 110 kW power level: The stator ground currents i_g increase by (30...40) % if shielded instead of unshielded motor cable is used. However, the *distinctive circulating bearing currents do not change significantly* (Fig. 4.20). At *elevated motor speed*, the higher stator ground currents i_g induce *circulating bearing currents* that are *(20...30) % larger.*

Use of a shielded instead of unshielded motor cable increases the stator ground currents by up to 40 %.
The cable type does not influence the EDM-bearing currents of small motors, but leads to increase of the circulating bearing currents at high motor speed of large motors.
The influence of the cable type is much smaller than the one of motor size in general.

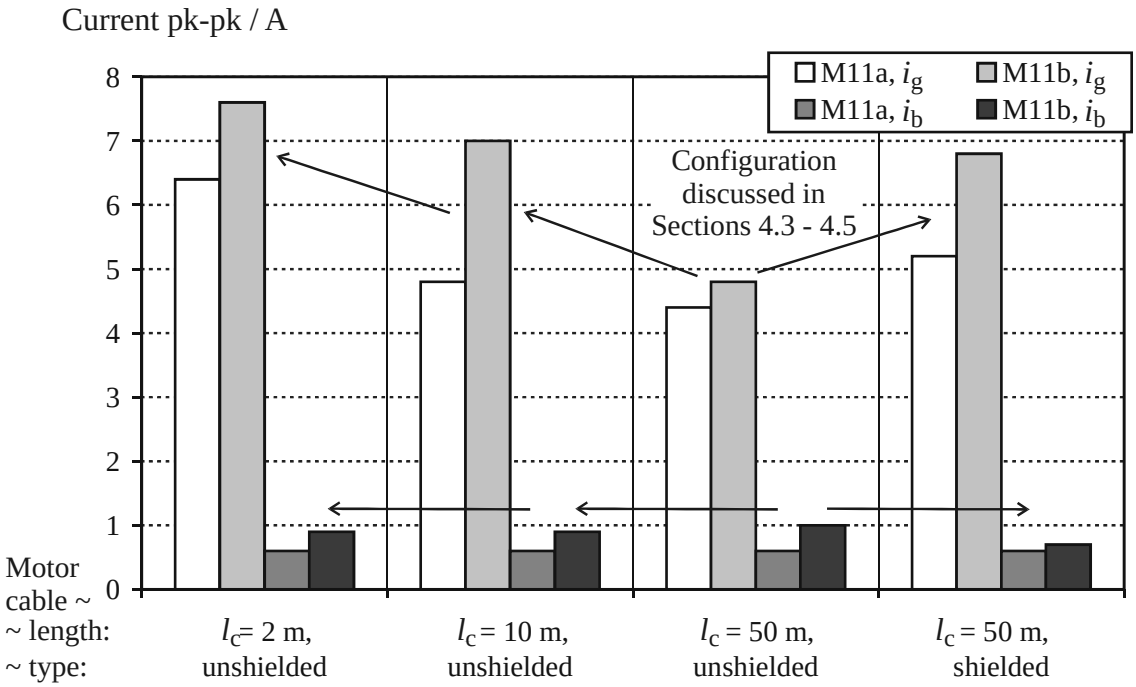

Figure 4.18: 11 kW power level - Measured influence of the *motor cable* on stator ground and bearing currents, induction motors M11a and M11b and inverter I11a, configurations E1/E1* (shielded/unshielded motor cable of different lengths l_c), motor speed $n = 1500$ /min, $\vartheta_b \approx 70°C$

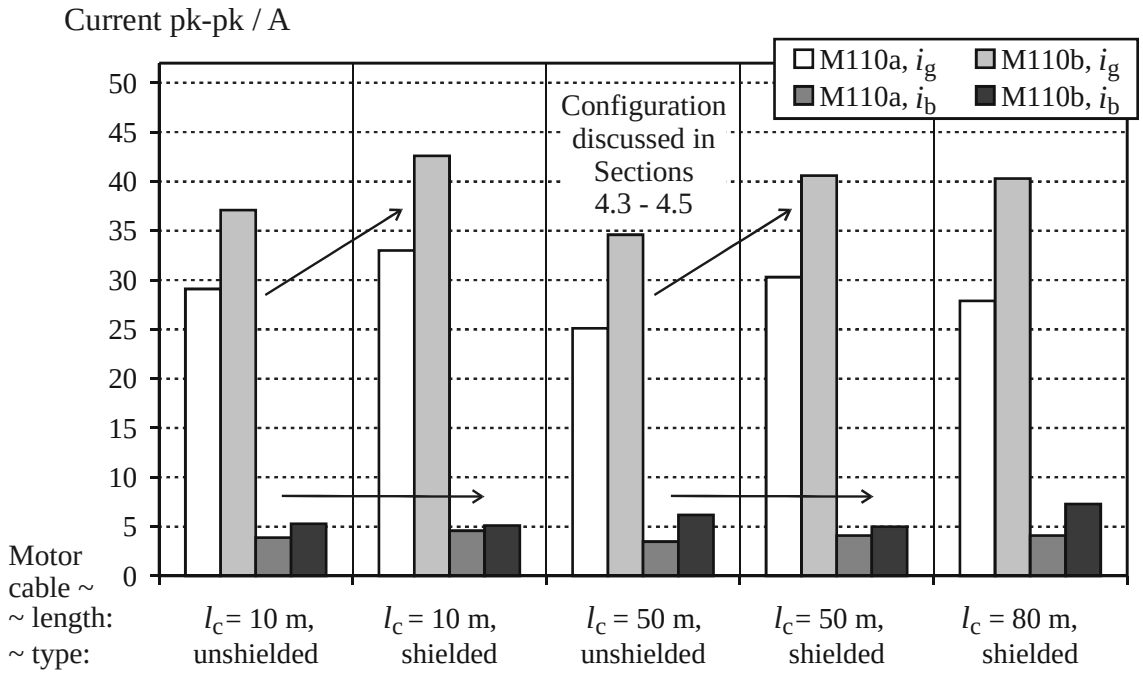

Figure 4.19: 110 kW power level - Measured influence of the *motor cable* on stator ground and bearing currents, induction motors M110a and M110b and inverter I110a, configurations E1/E1* (shielded/unshielded motor cable of different lengths l_c), motor speed $n = 15$ /min, $\vartheta_b \approx 70°C$

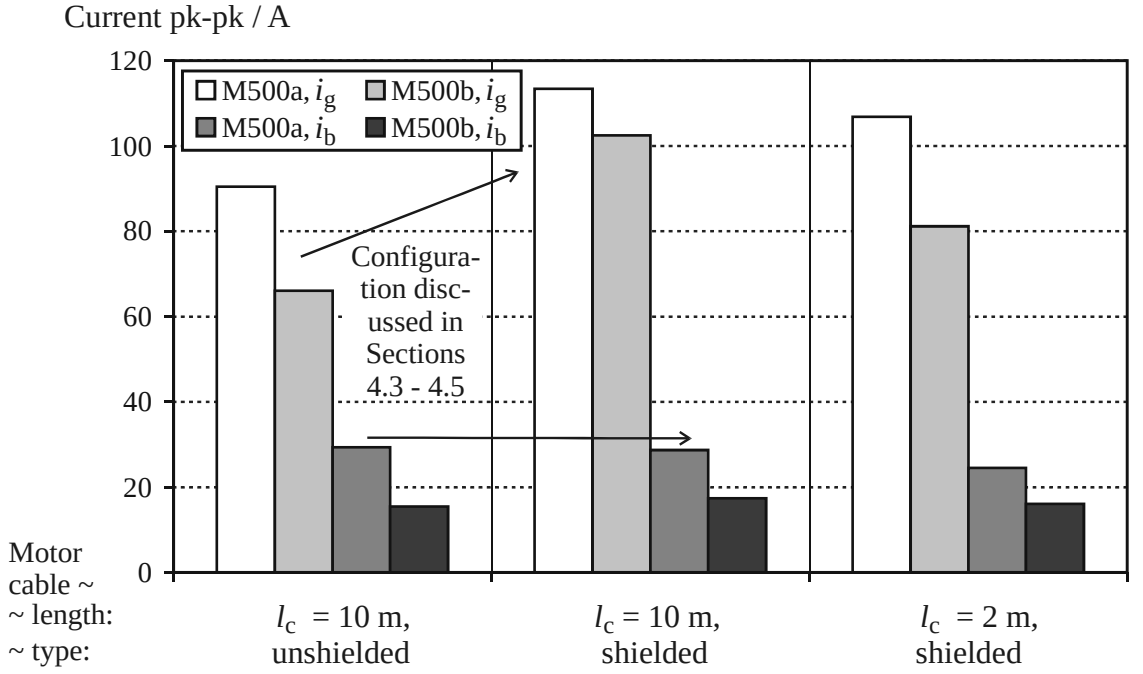

Figure 4.20: 500 kW power level - Measured influence of the *motor cable* on stator ground and bearing currents, induction motors M500a and M500b and inverter I500, configurations E1/E1* (shielded/unshielded motor cable of different lengths l_c), motor speed $n = 15$ /min, $\vartheta_b \approx 70°C$

4.8 Influence of Motor Cable Length

The influence of the motor cable length on stator ground and bearing currents i_g and i_b was investigated at the 11 kW, 110 kW and 500 kW power level in the main configuration with both shielded and unshielded motor cables (Table 4.3; Fig. 4.18, Fig. 4.19, Fig. 4.20).

♦ ***11 kW power level*:** The influence of motor speed n and bearing temperature ϑ_b on the bearing currents occurring at this power level *remains unchanged* if the motor is supplied via unshielded motor cable with length $l_c = 2$ m instead of $l_c = 50$ m (Fig. 4.11, Fig. 4.21). The stator ground currents i_g increase with decreasing cable length l_c up to 30 %. However, the *bearing currents of EDM-type* are the *same* for *motor cables of different length* (Fig. 4.18).

♦ ***110 kW power level*:** The *stator ground currents i_g increase about 10 %* with both types of motor cable, shielded and unshielded, when the motor is fed with a shorter cable, $l_c = 10$ m versus $l_c = 50$ m and $l_c = 50$ m versus $l_c = 80$ m. However, the *distinctive circulating bearing currents* remain *almost unaffected* (Fig. 4.19). The higher stator ground currents i_g induce larger bearing currents of circulating type at elevated motor speed n when a shorter motor cable is used. Yet, the maximum peak-to-peak values are e.g. (2...3) A at motor speed $n = 1500$ /min, what is much smaller than at low motor speed n. The increase of the bearing currents i_g at elevated motor speed results in *flatter curves* (Fig. 4.22).

♦ ***500 kW power level*:** At this power level, the *stator ground currents i_g* are *(10...20) % smaller* if the shorter motor cable, $l_c = 2$ m instead of $l_c = 10$ m, is used (Fig. 4.20). This is in contrast to the results obtained at the smaller power levels, where shorter cable length l_c results in increase of the stator ground current i_g. However, the *distinctive circulating bearing currents* i_b remain *almost unaffected* by the change of the length of the motor cable l_c.

In the majority of cases, reduction of the motor cable length leads to reduction of the stator ground current.
Reduction of the cable length does not influence the EDM-bearing currents, and leaves almost unaffected the distinctive circulating bearing currents that occur at low motor speed at larger motors.
The influence of motor cable length is smaller than the one of motor cable type. It is much smaller than the impact of motor size in general.

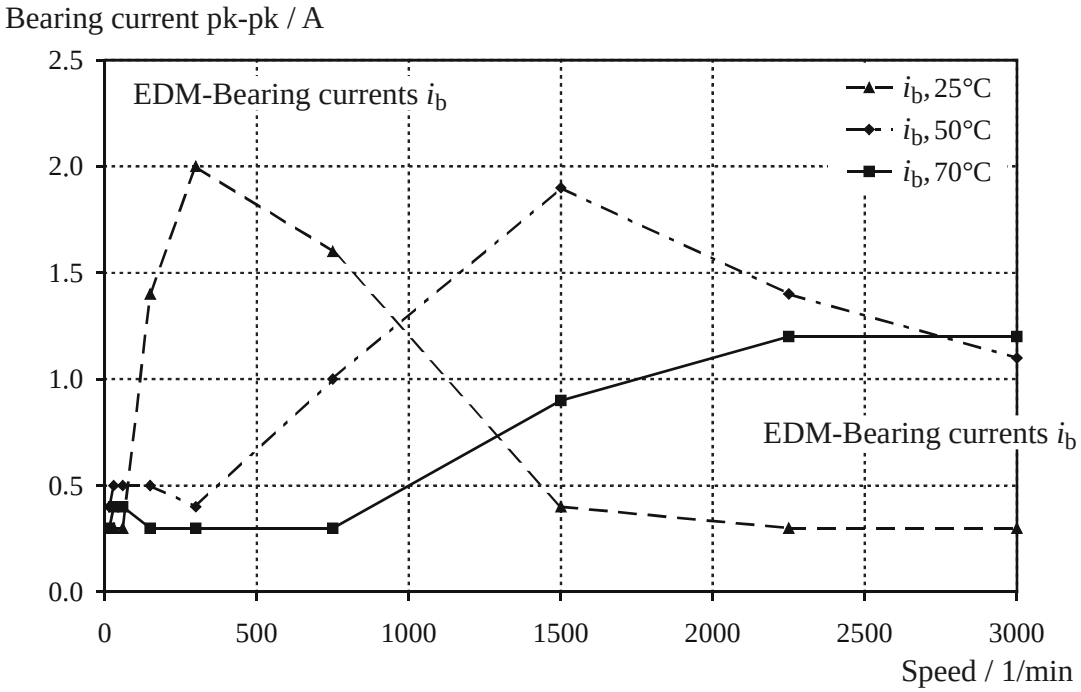

Figure 4.21: 11 kW power level - Measured influence of motor speed and bearing temperature on bearing currents, induction motor M11b and inverter I11a, configuration $E1_{02}$ (l_c = 2 m, unshielded motor cable); compare with Fig. 4.7 and Fig. 4.11

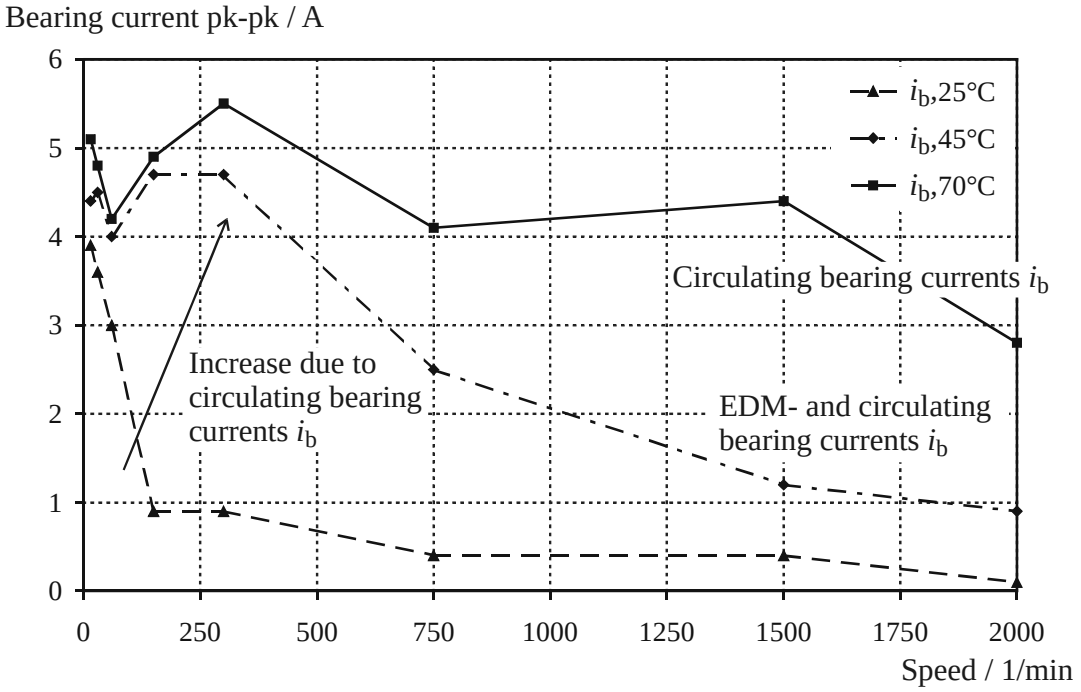

Figure 4.22: 110 kW power level - Measured influence of motor speed and bearing temperature on bearing currents, induction motor M110b and inverter I110a, configuration $E1^*_{10}$ (l_c = 10 m, shielded motor cable); compare with Fig. 4.8 and Fig. 4.13

4.9 Influence of Stator Grounding Configuration with Rotor not Grounded

Four different grounding configurations - configuration E1 to E4 - were investigated, of which detailed explanations and drawings are given in Chapter 2 (p. 23). This section deals only with configurations E1 to E3, where the rotor is not grounded. These configurations were investigated at both motors of the 11 kW and 110 kW power level (Table 4.4).

Power level	Inverter	Motor cable type and length
11 kW	I11a	unshielded cable, l_c = 2 m (configurations $E1_{02}$, $E2_{02}$, $E3_{02}$)
		unshielded cable, l_c = 10 m (configurations $E1_{10}$, $E2_{10}$, $E3_{10}$)
		unshielded cable, l_c = 50 m (configurations $E1_{50}$, $E2_{50}$, $E3_{50}$)
	I11b	unshielded cable, l_c = 50 m (configurations $E1_{50}$, $E2_{50}$, $E3_{50}$)
	I11c	unshielded cable, l_c = 50 m (configurations $E1_{50}$, $E2_{50}$, $E3_{50}$)
110 kW	I110a	unshielded cable, l_c = 10 m (configurations $E1_{10}$, $E2_{10}$, $E3_{10}$)
		unshielded cable, l_c = 50 m (configurations $E1_{50}$, $E2_{50}$, $E3_{50}$)
	I110b	unshielded cable, l_c = 50 m (configurations $E1_{50}$, $E2_{50}$, $E3_{50}$)
	I110c	unshielded cable, l_c = 50 m (configurations $E1_{50}$, $E2_{50}$, $E3_{50}$)

Table 4.4: Investigated combinations of inverters and motor cables for different *stator grounding configurations with rotor not grounded*

♦ ***11 kW power level*:** With configurations E2 and E3, the stator ground currents i_g of the motors are reduced (up to 50 % in configuration E3). However, in accordance with the previous results, the *EDM-currents remain almost unaffected* by the change of the stator ground current (Fig. 4.23). The same results are obtained if inverters and motor cable lengths other than inverter I11a and l_c = 50 m (Fig. 4.23) are used for motor supply.

♦ ***110 kW power level*:** Again, with grounding configurations E2 and E3, the stator ground currents i_g of the motors are reduced (again up to 50 % in configuration E3). Therefore, *up to 50% smaller circulating bearing currents* are induced at *low motor speed* n = 15 /min (Fig. 4.24). The measurement results are the same for motor supply with inverters and motor cable lengths other than I110a and l_c = 50 m (Fig. 4.24).

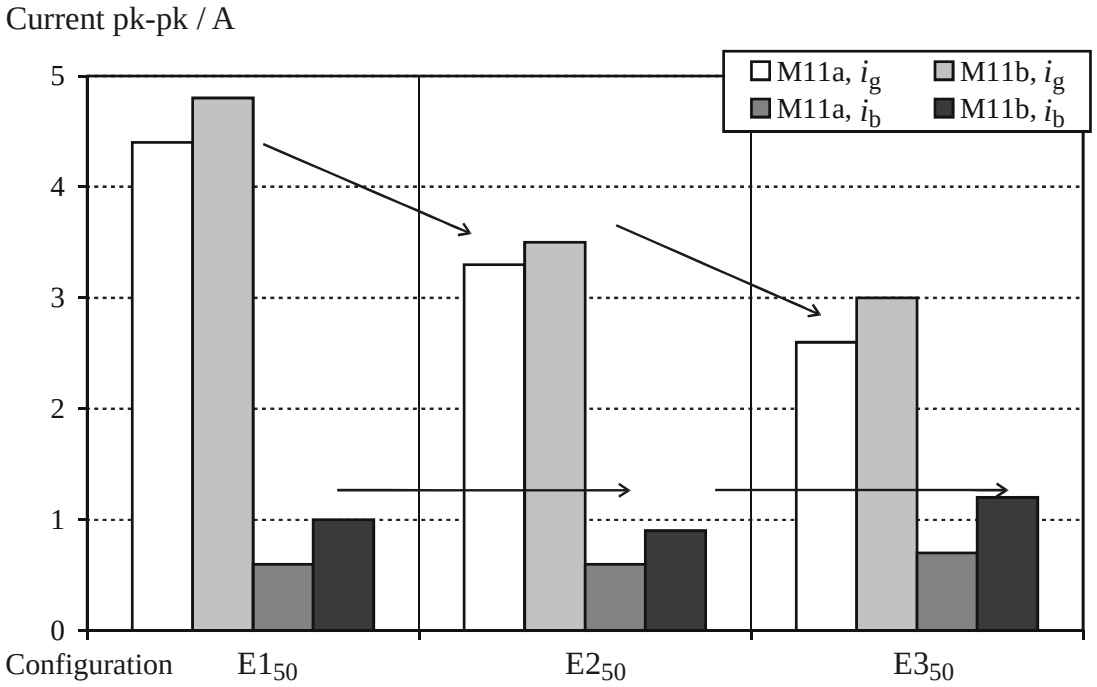

Figure 4.23: 11 kW power level - Measured influence of the *grounding configuration* (rotor not grounded), induction motors M11a and M11b and inverter I11a, configurations $E1_{50}$, $E2_{50}$ and $E3_{50}$ ($l_c = 50$ m, unshielded motor cable), motor speed $n = 1500$ /min, $\vartheta_b \approx 70°C$

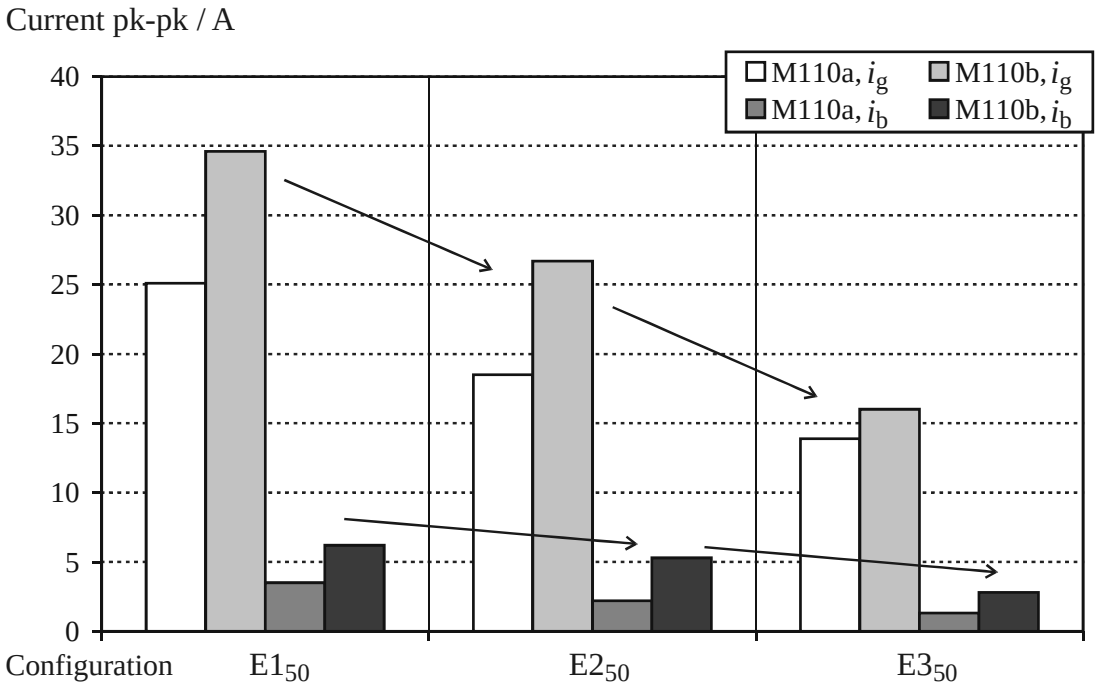

Figure 4.24: 110 kW power level - Measured influence of the *grounding configuration* (rotor not grounded), induction motors M110a and M110b and inverter I110a, configurations $E1_{50}$, $E2_{50}$ and $E3_{50}$ ($l_c = 50$ m, unshielded motor cable), motor speed $n = 15$ /min, $\vartheta_b \approx 70°C$

If the rotor is not grounded, the stator grounding configuration does not influence the EDM-bearing currents of small motors.
The circulating bearing currents of large motors depend on the stator ground currents of the motor. The reduction of the circulating bearing currents and of the stator ground currents was up to 50 % in the different investigated configurations.

4.10 Influence of Parasitic Current Path via Grounded Rotor

The dv/dt at the motor terminals causes additional ground currents at inverter-operation which may flow back along paths others than the PE and/or shield with which the stator housing is grounded (→ Section 1.5, p. 10). For that reason, configuration E4 had been set up, where the stator housing is grounded as in the main configuration E1 and the rotor is grounded additionally (Fig. 2.2, p. 23). The investigations of this configuration were done with both unshielded and shielded motor cables of different lengths at both motors of the 11 kW, 110 kW and 500 kW power level respectively (Table 4.5).

♦ ***11 kW power level*:** If unshielded motor cable with cable length $l_c = 50$ m is used, rotor ground currents with peak-to-peak values $i_{rg} \geq 2$ A flow, when the rotor is grounded. The rotor ground current i_{rg} passes the bearings, but is not equally distributed on both bearings. Therefore, bearing currents with higher amplitudes than half the total rotor ground current occur (Fig. 4.25). At high motor speed $n = 1500$ /min, the EDM-currents occur in addition and are superposing the bearing current that is part of the rotor ground current. If *unshielded motor cable* is used, the bearing currents increase in configuration E4 by partially *more than 100 %* when compared with configuration E1 (Fig. 4.26). With configuration E4, the *largest bearing currents* of *the 11 kW power level* were measured. The same results are obtained with inverter I11b, motor M11a and unshielded motor cable with $l_c = 10$ m / $l_c = 2$ m instead of inverter I11a, motor M11b and $l_c = 50$ m as it is the case for Fig. 4.26. The *situation is different with use of inverter* I11c that contains an integrated dv/dt-filter at the inverter-output. Here, the *rotor ground current* i_{rg} is *reduced down to 30 %. Therefore, the bearing currents are reduced also.* This is in analogy with the results presented in Sections 4.5 (p. 50) and 5.3 (p. 77).

If *shielded motor cable* is used, additional *grounding of the rotor* does *not influence* the stator ground and bearing currents i_g and i_b to a significant extent (Fig. 4.26).

♦ ***110 kW power level*:** At this power level, if unshielded motor cable with cable length $l_c = 50$ m is used, rotor ground currents with peak-to-peak values $i_{rg} \leq 10$ A flow. The rotor ground current is superimposed to the circulating bearing currents, resulting in peak-to-peak values of the bearing current in the NDE-bearing up to $i_b \leq 8$ A (Fig. 4.27).

Power level	Inverter	Motor cable type and length
11 kW	I11a	unshielded cable, l_c = 2 m (configurations $E1_{02}$, $E4_{02}$)
		unshielded cable, l_c = 10 m (configurations $E1_{10}$, $E4_{10}$)
		unshielded cable, l_c = 50 m (configurations $E1_{50}$, $E4_{50}$)
		shielded cable, l_c = 50 m (configurations $E1^*_{50}$, $E4^*_{50}$)
	I11b	unshielded cable, l_c = 50 m (configurations $E1_{50}$, $E4_{50}$)
	I11c	unshielded cable, l_c = 50 m (configurations $E1_{50}$, $E4_{50}$)
110 kW	I110a	unshielded cable, l_c = 10 m (configurations $E1_{10}$, $E4_{10}$)
		shielded cable, l_c = 10 m (configurations $E1^*_{10}$, $E4^*_{10}$)
		unshielded cable, l_c = 50 m (configurations $E1_{50}$, $E4_{50}$)
		shielded cable, l_c = 50 m (configurations $E1^*_{50}$, $E4^*_{50}$)
	I110b	unshielded cable, l_c = 50 m (configurations $E1_{50}$, $E4_{50}$)
	I110c	unshielded cable, l_c = 50 m (configurations $E1_{50}$, $E4_{50}$)
500 kW	I500	unshielded cable, l_c = 10 m (configurations $E1_{10}$, $E4_{10}$)
		shielded cable, l_c = 10 m (configurations $E1^*_{10}$, $E4^*_{10}$)

Table 4.5: Investigated combinations of inverters and motor cables for assessing the *influence on parasitic currents via grounded rotor*

Again, if *unshielded motor cable* is used, the bearing currents increase in configuration E4 by partially *more than 100 %* when compared with configuration E1 (Fig. 4.28). The results are the same with inverter I110b, motor M110a and unshielded motor cable with l_c = 10 m instead of inverter I110a, motor M110a and l_c = 50 m as in case of Fig. 4.27.

Motor supply with *inverter* I110*c* that has an integrated *dv/dt*-filter at the output leads again to reduction of stator and rotor ground currents i_g and i_{rg} down to about 30 %, resulting in *reduction of the bearing currents* i_b to about the same extent.

The same as at the 11 kW power level, if *shielded motor cable* is used, additional *grounding of the rotor* does *not influence* the stator ground and bearing currents i_g and i_b to a significant extent (Fig. 4.28). This is also true for the investigations with motor cable with length l_c = 10 m instead of l_c = 50 m (Fig. 4.28).

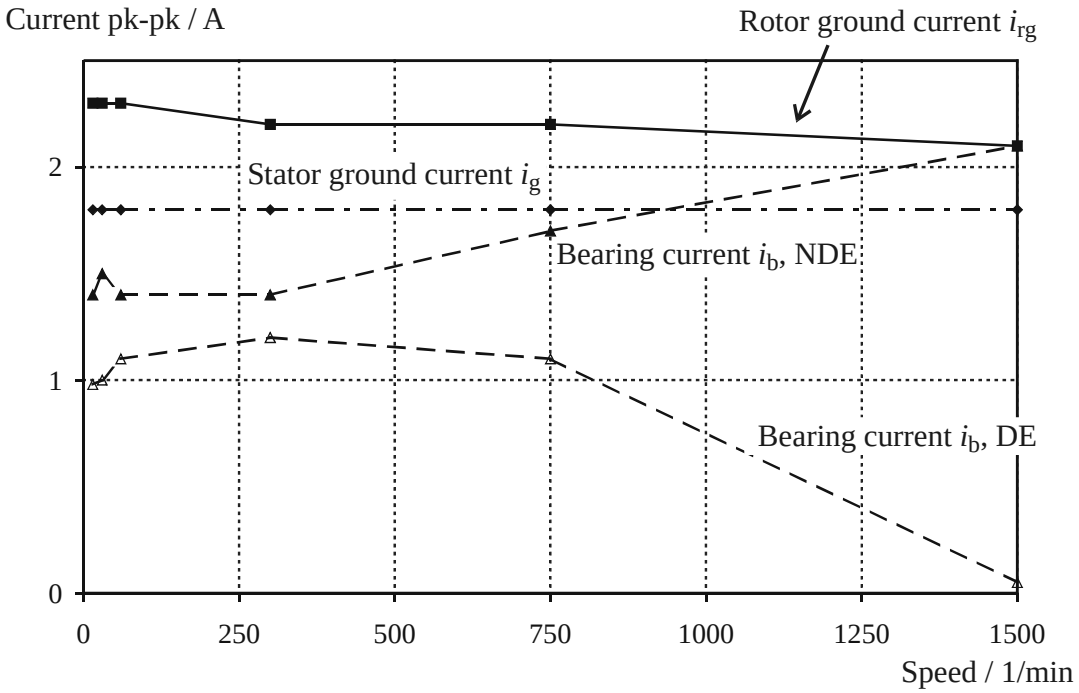

Figure 4.25: 11 kW power level - Measured stator and rotor ground currents and corresponding bearing currents *with grounded rotor*, induction motor M11b and inverter I11b, configuration $E4_{50}$ ($l_c = 50$ m, unshielded motor cable), $\vartheta_b \approx 70°C$

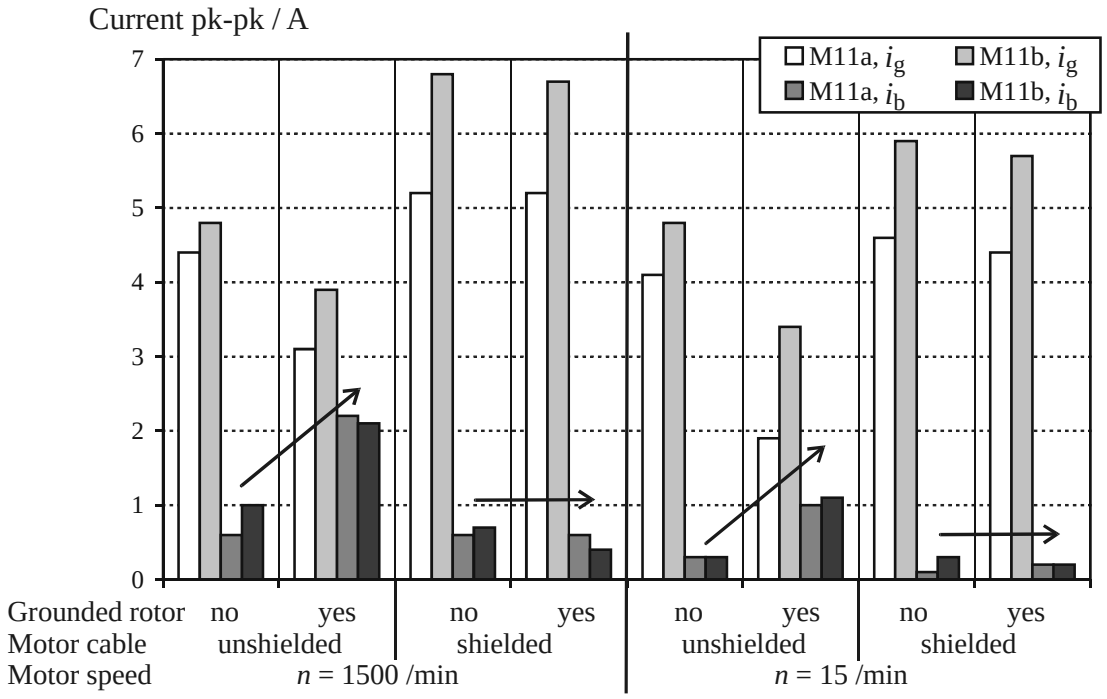

Figure 4.26: 11 kW power level - Measured influence of *shielded versus unshielded motor cable* on stator ground and bearing currents *with grounded and with insulated rotor*, induction motors M11a and M11b and inverter I11a, motor cable length $l_c = 50$ m, $\vartheta_b \approx 70°C$

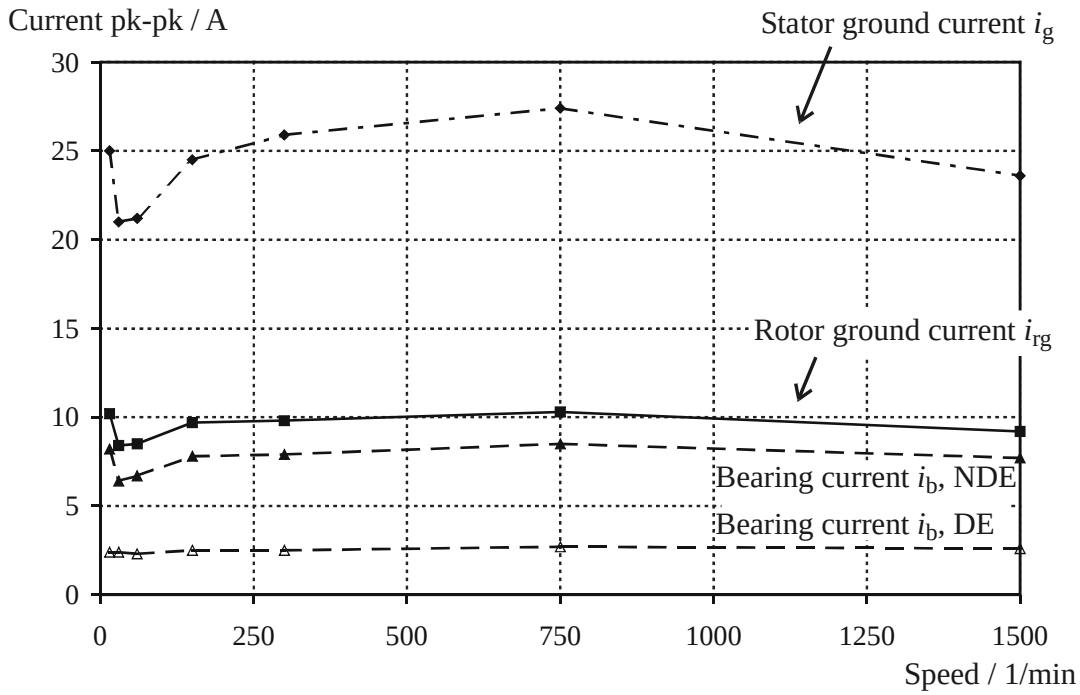

Figure 4.27: 110 kW power level - Measured stator and rotor ground currents and corresponding bearing currents *with grounded rotor*, induction motor M110b and inverter I110a, configuration $E4_{50}$ ($l_c = 50$ m, unshielded motor cable), $\vartheta_b \approx 70°C$

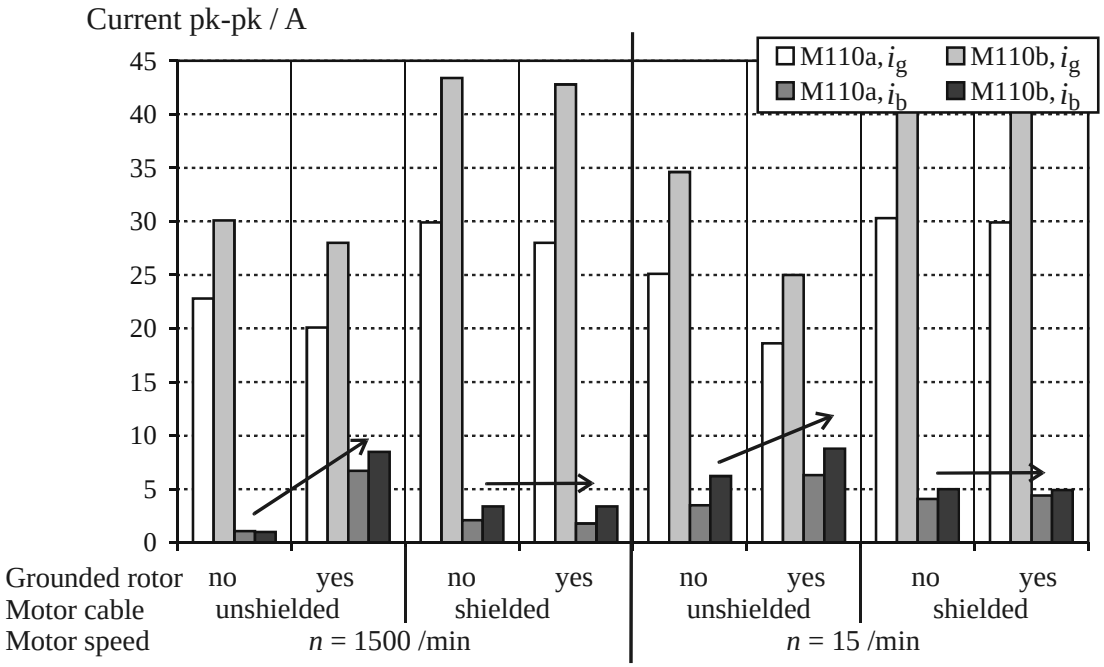

Figure 4.28: 110 kW power level - Measured influence of *shielded versus unshielded motor cable* on stator ground and bearing currents *with grounded and with insulated rotor*, induction motor M110a and M110b and inverter I110a, motor cable length $l_c = 50$ m, $\vartheta_b \approx 70°C$

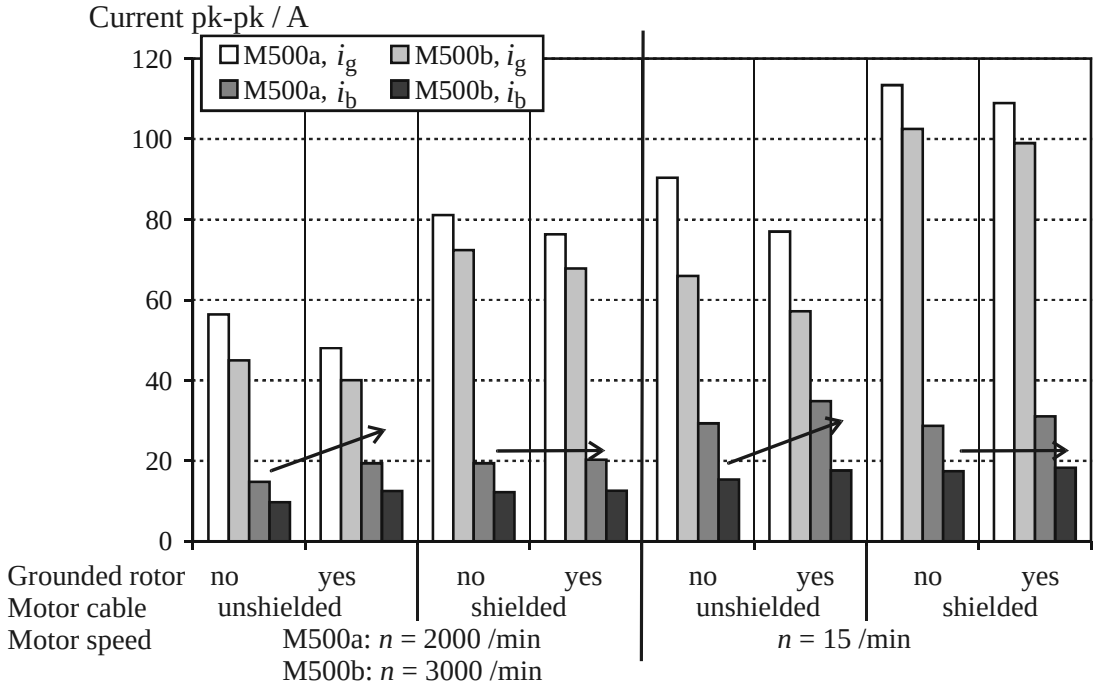

Figure 4.29: 500 kW power level - Measured influence of *shielded versus unshielded motor cable* on stator ground and bearing currents *with grounded and with insulated rotor*, induction motor M500a and M500b and inverter I500, motor cable length l_c = 50 m, $\vartheta_b \approx 70°C$

♦ ***500 kW power level*:** At this power level, the results are very similar to those obtained at the 110 kW power level. Again, *grounding of the rotor* leads to remarkable *increase* of the bearing currents if *unshielded motor cable* is used, whereas it does *not have any influence*, if *shielded motor cable* is used (Fig. 4.29).

If unshielded motor cable is used and the dv/dt at the motor terminals is not limited by a filter, large rotor ground currents pass the bearings.
The magnitude of the currents increases with increasing length of the motor cable.
Use of shielded motor cables almost eliminates the rotor ground currents. Maximum length of the motor cable in the investigations was l_c = 50 m.

4.11 Calculated Apparent Bearing Current Densities

Limits of "safe" or "dangerous" bearing current densities J_b that are ensured by experience do not exist today, due to the lack of large scale experiments (→ Section 1.5.1, p. 14 and Chapter 6, p. 93). However, for classification of the measurement results, the apparent bearing current densities that correspond to the measured bearing current amplitudes were calculated. For this purpose, the *Hertz*'ian contact area A_H of the load zone of the ball bearings is needed. The values of A_H were calculated at FAG, Schweinfurt, Mr. Ortegel,

with a special in-house calculation method, based on elasticity theory of *H. Hertz* [32], [33] (→ Appendix C, p. 211). The values of radial and axial forces F_R and F_A of the bearings of the test motors were provided by the manufacturers of the motors. Details of the calculations are discussed in Appendix C (p. 211). With the amplitude of the bearing current $\hat{i}_b$ being typically 2/3 of the peak-to-peak value $i_{b,\,pk\text{-}to\text{-}pk}$ (e.g. Fig. 4.2, Fig. 4.3, Fig. 4.4, Fig. 4.5), the apparent bearing current density J_b was derived according to (4.1). Figures showing the calculated values of apparent bearing current density J_b for selected configurations and points of operation are given in this section.

$$J_b = \frac{\hat{i}_b}{A_H} = \frac{2/3 \cdot i_{b,\,pk\text{-}to\text{-}pk}}{A_H} \tag{4.1}$$

♦ ***1 kW power level*:** With the bearing at ambient temperature, $\vartheta_b \approx 25°C$, apparent bearing current densities as high as 3.5 A/mm^2 are obtained. With the bearing at temperature typical for load operation, $\vartheta_b \approx 40°C$, the value is still about 1 A/mm^2 (Fig. 4.30; calculations based on measurement results shown in Fig. 4.10, p. 51).

♦ ***11 kW power level*:** With grounded rotor and use of unshielded motor cable, the calculated apparent bearing current densities reach values up to 0.5 A/mm^2. If the rotor is not grounded and / or shielded motor cable used, the values of J_b are smaller than 0.2 A/mm^2, in most cases even $\leq$ 0.1 A/mm^2 (Fig. 4.31; calculations based on measurement results shown in Fig. 4.26, p. 65).

♦ ***110 kW power level*:** At this power level, with grounded rotor and use of unshielded motor cable, the calculated apparent bearing current densities are as high as $\approx$ 0.5 A/mm^2. If the rotor is not grounded and / or shielded motor cable used, the values are $\approx$ 0.3 A/mm^2 for low motor speed, n = 15 /min, and (0.1...0.2) A/mm^2 for elevated motor speed, n = 1500 /min (Fig. 4.32; calculations based on measurement results shown in Fig. 4.28, p. 65). The calculated bearing current densities J_b are thus larger than those calculated at the 11 kW power level.

♦ ***500 kW power level*:** The motors of this power level show the largest calculated apparent bearing current densities J_b with values up to 1.5 A/mm^2. Even if the rotor is not grounded, the value of J_b is still about 1.0 A/mm^2 at low motor speed, n = 15 /min, and (0.5...1.0) A/mm^2 at elevated motor speed, n = 2000 / 3000 /min (motor M500a/M500b) (Fig. 4.33; calculations based on measurement results shown in Fig. 4.29, p. 67).

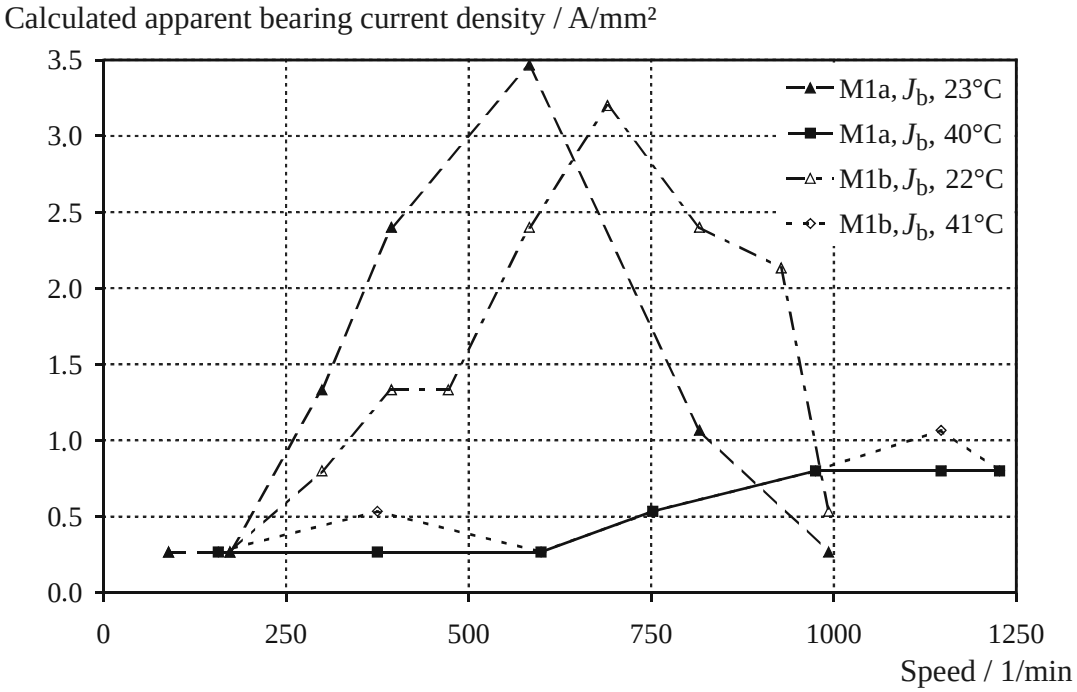

Figure 4.30: 1 kW power level - *Calculated apparent bearing current density* as function of motor speed and bearing temperature, permanent magnet motors M1a and M1b and EC-controller EC1, configuration $E1_{01}$ ($l_c = 1$ m, unshielded motor cable)

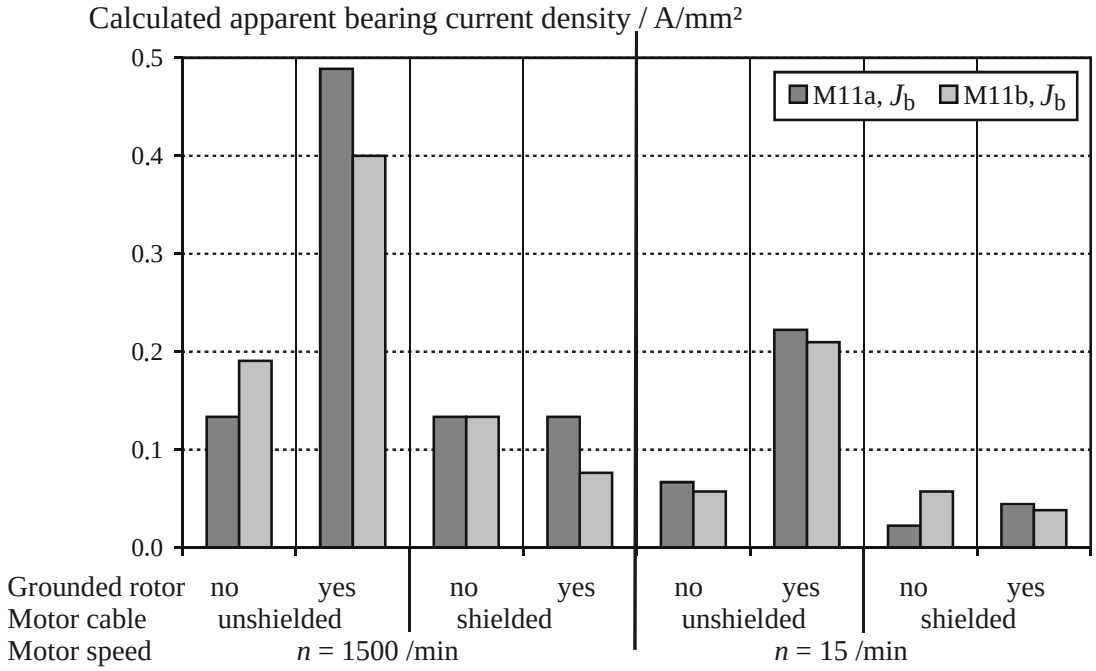

Figure 4.31: 11 kW power level - *Calculated apparent bearing current density* for motor operation with shielded and with unshielded motor cable and with grounded and with insulated rotor, induction motors M11a and M11b and inverter I11a, motor cable length $l_c = 50$ m, $\vartheta_b \approx 70°C$

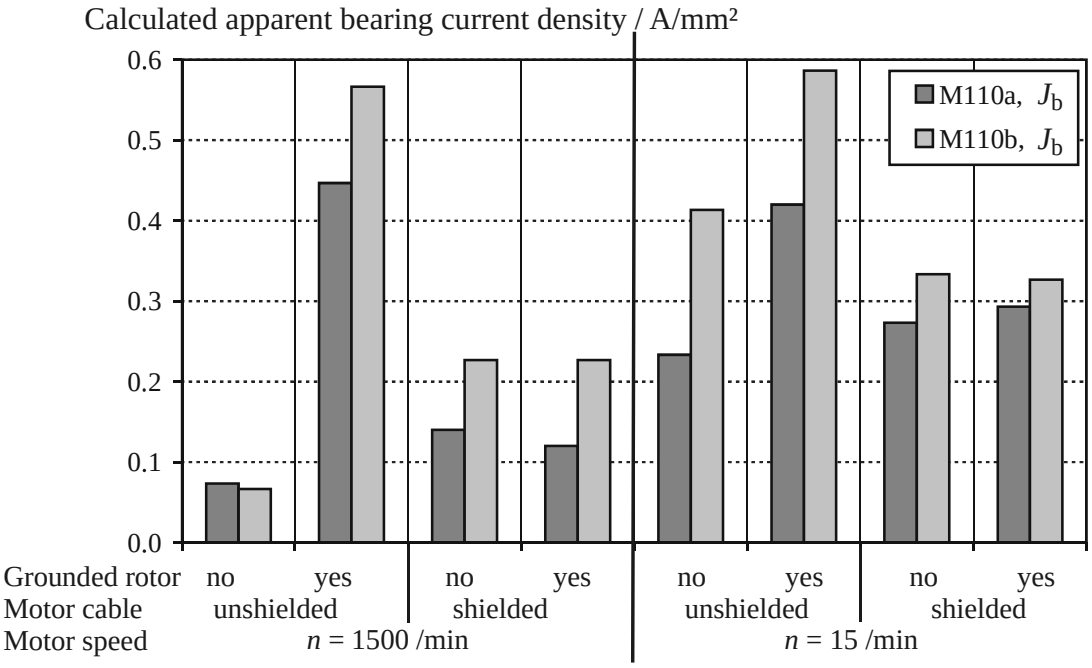

Figure 4.32: 110 kW power level - *Calculated apparent bearing current density* for motor operation with shielded and with unshielded motor cable and with grounded and with insulated rotor, induction motor M110a and M110b and inverter I110a, motor cable length $l_c = 50$ m, $\vartheta_b \approx 70°C$

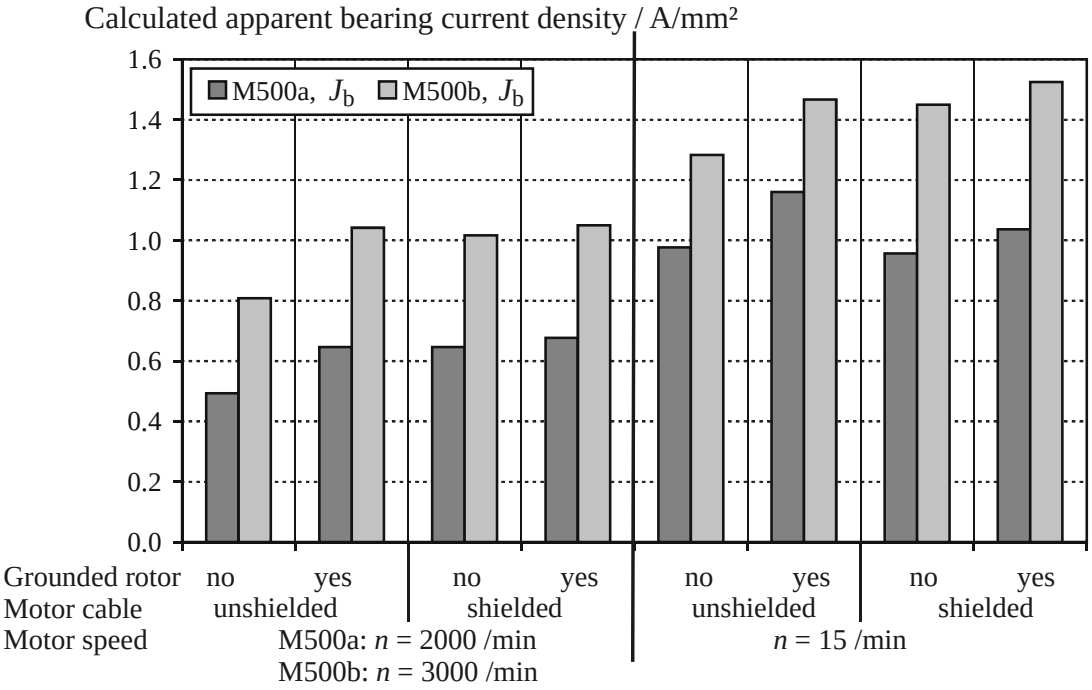

Figure 4.33: 500 kW power level - *Calculated apparent bearing current density* for motor operation with shielded and with unshielded motor cable and with grounded and with insulated rotor, induction motor M500a and M500b and inverter I500, motor cable length $l_c = 50$ m, $\vartheta_b \approx 70°C$

Chapter 5

Influence of Mitigation Techniques on Bearing Currents

5.1 Review of Mitigation Techniques

Different mitigation techniques have been proposed to eliminate inverter-induced bearing currents. They can be divided into two groups, depending on their function:

Group1: The first group comprises the *mitigation techniques on inverter side*. These mitigation techniques include

- ▶ inverter output filters, such as dv/dt-reactors, dv/dt-filters, sinusoidal filters and common mode chokes,
- ▶ special voltage modulation techniques and common mode filters to reduce or eliminate the common mode voltage.
- ▶ Special cables, i.e. shielded cables, may also be included (→ Section 4.10, p. 63).

Group2: The second group consists of *counter-measures against bearing currents within or at the motor*. These counter-measures include

- ▶ insulated bearings ("coated bearings"),
- ▶ ceramic or hybrid bearings,
- ▶ insulated couplings,
- ▶ low impedance grease,
- ▶ rotor brushes, and
- ▶ electrostatically shielded rotor [34].

The effect of the different techniques depends mainly on the type of bearing current to reduce or suppress. Table 5.1 summarizes different countermeasures and their effectiveness on the different types of bearing currents as given in literature [2], [5], [17], [21], [35], [36], [37], including the International standard IEC 60034 - 25: Rotating electrical machines - Part 25: "Guide for the design and performance of cage induction motors for converter supply" (Table 5) [37].

Different mitigation techniques were evaluated in the frame of the research program (→ Chapter 2, p. 15). The same measurement technique and setup as for the measurements of the influence of other system parameters (→ Chapter 4, p. 41) was used to obtain comparable measurement results (→ Chapter 3, p. 29).

Counter-measure	Bearing current type			Additional comments
	EDM-currents	Circulating bearing currents	Rotor ground currents	
Countermeasures of **Group1**				
dv/dt-filter	Not effective	Effective	Effective	Reduce also capacitive cable currents
Common mode voltage filter	Effective	Effective: Reduced HF voltage also decreases LF currents.	Effective	Greatest reduction of common mode voltage if filter fitted at converter output.
Modulation schemes that reduce the common mode voltage	Effective	Effective	Effective	
Countermeasures of **Group2**				
NDE bearing insulated, or ceramic rolling elements	Not effective: Protects only one bearing.	Effective	Not effective: Protects only one bearing.	NDE bearing insulated to avoid need for an insulated coupling.
NDE and DE bearing insulated, or ceramic rolling elements	Effective: May require additional brush contact.	Effective: One insulated bearing is adequate.	Effective	Most effective for small, less practical for large frame sizes.
NDE and DE bearing insulated, or ceramic rolling elements and additional insulated coupling and shaft grounding brush	Effective	Effective	Effective	Most effective (especially for larger machines)
One brush contact, no bearing insulation	Effective, but care needed to ensure low brush contact impedance.	Not effective: Protects only one bearing.	Effective, but does not protect bearings in driven load.	Servicing necessary.

Table 5.1: Effectiveness of bearing current countermeasures according to [2], [5], [17], [21], [35], [36], [37]

Counter-measure	Bearing current type			Additional comments
	EDM-currents	Circulating bearing currents	Rotor ground currents	
NDE bearing insulated, one DE brush contact	Effective, but care needed to ensure low brush contact impedance.	Effective: Brush unnecessary for this current type. NDE tachometer bearing, if fitted, needs protection.	Effective, but does not protect bearings in driven load.	Servicing necessary. Most practical for large frame sizes. DE brush used to avoid insulated coupling.
Two brush contacts, DE and NDE, no bearing insulation	Effective, but care needed to ensure low brush contact impedance.	Effective, but care needed to ensure low brush contact impedance.	Effective, but does not protect bearings in driven load.	Servicing necessary.
Low resistance lubrication and carbon-filled bearing seals	Effective: Depends on condition of materials.	Poor	Poor	No long term experience. Lubrication effectiveness reduced.
Rotor in faraday cage (Electrostatically shielded rotor)	Very effective	Not effective	Not effective	Problems from convertor generated circulating currents that normally only occur in larger motors.
Insulated coupling	Not effective	Not effective	Very effective	Also prevents possible damage to driven load.
Frame to driven load connection	Not effective	Not effective	Effective	Also prevents possible damage to driven load.

Table 5.1 (continued): Effectiveness of bearing current countermeasures according to [2], [5], [17], [21], [35], [36], [37]

The following mitigation techniques were chosen for study in this research program:

- ▶ protective elements at inverter output (integrated dv/dt-filter, inverters I11c and I110c, Section 4.5),
- ▶ dv/dt-reactors, sinusoidal filters (Section 5.3),
- ▶ common mode chokes (Section 5.3),
- ▶ common mode filter (Section 5.3),
- ▶ shielded motor cables (Section 4.7, p. 56 and 4.10, p. 63),
- ▶ insulated bearings (Section 5.4),
- ▶ hybrid bearings (Section 5.5).

Low impedance grease was not investigated, as the electrical and mechanical properties of the lubrication need to be discussed with the supplier of the lubricating grease. This was beyond the scope of the research program. Grounding brushes were not tested, as they need servicing, and are therefore no good solution for smaller machines. Furthermore, the electrostatically shielded rotor was not studied.

5.2 Basic Function of Filters

The ***principal design*** of the different investigated ***inverter-output filters is shortly reviewed***.

♦ ***dv/dt-reactors*** comprise three coils that are inserted into the motor phases (Fig. 5.1a). The function of these reactors is to increase the voltage rise time t_r and to reduce thereby the voltage change rate dv/dt (Fig. 5.2). The rise time t_r increases with L, therefore the rated voltage drop at the reactor v_k, determined at rated motor frequency f_sr, has to be relatively large (5.1).

$$v_\mathrm{k} = \frac{V_\mathrm{k}}{V_\mathrm{sr}} = 2\pi f_\mathrm{sr} L \frac{I_\mathrm{r}}{V_\mathrm{sr}} \propto L \tag{5.1}$$

where:

v_k = rated voltage drop at reactor,
V_k = voltage drop at reactor (rms-value),
V_sr = rated motor voltage (rms-value),
f_sr = rated motor frequency,
I_r = rated motor current (rms-value).

The value v_k ranges typically between $v_\mathrm{k} = (2...8)$ %.

These dv/dt-reactors have originally been designed to reduce capacitive currents in the motor cable. With a given phase capacitance C_cable and voltage change rate dv/dt, the capacitive cable current $i_\mathrm{c,cap}$ is (5.2).

$$i_\mathrm{c,cap} = C_\mathrm{cable} \frac{dv}{dt} \tag{5.2}$$

As C_cable increases with cable length l_c, these reactors are recommended especially for long motor cables. The capacitive cable current $i_\mathrm{c,cap}$ loads the cable thermally, but does *not* reach the motor. Therefore, it has to be regarded as a parasitic effect. With reduced dv/dt, these currents are reduced likewise.

♦ ***Sinusoidal filters*** consist of three phase reactors (with phase inductivity L_{ph}) and condensers (with line-to-earth capacity CLg or line-to-line capacity CLL) forming a low pass filter (Fig. 5.1b). Voltages with frequencies below the resonance frequency f_0 (5.3) pass almost without reduction of amplitude, whereas voltage signals with $f > f_0$ are diminished with $1/f^2$, thus, with 40 dB/decade.

$$f_0 = \frac{1}{2\pi\sqrt{L_{\mathrm{ph}} C_{\mathrm{Lg}}}} = \frac{1}{2\pi\sqrt{3 L_{\mathrm{ph}} C_{\mathrm{LL}}}} \tag{5.3}$$

where:

f_0 = resonance frequency of filter,
L_{ph} = inductivity of phase reactor,
C_{Lg} = capacity of line-to-earth condenser,
C_{LL} = capacity of line-to-line condenser.

Usually, these filters are designed in the following way: The resonance frequency f_0 must be well above the fundamental frequency of the inverter that operates the motor and well below the inverter switching frequency f_{c} to reduce high frequency current ripples, which may cause additional motor losses and noise.

The line-to-line voltage v_{LL} (→ Section 1.3, p. 6) is nearly ideally sinusoidal at the motor terminals. The two parameters L_{ph} *and* C_{Lg}, respectively C_{LL}, may be chosen. Usually, L_{ph} is chosen as a much lower value than with dv/dt-reactors, in order to avoid the unwished voltage drop v_{k}. As a result, the value C_{Lg}, respectively C_{LL}, has to be increased. A sinusoidal filter acts mainly on the line-to-line voltage v_{LL}. The common mode voltage v_{com} is *not* suppressed. Sinusoidal filters are usually very large and expensive, as the full apparent power of the voltage harmonics determines the voltage rating.

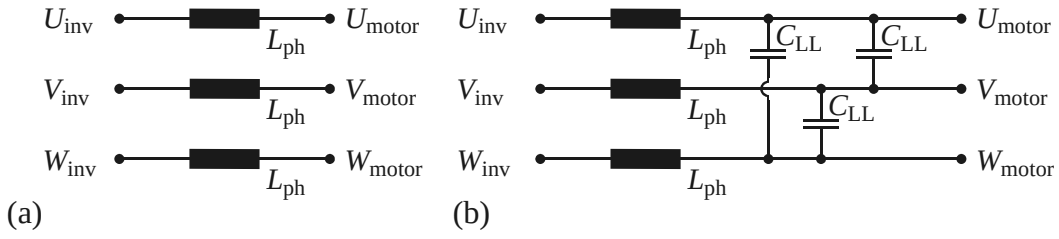

Figure 5.1: Principal design of (a) a dv/dt-reactor and (b) a sinusoidal filter

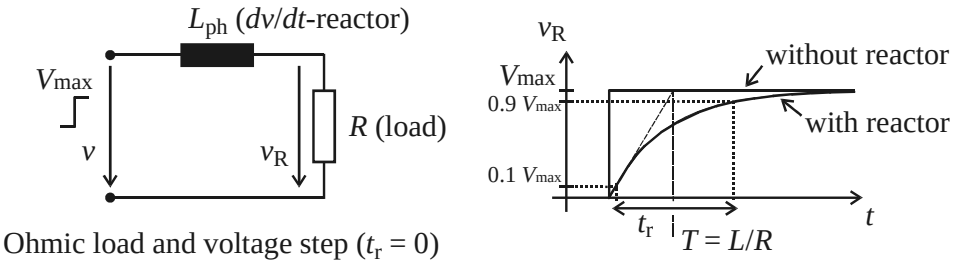

Figure 5.2: Basic example of function of a dv/dt-reactor

♦ ***dv/dt-filters*** are RLC-components with resistances added to attenuate the high frequency components (Fig. 5.3a). A huge variety of dv/dt-filters is available to meet different technical specifications. These filters are often complex circuits, some including connections to the dc-link of the inverter, diodes, and / or capacitances to the grounding connection. The main difference in comparison with sinusoidal filters is, that the resonance frequency f_0 is much higher than the inverter switching frequency f_c, due to usually small values of L and C. Therefore, only the dv/dt is reduced, but the inverter-output voltages v_{LL} and v_{Lg} are still a pulse pattern. An advantage of dv/dt-filters is that, due to the small L and C, the filter itself is small and rather cheap.

♦ ***Common mode chokes*** are specially wound coils to suppress the zero sequence current i_0 (Fig. 5.3b). The three phases are generally wound in the same direction around a common core. Thereby, a considerable inductance L_{com} in the zero-sequence system is given, which suppresses i_{com}. Symmetrical three phase current systems, i_u, i_v and i_w (of arbitrary frequency) have *no* zero sequence component, as $i_{com} = 3\ (i_u + i_v + i_w) = 0$. Therefore, no resulting flux is generated by symmetrical three phase systems, leaving them unaffected by the common mode choke. Note, that the zero sequence inductance L_{com} reduces i_{com} ripple, but *not* the zero sequence voltage v_{com}, which is a value that is impressed by the inverter, $di_{com}/dt = v_{com}/L_{com}$. Therefore, the common mode voltage v_{com} remains unaffected.

♦ ***Common mode filters*** are filters that are designed to eliminate the high-frequency components of the common mode *voltage*. These filters are complex circuits and many different designs have been proposed. Fig. 5.4 shows the principal design of the investigated common mode filter CMF11. The common mode voltage v_{com} (→ (1.1), p. 7) is given by the potential difference of node 1 and node 2 in Fig. 5.4, respectively. By clamping these two nodes to plus and minus dc-link, the oscillations of v_{com}, that are caused by the power switches of the inverter, are suppressed. The large dc-link capacitors keeps the plus and minus potential of the dc-link rather fixed.

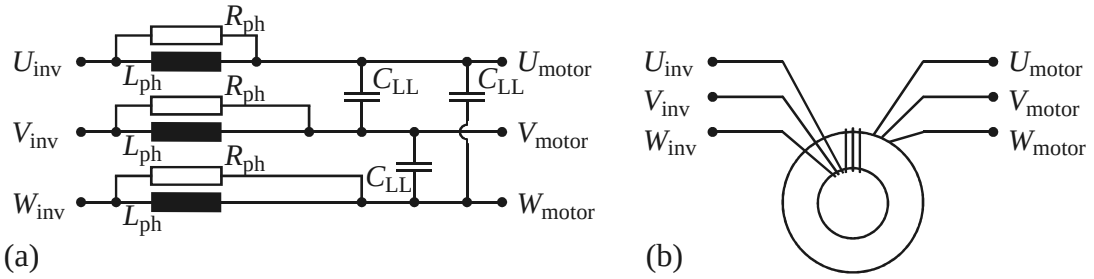

Figure 5.3: Principal design of (a) a dv/dt-filter and (b) a common mode choke

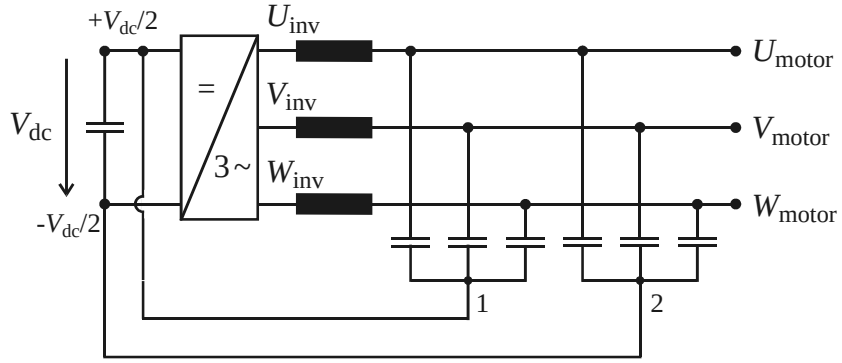

Figure 5.4: Principal design of a common mode (voltage) filter (e.g. CMF11)

Filter design is a complicated technique that needs to be done by experts. *All filters investigated here are standard components that are available on the market.*

5.3 Influence of Filters

Almost all measurements with use of filters were performed on both motors of the 11 kW, 110 kW and 500 kW power level respectively, in the main configuration, using inverters and motor cables as summarized in Table 5.2.

Power level	Inverter	Motor cable type and length
11 kW	I11a	unshielded cable, l_c = 2 m (configuration $E1_{02}$)
	I11c	unshielded cable, l_c = 50 m (configuration $E1_{50}$)
110 kW	I110a	shielded cable, l_c = 10 m (configuration $E1^*_{10}$)
	I110c	unshielded cable, l_c = 50 m (configuration $E1_{50}$)
500 kW	I500	shielded cable, l_c = 10 m (configuration $E1^*_{10}$)

Table 5.2: Inverters and motor cables used for investigation of *filters operation*

All filters reduce the dv_{Lg}/dt of the line-to-earth voltage at the motor terminals down to $dv/dt \leq 0.5$ kV/μs (→ Appendix G, p. 229), thereby reducing the stator ground currents i_g down to 10 %, depending on the type of filter. The influence of filters on the bearing currents depends strongly on the type of bearing current occurring. In this section, figures are given that compare values of measured stator ground and bearing currents i_g and i_b for use of different filters at selected speed level (Fig. 5.8 to Fig. 5.17). Fig. 5.5 and Fig. 5.6 show examples of waveforms of measured stator ground and bearing currents with use of filters.

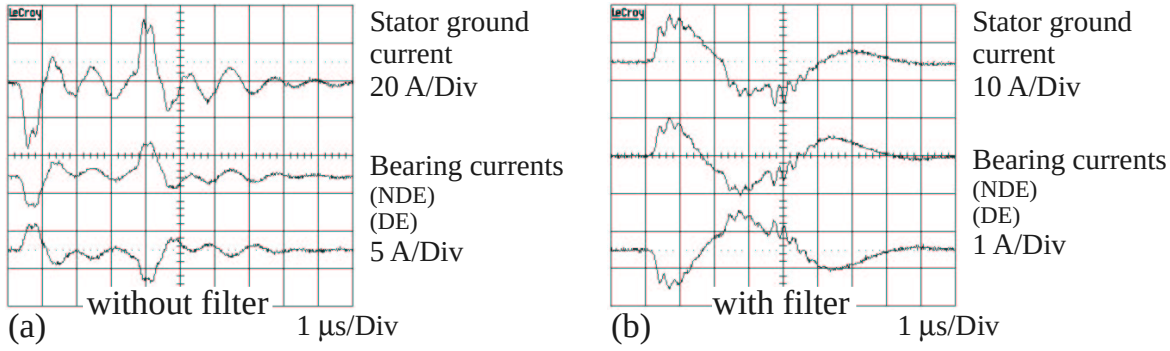

Figure 5.5: 110 kW power level - Measured bearing currents (a) *without* and (b) *with use of dv/dt-reactor* DV110a, induction motor M110b and inverter I110a, configuration E1*$_{10}$ (l_c = 10 m, shielded motor cable), motor speed n = 15 /min, $\vartheta_b \approx 70°C$

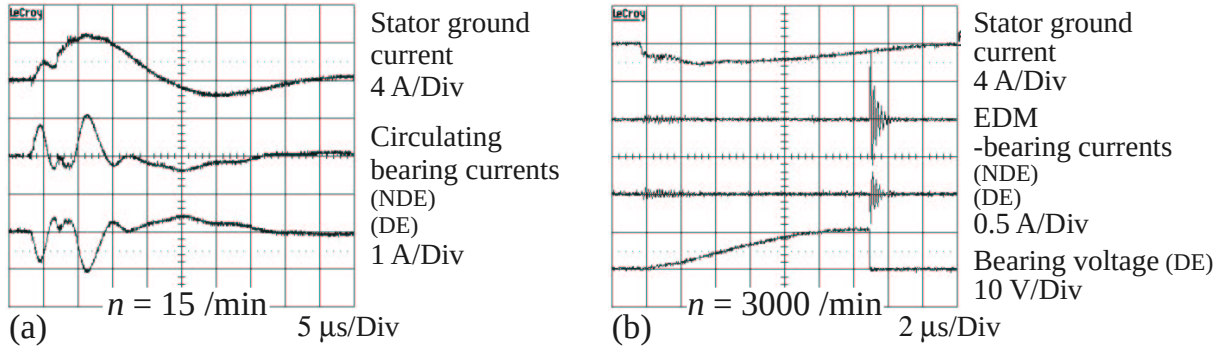

Figure 5.6: 500 kW power level - Measured bearing currents with *use of common mode choke* CMC500, induction motor M500b and inverter I500, configuration E1*$_{10}$ (l_c = 10 m, shielded motor cable), $\vartheta_b \approx 70°C$, motor speed (a) n = 15 /min (b) n = 3000 /min

♦ ***11 kW power level*:** The filters *reduce the stator ground current* i_g *down to 30 %*. Yet, the *bearing currents of EDM-type are NOT influenced* (Fig. 5.8, Fig. 5.9, and Section 4.5 (p. 50) for the results on the output-filter of inverter I11c). *None* of the filters *eliminates the common mode voltage*, thus leaving the *voltage buildup over the bearing unchanged*.

The *situation is different* for operation with the common mode *filter* CMF11, as this filter cancels the high-frequency components of the common mode voltage (Fig. 5.7 and Fig. 5.9). *No bearing currents occur*.

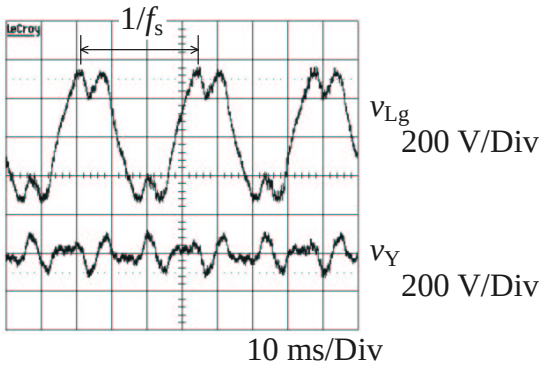

Figure 5.7: 11 kW power level - Measured line-to-earth voltage at the motor terminals v_{Lg} and stator winding common mode voltage v_Y of induction motor M11a and inverter I11a, configuration E1$_{02}$ (l_c= 2 m, unshielded motor cable), V_s = 400 V Y, f_s = 30 Hz / motor speed n = 900 /min

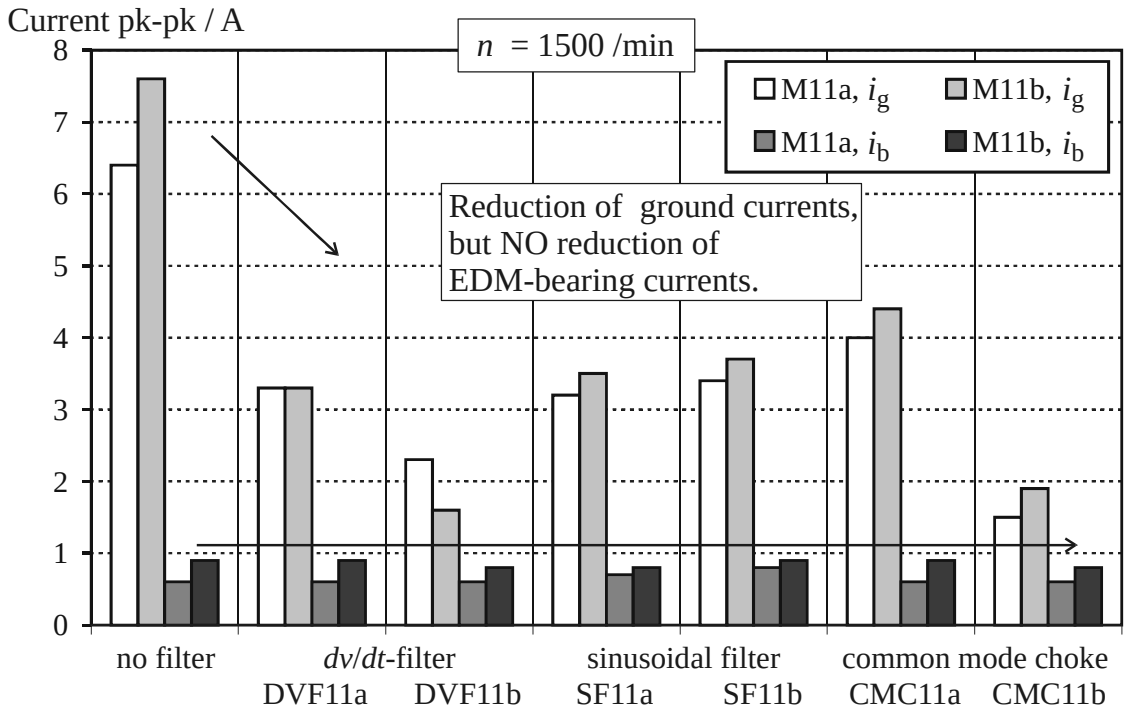

Figure 5.8: 11 kW power level - Measured stator ground and bearing currents with *use of different filters*, induction motors M11a and M11b and inverter I11a, configuration $E1_{02}$ ($l_c = 2$ m, unshielded motor cable), motor speed $n = 1500$ /min, $\vartheta_b \approx 70°C$

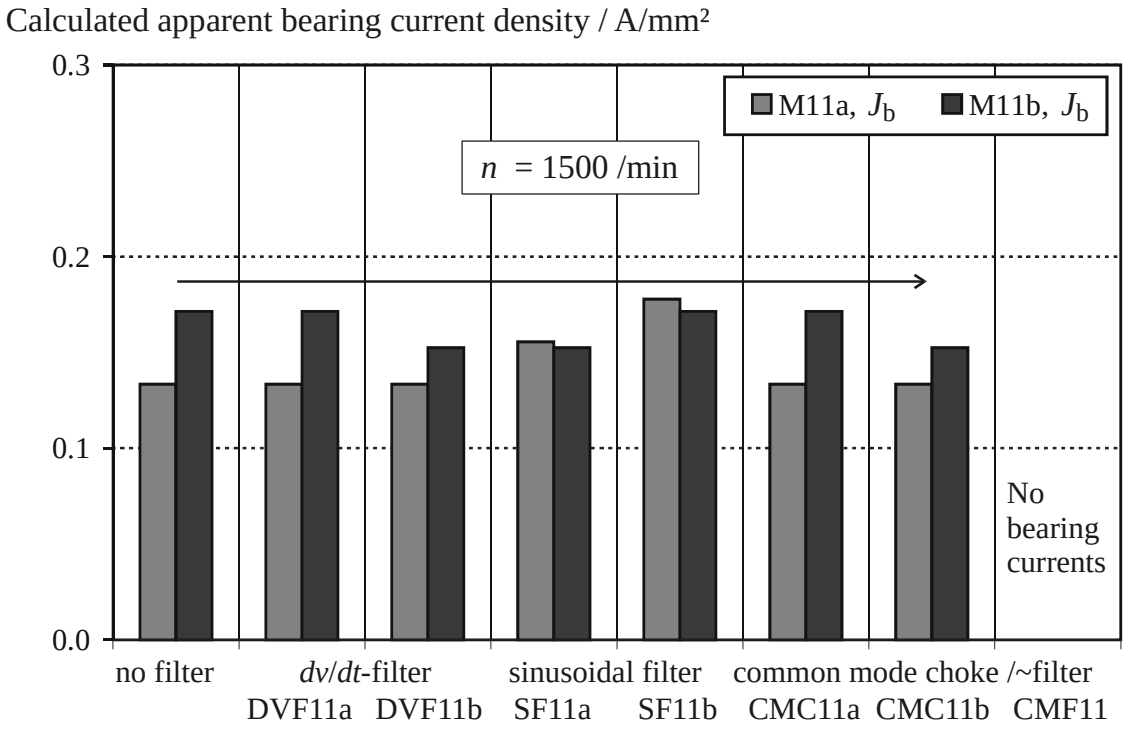

Figure 5.9: 11 kW power level - *Calculated apparent bearing current density* with *use of different filters*, induction motors M11a and M11b and inverter I11a, configuration $E1_{02}$ ($l_c = 2$ m, unshielded motor cable), motor speed $n = 1500$ /min, $\vartheta_b \approx 70°C$; calculation of apparent bearing current density as described in Section 4.11 (p. 67)

♦ ***110 kW power level*:** All filters lead to *reduction of the stator ground currents* i_g of *up to 90 %*, depending on the type of filter. At *low motor speed*, $n = 15$ /min, the *circulating* bearing currents are reduced by *about (70...95) %*. At *high motor speed*, $n = 1500$ /min, *small, and thus harmless EDM-currents occur instead of circulating bearing currents* (Fig. 5.10 to Fig. 5.13). The calculated apparent bearing current density J_b (→ Section 4.11, p. 67) at $n = 15$ /min is reduced down to about $J_b \approx 0.1$ A/mm^2 (Fig. 5.18). In order to distinguish the influence of the filter from other parameters like inverter control method, the *dv/dt*-filter at the inverter output of inverter I110c was bypassed (Table 5.3). With bypassed filter, the bearing currents are in the same range as with use of inverters I110a and I110b (→ Section 4.5, p. 50), whereas they are reduced by about 50 % with filter.

Motor	*Without dv/dt*-filter		*With dv/dt*-filter	
	i_b	i_g	i_b	i_g
	A pk-to-pk	A pk-to-pk	A pk-to-pk	A pk-to-pk
M110a	3.0	16.2	1.2	10.2
M110b	3.5	24.7	1.8	10.6

Table 5.3: 110 kW power level - Measured influence of the integrated *dv/dt*-filter at the output of inverter I110c on stator ground and bearing currents, induction motors M110a and M110b, configuration $E1_{50}$ ($l_c = 50$ m, unshielded motor cable), motor speed $n = 15$ /min, $\vartheta_b \approx 70°C$

♦ ***500 kW power level*:** Sinusoidal filter and *dv/dt*-reactor reduce *stator ground current* i_g and *circulating bearing currents* i_b *by about (30...50) %*. The common mode choke reduces the stator ground current i_g by *more than 90 %*, and the circulating bearing current occurring at low motor speed, $n = 15$ /min, by *about 75 %*. At high motor speed, $n = 1000$ /min, *reduction is larger than 90 %*, as only small, and therefore harmless EDM-bearing currents occur (Fig. 5.14 to Fig. 5.17). However, the calculated apparent bearing current density J_b (→ Section 4.11, p. 67) at $n = 15$ /min is still as high as $J_b \approx 0.7$ A/mm^2 for the sinusoidal filter and the *dv/dt*-reactor, and $J_b \approx 0.4$ A/mm^2 for the common mode choke (Fig. 5.19).

Filters that reduce the dv/dt of the line-to-earth voltage at the motor terminals reduce the ground currents and therefore the circulating bearing currents and rotor ground currents significantly. Filters without common mode voltage elimination do not reduce EDM-bearing currents.
Filter that cancel the high frequency components of the common mode voltage suppress all types of bearing currents.

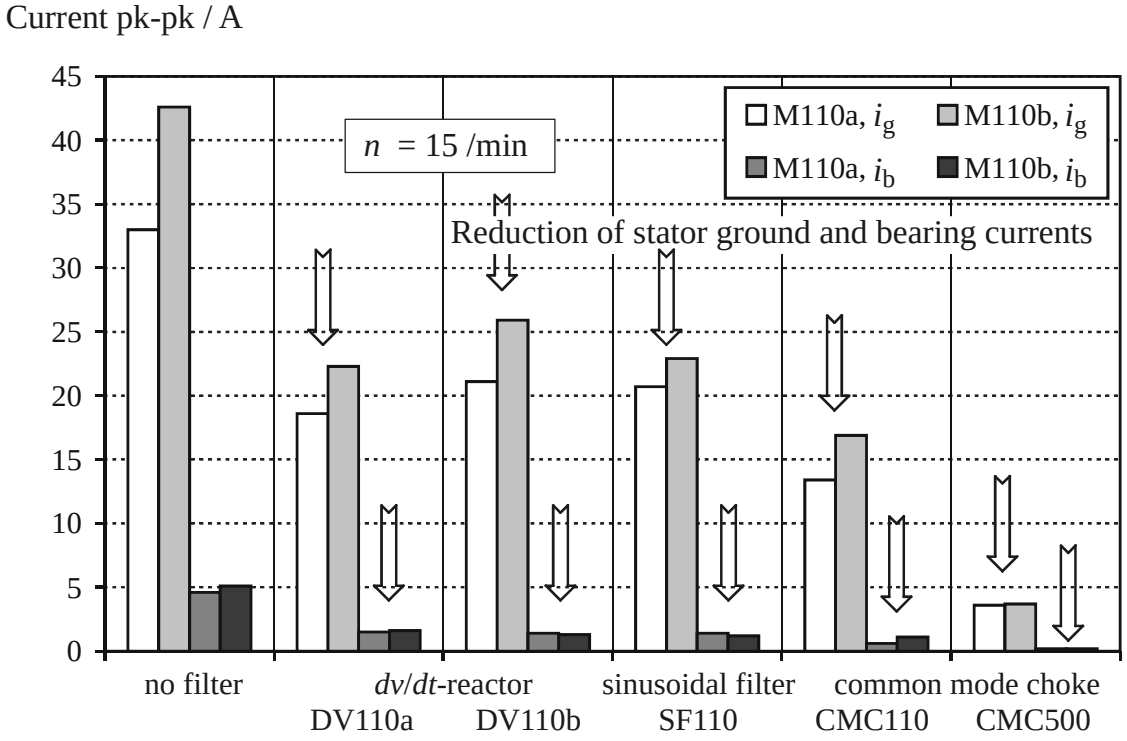

Figure 5.10: 110 kW power level - Measured stator ground and bearing currents with *use of filters*, induction motors M110a and M110b and inverter I110a, configuration E1*$_{10}$ (l_c = 10 m, shielded motor cable), motor speed n = 15 /min, $\vartheta_b \approx 70°C$

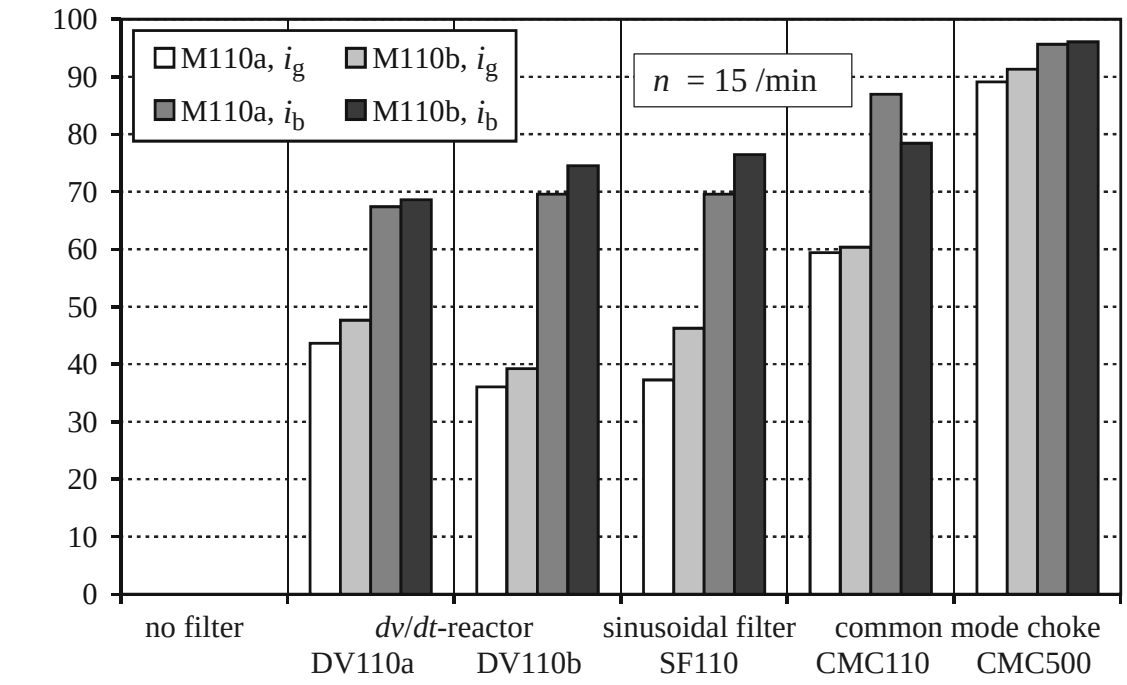

Figure 5.11: 110 kW power level - Measured percentage of reduction of stator ground and bearing currents with *use of filters*, 100 %: currents without use of a filter, induction motors M110a and M110b and inverter I110a, configuration E1*$_{10}$ (l_c = 10 m, shielded motor cable), motor speed n = 15 /min, $\vartheta_b \approx 70°C$

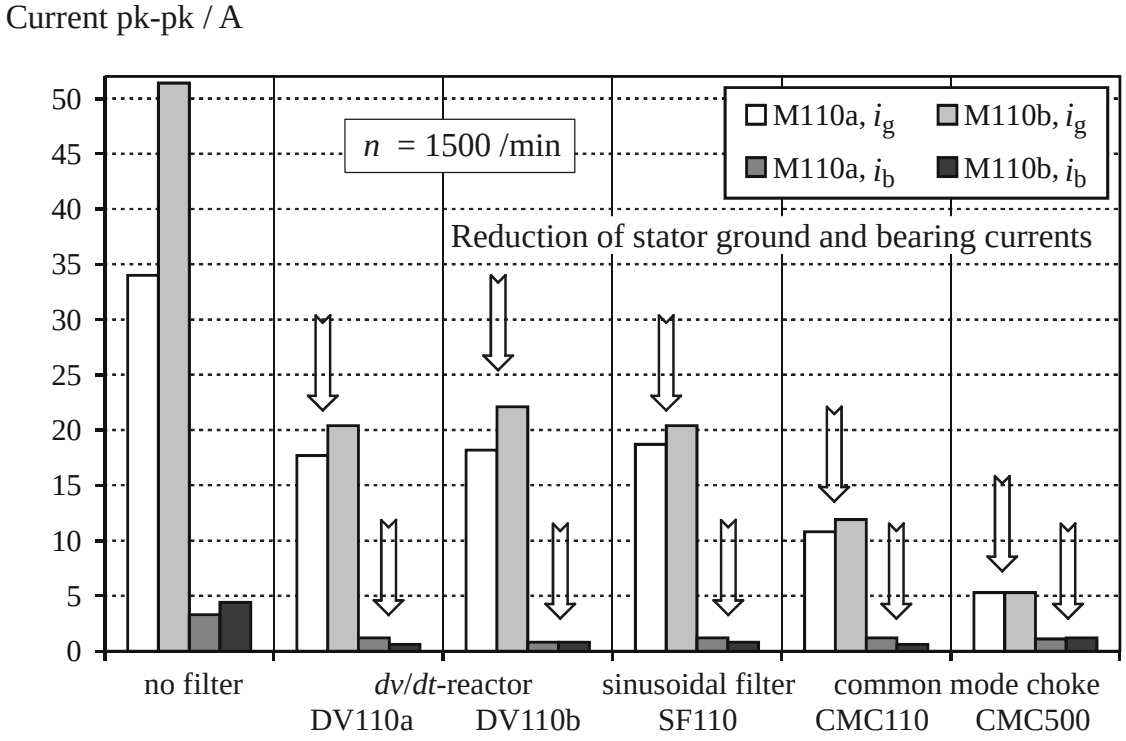

Figure 5.12: 110 kW power level - Measured stator ground and bearing currents with *use of filters*, induction motors M110a and M110b and inverter I110a, configuration E1*$_{10}$ (l_c = 10 m, shielded motor cable), motor speed n = 1500 /min, $\vartheta_b \approx 70°C$

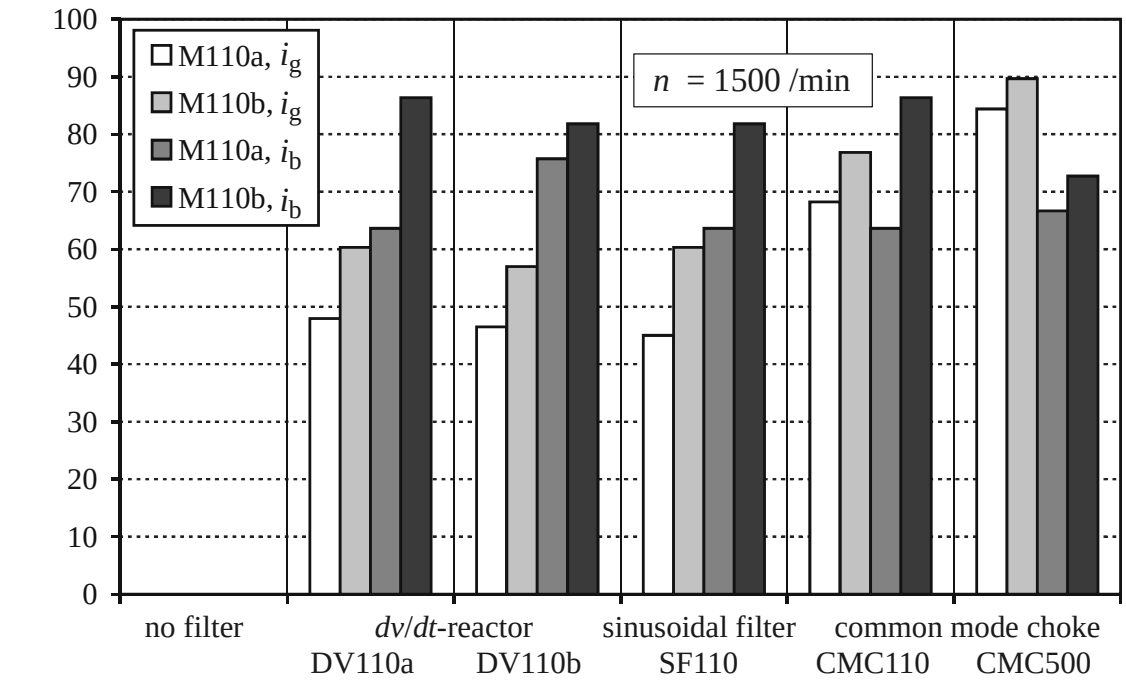

Figure 5.13: 110 kW power level - Measured percentage of reduction of stator ground and bearing currents with *use of filters*, 100 %: currents without use of a filter, induction motors M110a and M110b and inverter I110a, configuration E1*$_{10}$ (l_c = 10 m, shielded motor cable), motor speed n = 1500 /min, $\vartheta_b \approx 70°C$

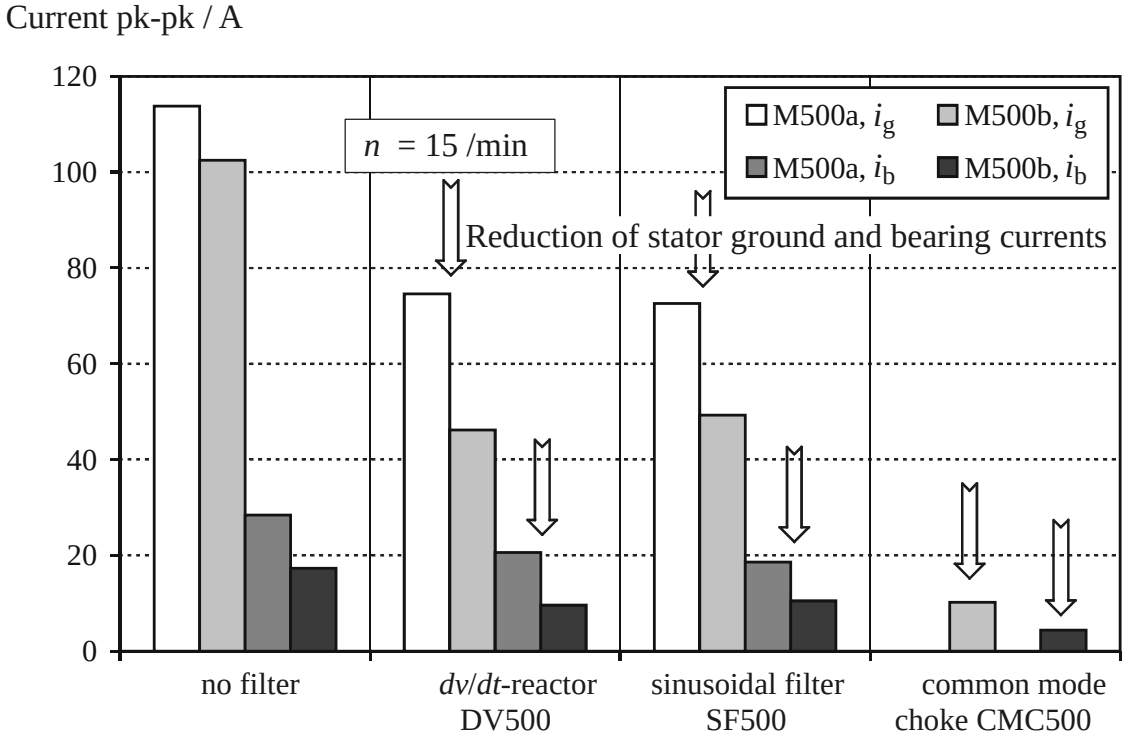

Figure 5.14: 500 kW power level - Measured stator ground and bearing currents with *use of filters*, induction motors M500a and M500b and inverter I500, configuration E1*$_{10}$ (l_c = 10 m, shielded motor cable), motor speed n = 15 /min, $\vartheta_b \approx 70°C$

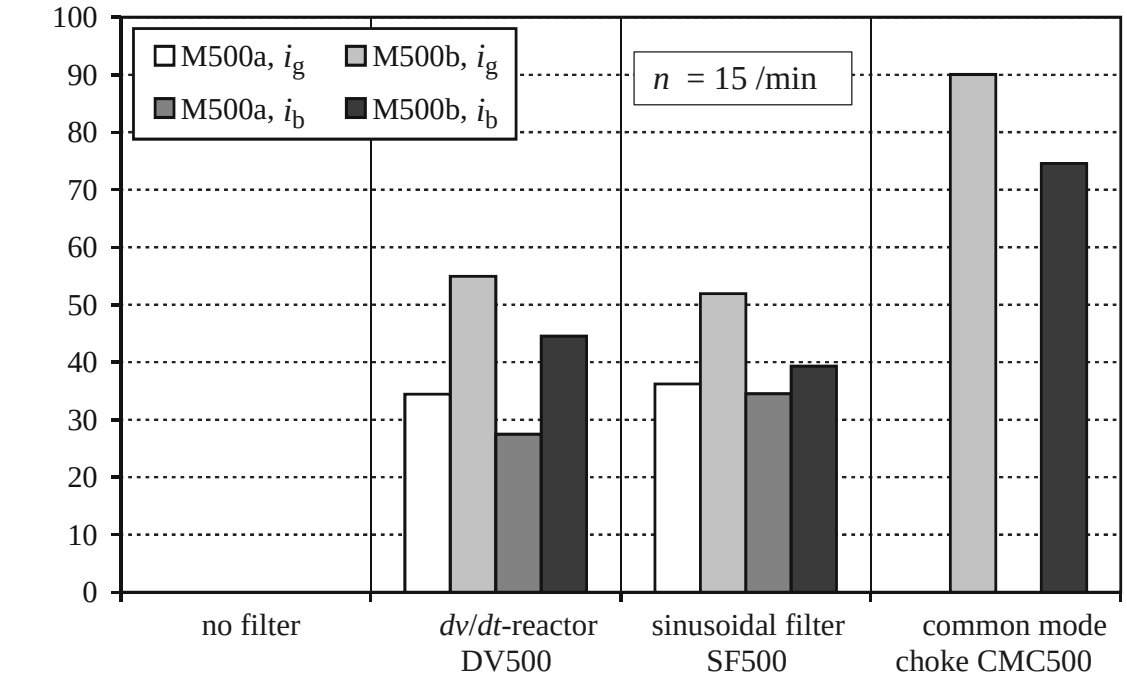

Figure 5.15: 500 kW power level - Measured percentage of reduction of stator ground and bearing currents with *use of filters*, 100 %: currents without use of a filter, induction motors M500a and M500b and inverter I500, configuration E1*$_{10}$ (l_c = 10 m, shielded motor cable), motor speed n = 15 /min, $\vartheta_b \approx 70°C$

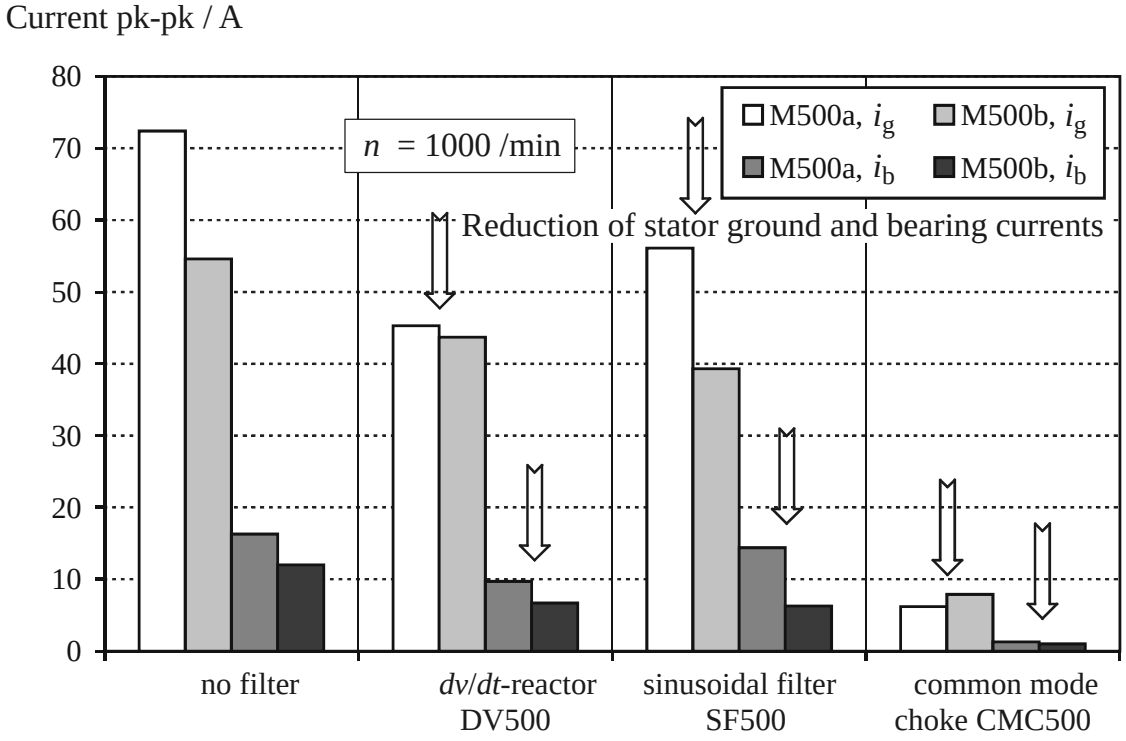

Figure 5.16: 500 kW power level - Measured stator ground and bearing currents with *use of filters*, induction motors M500a and M500b and inverter I500, configuration E1*$_{10}$ (l_c = 10 m, shielded motor cable), motor speed n = 1000 /min, $\vartheta_b \approx 70°C$

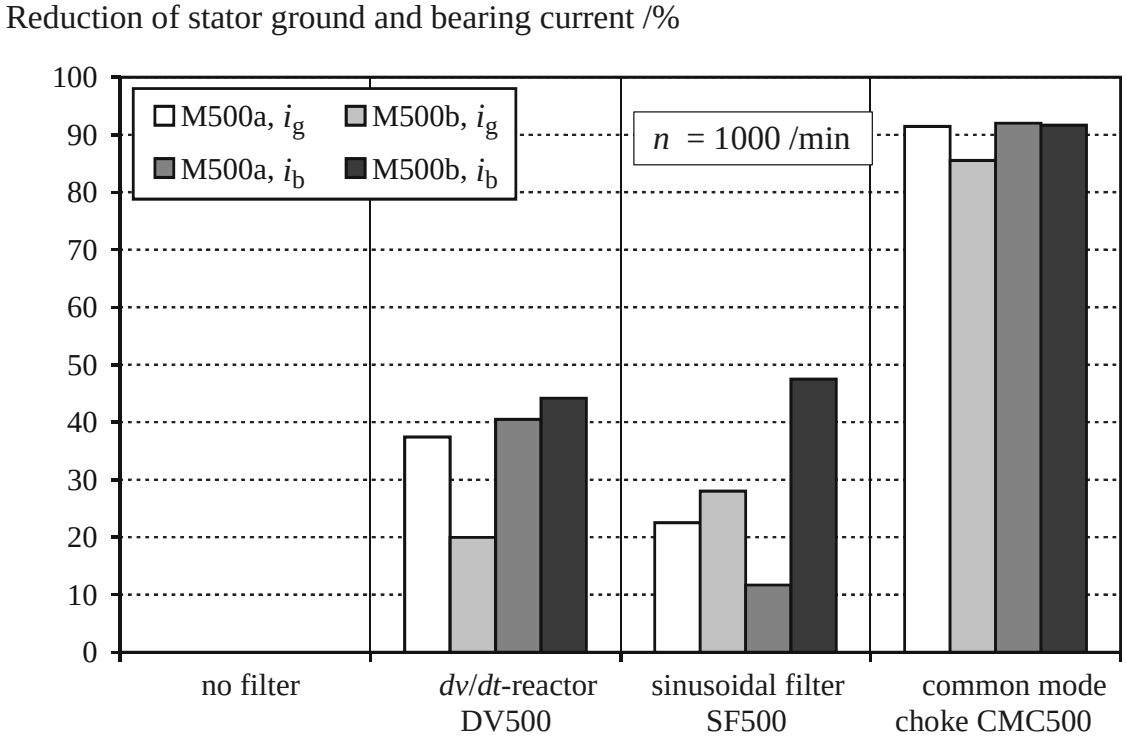

Figure 5.17: 500 kW power level - Measured percentage of reduction of stator ground and bearing currents with *use of filters*, 100 %: currents without use of a filter, induction motors M500a and M500b and inverter I500, configuration E1*$_{10}$ (l_c = 10 m, shielded motor cable), motor speed n = 1000 /min, $\vartheta_b \approx 70°C$

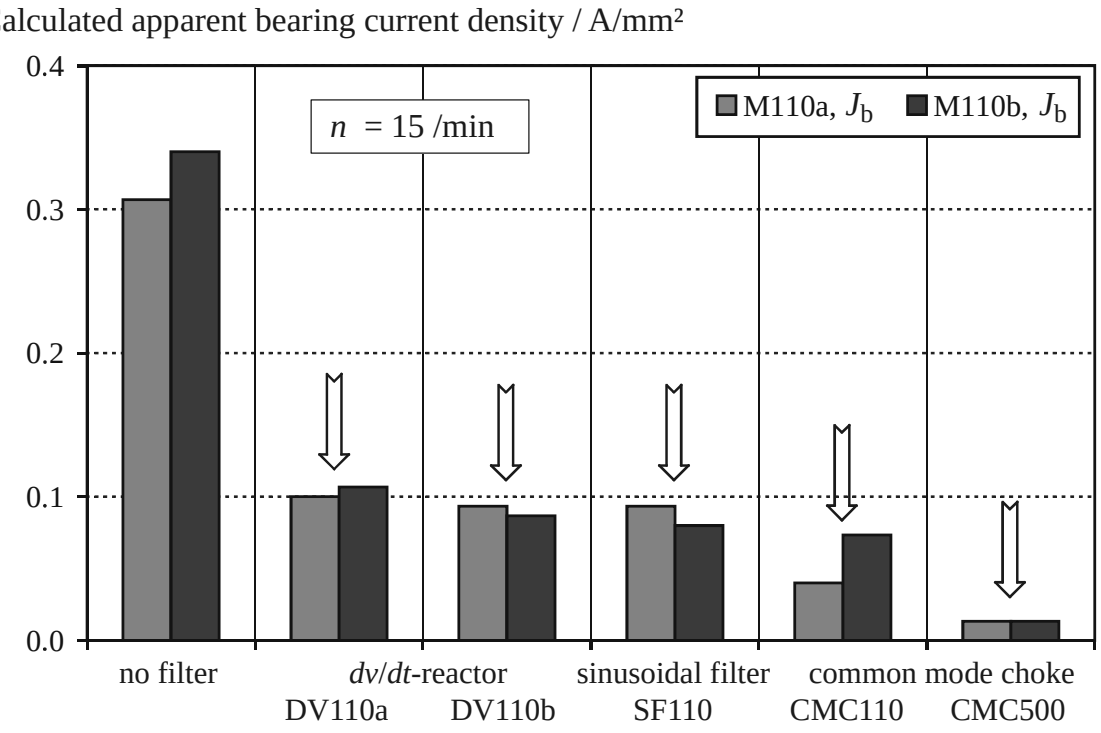

Figure 5.18: 110 kW power level - *Calculated apparent bearing current density* with *use of filters*, induction motors M110a and M110b and inverter I110a, configuration E1*$_{10}$ (l_c = 10 m, shielded motor cable), motor speed n = 15 /min, $\vartheta_b \approx 70°C$; calculation of apparent bearing current density as described in Section 4.11 (p. 67)

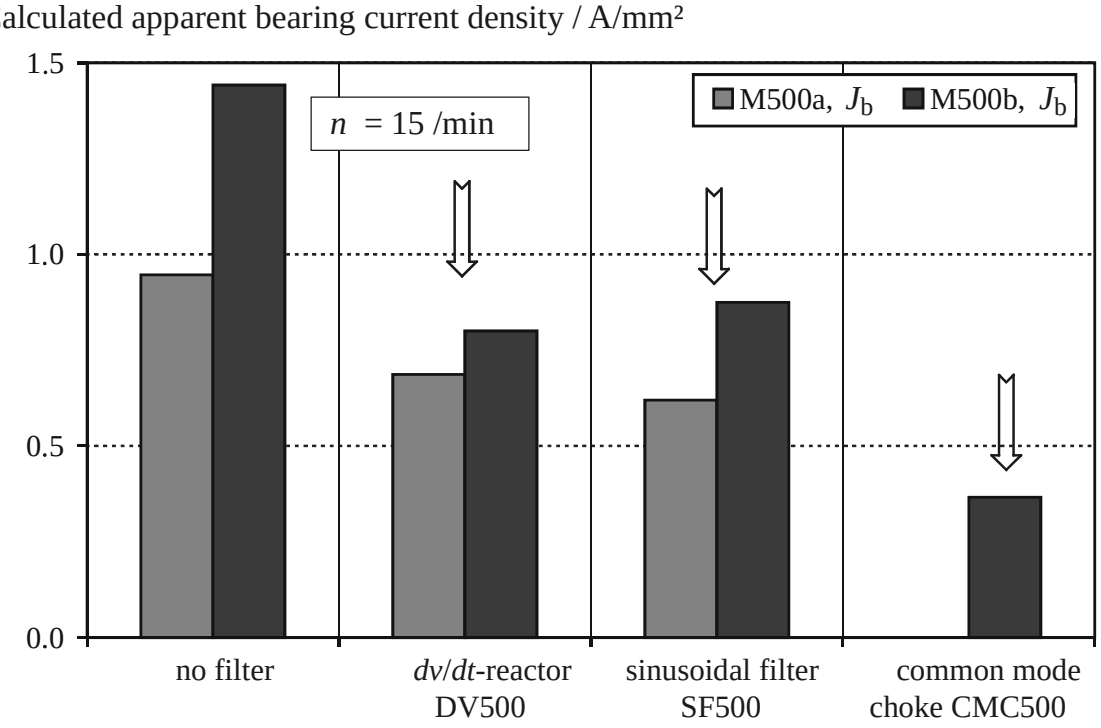

Figure 5.19: 500 kW power level - *Calculated apparent bearing current density* with *use of filters*, induction motors M500a and M500b and inverter I500, configuration E1*$_{10}$ (l_c = 10 m, shielded motor cable), motor speed n = 15 /min, $\vartheta_b \approx 70°C$, calculation of apparent bearing current density as described in Section 4.11 (p. 67)

5.4 Influence of Insulated Bearings

The influence of insulated bearings (→ Section 2.1, p. 15) was investigated at the 11 kW, 110 kW and 500 kW power level at one motor respectively, in the main configuration, using inverters and motor cables as summarized in Table 5.4.

Power level	Inverter	Motor	Motor cable type and length
11 kW	I11a	M11b	unshielded motor cable, $l_c = 2$ (configuration $E1_{02}$)
110 kW	I110a	M110b	shielded motor cable, $l_c = 10$ (configuration $E1_{10}$)
500 kW	I500	M500a	shielded motor cable, $l_c = 10$ (configuration $E1_{10}$)

Table 5.4: Motor-inverter-combinations and motor cables used for investigation of *insulated bearings*

The type of bearing does not influence the stator ground current. For this reason, no results of values of stator ground currents i_g are given. Fig. 5.20 and Fig. 5.21 show examples of waveforms of measured stator ground and bearing currents with use of insulated bearings. The measurement results of the value of the bearing currents i_b are shown as a function of motor speed n and bearing temperature ϑ_b for each power level 11 kW, 110 kW and 500 kW (Fig. 5.22 to Fig. 5.26).

♦ ***11 kW power level*:** The insulating layer of the bearings of 50 μm is not thick enough to suppress the EDM-currents occurring at this power level completely. However, it leads to a certain reduction of the *measurable current* that is measured in the copper loop applied for bearing current measurement (→ Section 3.3.1, p. 30). If one insulated bearing is used (NDE), the *measured bearing currents* are reduced down to less than 60 % at motor speed $n = 3000$ /min. However, in this case the *incidence frequency of the bearing currents in the other, conventional, bearing increases* (DE). With *two insulated bearings*, the *measured bearing currents* are *reduced down to 40 %* at motor speed $n = 3000$ /min at both bearings (Fig. 5.22). It will be shown in Section 7.4.3 (p. 125) that *the influence of the insulating layer on the "real" bearing current and on the measurable current is not the same. Such insulated bearings do not reduce EDM-bearing currents.*

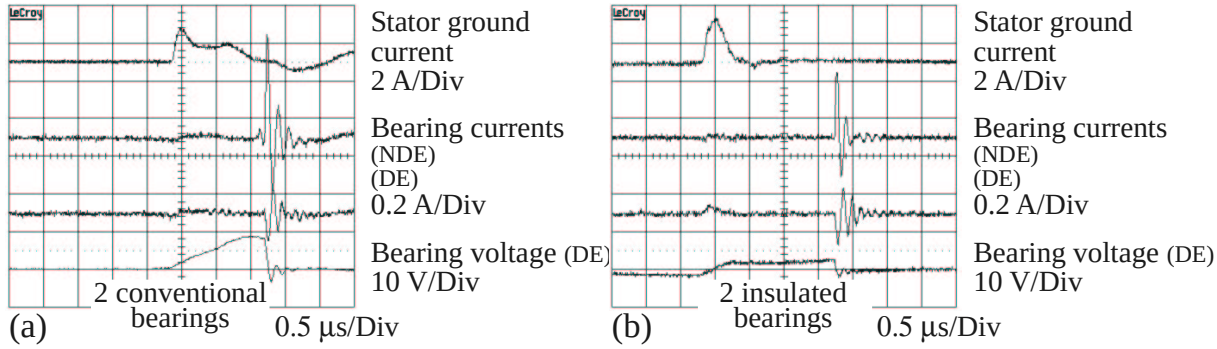

Figure 5.20: 11 kW power level - Measured bearing currents *without and with use of insulated bearings*, induction motor M11b and inverter I11a, motor speed $n = 1500$ /min, configuration $E1_{02}$ ($l_c = 2$ m, unshielded motor cable), $\vartheta_b \approx 70°C$, (a) DE and NDE conventional bearings, (b) DE and NDE insulated bearings

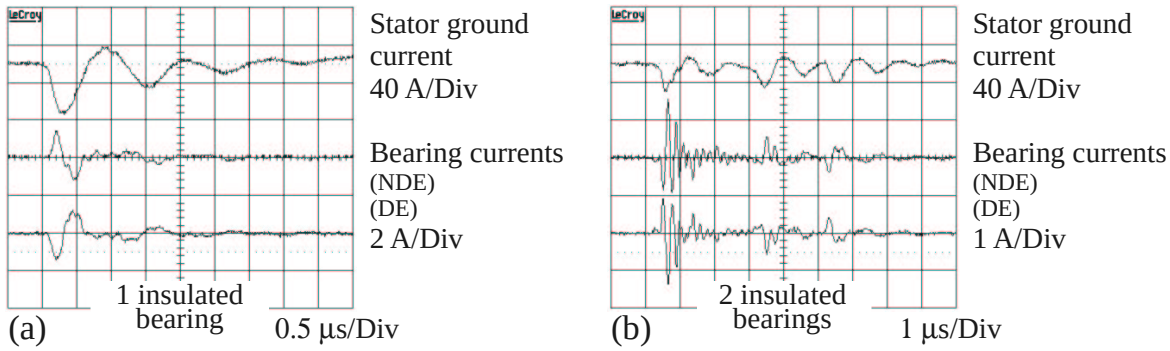

Figure 5.21: 500 kW power level - Measured bearing currents with *use of insulated bearings*, induction motor M500b and inverter I500, motor speed $n = 15$ /min, configuration $E1^*_{02}$ ($l_c = 2$ m, shielded motor cable), $\vartheta_b \approx 70°C$, (a) DE insulated and NDE conventional bearing, (b) DE and NDE insulated bearings

♦ ***110 kW power level*:** No significant influence of the bearing insulation of 250 μm thickness exists on the small EDM-bearing currents occurring at motor speed $n \geq 150$ /min and low bearing temperature $\vartheta_b \approx 25°C$ (Fig. 5.23). At increased bearing temperature ϑ_b and therefore lower oil viscosity, the insulation film thickness decreases, causing a decreased bearing impedance and thus increased circulating bearing currents. The *circulating bearing currents* that are notably distinctive at low motor speed n and elevated bearing temperature ϑ_b are *reduced down to less than 40 % if one, and less than 20 % if two insulated bearings are used* (Fig. 5.24). It will be shown in Section 7.7.3 (p. 160) that *the reduction is even larger, if no copper loop for bearing current measurement is applied. It is down to about 20 % with use of one and down to about 14 % with use of two insulated bearings respectively.*

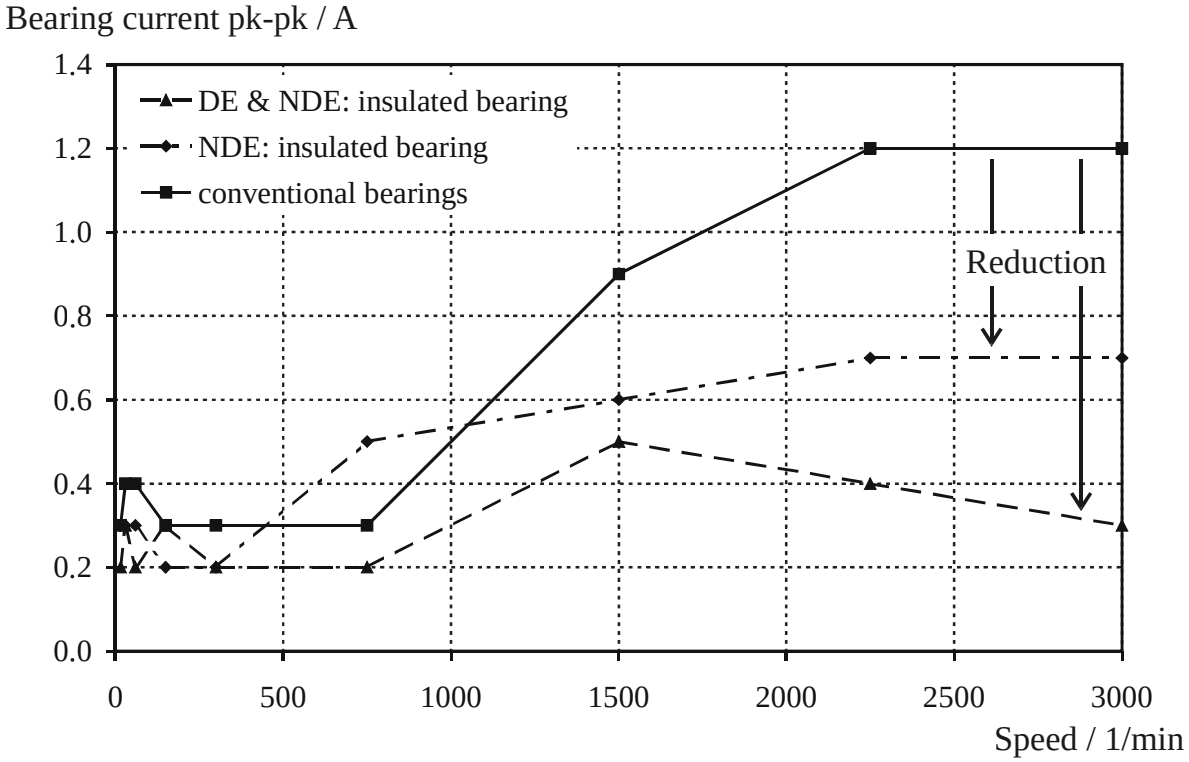

Figure 5.22: 11 kW power level - *Measured* bearing currents with *use of insulated bearings*, induction motor M11b and inverter I11a, configuration $E1_{02}$ ($l_c = 2$ m, unshielded motor cable), $\vartheta_b \approx 70°C$. Note that the "real" bearing current is not necessarily reduced.

♦ ***500 kW power level*:** The results obtained at this power level are the same as at the 110 kW power level: The *large circulating bearing currents* occurring at low motor speed n are *reduced down to less than 30 % if one, and less than 20 % if two insulated bearings* are used. The EDM-bearing currents occurring at motor speed $n \geq 750$ /min and bearing temperature $\vartheta_b \approx 25°C$ that are - due to their small magnitude - tolerable for this power level, remain unaffected (Fig. 5.25 and Fig. 5.26). The influence of the copper loop (→ Section 7.7.3, p. 160) is smaller than at the 110 kW power level.

The measured bearing currents show a reduction of EDM-bearing currents to less than 40 % by the use of two insulated bearings. According to the present understanding, the "real" bearing currents remain unaffected by such insulated bearings (→ Section 7.4.3, p. 125).
Use of one insulated bearing reduces circulating bearing currents down to at least less than 40 %, use of two insulated bearings to at least less than 20 %.

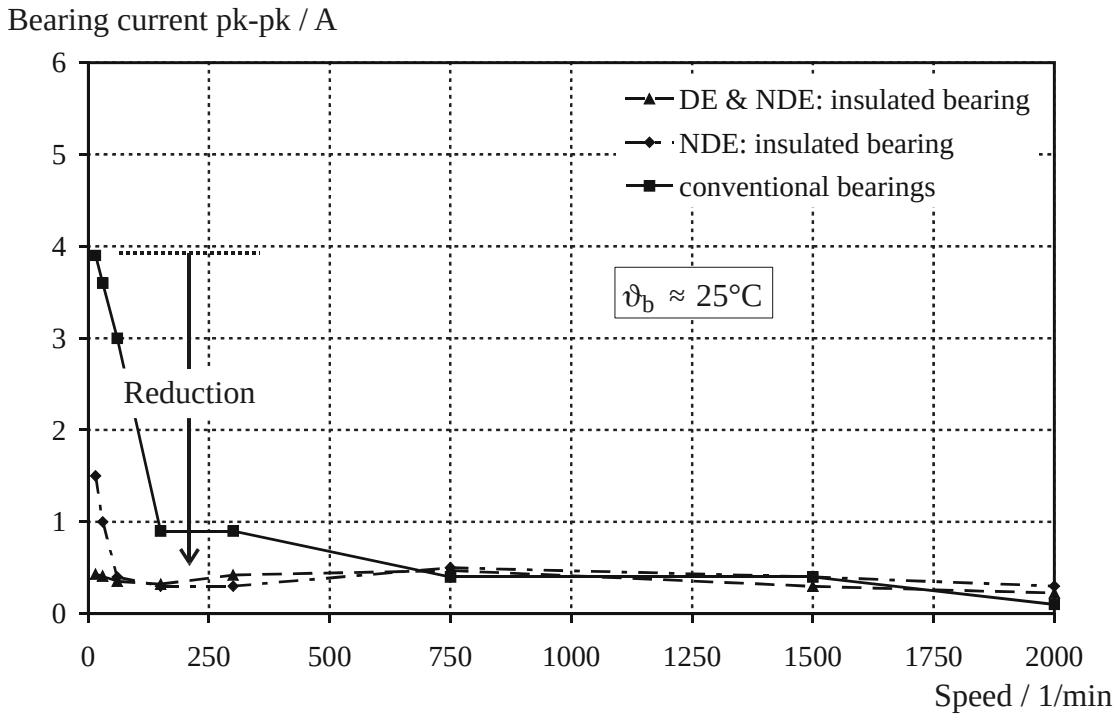

Figure 5.23: 110 kW power level - Measured bearing currents with *use of insulated bearings at* $\vartheta_b \approx$ **25°C**, induction motor M110b and inverter I110a, configuration $E1^*_{10}$ ($l_c = 10$ m, shielded motor cable)

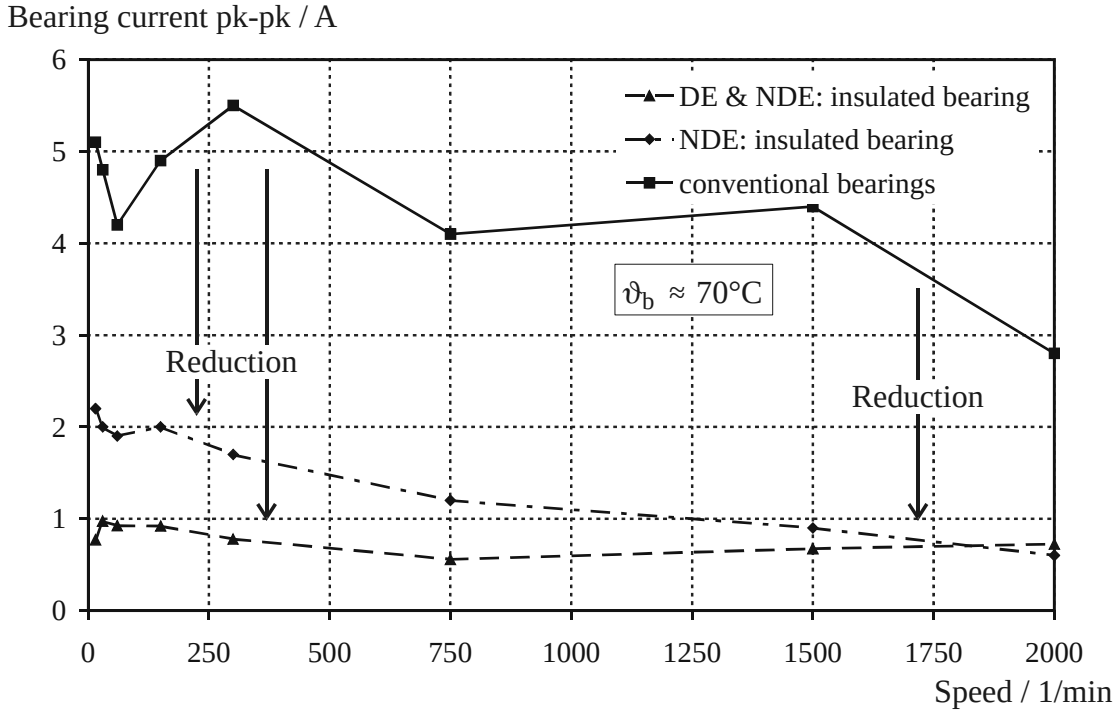

Figure 5.24: 110 kW power level - Measured bearing currents with *use of insulated bearings at* $\vartheta_b \approx$ **70°C**, induction motor M110b and inverter I110a, configuration $E1^*_{10}$ ($l_c = 10$ m, shielded motor cable)

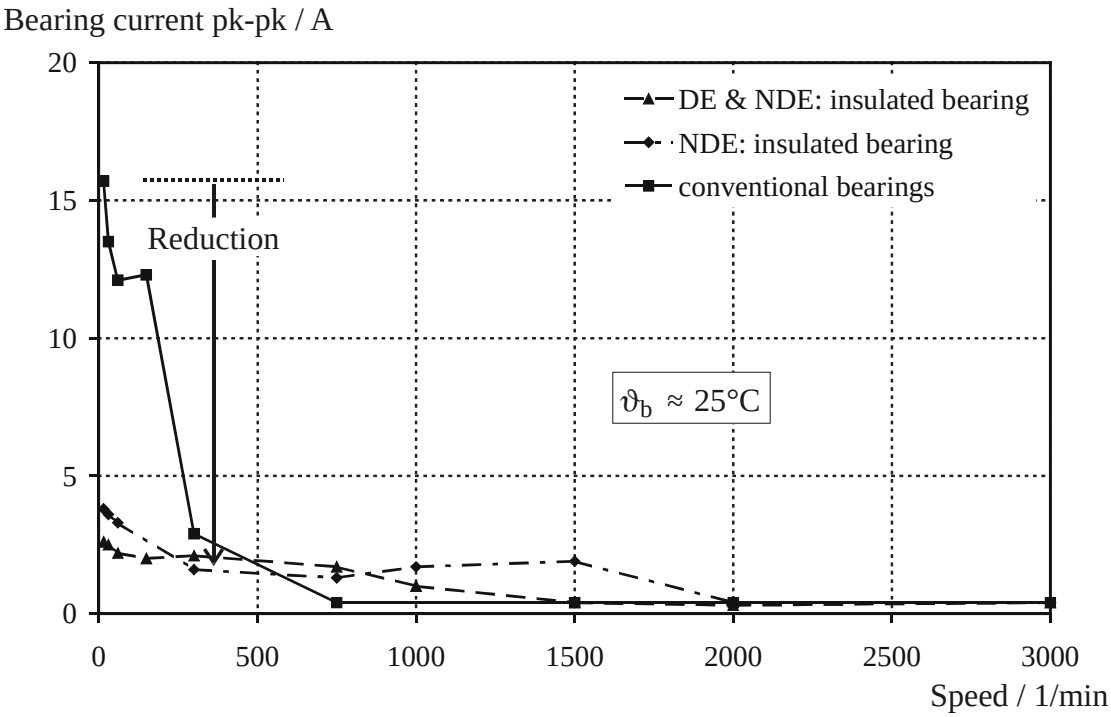

Figure 5.25: 500 kW power level - Measured bearing currents with *use of insulated bearings at* $\vartheta_b \approx \mathbf{25°C}$, induction motor M500b and inverter I500, configuration E1*$_{02}$ ($l_c = 2$ m, shielded motor cable)

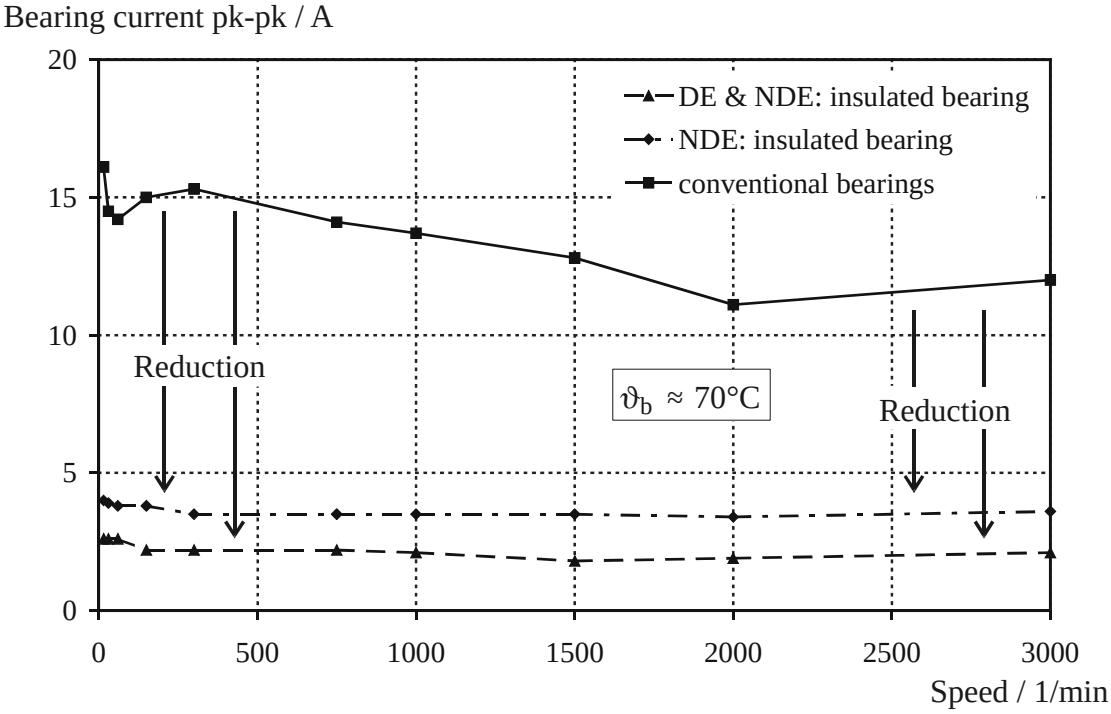

Figure 5.26: 500 kW power level - Measured bearing currents with *use of insulated bearings at* $\vartheta_b \approx \mathbf{70°C}$, induction motor M500b and inverter I500, configuration E1*$_{02}$ ($l_c = 2$ m, shielded motor cable)

5.5 Influence of Hybrid Bearings

Hybrid bearings (→ Section 2.1, p. 15) were investigated at the 11 kW and 110 kW power level, in the main configuration, using motor-inverter-combination and motor cables as summarized in Table 5.5.

Power level	Inverter	Motor	Motor cable type and length
11 kW	I11a	M11b	unshielded motor cable, $l_c = 2$ (configuration $E1_{02}$)
110 kW	I110a	M110b	shielded motor cable, $l_c = 10$ (configuration $E1_{10}$)

Table 5.5: Motor-inverter-combinations and motor cables used for investigation of *hybrid bearings*

♦ ***11 kW power level*:** With hybrid bearings, *no bearing currents with peak-to-peak values greater than* $i_b = 0.1$ A, which are harmless capacitive bearing currents, occur at this power level (Fig. 5.27). The *EDM-currents are eliminated.*

♦ ***110 kW power level*:** The results obtained at the larger motors of the 110 kW power level are the same as with the smaller motors: *Only small, harmless capacitive bearing currents with peak-to-peak values smaller than* $i_b \leq 0.2$ A occur at this power level (Fig. 5.28). The *EDM- and circulating bearing currents are eliminated.*

Hybrid bearings eliminate EDM- and circulating bearing currents and rotor ground currents. The whole diameter of the ceramic balls (Si_3N_4) of the bearings represents the length of the insulating gap. The bearing voltage is not large enough to generate sufficient electric field strength across this length to discharge the lubricating film. No EDM-currents occur.
The ceramic balls act as an electrical insulation and interrupt the circulating bearing currents.

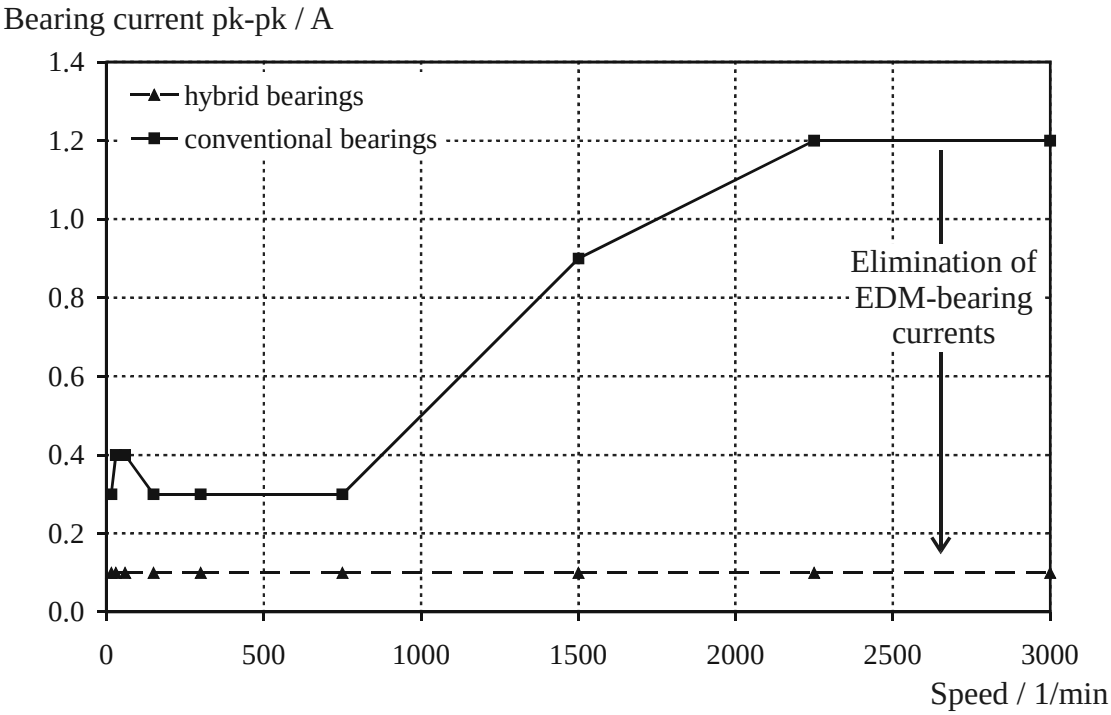

Figure 5.27: 11 kW power level - Measured bearing currents with *use of hybrid bearings*, induction motor M11b and inverter I11a, configuration $E1_{02}$ ($l_c = 2$ m, unshielded motor cable), $\vartheta_b \approx 70°C$

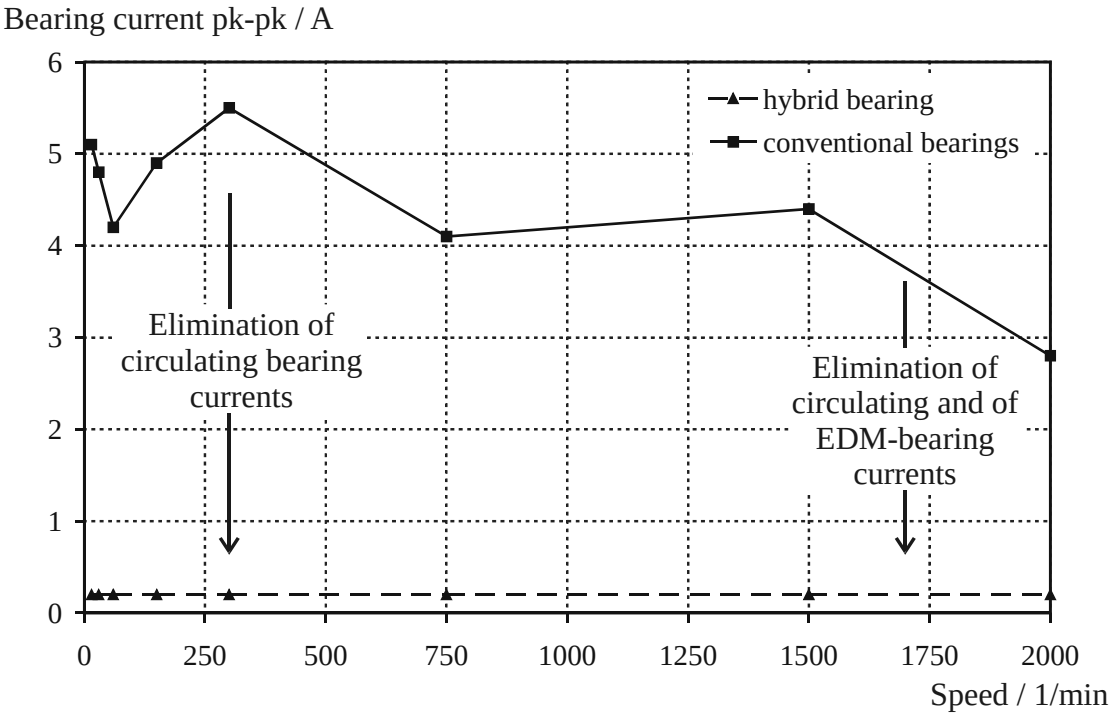

Figure 5.28: 110 kW power level - Measured bearing currents with *use of hybrid bearings*, motor M110b and inverter I110a, configuration $E1^*_{10}$ ($l_c = 10$ m, shielded motor cable), $\vartheta_b \approx 70°C$

Chapter 6

Tests for Bearing Damage Assessment

6.1 Setup

Limits of permissible bearing current densities J_b have been taken from experiences with dc- and low frequency ac-applications to evaluate the endangerment caused by "classical" bearing currents (→ Section 1.5.1, p. 14).

The frequencies of inverter-induced bearing currents are much higher than $f = 50/60$ Hz, ranging from several 100 kHz of circulating bearing currents and rotor ground currents to several MHz for EDM-bearing currents.

A series of different short and long term tests was carried out to study if these limits of apparent bearing current density J_b are also true for inverter-induced bearing currents. Furthermore, these tests should allow a better understanding of the mechanisms of the bearing damage due to HF-bearing currents.

Therefore, four squirrel cage induction motors with shaft height 160 mm and rated power $P_r = 11$ kW, motors M11c, M11d, M11e and M11f, were prepared in the same way as the other test motors to measure bearing voltage and bearing current (→ Section 3.3, p. 30). These motors have bearings of types 6209 C3, 6309 C3 and 6308 C3. Two standard voltage-source IGBT-inverters, (a) inverter I11b operating with hysteresis control with variable switching frequency, and (b) inverter I11d operating with asynchronous PWM with fixed switching frequency were used for motor supply.

In total, 22 test runs were performed. Therefore, 44 bearings could be investigated. As only four motors were used, the bearings were exchanged several times. Each test run started with a new pair of bearings. All bearings were lubricated with the same high impedance grease used for the other investigations, that is *Norlith* STM3 (→ Section A.5, p. 207).

Time of operation t_{op}, calculated apparent bearing current density J_b, and IGBT switching frequency f_c were varied within the following ranges:

▷ $J_b = (0...4.2)$ A/mm^2, ▷ $t_{op} = (50...2000)$ h and ▷ $f_c = (3...10)$ kHz.

For determination of the apparent bearing current density J_b the *Hertz*'ian contact area A_H was calculated by FAG, Schweinfurt, Mr.Ortegel, as described in Section 4.11 (p. 67). The values of radial force F_R with and without magnetic pull due to rotor eccentricy, as well as axial force F_A of DE- and NDE-bearings of the motors for the test runs were provided by the manufacturers of the motors. Typical values of radial play Δ_R were chosen by FAG. The calculated *Hertz*'ian contact areas ranged as shown in Table 6.1. For further calculation, average values for A_H were taken, as listed in Table 6.2. The apparent bearing current density J_b was derived from the measured peak-to-peak values of the bearing current $i_{b,\,pk\text{-}to\text{-}pk}$ and the calculated values of the *Hertz*'ian contact area A_H according to (4.1) (Section 4.11, p. 67).

Four types of tests were performed:
▷ LTMF (*L*ong *T*ime *M*edium *F*requency): Rotor ground current,
▷ STMF (*S*hort *T*ime *M*edium *F*requency): Rotor ground current,
▷ LTHF (*L*ong *T*ime *H*igh *F*requency): EDM-current,
▷ STHF (*S*hort *T*ime *H*igh *F*requency): EDM-current.

"Long term" means time of operation $t_{op} \geq 500$ h, "short term" means $t_{op} < 500$ h, which is an arbitrarily chosen distinction. It was expected that with $t_{op} < 500$ h, the deterioration of the bearing races by bearing currents is still visible without too much mechanical levelling effect by the rolling balls. Table 6.3 gives an overview of these tests and the respective range of the parameters time of operation t_{op}, calculated apparent bearing current density J_b and operated switching frequency f_c.

LTMF- and STMF-tests had been set up to study the endangerment of the bearings through currents with frequencies of several 100 kHz. This is typical for circulating bearing currents and rotor ground currents passing through the bearing. As for 11 kW motors no circulating bearing currents occur, rotor ground currents were provoked. The stator housing of the test motors was left ungrounded, but the rotor was grounded on both ends to enhance rotor ground current flow (Fig. 6.1a). Additional capacitors with $C = 1.1$ / 2.2 / 3.3 nF were connected in Y-connection between the terminals and the grounding connection of the motors to increase the stator winding-to-frame capacitance C_{wf}. Thus, the ground current was increased drastically and allowed realization of very large and therefore critical bearing currents, which otherwise would have been too low. The STMF-tests were carried out as a result of the LTMF-tests to allow identification of the mechanism of damage at an early stage.

	Motor M11c		Motor M11d	
Bearing	DE 6209 C3	NDE 6209 C3	DE 6209 C3	NDE 6209 C3
Radial force F_R *without* magnetic pull	119 N	119 N	295 N	255 N
Axial force F_A	458 N	458 N	736 N	736 N
	Radial play $\Delta_R = 5$ μm $A_H = 3.16$ mm^2 $A_H = 3.16$ mm^2		Radial play $\Delta_R = 5$ μm $A_H = 4.06$ mm^2 $A_H = 4.06$ mm^2	
	Radial play $\Delta_R = 15$ μm $A_H = 2.82$ mm^2 $A_H = 2.82$ mm^2		Radial play $\Delta_R = 15$ μm $A_H = 3.70$ mm^2 $A_H = 3.70$ mm^2	
Radial force F_R *with* magnetic pull	396 N	396 N	2060 N	981 N
Axial force F_A	458 N	458 N	736 N	736 N
	Radial play $\Delta_R = 5$ μm $A_H = 3.14$ mm^2 $A_H = 3.14$ mm^2		Radial play $\Delta_R = 5$ μm $A_H = 3.81$ mm^2 $A_H = 4.02$ mm^2	
	Radial play $\Delta_R = 15$ μm $A_H = 2.80$ mm^2 $A_H = 2.80$ mm^2		Radial play $\Delta_R = 15$ μm $A_H = 3.31$ mm^2 $A_H = 3.63$ mm^2	
	Motor M11e		Motor M11f	
Bearing	DE 6309 C3	NDE 6308 C3	DE 6309 C3	NDE 6308 C3
Radial force F_R *without* magnetic pull	105 N	105 N	105 N	467 N
Axial force F_A	200 N	200 N	200 N	200 N
	Radial play $\Delta_R = 5$ μm $A_H = 2.63$ mm^2 $A_H = 2.41$ mm^2		Radial play $\Delta_R = 5$ μm $A_H = 2.63$ mm^2 $A_H = 2.41$ mm^2	
	Radial play $\Delta_R = 15$ μm $A_H = 2.28$ mm^2 $A_H = 2.10$ mm^2		Radial play $\Delta_R = 15$ μm $A_H = 2.28$ mm^2 $A_H = 2.10$ mm^2	
Radial force F_R *with* magnetic pull	467 N	467 N	167 N	467 N
Axial force F_A	200 N	200 N	200 N	200 N
	Radial play $\Delta_R = 5$ μm $A_H = 2.58$ mm^2 $A_H = 2.37$ mm^2		Radial play $\Delta_R = 5$ μm $A_H = 2.58$ mm^2 $A_H = 2.37$ mm^2	
	Radial play $\Delta_R = 15$ μm $A_H = 2.19$ mm^2 $A_H = 2.02$ mm^2		Radial play $\Delta_R = 15$ μm $A_H = 2.19$ mm^2 $A_H = 2.02$ mm^2	

Table 6.1: Calculated *Hertz*'ian contact areas A_H for test motors of tests for bearing damage assessment for different bearing parameters

The STHF- and LTHF-tests were set up to study the endangerment of the bearings through EDM-currents with frequencies of several MHz. For the STHF-tests, motor setup was the main configuration, using unshielded motor cable with $l_c = 2$ m (configuration $E1_{02}$, Fig. 6.1b).

Motor	Bearing type	A_H
M11c	6209 C3	3.0 mm^2
M11d	6209 C3	3.5 mm^2
M11e and M11f, DE-bearing	6309 C3	2.4 mm^2
M11e and M11f, NDE-bearing	6308 C3	2.2 mm^2

Table 6.2: Average values of calculated *Hertz*'ian contact area for the bearings of test motors of tests for bearing damage assessment

Type of test	Number of test runs	Load		
		Time of operation t_{op}	Calculated bearing current density J_b	Switching frequency f_c
LTMF (*L*ong *T*ime *M*edium *F*requency): Rotor ground current	10	(500...2000) h	(0...4.2) A/mm^2	(3...10) kHz
STMF (*S*hort *T*ime *M*edium *F*requency): Rotor ground current	8	50 h	(< 0.2...4.5) A/mm^2	(3...10) kHz
STHF (*S*hort *T*ime *H*igh *F*requency): EDM-current	3	(50...200) h	(0.04...0.15) A/mm^2	10 kHz
LTHF (*L*ong *T*ime *H*igh *F*requency): EDM-current	1	500 h	(0.07...0.11) A/mm^2	10 kHz

Table 6.3: Tests for bearing damage assessment

Table 6.4 shows the parameters of the 22 test runs, respectively 44 bearings in detail with name of test, bearing type, motor, inverter, measured bearing current peak-to peak value i_b, calculated apparent bearing current density J_b, switching frequency f_c and time of operation t_{op}.

Different methods were used for analysis of the bearing wear and damage caused by inverter-induced bearing currents:

First, the bearings were *visually inspected*.

Afterwards, the bearings were cut up into segments for analysis of race and bearing ball surfaces with a *light-optical microscope* (amplification 6.3 and 8.0) and a *scanning electron microscope* (typical amplifications 1500 and 3000).

Furthermore, the deterioration of the grease of the bearings was analyzed by determination of the *infrared spectroscopy of the evaporated grease*.

These investigations were done at Siemens AG, Nuremberg (visual inspection and analysis with light-optical and scanning electron microscope), and FAG, Schweinfurt (infrared spectroscopy), by experts.

Name of test run	DE / NDE	Bearing type	Motor	Inverter	Time of operation t_{op}	Bearing current i_b	Bearing current density J_b	Switching frequency f_c
						A pk-to-pk	A/mm^2	kHz
LTMF1	DE	6209 C3	M11c	I11b	2076 h	0	0	3_{av}
LTMF1	NDE	6209 C3	M11c	I11b	2076 h	2.0	0.44	3_{av}
LTMF2	DE	6209 C3	M11d	I11b	1990 h	0	0	3_{av}
LTMF2	NDE	6209 C3	M11d	I11b	1990 h	2.0	0.38	3_{av}
LTMF3	DE	6309 C3	M11e	I11d	1275 h	9.1	2.53	10
LTMF3	NDE	6308 C3	M11e	I11d	1275 h	10.9	3.30	10
LTMF4	DE	6309 C3	M11f	I11d	1275 h	7.3	2.03	10
LTMF4	NDE	6308 C3	M11f	I11d	1275 h	11.9	3.61	10
LTMF5	DE	6209 C3	M11c	I11b	1000 h	2.8	0.62	3_{av}
LTMF5	NDE	6209 C3	M11c	I11b	1000 h	3.0	0.67	3_{av}
LTMF6	DE	6209 C3	M11d	I11b	2000 h	1.6	0.30	3_{av}
LTMF6	NDE	6209 C3	M11d	I11b	2000 h	1.7	0.32	3_{av}
LTMF7	DE	6309 C3	M11e	I11d	1367 h	3.2	1.72	10/8
LTMF7	NDE	6308 C3	M11e	I11d	1367 h	7.5	2.27	10/8
LTMF8	DE	6309 C3	M11f	I11d	500 h	0	0	10
LTMF8	NDE	6308 C3	M11f	I11d	500 h	13.9	4.21	10
LTMF9	DE	6209 C3	M11c	I11b	1026 h	5.1	1.13	8
LTMF9	NDE	6209 C3	M11c	I11b	1026 h	5.4	1.20	8
LTMF10	DE	6309 C3	M11f	I11d	846 h	0	0	8
LTMF10	NDE	6308 C3	M11f	I11d	846 h	10.8	3.27	8
STMF1	DE	6209 C3	M11c	I11b	50 h	2.3	0.51	10
STMF1	NDE	6209 C3	M11c	I11b	50 h	2.8	0.62	10
STMF2	DE	6309 C3	M11e	I11d	50 h	9.7	2.94	10
STMF2	NDE	6308 C3	M11e	I11d	50 h	10.1	2.81	10
STMF3	DE	6209 C3	M11c	I11b	50 h	2.4	0.53	10
STMF3	NDE	6209 C3	M11c	I11b	50 h	2.6	0.58	10
STMF4	DE	6309 C3	M11e	I11d	50 h	10.4	3.15	10
STMF4	NDE	6308 C3	M11e	I11d	50 h	9.8	2.72	10
STMF5	DE	6209 C3	M11c	I11b	50 h	(0.3...0.9)	≤ 0.2	10
STMF5	NDE	6209 C3	M11c	I11b	50 h	(0.5...0.8)	< 0.2	10
STMF6	DE	6309 C3	M11e	I11d	50 h	5.6	1.56	10
STMF6	NDE	6308 C3	M11e	I11d	50 h	5.8	1.76	10
STMF7	DE	6209 C3	M11c	I11b	50 h	3.0	0.67	10
STMF7	NDE	6209 C3	M11c	I11b	50 h	2.1	0.47	10
STMF8	DE	6309 C3	M11e	I11d	50 h	4.8	1.33	10
STMF8	NDE	6308 C3	M11e	I11d	50 h	14.7	4.45	10
STHF1	DE	6309 C3	M11e	I11d	50 h	0.5	0.15	10
STHF1	NDE	6308 C3	M11e	I11d	50 h	0.3	0.14	10
STHF2	DE	6209 C3	M11c	I11b	200 h	0.2	0.04	10
STHF2	NDE	6209 C3	M11c	I11b	200 h	0.6	0.13	10
STHF3	DE	6309 C3	M11e	I11d	50 h	0.4	0.12	10
STHF3	NDE	6308 C3	M11e	I11d	50 h	0.5	0.11	10
LTHF1	DE	6209 C3	M11c	I11b	500 h	0.3	0.07	10
LTHF1	NDE	6209 C3	M11c	I11b	500 h	0.5	0.11	10

Table 6.4: Time of operation, measured bearing currents, calculated bearing current densities and operated switching frequencies of 44 bearings of 22 test runs for bearing damage assessment (av. = average)

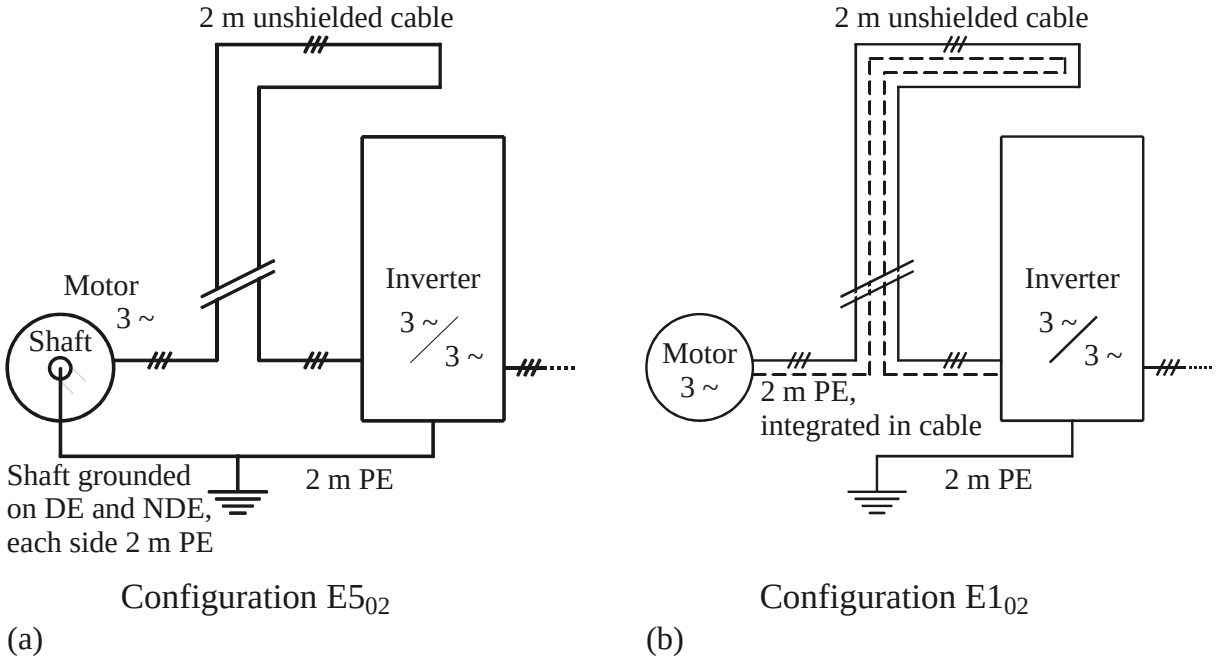

Figure 6.1: Setups for tests for bearing damage assessment, (a) setup for LTMF- and STMF-tests, (b) setup for LTHF- and STHF-tests

6.2 Results of Bearing Inspection

The damage of bearing race surface can be described in general as follows: The puncturing of the lubrication film is caused by short arcs, leaving small craters on the smooth polished metallic surface. These craters (pittings) are formed by the local melting of the metal due to the arc current. These pittings can be seen in Fig. 6.2, showing an average diameter of about 0.5 μm. As the balls roll over these craters, they are flattened again and vanish. In the meantime new craters are created by further bearing current flow. So, bearing current flow has to be understood as a current flow in local contact points with very small diameters, thus yielding a "local bearing current density" J which is much higher than the "apparent bearing current density" J_b. This very high current density leads - along with the metal conductivity κ - to very high local power loss density (6.1), which is the reason for locally very high temperature causing melting of metal and thus forming the above noted craters.

$$\frac{P}{V} = \frac{J^2}{\kappa} \tag{6.1}$$

where:

P/V = power loss density = unit power loss per unit volume,
J = local current density,
κ = metal conductivity.

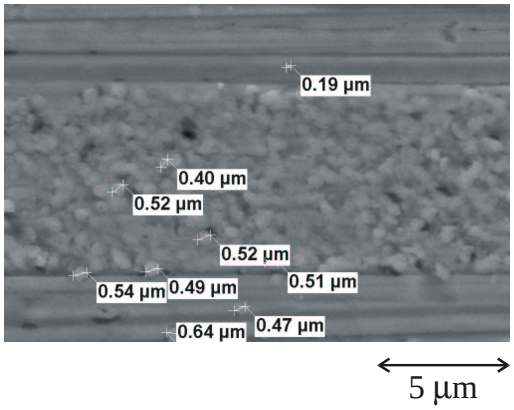

Scanning electron microscope:

diameter of pittings on bearing race,
average diameter ca. 0.5 µm,

J_b = 0.13 A/mm²,
200 hours of operation, ,
f_c = 10 kHz,
bearing type 6209 C3,
NDE-bearing of test run STHF2,
inner race

Figure 6.2: Example of average diameter of the pittings on race surface (evaluation by Siemens AG, Dr. Vogel, Dr. Kowalewski)

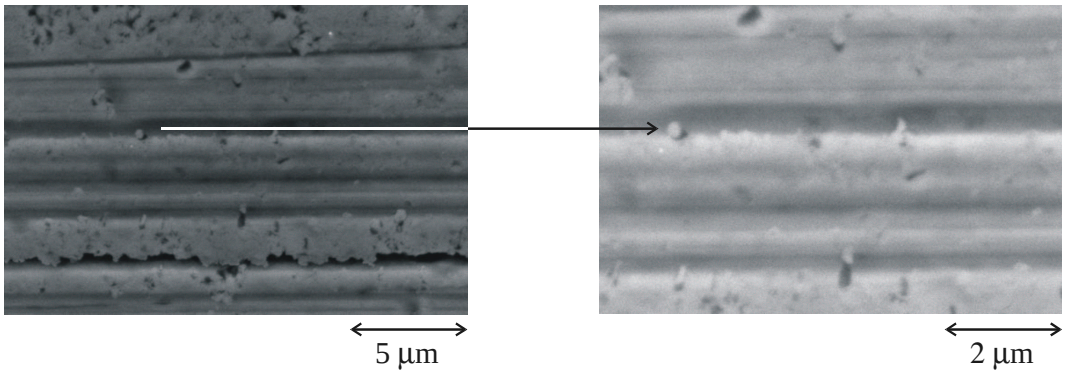

Scanning electron microscope: singular pittings on race surface,
J_b = 0.15 A/mm², 50 hours of operation, f_c = 10 kHz,
bearing type 6309 C3, DE-bearing of test run STHF1, outer race

Figure 6.3: Example of singular pittings on race surface (Siemens AG)

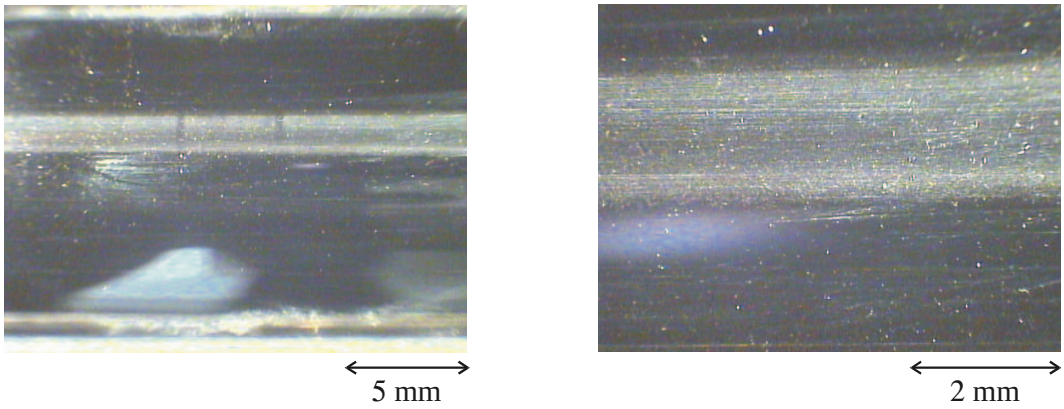

Light optical microscope: grey trace on race surface,
J_b = 0.15 A/mm², 50 hours of operation, f_c = 10 kHz,
bearing type 6309 C3, DE-bearing of test run STHF1, outer race

Figure 6.4: Examples of grey trace on race surface (Siemens AG)

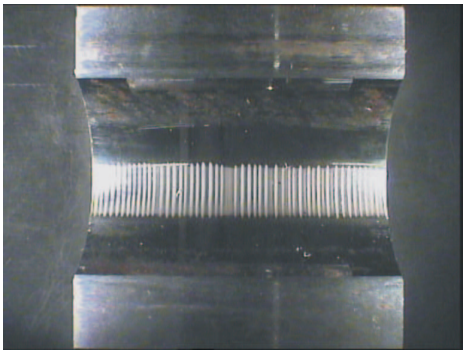

(a) 10 mm

Light optical microscope:
fluting of bearing race,
J_b = 2.0 A/mm²,
1275 hours of operation,
f_c = 10 kHz,
bearing type 6309 C3,
DE-bearing of test run LTMF4,
inner race

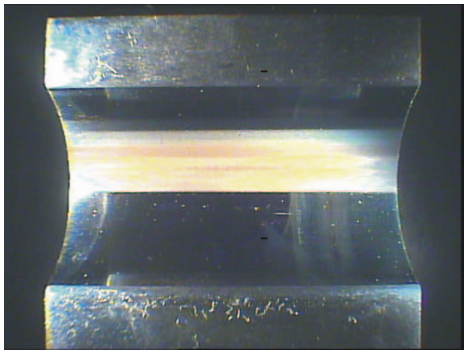

(b) 10 mm

Light optical microscope:
grey trace on bearing race,
J_b = 2.5 A/mm²,
1275 hours of operation,
f_c = 10 kHz,
bearing type 6309 C3,
DE-bearing of test run LTMF3,
inner race

Figure 6.5: Examples of (a) fluting and (b) grey trace on race surface (Siemens AG)

This has been already noted by Andreason [6]. The early stage of these pittings is seen in Fig. 6.3, after only 50 h of operation time. The pattern of the polishing of the metal surface during manufacturing process is still visible (parallel lines), already dotted with craters. For the eye, these small pittings are not visible, but they lead to a grey, now reflecting trace, which is an early indication of current flow through the bearing (Fig. 6.4). This grey trace may also be still visible after 1000 h and more (Fig. 6.5b), but often a dramatic change in surface deterioration occurs, the so-called fluting (Fig. 6.5a). Kohaut [38] postulates that not always the pittings are flattened ideally, but that the balls are forced to "jump" over these elevations, leaving bumping holes behind the craters. A regular "hill-and-valley" pattern is created, which is clearly visible on the race surface of the outer ring in the load zone, on the whole inner ring, as it is loaded continuously along the circumference, and on the balls. This fluting pattern occurs in groups. Why for the same apparent bearing current density one bearing shows fluting, whereas the other one only shows a grey trace, is quite unclear up to now. Here, additional research is needed for the future. The roughened surface anyway penetrates the lubricating film mechanically, yields metallic contact between balls and races with increased heat generation within the bearing, increased wear and may even lead to breaking of the bearing cage, as it was the case for the NDE-bearing of test run LTMF4. The results of the test runs are listed in Table 6.5.

Name of test run	DE / NDE	Degree of fluting (subjective judgement)		Width of fluting or grey trace		Degree of melting	
		Inner ring	Outer ring	Inner ring	Outer ring	Inner ring	Outer ring
LTMF1	DE	no fluting	no fluting	3.0 mm	1.5 mm	1 %	9.1%
LTMF1	NDE	medium	no fluting	2.7 mm	1.9 mm	100 %	100 %
LTMF2	DE	no fluting	no fluting	2.2 mm	1.8 mm	100 %	100 %
LTMF2	NDE	no fluting	no fluting	2.5 mm	1.5 mm	100 %	100 %
LTMF3	DE	no fluting	no fluting	4.4 mm	4.0 mm	100 %	100 %
LTMF3	NDE	slight	no fluting	5.3 mm	3.7 mm	100 %	100 %
LTMF4	DE	heavy	heavy	3.3-3.9 mm	2.7-3.1 mm	100 %	100 %
LTMF4	NDE	broken cage, bearing destroyed			4.2 mm	100 %	100 %
LTMF5	DE	no fluting	no fluting	2.9 mm	1.5 mm	100 %	100 %
LTMF5	NDE	medium	no fluting	3.2 mm	1.5 mm	100 %	100 %
LTMF6	DE	medium	no fluting	2.7 mm	1.4 mm	100 %	100 %
LTMF6	NDE	slight	no fluting	3.0 mm	1.5 mm	100 %	100 %
LTMF7	DE	slight	no fluting	3.3 mm	1.7 mm	100 %	100 %
LTMF7	NDE	beginning	beginning	3.2 mm	2.3 mm	100 %	100 %
LTMF8	DE	no fluting	no fluting	2.9 mm	1.0 mm	53.3 %	72.4 %
LTMF8	NDE	no fluting	no fluting	4.5 mm	2.6 mm	100 %	100 %
LTMF9	DE	no fluting	no fluting	2.5 mm	1.8 mm	100 %	90.8 %
LTMF9	NDE	slight	no fluting	3.2 mm	2.1 mm	100 %	100 %
LTMF10	DE	no fluting	no fluting	3.7 mm	2.6 mm	99.5 %	78.7 %
LTMF10	NDE	slight	no fluting	4.7 mm	3.3 mm	100 %	100 %
STMF1	DE	no fluting	no fluting	2.2 mm	1.5 mm	86.2 %	73.2 %
STMF1	NDE	no fluting	no fluting	2.9 mm	1.8 mm	84.4 %	90 %
STMF2	DE	no fluting	no fluting	3.2 mm	1.9 mm	94.5 %	95.3 %
STMF2	NDE	no fluting	no fluting	3.2 mm	2.0 mm	96.9 %	83.6 %
STMF3	DE	no fluting	no fluting	2.7 mm	1.6 mm	87.4 %	82.1 %
STMF3	NDE	no fluting	no fluting	2.2 mm	1.8 mm	91.9 %	93.1 %
STMF4	DE	no fluting	no fluting	3.0 mm	2.0 mm	99.1 %	98.7 %
STMF4	NDE	no fluting	no fluting	3.8 mm	2.4 mm	99.7 %	98.3 %
STMF5	DE	no fluting	no fluting	1.2 mm	1.2 mm	0 %	0 %
STMF5	NDE	no fluting	no fluting	2.2 mm	1.3 mm	3.2 %	16.3 %
STMF6	DE	no fluting	no fluting	3.3 mm	2.2 mm	99.1 %	82.3 %
STMF6	NDE	no fluting	no fluting	3.2 mm	2.4 mm	98.7 %	82.1 %
STMF7	DE	no fluting	no fluting	2.5 mm	1.5 mm	99.1 %	72.6 %
STMF7	NDE	no fluting	no fluting	2.6 mm	1.9 mm	97.5 %	77.1 %
STMF8	DE	no fluting	no fluting	2.9 mm	2.0 mm	97.9 %	94.3 %
STMF8	NDE	no fluting	no fluting	2.8 mm	2.1 mm	100 %	96.9 %
STHF1	DE	no fluting	no fluting	4.0 mm	1.7 mm	0 %	0 %
STHF1	NDE	no fluting	no fluting	4.1 mm	0.5 mm	0 %	0 %
STHF2	DE	no fluting	no fluting	3.4 mm	1.3 mm	0 %	0 %
STHF2	NDE	no fluting	no fluting	2.8 mm	2.1 mm	44 %	16.3 %
STHF3	DE	no fluting	no fluting	1.8 mm	2.9 mm	0 %	5.5 %
STHF3	NDE	no fluting	no fluting	2.3 mm	no clear trace	42.3 %	21.5 %
LTHF1	DE	no fluting	no fluting	2.1 mm	1.3 mm	0.8 %	1.7 %
LTHF1	NDE	no fluting	no fluting	2.2 mm	2.2 mm	83.2 %	60.5 %

Table 6.5: Degree of fluting, width of fluting or grey trace and degree of melting of 44 bearings of 22 test runs for bearing damage assessment (Siemens AG)

Local energy input for melting metallic surface is given per arc with

$$W_{\mathrm{arc}} \;=\; V_{\mathrm{arc}} \;\cdot\; I_{\mathrm{arc}} \;\cdot\; t_{\mathrm{arc}} \tag{6.2}$$

where:

V_{arc} = arc voltage of "short arc"
= bearing voltage at breakdown (ranging up to about 30 V),
I_{arc} = arc current,
t_{arc} = duration of current flow.

The current flow I_{arc} equals the product of a local bearing current density and an area, where the area may be chosen as the average crater area, hence the bearing current density is the arc current by the average crater area (6.3).

$$I_{\mathrm{arc}} \;=\; J_{\mathrm{arc}} \;\cdot\; A_{\mathrm{crater,av}} \;=\; J \;\cdot\; \frac{\pi}{4} \;\cdot\; d^2_{\mathrm{crater,av}} \tag{6.3}$$

where:

I_{arc} = arc current,
J_{arc} = current density of current arc,
$A_{\mathrm{crater,av}}$ = average crater area,
$d_{\mathrm{crater,av}}$ = average crater diameter $\cong 0.5\ \mu$m.

The bearing current i_{b} is proportional to the arc current I_{arc} (6.4). Hence, the arc current I_{arc} is proportional to the product of apparent bearing current density J_{b} and *Hertz*'ian contact area A_{H} (6.5).

$$i_{\mathrm{b}} \;\propto\; I_{\mathrm{arc}} \tag{6.4}$$

$$I_{\mathrm{arc}} \;\propto\; i_{\mathrm{b}} \;=\; J_{\mathrm{b}} \;\cdot\; A_{\mathrm{H}} \tag{6.5}$$

where:

J_{b} = apparent bearing current density,
A_{H} = *Hertz*'ian contact area.

The arc voltage equals the bearing voltage $\tilde{v}_{\mathrm{b}}$ at breakdown. The number of bearing current arcs N_{arc} increases linearly with switching frequency f_{c} [3] and time of operation t_{op}. Hence, the total energy dissipated in the bearing $W_{\mathrm{b,arc}}$ is proportional to the product of apparent bearing current density J_{b}, time of operation t_{op} and IGBT switching frequency f_{c} (6.6).

$$\begin{aligned} W_{\mathrm{b,arc}} \;&=\; V_{\mathrm{arc}} \;\cdot\; I_{\mathrm{arc}} \;\cdot\; N_{\mathrm{arc}} \;\cdot\; t_{\mathrm{arc}} \\ &\propto\; \tilde{v}_{\mathrm{b}} \;\cdot\; i_{\mathrm{b}} \;\cdot\; N_{\mathrm{arc}} \;\cdot\; t_{\mathrm{arc}} \\ &=\; \tilde{v}_{\mathrm{b}} \;\cdot\; J_{\mathrm{b}} \;\cdot\; A_{\mathrm{H}} \;\cdot\; N_{\mathrm{arc}} \;\cdot\; t_{\mathrm{arc}} \\ &\propto\; J_{\mathrm{b}} \;\cdot\; t_{\mathrm{op}} \;\cdot\; f_{\mathrm{c}} \end{aligned} \tag{6.6}$$

where:

N_{arc} = number of bearing current arcs,

$\tilde{v}_{\mathrm{b}}$ = bearing voltage at breakdown,

t_{op} = time of operation,

f_{c} = inverter switching frequency.

As a result, the electrical bearing stress can be expressed by $W_{\mathrm{b,arc}}$, which is proportional to the value $W = J_{\mathrm{b}} \cdot t_{\mathrm{op}} \cdot f_{\mathrm{c}}$.

With these basic considerations, the following results of the bearing damage investigation may be concluded:

♦ Some bearings of the LTMF-tests show ***fluting***, some ***only grey traces and no fluting*** on the race surface for the same apparent bearing current density. *Today's understanding of the mechanism of fluting generation is not sufficient for explanation* (Fig. 6.5 and Fig. 6.6).

If fluting exists, periodic fluting (ripple) groups can be identified. Within these groups, material is displaced from the light-colored to the dark-colored zones.

Fluting does not appear at any bearing of the STMF-tests (rotor ground currents, time of operation $t_{\mathrm{op}} = 50$ h) and STHF-tests (EDM-currents: $J_{\mathrm{b}} \approx 0.1$ A/mm^2, $t_{\mathrm{op}} \leq 500$ h).

♦ The surfaces of the bearing races of LTMF-tests are ***melted*** several times due to the small craters. The bearings of the STMF-tests are melted partially: some areas are melted several times, whereas other areas are only melted partially.

The situation is different with the bearings of the STHF-tests. Here, only singular ***pittings*** exist (Fig. 6.3 and Fig. 6.4). The *mean diameter of a pitting* is about 0.5 μm (Fig. 6.2).

The grade of melting of the bearing race is a function of $W = J_{\mathrm{b}} \cdot t_{\mathrm{op}} \cdot f_{\mathrm{c}}$ (Fig. 6.7).

♦ The ***infrared spectroscopy of the evaporated grease***, performed by FAG, Schweinfurt, gives clearer results than the other methods of investigation discussed so far. According to *Beer*'s law, the logarithm of the recorded transmission T at the selected wavelength is a direct measure of the chemical compounds [39]. A typical infrared spectrum of evaporated grease is shown in Fig. 6.8. Clearly, the absorption peak at around 1711 cm^{-1} demonstrates the presence of carboxylic acid in the grease. The degree of reduction of the carboxylic acid and hence the ageing of the grease could therefore be obtained by monitoring the area under the absorption peak of the -COOH group. Since the transmission depends sensitively on the thickness of the grease films, the degree of reduction of carboxylic acid was obtained by comparing the transmission at 1711 cm^{-1} (-COOH

group) with the absorption of a standard at 723 cm^{-1} (-CH_2 group). In Fig. 6.9, the reduction of carboxylic acid is shown as a function of the parameter W, clearly indicating that *the degree of reduction of carboxylic acid increases with increasing* $W = J_b \cdot t_{op} \cdot f_c$.

♦ Based on these results, the ***degree of electrical bearing stress "W"*** has been introduced (6.7). W is *proportional to a dissipated electric energy in the bearing*:

$$W = \text{electrical bearing stress} := J_b \cdot t_{op} \cdot f_c \qquad (6.7)$$

The reduction of the carboxylic acid depends strongly on W, hence the deterioration of the grease depends also strongly on W. Furthermore, the degree of melting of the race surface increases with W.

At $W = 4.45\ A/mm^2 \cdot 50\ h \cdot 10\ kHz = 8 \cdot 10^9\ A/mm^2$ the whole race surface has been melted once (STMF8, NDE-bearing).

No fluting was found up to $W = 0.11\ A/mm^2 \cdot 500\ h \cdot 10\ kHz = 2 \cdot 10^9\ A/mm^2$ (STHF1, DE-bearing).

A series of 22 test runs for bearing damage assessment was performed. The corresponding bearing loads cover a wide spectrum of bearing current amplitudes, apparent bearing current densities, times of operation and switching frequencies. Bearing currents with oscillating frequencies of several 100 kHz and with several MHz were analyzed.
The degree of electrical bearing stress " W " was introduced. The degree of melting of the bearing race surface is a function of W. Furthermore, the grade of reduction of the carboxylic acid, which is an indicator of the deterioration of the grease, correlates with W.

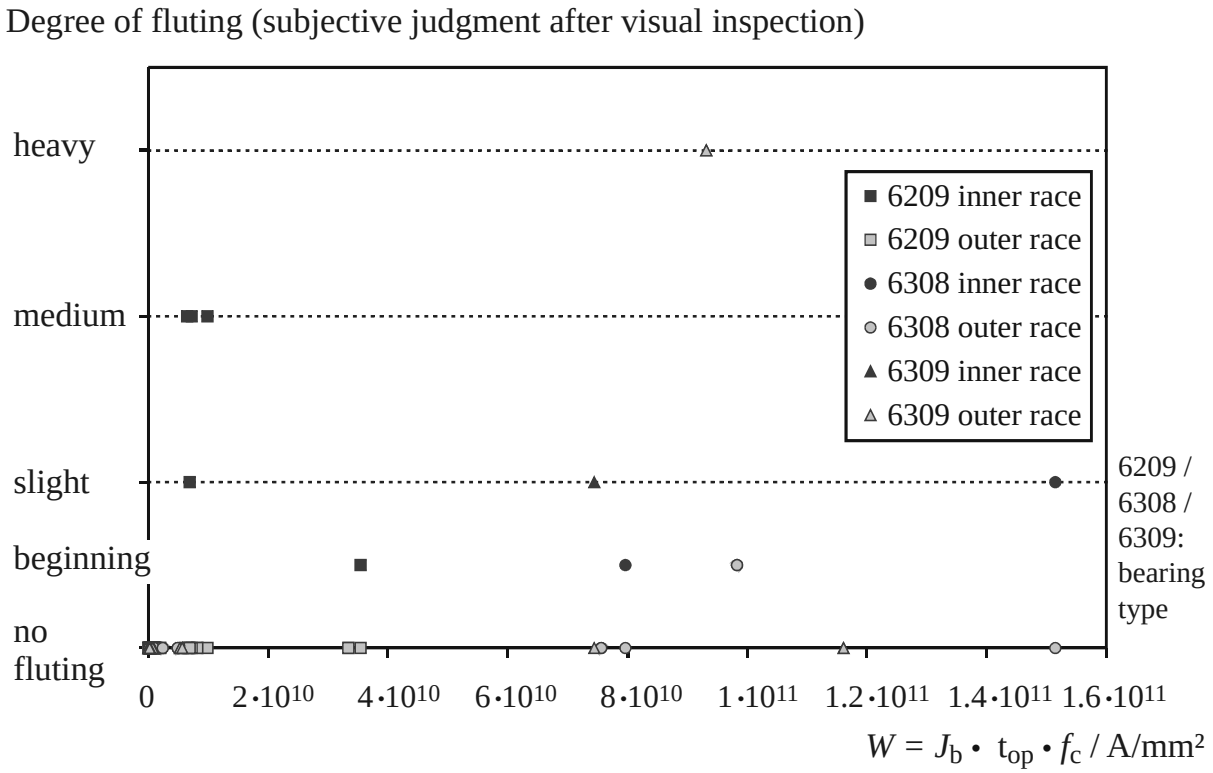

Figure 6.6: Degree of fluting of bearing race as function of $W = J_\mathrm{b} \cdot t_\mathrm{op} \cdot f_\mathrm{c}$ (Siemens AG)

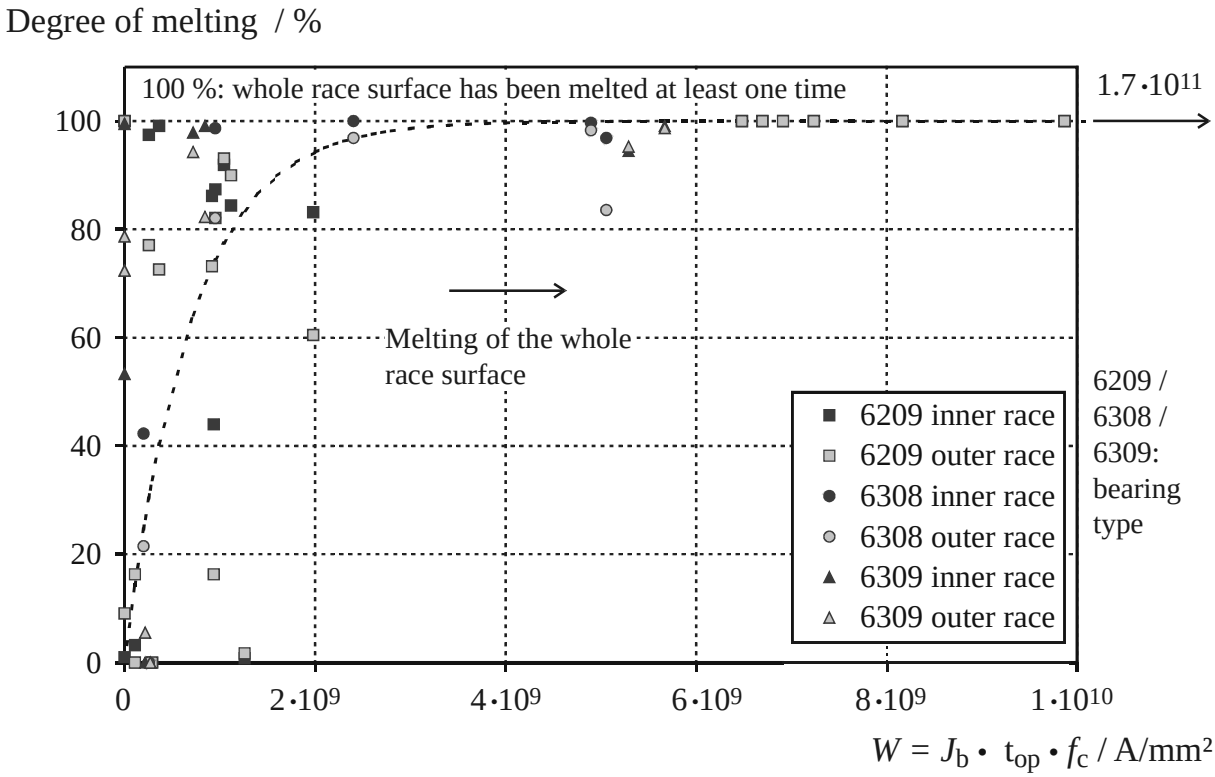

Figure 6.7: Degree of melting of bearing race as function of $W = J_\mathrm{b} \cdot t_\mathrm{op} \cdot f_\mathrm{c}$ (Siemens AG)

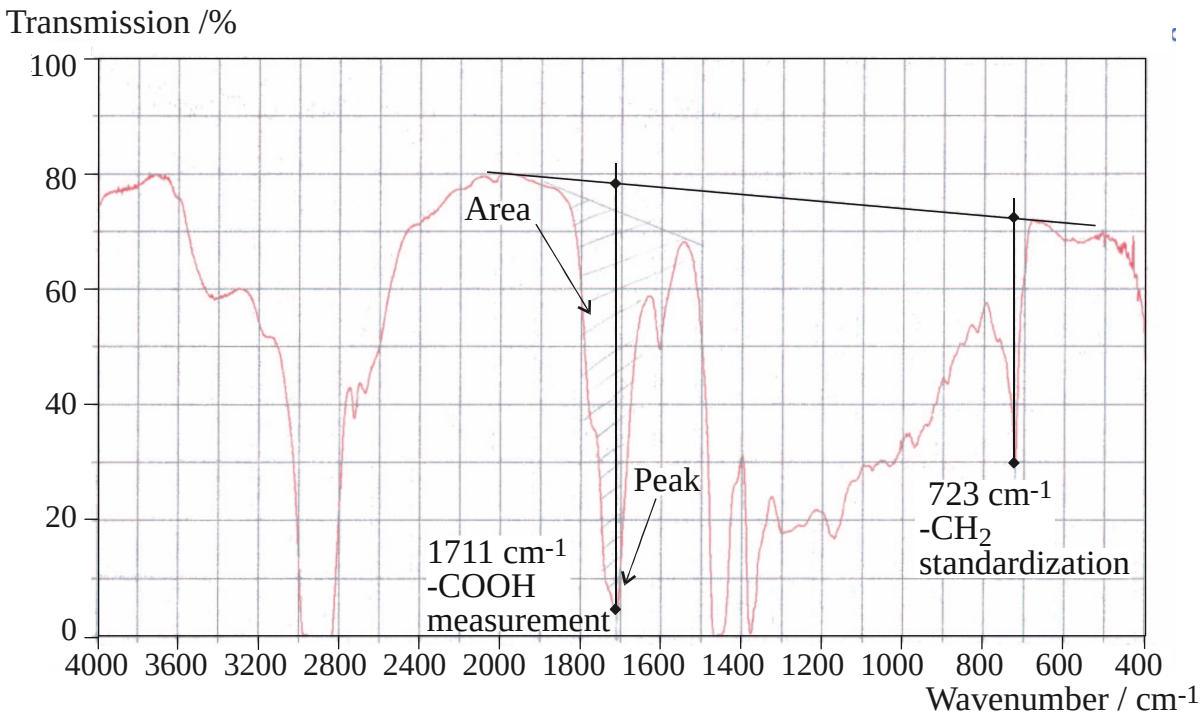

Figure 6.8: Example of spectrogram of evaporated grease, recorded transmission T as function of wavenumber = wavelength^{-1}, J_b = 3.3 A/mm^2, 846 hours of operation, f_c = 8 kHz, bearing type 6308 C3, NDE-bearing of test run LTMF10, inner race (FAG)

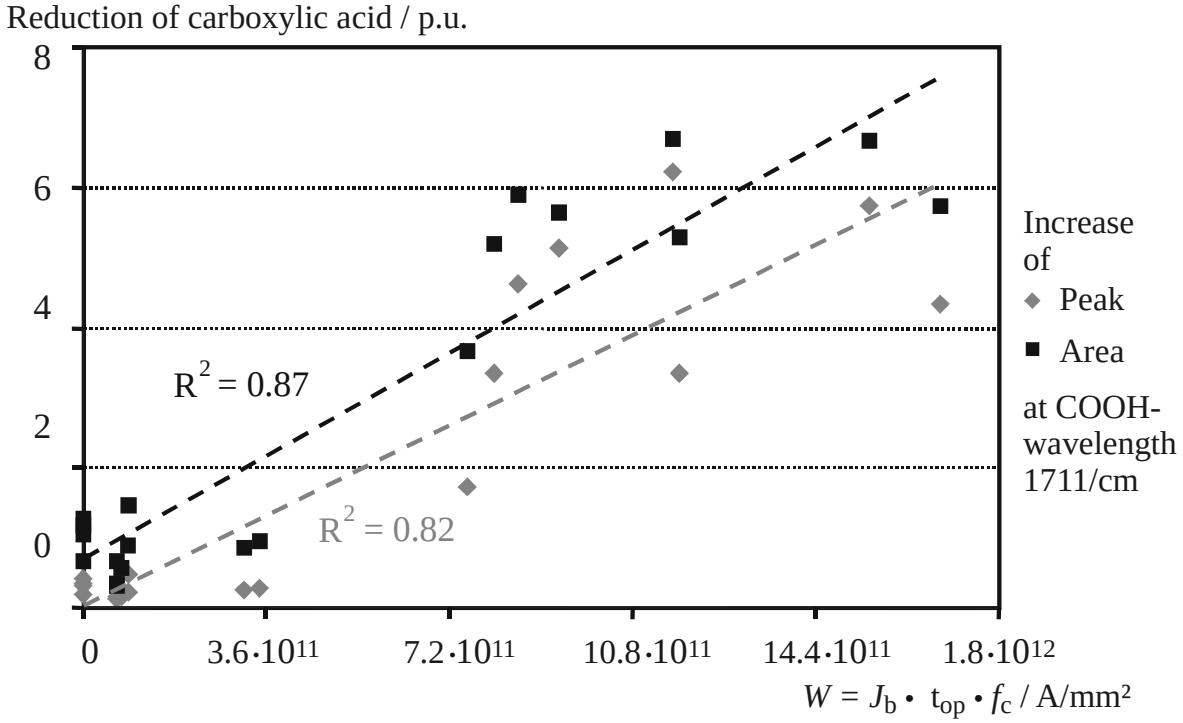

Figure 6.9: Reduction of carboxylic acid as function of $W = J_\mathrm{b} \cdot t_\mathrm{op} \cdot f_\mathrm{c}$, expressed as normalized change of spectrogram, R^2: Quality of correlation of the linear regression (FAG)

Chapter 7

Modeling of Drive Systems for Bearing Current Determination

In this chapter the order of magnitude of bearing currents will be predicted by calculation. Experience of the measurements shall be introduced for simple modeling.

7.1 The Bearing as an Electrical Impedance

The bearing is a complex, non-linear impedance in the equivalent electric circuit of the motor. The characteristics depend on the geometrical dimensions of the bearing and properties of the material, but mainly on the operational parameters of the drive.

Each bearing contains a number N_b of rolling elements between the inner and outer race. These rolling elements rotate with the rotating speed n_b around their own rotating axis, while the rotating (inner) ring of the bearing itself turns with the motor speed n. The mechanical load on the bearing depends on the mass of the rotor, the radial and magnetic drag due to static and dynamic eccentricity and additional forces of the load. Usually, at every instantaneous moment, about 1/3 of the rolling elements carry the load, thus defining the "load zone" [38]. These elements are submitted to elastic deformation that results in a total contact area A. The contact area of the other elements is about zero. *Heinrich Hertz* was the first to calculate this area based on theory of linear elasticity (→ Appendix C, p. 211). His approach is widely used to calculate the contact area. In this case, the area is referred to as *Hertz'ian contact area* A_H.

At motor operation, bearing grease is used to provide a thin lubrication film, in order to avoid metallic contact. The thickness of the film is determined by the laws of hydrodynamics and depends on the operational parameters of the motor and on the mechanical properties of the grease, that are influenced by the operational parameters of the motor. The minimum film thickness $h_\mathrm{lb,min}$ is calculated for the range of bearings and operational parameters covered within the frame of the research carried out (→ Appendix D, p. 215). At bearing temperature $\vartheta_\mathrm{b} \approx 70°\mathrm{C}$ and motor speed $n \leq 3000$ /min, $h_\mathrm{lb,min}$ of

the test motors is *smaller than 1 μm*. For motor speed $n = 1000$ /min, it is as small as $h_{\mathrm{lb,min}} < 0.5$ μm.

Extensive studies have been done on the mechanisms of current conduction through the lubricating film [6], [7], [8], [27], [40], [41], [42], [43]. Different ranges of operation can be distinguished:

♦ At *standstill*, only some 5 nm of $h_{\mathrm{lb,min}}$ remain between rolling element and bearing race [6]. If voltage is applied across the bearing, conducting electrons can cross this very thin insulating layer due to the quantummechanical tunnel effect. The bearing acts as an ohmic resistance, the so-called "tunneling resistance", as the flux lines of current have to edge through the points of metallic contact [6]. This resistance is almost zero.

At this point of operation, the local contact area is relatively large. Hence, bearings at standstill can be exposed to relatively large currents without being damaged [42].

♦ The lubrication film of *rotating* bearings is much thicker than the lubrication film of bearings at standstill. Generally, with high-impedance grease, it has insulating properties as long as no voltage greater than a certain break-through voltage ("threshold voltage") $v_{\mathrm{b,th}}$ is applied. In the presence of this mode, the bearing acts mainly as a capacitance. Due to the surface roughness and metallic particles resulting from metallic wear, the lubrication film may be punctured in a statistical way.

♦ If an electric field of sufficient strength exists, this may lead to fritting, which is built up of a current conducting bridge. The following considerations are valid for dc and low frequency ac operation ($\approx$ (50...100) Hz). Following the first current pulse, more conducting bridges are generated due to the increase of local temperature because of the heating of the small conducting area. Fritting occurs if the threshold voltage of the bearing $v_{\mathrm{b,th}}$ is surpassed. The threshold voltage is strongly determined by the properties of the grease. It is (0.5...0.8) V at dc- or low frequency ac-operation [7]. Once $v_{\mathrm{b,th}}$ is reached, a further small increase in the voltage results in a large increase in current. The correlation is linear with less than one Ω up to some Ω gradient. Sometimes, a second threshold voltage exists. At this voltage a decrease of the voltage results in a further increase of the current before the bearing has ohmic characteristic [7].

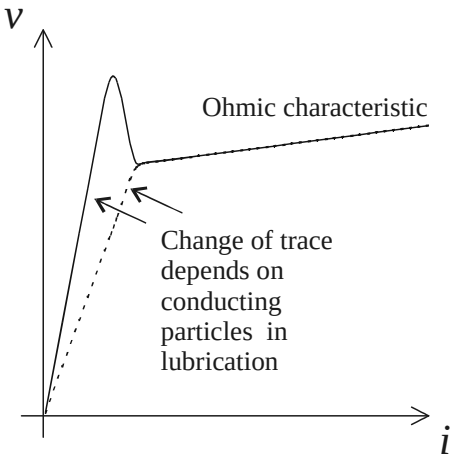

Figure 7.1: Current flow in a roller bearing [7]

Hence, the *resistance of a rotating bearing is not constant*. It is in the MΩ range before fritting, and up to a few Ω after fritting. Furthermore, if the bearing is conducting, the resistance decreases with increase of the current, because more current conducting bridges are built up. For example, measured values of the resistance of a rolling bearing NU 330 for different revolutionary speed of the bearing, bearing load and amplitude of the passing current are reported in [42]. The following values are taken from the sets of measurements presented in [42]: $R_\mathrm{b}(i_\mathrm{b}$=40mA) ≈ 12 Ω, $R_\mathrm{b}(i_\mathrm{b}$=120mA) ≈ 5 Ω, $R_\mathrm{b}(i_\mathrm{b}$ >1A) ≈ 0.5 Ω. In addition, buildup and reduction of the bridges do not happen instantaneously. Hence, the steady-state and the instantaneous resistance for a certain current are different.

In addition to the properties of the grease, the threshold voltage $v_\mathrm{b,th}$ depends to a large extent on the form of the excitation. At PWM operation, with a very quick voltage buildup (high dv/dt), $v_\mathrm{b,th}$ is much higher than at dc and low frequency ac (50 / 60 Hz) operation. With an electric field strength of 15 V/μm [27] and lubrication film thicknesses $h_\mathrm{lb,min}$ = (0.1...2) μm [6], $v_\mathrm{b,th}$ is in the range of (1.5...30) V. This is due to the fact, that statistical film breakdown due to particles in the film allows high voltages during short time intervals.

The bearing is a complex, non-linear impedance in the equivalent electric circuit of the motor. A rotating bearing, with use of high-impedance grease, acts mainly as a capacitance, as long as the lubricating film is insulating. At standstill, and after electrical breakdown of the insulating film, the bearing behaves mainly ohmically and the resistance depends on the amplitude of the current that flows through the bearing.

7.2 High-Frequency Behavior of Motors

When exposed to frequencies significantly higher than the fundamental frequency of the drive, the standard equivalent circuit diagram for the motor is no longer valid. Depending on the frequency range considered, different models have been proposed to describe the physical behavior of the motor.

According to [44] and [45], in which research on the stress on random-wound windings following a voltage surge at inverter-operation is reported, three different frequency ranges can be distinguished:

$f \leq f_a$	$f \leq$ several 10 kHz	uniform voltage distribution in the winding
$f_a \leq f \leq f_b$	several 10 kHz $\leq$ (90...100) kHz	possibility of wave propagation
$f_b \leq f$	(90...100) kHz $\leq f$	behavior is almost totally capacitive

Table 7.1: Frequency ranges of motor behavior [44], [45]

where:

f = frequency,
f_a = limiting frequency for uniform voltage distribution,
f_b = limiting frequency for possibility of wave propagation.

The frequency f_a is given by the resonance between self-inductance and winding-to-frame capacitance of the winding. For frequencies $f < f_a$, the voltage distributes almost evenly along the length of the wire.

The frequency f_b is the resonance frequency given by the self-inductance of the coil per unit length, the capacitance between the turns of the coil per unit length and the length of the coil. For $f > f_b$, the self-inductance of the winding is no longer of influence. The behavior in this region is described as "*quasi capacitive*", because the *non-linear voltage distribution in the winding of the machine does no longer depend on the frequency.* Some magnetic coupling still exists, which is, however, negligible.

A third resonance frequency exists in the MHz-range, which is due to the resonance between winding leakage inductance, capacitance between turns of the coil and capacitance between winding and frame. As the motor-cable-connection acts as a low pass filter, this resonance is not important for the stress of the winding resulting from a voltage surge [45].

This classification is generally accepted, as other authors who describe transient effects outside the motor also describe the motor as a single, lumped capacitance (e.g. [46], [47]). Furthermore, in [48], the limit for quasi capacitive behavior is also given at about 100 kHz.

According to [49] and [50], the equivalent frequency f of a pulse rise with rise time t_r is given by (7.1).

$$f = \frac{1}{\pi t_\mathrm{r}} \tag{7.1}$$

With this correlation, it is possible to correlate measurements of dv/dt, voltage rise time t_r and frequency f.

The same order of magnitude for the maximum frequency that penetrates the winding as stated above was found by measurement (→ Appendix E, p. 219). The dv/dt of the stator common mode voltage measured at the star point connection of the motor terminals is about 20 times smaller than the dv_Lg/dt of the line-to-earth voltage v_Lg at the motor terminals.

The largest dv_Y/dt of the voltage at the star point of the motors v_Y measured in the frame of the investigations is $dv_\mathrm{Y}/dt \approx 0.14\ \mathrm{kV}/\mu\mathrm{s}$ (motor M110b). With the maximum amplitude of the common mode voltage $\hat{v}_\mathrm{com} = 280$ V as amplitude of the voltage rise in the star point of the motors, $dv_\mathrm{Y}/dt = 0.14\ \mathrm{kV}/\mu\mathrm{s}$ corresponds to a rise time of $t_\mathrm{r} = 2\ \mu$s, and, using (7.1), a frequency of $f = 159$ kHz. This is in accordance with the above stated theories.

The model to calculate the BVR is also based on the approach of capacitive behavior of the machine (Fig. 1.5, p. 8, and Fig. 3.9b, p. 38).

A capacitive model of a machine is not sufficient to describe phenomena in the MHz range, e.g. in the context of electromagnetic interference, reduction of common mode voltage and inverter-induced bearing currents. Depending on the context, the models consist of several series and / or parallel inductances, capacitances and reactances. *Identification of the parameters* is generally done by measurements (e.g. [51], [52], [53], [54], [55], [56], [57], [58]).

Modeling and calculation of HF effects is here done only for the motors of the 11 kW, 110 kW and 500 kW power level, which have an inner rotor. The motors of the 1 kW power level have an outer rotor structure and therefore calculation is slightly different.

Different models have been proposed to describe the physical behavior of an electric motor for high frequencies. The models depend on the context, and identification of the parameters is generally done by measurements.

7.3 Motor Capacitances and Bearing Voltage Ratios

7.3.1 Stator winding-to-frame Capacitance

The stator winding-to-frame capacitances C_{wf} of the test motors were measured along with the phase-to-phase capacitances C_{ph} as described in Section 3.5 (p. 37). It is reminded that, in this work, the capacitance C_{wf} is per definition the capacitance *per phase*. The results are given in Table 7.2. Both capacitances increase with motor size.

However, C_{ph} is *almost an order of magnitude smaller* than C_{wf}. This difference is attributed to the different parts of a machine that form the capacitances. The stator windings are embedded into the stator slots of the stator core iron stack where the area of contact is large and the distance small when compared with the area and the distance between the phases in the winding overhang. Accordingly, C_{ph} is - in the present context - negligible [59]. It is not used in any later modeling of ground and bearing currents in the frame of the research presented. Therefore, analytical calculation of C_{ph} is dispensed.

The stator winding-to-frame capacitance C_{wf} is modeled as a number of $Q_{\mathrm{s}}/3$ parallel plate capacitors. The stator winding of these motors is a random wound winding and does not consist of preformed coils. The winding is insulated with thin multi-layer insulation tape and is impregnated with epoxy resin. In [45] a form factor F_{c} is introduced to take into account the irregular surface of the coils. The form factor F_{c} is a function of the thickness of the slot insulation d_{slot} and the diameter of the wire d_{wire}. As a result, C_{wf} is given by (7.2). For the investigated machines, F_{c} is in the order of $F_{\mathrm{c}} = 0.8...0.9$:

$$C_{\mathrm{wf}} \;=\; F_{\mathrm{c}}\varepsilon_{\mathrm{r}}\varepsilon_0\frac{Q_{\mathrm{s}}}{3}\frac{U_{\mathrm{slot}}l_{\mathrm{Fe}}}{d_{\mathrm{slot}}} \tag{7.2}$$

where:

F_{c} = form factor according to [45],
ε_{r} = relative permittivity,
$\varepsilon_{\mathrm{r}} \approx 3$ = typical value for slot insulation material,
derived from exact values that were obtained from manufacturers.
Q_{s} = number of stator slots,
ε_0 = permittivity of vacuum = $8.8542 \cdot 10^{-12}$ As/Vm,
U_{slot} = circumference of stator slot,
l_{Fe} = length of stator lamination stack,
d_{slot} = thickness of the slot insulation.

Equation 7.2 indicates that C_{wf} *increases with the square of the shaft height*, because it increases

▷ linearly with the length of the stator lamination stack l_{Fe} and
▷ linearly with the circumference of the stator slot U_{slot}.

MOTOR	C_{wf}	C_{ph}
M11a	1.9 nF	0.3 nF
M11b	1.9 nF	0.3 nF
M110a	12.1 nF	1.0 nF
M110b	9.9 nF	1.7 nF
M500a	28.0 nF	4.0 nF
M500b	23.0 nF	2.8 nF

Table 7.2: Measured stator winding-to-frame and phase-to-phase capacitances

MOTOR	C_{wf} measured	C_{wf} calculated equ. 7.2, $\varepsilon_r = 1.27$	C_{wf} calculated equ. 7.2, $\varepsilon_r = 3\ k_f$	C_{wf} calculated equ. 7.2, $\varepsilon_r = 1.27\ k_f$	C_{wf} calculated equ. 7.3
	nF	nF	nF	nF	nF
M11a	1.9	5.2	8.5	3.6	2.1
M11b	1.9	2.1	2.0	0.8	2.1
M110a	12.1	14.5	24.0	9.9	10.1
M110b	9.9	17.1	30.2	12.8	10.1
M500a	28.0	28.9	53.9	22.8	25.0
M500b	23.0	25.2	28.5	12.1	25.0

Table 7.3: Measured and calculated stator winding-to-frame capacitances

In [45] the use of $\varepsilon_r = 1.27$ instead of $\varepsilon_r = 4$ is suggested to consider the *unsystematic arrangement of the individual wires in the slot* as well as the fact that *not all space between the wires might be filled with epoxy resin.* The results of calculation of C_{wf} using (7.2) and $\varepsilon_r = 1.27$ are given in Table 7.3. The deviation between calculation and measurement is below 20 % for motors M11b, M110b, M500a and M500b, but 73 % for motor M110a and 174 % for motor M11a.

Another approach was taken to calculate C_{wf} *taking the slot fill factor* k_f *into account.* The slot fill factor k_f is defined as ratio of total copper-conductor cross section in a slot versus slot cross section area and ranges for random-wound coils typically between $k_f = 0.35...0.45$. If the slot cross section is assumed rectangular, the influence of k_f on C_{wf} should be linear. The number of slot wires being one of the two "electrodes" of C_{wf} results in a reduction of C_{wf} by k_f. The capacitance C_{wf} was calculated with $\varepsilon_r = 3\ k_f$ as well as with $\varepsilon_r = 1.27\ k_f$. The results are also given in Table 7.3. While the deviation is rather large for use of $\varepsilon_r = 3\ k_f$, it is below 20 % for motors M110a, M110b and M500b, but 89 %, 58 % and 47 % for motors M11a, M11b and M500a respectively for $\varepsilon_r = 1.27\ k_f$. Hence, *consideration of* k_f *does not lead to better results.*

Calculation of C_{wf} is very difficult because of the irregular arrangement of the individual wires inside the slot and because the effective distance between the two "plates" of electrodes, that is the wires and the iron, is unknown. The thicknesses of the slot insulation of the motors value d_{slot} = (0.3...0.4...0.5) mm and the diameters of the wire d_{wire} = (0.8...1.5...1.9) mm. Hence, the ratio of the two parameters is close to one, notably for the small motors of the 11 kW power level. This results in a *large uncertainty in the calculated capacitance* because the effective distance of the wires may vary by more than 100 %. Therefore, [52] states that analytical calculation of C_{wf} for machines with *random-wound winding* is not possible; it can only be a rough estimate.

The measured stator winding-to-frame capacitances differ only 20 % per power level, even if the design parameters of the stator windings and slots differ remarkably. Therefore, equation 7.3 was derived from the measurement results, taking the square influence of the shaft height of the machine into account. Equation 7.3 is *suggested for calculation of* C_{wf} *of standard random-wound low-voltage machines*. The values obtained for the test motors with this equation are also given in Table 7.3.

$$C_{\mathrm{wf}} \;=\; 0.00024 \cdot H^2 - 0.039 \cdot H + 2.2 \tag{7.3}$$

C_{wf} in nF,
H = shaft height in mm.

7.3.2 Rotor-to-frame Capacitance

The stator iron stack is usually shrunk in the stator housing, also called the frame. Therefore, rotor and frame of a machine are separated only by the air gap and form the rotor-to-frame capacitance C_{rf}.

For analytical calculation of C_{rf}, stator and rotor are considered as a cylindrical capacitor. The air gap δ is much smaller than the outer diameter of the rotor d_{re}. Therefore, the natural logarithm of the inner diameter of the stator lamination d_{si} and the outer diameter of the rotor lamination d_{re} can be approximated according to (7.4). Linearization in (7.4) leads to maximum error calculated of $< 1\%$.

$$\ln\frac{d_{\mathrm{si}}}{d_{\mathrm{re}}} \;=\; ln\frac{d_{\mathrm{re}} + 2\delta}{d_{\mathrm{re}}} \;=\; \ln(1 + \frac{2\delta}{d_{\mathrm{re}}}) \;\approx\; \frac{2\delta}{d_{\mathrm{re}}} \tag{7.4}$$

where:

d_{si} = stator lamination inner diameter,
d_{re} = rotor lamination outer diameter,
δ = (mechanical) air gap.

In magnetostatic calculations of machines, the reduction of the air gap flux density due to the slot openings is commonly considered by the *Carter*-factor k_c (7.5), (7.6).:

$$\delta_\mathrm{e} = k_\mathrm{c}\delta \tag{7.5}$$

such that

$$B_\delta = \frac{\hat{B}_\delta}{k_\mathrm{c}} \tag{7.6}$$

where:

k_c = *Carter*-factor,
δ = (mechanical) air gap,
δ_e = equivalent air gap including effect of slotting,
B_δ = average magnetic field density in the air gap along circumference,
$\hat{B}_\delta$ = maximum magnetic field density in the air gap.

An analogous situation may be given by the influence of the slot openings on the electrostatic field in the air gap, because the same kind of differential equation rules for magnetostatic and electrostatic field. The approach given below considers the reduction of the capacitance C_rf - when compared with a cylindrical capacitor without slot openings - due to the flux reduction by slot openings (7.7) to (7.10).

$$C_\mathrm{rf} = \frac{Q_\mathrm{rf}}{V_\mathrm{rf}} \tag{7.7}$$

$$Q_\mathrm{rf} = D_\mathrm{rf}A_\mathrm{rf} = \varepsilon_\mathrm{r}\varepsilon_0 E_\mathrm{rf}A_\mathrm{rf} \tag{7.8}$$

where:

Q_rf = electric charge on rotor and frame,
V_rf = voltage between rotor and frame,
D_rf = average electric flux density between rotor and frame along circumference,
A_rf = area between rotor and frame with assumption of closed stator slots,
E_rf = average electric field strength between rotor and frame along circumference.

The opening of the rotor slots is of no influence, as the aluminum cage is at the same potential as the rotor iron stack and the rotor surface is a smooth rotational cylinder. With consideration of (7.4), it is

$$Q_\mathrm{rf} = \varepsilon_r\varepsilon_0\frac{V_\mathrm{rf}}{\delta}l_\mathrm{Fe}\pi d_\mathrm{re} \tag{7.9}$$

Hence, using (7.5), (7.7), (7.9) and $\varepsilon_r = 1$ for air

$$C_\mathrm{rf} \;=\; \varepsilon_0 l_\mathrm{Fe}\frac{\pi d_\mathrm{re}}{k_\mathrm{c}\delta} \tag{7.10}$$

The calculated capacitances C_rf are given in Table 7.4. Measurements of $C_\mathrm{rf} + C_\mathrm{wr}$ as described in Section 3.5 (p. 37) were done on motors M11a, M11b, M110a and M110b. The measured values are also given in Table 7.4. The discussion of the results is part of the next section, together with the results on the stator winding-to-rotor capacitance C_wr.

Motor	$C_{rf} + C_{wr}$ measured	C_{rf} calculated $k_c > 1$	C_{rf} calculated $k_c = 1$	C_{wr} calculated
M11a	1.4 nF	0.92 nF	1.15 nF	0.04 nF
M11b	1.7 nF	1.28 nF	1.53 nF	0.15 nF
M110a	2.4 nF	2.14 nF	2.53 nF	0.23 nF
M110b	3.2 nF	2.57 nF	2.81 nF	0.19 nF
M500a	not measured	4.52 nF	4.89 nF	0.22 nF
M500b	not measured	1.29 nF	1.38 nF	0.14 nF

Table 7.4: Measured and calculated rotor-to-frame and winding-to-rotor capacitances

7.3.3 Stator winding-to-rotor Capacitance

The stator winding-to-rotor capacitance C_{wr} is formed by the stator windings in the slots and the rotor surface. The value of C_{wr} is small when compared with the other capacitances, because of the relatively large distance and small area between stator winding and rotor. However, it is a fundamental cause for the bearing voltage v_b that mirrors the stator winding common mode voltage v_Y at intact lubrication film (→ Section 7.3.5). The stator winding-to-rotor capacitance C_{wr} is modeled as Q_s parallel plate capacitors. Each plate capacitor is a series connection of the capacitance of the air gap and the height of the slot opening with $\varepsilon_r = 1$ (7.11), and the capacitance of the slot wedge and the upper slot insulation with $\varepsilon_r \approx 3$ (7.12), giving (7.13).

$$C_{wr0} = Q_s \varepsilon_0 b_o \frac{l_{Fe}}{\delta + h_o} \tag{7.11}$$

$$C_{wr1} = Q_s 3 \varepsilon_0 b_o \frac{l_{Fe}}{h_{wedge+ins}} \tag{7.12}$$

$$C_{wr} = \frac{1}{\frac{1}{C_{wr0}} + \frac{1}{C_{wr1}}} \tag{7.13}$$

where:

C_{wr0} = stator winding-to-rotor capacitance, part of air gap and slot opening,
C_{wr1} = stator winding-to-rotor capacitance, part of slot wedge and slot insulation,
b_o = width of slot opening,
δ = (mechanical) air gap,
h_o = height of slot opening,
$h_{wedge+ins}$ = thickness of slot wedge + thickness of slot insulation.

The calculated capacitances C_{wr} for $k_{\mathrm{c}} > 1$ and for $k_{\mathrm{c}} = 1$ are given in Table 7.4. Measurements of $C_{\mathrm{wr}} + C_{\mathrm{rf}}$ as described in Section 3.5 (p. 37) were done on motors M11a, M11b, M110a and M110b. The measured values are also given in Table 7.4. The calculated values are up to 30 % too small for $k_{\mathrm{c}} > 1$ and up to 15 % too small for $k_{\mathrm{c}} = 1$. This error is supposed to be due to the calculation of C_{rf} that is *calculated too small*, because the BVR is calculated too large (→ Subsection 7.3.5). It is assumed that this is due to the contribution of the cage ring to the capacitance that is not considered in the calculations.

7.3.4 Bearing Capacitance

If the bearing rotates at sufficient speed for an insulating lubricating film to build up, and no voltage greater than the threshold voltage $v_{\mathrm{b,th}}$ is applied that leads to a breakdown, the bearing acts as a capacitor (→ Section 7.1). Calculation of the capacitance is very difficult, because the geometrical structure is rather complex. The capacitance of a ball bearing consist of two capacitances in series, the capacitance from the outer bearing race to the balls that are connected via the bearing cage, and the capacitance from the balls to the inner bearing race. The parallel capacitance between the inner and the outer bearing race is much smaller, because of the large distance between the two bearing races. Therefore, it is neglected.

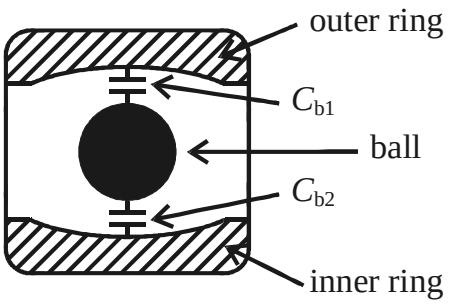

Figure 7.2: Schematic figure of two capacitances of a ball in a ball bearing

The minimum thickness of the lubrication film of the bearing $h_{\mathrm{lb,min}}$ is about an order of magnitudes smaller than the radial bearing play. It is about 1 μm versus 10 μm for the investigated motors (→ Appendix C, p. 211, and Appendix D, p. 215). Therefore, the capacitance will be mainly determined by this part of the bearing. The *Hertz*'ian contact area is taken as corresponding electrode area. The two capacitances C_{b1} and C_{b2} of the bearing are supposed to be of the same value, therefore the bearing capacitance is half the capacitance between the bearing race and balls (7.14). The calculated values are given in Table 7.5.

$$C_{\mathrm{b}} = \frac{1}{2}\frac{\varepsilon_{\mathrm{r}}\varepsilon_0 A_{\mathrm{H}}}{h_{\mathrm{lb}}} \tag{7.14}$$

where:

$\varepsilon_{\mathrm{r}} = 3$,
A_{H} = *Hertz*'ian contact area,
$h_{\mathrm{lb,min}}$ = minimum thickness of lubricating film.

Measurement of the bearing capacitance C_{b} was not done, so no comparison with calculation is possible.

7.3.5 Bearing Voltage Ratio BVR

The capacitive voltage divider "BVR" determines the percentage of amplitude of the stator winding common mode voltage v_Y over the bearing as bearing voltage v_b. According to the model (→ Section 7.2), it is determined by the stator winding-to-rotor, the rotor-to-frame and the bearing capacitances C_{wr}, C_{rf} and C_b, as given by (7.15) (→ Fig. 3.9b, p. 37):

$$\text{BVR} = \frac{\text{bearing voltage}}{\text{stator winding common mode voltage}} = \frac{v_b}{v_Y} = \frac{C_{wr}}{C_{wr} + C_{rf} + 2C_b} \tag{7.15}$$

Table 7.5 summarizes the calculated values of the capacitances involved, and the calculated as well as the measured BVRs. Generally, the calculated BVRs are larger than the measured ones. Due to the difference of calculated and measured $C_{rf} + C_{wr}$, the differences in calculated and measured BVRs are supposed to be due to a too low value for the calculated C_{rf}. However, the calculations confirm the tendencies measured: motor M11b has a larger BVR than motor M11a, and motor M110b with a relatively large slot depth has a larger BVR than motor M110a, because of a smaller value of C_{wr} in each case that is due to a larger depth of the slot top.

It is important to note that the *BVR is low for all motors*. This fact is also revealed by the calculations.

The following ratios of the involved capacitances are identified:

$$C_{wr} \;=\; (\frac{1}{10} \;...\; \frac{1}{20})C_{rf} \tag{7.16}$$

$$C_b \;\approx\; C_{wr} \tag{7.17}$$

Motor	C_{rf} calculated k_c >1	C_{rf} calculated k_c=1	C_{wr} calculated	BVR (C_b=0) calculated k_c >1	BVR (C_b=0) calculated k_c=1	C_b calculated	BVR calculated k_c >1	BVR calculated k_c=1	BVR measured
	pF	pF	pF	%	%	pF	%	%	%
M11a	916	1151	38	4.0	3.2	40	3.6	3.0	2.5
M11b	1277	1529	147	10.3	8.7	47	9.7	8.3	7.5
M110a	2137	2527	193	8.3	7.1	60	7.9	6.8	3.5
M110b	2571	2812	225	8.0	7.4	60	6.6	7.1	2.5
M500a	4152	4885	218	4.6	4.3	41	4.9	4.2	not meas.
M500b	1293	1375	137	9.6	9.0	41	9.1	8.6	7.5

Table 7.5: Calculated BVRs and motor capacitances (motor speed $n = 1000$ /min, bearing temperature $\vartheta_b = 20°C$)

$C_{\mathrm{wr}} = \frac{1}{10}\, C_{rf}$		$C_{\mathrm{wr}} = \frac{1}{20}\, C_{\mathrm{rf}}$	
$C_{\mathrm{b}} = 0$	$C_{\mathrm{b}} = C_{\mathrm{wr}}$	$C_{\mathrm{b}} = 0$	$C_{\mathrm{b}} = C_{\mathrm{wr}}$
9.0 %	7.7 %	4.8 %	4.3 %

Table 7.6: Calculated values of BVRs for the identified ratios of the capacitances involved (7.16) and (7.17)

Summarizing (7.15) to (7.17), the *influence of* C_{b} on the BVR is *small*. Therefore, the BVRs of the test motors were calculated for $C_{\mathrm{b}} = 0$ (Table 7.5). The difference towards the results for $C_{\mathrm{b}} > 0$ is small, notably for the small motors of the 11 kW power level.

Based on the ratios of the capacitances involved (7.16) and (7.17), the BVR was calculated as function of these ratios (Table 7.6). The calculated BVR does *not exceed* 10 %. This is in line with measurement experience that the BVR is generally low - BVR $\approx$ (5...10) % - for standard motors.

Change of C_{b} with change of *motor speed due to increased lubricating-film thickness is negligible*, because of the identified ratios (7.16) and (7.17). As long as the lubrication film allows voltage buildup over the bearing, the *BVR is not affected remarkably.*

The length l_{c} of the motor cable and the type - shielded versus unshielded motor cable - do not affect the BVR, because the BVR is a parameter that is only defined by the parameters of the machine. The measurements showed that, for the investigated range of cable lengths and types, the maximum amplitude of the stator winding common mode voltage at the motor terminals v_{Y} remains unaffected by the motor cable (→ Appendix E, p. 219). Hence, the maximum bearing voltage v_{b} that might occur is *not influenced.* Therefore, no influence of the system parameters

▷ motor cable length l_{c} and

▷ motor cable type (shielded versus unshielded motor cable)

on the *amplitude of the EDM-bearing currents* was found (→ Section 4.7, p. 56, and Section 4.8, p. 59).

The capacitance of the insulating layer of an insulated ("coated") bearing is about ten times as large as the bearing capacitance C_{b} (→ Section 7.7.4).

$$C_{\mathrm{b}}^{*} = \frac{1}{\frac{1}{C_{\mathrm{b}}} + \frac{1}{C_{\mathrm{ins}}}} = \frac{C_{\mathrm{b}}}{\frac{1}{1} + \frac{1}{10}} = \frac{10}{11}\, C_{\mathrm{b}} \approx C_{\mathrm{b}} \tag{7.18}$$

where:

C_{b}^{*} = resultant capacitance of bearing and insulating coat,

C_{ins} = capacitance of insulating coat.

The capacitance $C_{\mathrm{b,hybrid}}$ of a hybrid bearing is orders of magnitude smaller than the capacitance C_{b} of an ordinary bearing, because the whole diameter d of the ceramic balls

represents the length of the insulating gap between the two electrodes of the capacitance that are given by the inner and the outer race of the bearing. Therefore, the BVR of a motor with hybrid bearings can be calculated with $C_\mathrm{b}^* = 0$.

Thus, the BVR *remains almost unaffected* by use of

- ▷ insulated ("coated") bearings or
- ▷ hybrid bearings.

The BVRs of the test motors were measured for different motor - inverter - combinations on both drive end and non-drive end side of the motors, motor speed $n = 900$ /min and $n = 1500$ /min, use of motor cables with different length l_c and types (shielded and unshielded), as well as use of insulated and of hybrid bearings. Insulated and hybrid bearings were investigated only at the 11 kW power level. The measurements confirm the statements. The measurement results of v_Y and v_b are given in Appendix E (p. 219).

The BVR does not only connect the amplitudes, but also the dv_Y/dt of the stator winding common mode voltage and the dv_b/dt and the bearing voltage. Table 7.7 summarizes the measured values of dv_Y/dt and the calculated values of dv_b/dt, using (7.19), in comparison with the measured values of dv_b/dt. *Measured and calculated results are in line.*

$$\frac{dv_\mathrm{b}}{dt} = \mathrm{BVR}\frac{dv_\mathrm{Y}}{dt} \tag{7.19}$$

The BVR is low ($\mathrm{BVR} < 10\%$*) for all investigated motors. The influence of the bearing capacitance on the BVR is small, therefore, the influence of change of motor speed and of use of insulated or hybrid bearings on the BVR is negligible.*

Motor	$\frac{dv_\mathrm{Y}}{dt}$ measured	$\frac{dv_\mathrm{b}}{dt}$ calculated	$\frac{dv_\mathrm{b}}{dt}$ measured
	kV/μs	V/μs	V/μs
M11a	0.08	2.0	1...2
M11b	0.06	4.5	4
M110a	0.08	3.6	2...3
M110b	0.14	3.5	3...4
M500b	0.06	4.5	3

Table 7.7: Calculated and measured dv_b/dt of the voltage over the bearing

7.4 EDM-Bearing Currents

7.4.1 Modeling of Bearing Current Measurement Circuit

At intact lubrication film, the bearing voltage v_b mirrors the common mode voltage at the stator terminals v_Y via the capacitive voltage divider BVR (1.2). The lubrication film discharges when the threshold voltage $v_\mathrm{b,th}$ of the bearing is surpassed. This mechanism is influenced by metallic particles due to wear in the grease and the breakdowns occur statistically distributed in DE- and NDE-bearing more or less independently as common mode current (→ Section 1.5, p. 10).

The details of the discharge mechanism *inside the bearing* are still unknown and are beyond the scope of this thesis. The phenomenon is modeled by a simple circuit: The loaded bearing capacity $C_\mathrm{b,b}$ discharges via the bearing resistance R_b after the breakdown. This results in a current impulse with maximum amplitude $\hat{i}_\mathrm{b} = \tilde{v}_\mathrm{b}/R_\mathrm{b}$, where $\tilde{v}_\mathrm{b}$ is the bearing voltage at breakdown and R_b the bearing resistance (Fig. 7.3). The bearing resistance R_b is highly nonlinear (→ Section 7.1). The rotor-to-frame capacitance C_rf and the capacitance of the second bearing $C_\mathrm{b,a}$ are in parallel to the capacitance of the bearing that suffers from the breakdown $C_\mathrm{b,b}$. These two capacitances discharge over the shorted bearing. The bearing current impulse i_b cannot be measured directly. In the setup, the bearing current impulse i_b is derived from the current i_bL measured in the copper loop (Fig. 7.4).

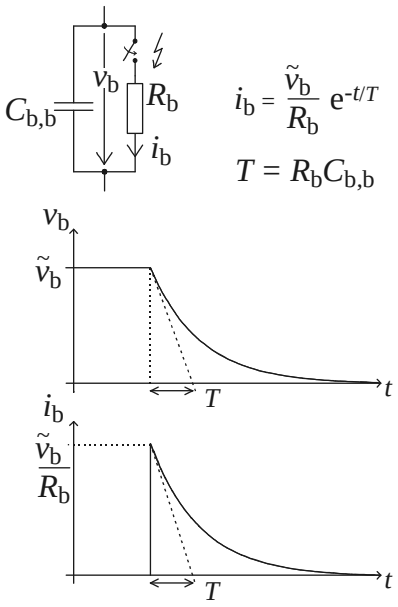

Figure 7.3: Simplified view of discharge of loaded bearing capacity at breakdown over bearing resistance

The capacitance C_i of the insulating layer of the end-shields, the resistance R_cu and the inductance L_cu of the copper loop applied for bearing current measurement are added in the equivalent circuit (Fig. 7.4). *The correlation between measured and occurring bearing current is derived from this equivalent circuit.*

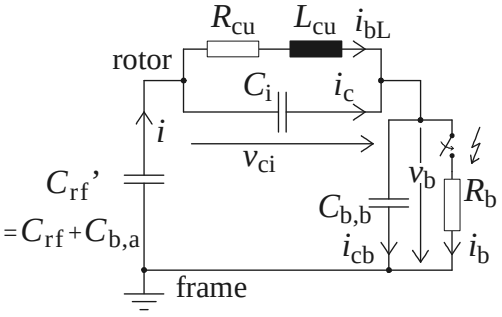

Figure 7.4: Equivalent circuit for representing the EDM-current measurement setup

For frequencies of several MHz, which is the frequency range of EDM-bearing currents, the resistance R_Fe and the inductance L_Fe of the path of the bearing current through the stator lamination can be neglected with respect to the bearing resistance and the inductance of the copper loop L_cu (→ Section 7.7).

The current contribution from the stator winding is negligible, because the ratio between the stator-to-rotor capacitance C_{wr} and the rotor-to-frame capacitance C_{rf} is in the order of 0.05...0.1 (7.16). Furthermore, the breakdowns need not necessarily occur with a switching incident of the stator phase voltages. On the contrary, they generally occur when the rise of the common mode voltage is finished, hence, the common mode voltage is about constant at the moment of breakdown (Fig. 7.5, (7.20) to (7.22)).

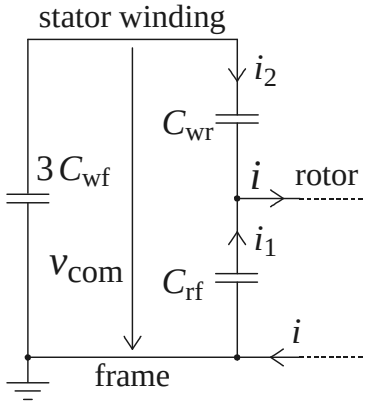

Figure 7.5: Current contribution from stator winding and motor frame to EDM-bearing currents

$$i = i_1 + i_2 \tag{7.20}$$

$$\frac{\mathrm{d}v_{\mathrm{com}}}{\mathrm{d}t} = -\frac{1}{C_{\mathrm{rf}}} i_1 + \frac{1}{C_{\mathrm{wr}}} i_2$$

$$= -(\frac{1}{C_{\mathrm{rf}}} + \frac{1}{C_{\mathrm{wr}}}) i_1 + \frac{1}{C_{\mathrm{wr}}} i \approx 0 \tag{7.21}$$

$$\Rightarrow i = i_1(\frac{C_{\mathrm{wr}}}{C_{\mathrm{rf}}} + 1) \approx i_1 \tag{7.22}$$

where:

i = current through rotor,

i_1 = current from frame to rotor,

i_2 = current from winding to rotor.

7.4.2 Analytical Solution

The analytical solution for the currents i_{bL} and i_{b} of the equivalent circuit (Fig. 7.4) are given by (7.23) to (7.27).

$$0 = \mathrm{a}_3 \frac{\mathrm{d}^3 i_{\mathrm{bL}}}{\mathrm{d}t^3} + \mathrm{a}_2 \frac{\mathrm{d}^2 i_{\mathrm{bL}}}{\mathrm{d}t^2} + \mathrm{a}_1 \frac{\mathrm{d}i_{\mathrm{bL}}}{\mathrm{d}t} + i_{\mathrm{bL}} \tag{7.23}$$

$$\mathrm{a}_3 = R_{\mathrm{b}} L_{\mathrm{cu}} (C'_{\mathrm{rf}} C_{\mathrm{i}} + C_{\mathrm{i}} C_{\mathrm{b}} + C_{\mathrm{b}} C'_{\mathrm{rf}}) \tag{7.24}$$

$$\mathrm{a}_2 = L_{\mathrm{cu}} (C'_{\mathrm{rf}} + C_{\mathrm{i}}) + R_{\mathrm{b}} R_{\mathrm{cu}} C_{\mathrm{i}} (C'_{\mathrm{rf}} + C_{\mathrm{b}}) \tag{7.25}$$

$$\mathrm{a}_1 = R_{\mathrm{cu}} (C'_{\mathrm{rf}} + C_{\mathrm{i}}) + R_{\mathrm{b}} (C'_{\mathrm{rf}} + C_{\mathrm{b}}) \tag{7.26}$$

$$i_{\mathrm{b}} = i - i_{\mathrm{cb}} = i + \frac{C_{\mathrm{b}}}{C'_{\mathrm{rf}}} i + \frac{C_{\mathrm{b}}}{C_{\mathrm{i}}} i_{\mathrm{c}} = (1 + \frac{C_{\mathrm{b}}}{C'_{\mathrm{rf}}}) i + \frac{C_{\mathrm{b}}}{C_{\mathrm{i}}} i_{\mathrm{c}}$$

$$= \{1 + \frac{C_{\mathrm{b}}}{C'_{\mathrm{rf}}}\} i_{\mathrm{bL}} + \{R_{\mathrm{cu}} C_{\mathrm{i}} (1 + \frac{C_{\mathrm{b}}}{C'_{\mathrm{rf}}}) + R_{\mathrm{cu}} C_{\mathrm{b}}\} \frac{\mathrm{d}i_{\mathrm{bL}}}{\mathrm{d}t}$$

$$+ \{L_{\mathrm{cu}} C_{\mathrm{i}} (1 + \frac{C_{\mathrm{b}}}{C'_{\mathrm{rf}}}) + L_{\mathrm{cu}} C_{\mathrm{b}}\} \frac{\mathrm{d}^2 i_{\mathrm{bL}}}{\mathrm{d}t^2} \tag{7.27}$$

With the linear expansion general approach $i_{\mathrm{bL}} = \sum_{\mathrm{i}=1}^{3} \underline{\mathrm{C}}_{\mathrm{i}} e^{\underline{\lambda}\mathrm{i}t}$, where $\underline{\mathrm{C}}_{\mathrm{i}}$ are constants to be determined from the initial conditions, (7.23) becomes (7.28), what is transformed to (7.29), respectively.

$$0 = \mathrm{a}_3\underline{\lambda}_{\mathrm{i}}^3 + \mathrm{a}_2\underline{\lambda}_{\mathrm{i}}^2 + \mathrm{a}_1\underline{\lambda}_{\mathrm{i}} + 1 \tag{7.28}$$

$$0 = \underline{\lambda}_{\mathrm{i}}^3 + \frac{\mathrm{a}_2}{\mathrm{a}_3}\underline{\lambda}_{\mathrm{i}}^2 + \frac{\mathrm{a}_1}{\mathrm{a}_3}\underline{\lambda}_{\mathrm{i}} + \frac{1}{\mathrm{a}_3} = \underline{\lambda}_{\mathrm{i}}^3 + \mathrm{b}_2\underline{\lambda}_{\mathrm{i}}^2 + \mathrm{b}_1\underline{\lambda}_{\mathrm{i}} + \mathrm{b}_0 \tag{7.29}$$

where:

$$\mathrm{b}_0 = \frac{1}{\mathrm{a}_3} \tag{7.30}$$

$$\mathrm{b}_1 = \frac{\mathrm{a}_1}{\mathrm{a}_3} \tag{7.31}$$

$$\mathrm{b}_2 = \frac{\mathrm{a}_2}{\mathrm{a}_3} \tag{7.32}$$

Using (7.33), (7.29) is transformed to (7.34), where p and q are given by (7.35) and (7.36).

$$\underline{\lambda} = \underline{y} + \mathrm{b}_2/3 \tag{7.33}$$

$$0 = \underline{y}^3 + \underline{y}\mathrm{p} + \mathrm{q} \tag{7.34}$$

where:

$$\mathrm{p} = -\frac{1}{3}\mathrm{b}_2^2 + \mathrm{b}_1 \tag{7.35}$$

$$\mathrm{q} = \frac{2}{27}\mathrm{b}_2^3 - \frac{1}{3}\mathrm{b}_2\mathrm{b}_1 + \mathrm{b}_0 \tag{7.36}$$

Using (7.37), the cubic ordinary differential equation (7.34) is transformed to a quadratic ordinary differential equation in $\underline{u}^3$ (7.38). The solutions for $\underline{u}$ and $\underline{v}$ are given by (7.39) and (7.40), and the solutions for $\underline{y}_{\mathrm{i}}$, i = 1, 2, 3 by (7.41) to (7.43).

$$\underline{y} = \underline{u} + \underline{v}, \quad \text{where: } \underline{u} \cdot \underline{v} = -\mathrm{p}/3 \tag{7.37}$$

$$0 = \underline{u}^6 + \underline{u}^3\mathrm{q} - \frac{\mathrm{p}}{27} \tag{7.38}$$

$$\underline{u}^3 = -\frac{\mathrm{q}}{2} + \{(\frac{\mathrm{q}}{2})^2 + (\frac{\mathrm{p}}{3})^3\}^{1/2} \tag{7.39}$$

$$\underline{v}^3 = -\frac{\mathrm{q}}{2} - \{(\frac{\mathrm{q}}{2})^2 + (\frac{\mathrm{p}}{3})^3\}^{1/2} \tag{7.40}$$

$$\underline{y}_1 = \underline{u} + \underline{v} \tag{7.41}$$

$$\underline{y}_2 = \underline{u}e^{j2\pi/3} + \underline{v}e^{-j2\pi/3} \tag{7.42}$$

$$\underline{y}_3 = \underline{u}e^{-j2\pi/3} + \underline{v}e^{j2\pi/3} \tag{7.43}$$

The solutions for $\underline{\lambda}_\mathrm{i}$, i = 1, 2, 3 are obtained from (7.44), where one solution $\underline{\lambda}_1$ is a real, negative number (7.45), and the other two solutions $\underline{\lambda}_2$ and $\underline{\lambda}_3$ are conjugate, (7.46) and (7.47).

$$\underline{\lambda}_\mathrm{i} = \underline{y}_\mathrm{i} + \mathrm{b}_2/3, \quad \mathrm{i} = 1, 2, 3 \tag{7.44}$$

$$\underline{\lambda}_1 = \lambda < 0 \tag{7.45}$$

$$\underline{\lambda}_2 = -\alpha + j\beta \tag{7.46}$$

$$\underline{\lambda}_3 = -\alpha - j\beta \tag{7.47}$$

The general solution for the measurable current i_bL (7.23) (Fig. 7.4) is given by (7.48). The constants $\underline{\mathrm{C}}_1$ to $\underline{\mathrm{C}}_3$ are determined from the initial conditions (7.49) to (7.51). $\underline{\mathrm{C}}_1$ is a real number, $\underline{\mathrm{C}}_2$ and $\underline{\mathrm{C}}_3$ are conjugate. $\underline{\mathrm{C}}_1$ to $\underline{\mathrm{C}}_3$ can be expressed by (7.52), (7.53) and (7.54), where K_1 to K_3 are real numbers.

$$i_\mathrm{bL} = \underline{\mathrm{C}}_1 e^{\lambda t} + \underline{\mathrm{C}}_2 e^{(-\alpha+j\beta)t} + \underline{\mathrm{C}}_3 e^{(-\alpha-j\beta)t} \tag{7.48}$$

$$i_\mathrm{bL}|_{t=0} = 0 \tag{7.49}$$

$$v_\mathrm{ci}|_{t=0} = 0 \Rightarrow \frac{\mathrm{d}i_\mathrm{bL}}{\mathrm{d}t}|_{t=0} = 0 \tag{7.50}$$

$$v_\mathrm{b}|_{t=0} = \tilde{v}_\mathrm{b} \tag{7.51}$$

$$\underline{\mathrm{C}}_1 = \mathrm{K}_1 \tag{7.52}$$

$$\underline{\mathrm{C}}_2 = \frac{1}{2}(\mathrm{K}_2 + j\mathrm{K}_3) \tag{7.53}$$

$$\underline{\mathrm{C}}_3 = \frac{1}{2}(\mathrm{K}_2 - j\mathrm{K}_3) \tag{7.54}$$

The solution for i_bL (7.23) is given by (7.55), with the values of K_1 to K_3 according to (7.56), (7.57) and (7.58).

$$i_\mathrm{bL} = \mathrm{K}_1 e^{\lambda t} + e^{-\alpha t}\{\mathrm{K}_2 \cos(\beta t) + \mathrm{K}_3 \sin(\beta t)\} \tag{7.55}$$

$$\mathrm{K}_1 = +\frac{\beta\tilde{v}_\mathrm{b}}{\{\beta\lambda^2 - \beta(\alpha^2-\beta^2) + \alpha\beta(\alpha+\beta)\}\{L_\mathrm{cu}C_\mathrm{i}(1+C_\mathrm{b}/C_\mathrm{i}) + L_\mathrm{cu}C_\mathrm{b}\}R_\mathrm{b}} \tag{7.56}$$

$$\mathrm{K}_2 = -\frac{\beta\tilde{v}_\mathrm{b}}{\{\beta\lambda^2 - \beta(\alpha^2-\beta^2) + \alpha\beta(\alpha+\beta)\}\{L_\mathrm{cu}C_\mathrm{i}(1+C_\mathrm{b}/C_\mathrm{i}) + L_\mathrm{cu}C_\mathrm{b}\}R_\mathrm{b}} \tag{7.57}$$

$$\mathrm{K}_3 = -\frac{(\alpha+\lambda)\tilde{v}_\mathrm{b}}{\{\beta\lambda^2 - \beta(\alpha^2-\beta^2) + \alpha\beta(\alpha+\beta)\}\{L_\mathrm{cu}C_\mathrm{i}(1+C_\mathrm{b}/C_\mathrm{i}) + L_\mathrm{cu}C_\mathrm{b}\}R_\mathrm{b}} \tag{7.58}$$

The solution for the "real" bearing current i_b (Fig. 7.4) is obtained from (7.27), using the solution for i_bL (7.55) and the values of K_1 to K_3 (7.56) to (7.58).

7.4.3 Calculated Bearing and Loop Current

♦ ***Comparison of the measurable current in the copper loop i_{bL} and the "real" bearing current occurring inside the bearing i_{b}*** (Fig. 7.4):

Fig. 7.6 shows the simulated currents i_{b} and i_{bL} for motor M11b, which shows the most distinctive EDM-bearing currents among the investigated motors. The parameters were chosen according to data set (7.59). The values of the bearing capacity C_{b} and the bearing voltage at breakdown $\tilde{v}_{\mathrm{b}}$ are taken at motor speed $n = 1000$ /min and bearing temperature $\vartheta_{\mathrm{b}} \approx 20°\mathrm{C}$.

$$\left\{\begin{array}{lcl} \triangleright\, C_{\mathrm{b}} & = & C_{\mathrm{b,a}} = C_{\mathrm{b,b}} = 0.047 \text{ nF (calculated, Table 7.5)}, \\ \triangleright\, C_{\mathrm{rf}} & = & 1.529 \text{ nF (calculated, Table 7.5)}, \\ \triangleright\, C_{\mathrm{i}} & = & 1.5 \text{ nF (measured)}, \\ \triangleright\, L_{\mathrm{cu}} & = & 0.1\ \mu \text{ H (measured)}, \\ \triangleright\, R_{\mathrm{cu}} & = & 0.2\ \Omega \text{ (estimated from measured value } R_{\mathrm{cu,dc}} = 0.02\ \mathrm{m}\Omega), \\ \triangleright\, R_{\mathrm{b}} & = & 10\ \Omega \text{ (estimated)}, \\ \triangleright\, \tilde{v}_{\mathrm{b}} & = & 15 \text{ V (measured)}. \end{array}\right. \tag{7.59}$$

With data set (7.59), the calculated peak amplitude of the measurable current i_{bL} values $\hat{i}_{\mathrm{bL}} = 0.95$ A (Fig. 7.6). With the simple model of Fig. 7.3, the peak current $\hat{i}_{\mathrm{b}}$ occurs at $t = 0$ and is $\hat{i}_{\mathrm{b}} = \tilde{v}_{\mathrm{b}}/\ R_{\mathrm{b}} = 15$ V/ 10 $\Omega = 1.5$ A. With the extended model (Fig. 7.4), the *same* peak bearing current $\hat{i}_{\mathrm{b}} = 1.5$ A is determined, but is decreasing with some oscillations due to the loop inductance (oscillating frequency $f = \beta/2\pi \approx 10$ MHz). It has to be noted that, with *this* model, $\hat{i}_{\mathrm{b}}$ always occurs at $t = 0$ and is given by $\tilde{v}_{\mathrm{b}}/\ R_{\mathrm{b}}$, independently of the values of the other system parameters. The other parameters determine only the oscillating current decrease.

The calculated peak amplitude $\hat{i}_{\mathrm{bL}}$ is about 2/3 of the not measurable bearing current $\hat{i}_{\mathrm{b}}$ (data set (7.59)). *The simulated measurable current i_{bL} fits well to the bearing current measured in the investigations* (Fig. 7.6). The *measurable current i_{bL} allows only a rough estimate of the real bearing current inside the bearing*, which can be described by the ratio $\hat{i}_{\mathrm{bL}}/\hat{i}_{\mathrm{b}}$. However, because of the identical measurement technique for all investigated setups, *comparison among the different setups is feasible.*

With the given orders of magnitudes, the value of the *resistance R_{cu} of the copper loop for bearing current measurement* has only a small influence on the amplitude of the measured current. The value of the *inductance L_{cu} of the copper loop* is more important, as increase by a factor of 10 leads to reduction of the measurable current i_{bL} of more than 50 %. However, decrease of L_{cu} by a factor of 10 does not result in a significant improvement of the ratio $\hat{i}_{\mathrm{bL}}/\hat{i}_{\mathrm{b}}$ towards 1 (Table 7.8). The same is true for the value of

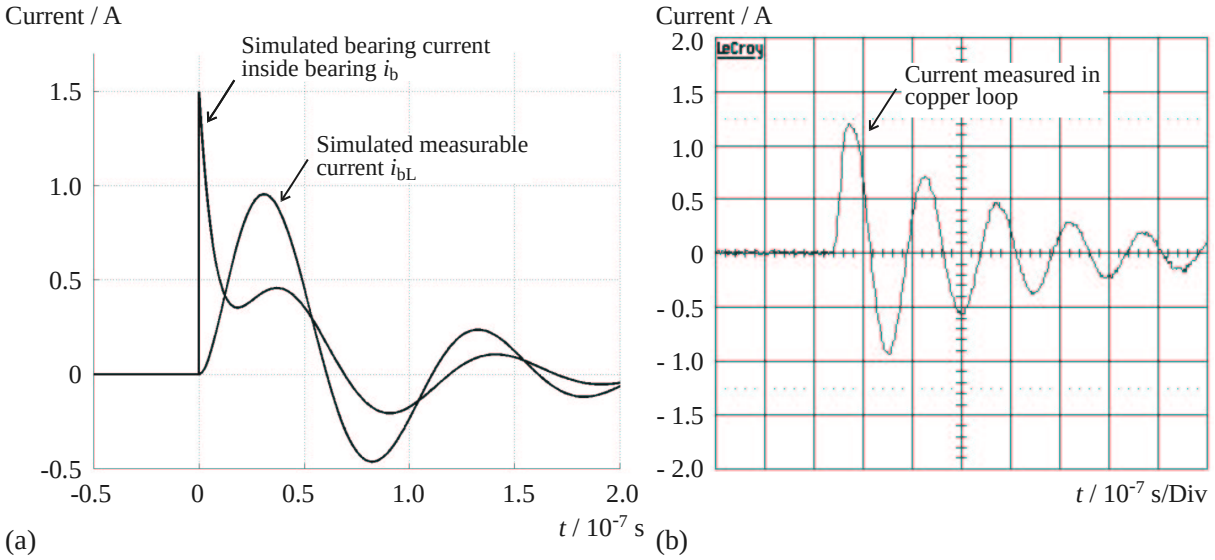

Figure 7.6: (a) Calculated bearing current inside the bearing i_b and measurable current in copper loop i_{bL}, induction motor M11b, data set (7.59), (b) current measured in copper loop, induction motor M11b, configuration $E1_{50}$ ($l_c = 50$ m, unshielded motor cable), motor speed $n = 300$ /min, bearing temperature $\vartheta_b \approx 25°C$

C_b, C_{rf}, C_i, R_b and $\tilde{v}_b$ according to data set (7.59)	$L_{cu} = 0.01$ μH	$R_{cu} = 0.02$ Ω	$\hat{i}_{bL}/\hat{i}_b = 1.80$ A/1.5 A $= 1.20$
		$R_{cu} = 0.20$ Ω	$\hat{i}_{bL}/\hat{i}_b = 1.69$ A/1.5 A $= 1.13$
		$R_{cu} = 2.00$ Ω	$\hat{i}_{bL}/\hat{i}_b = 1.04$ A/1.5 A $= 0.69$
	$L_{cu} = 0.10$ μH	$R_{cu} = 0.02$ Ω	$\hat{i}_{bL}/\hat{i}_b = 0.97$ A/1.5 A $= 0.65$
		$R_{cu} = 0.20$ Ω	$\hat{i}_{bL}/\hat{i}_b = 0.96$ A/1.5 A $= 0.64$
		$R_{cu} = 2.00$ Ω	$\hat{i}_{bL}/\hat{i}_b = 0.79$ A/1.5 A $= 0.53$
	$L_{cu} = 1.00$ μH	$R_{cu} = 0.02$ Ω	$\hat{i}_{bL}/\hat{i}_b = 0.38$ A/1.5 A $= 0.25$
		$R_{cu} = 0.20$ Ω	$\hat{i}_{bL}/\hat{i}_b = 0.38$ A/1.5 A $= 0.25$
		$R_{cu} = 2.00$ Ω	$\hat{i}_{bL}/\hat{i}_b = 0.35$ A/1.5 A $= 0.23$
C_b, C_{rf}, L_{cu}, R_{cu}, R_b and $\tilde{v}_b$ according to data set (7.59)	$C_i = 0.15$ nF		$\hat{i}_{bL}/\hat{i}_b = 0.96$ A/1.5 A $= 0.64$
	$C_i = 1.5$ nF		$\hat{i}_{bL}/\hat{i}_b = 0.96$ A/1.5 A $= 0.64$
	$C_i = 15$ nF		$\hat{i}_{bL}/\hat{i}_b = 0.53$ A/1.5 A $= 0.35$

Table 7.8: Calculated influence of *resistance and inductance of copper loop and capacitance of the insulating layer for bearing current measurement* on the ratio $\hat{i}_{bL}/\hat{i}_b$, motor M11b

the *capacitance* C_i. Simulation results show that increase of C_i by a factor of 10 reduces the amplitude of the measurable current i_{bL} by almost 50 %, whereas the change of the amplitude of the measurable current i_{bL} is negligible, if the value of C_i is decreased by a factor of 10 (Table 7.8).

♦ ***Discussion of the the influence of the parameters of the electrical equivalent circuit R_b, C_b, C_{rf} and of bearing voltage v_b*** (Fig. 7.4):

With *increasing bearing resistance R_b both the peak amplitude of the bearing current inside the bearing $\hat{i}_b$ and of the measurable current in the copper loop $\hat{i}_{bL}$* decrease (Table 7.9). The bearing current amplitude $\hat{i}_b$ is inversely proportional to R_b. By other authors, typical R_b is given in the range of (5...20) Ω [2], [42], so that *here a typical ratio $\hat{i}_{bL}/\hat{i}_b$ = 2/3 is concluded* (Fig. 7.6, Table 7.8).

Due to the assumed constant parameters, the system is linear. Therefore, *both the amplitude of $\hat{i}_b$ and of $\hat{i}_{bL}$ increase linearly with the value of the bearing voltage at breakdown* $\tilde{v}_b$ (Table 7.10).

With the *bearing capacitance C_b* rising three decades from 0.0047 nF to 4.7 nF and the other parameters according to data set (7.59), the ratio $\hat{i}_{bL}/\hat{i}_b$ increases only from 0.63 to 0.78 (Table 7.11). Hence, *the influence of the bearing capacitance C_b is very small.*

The *situation is very different for the value of the rotor-to-frame capacitance C_{rf}*, where the waveform of the "real" bearing current i_b changes considerably as the value of C_{rf} changes. The same does the waveform of i_{bL}: As the energy stored in the capacitance C_{rf} discharges via the bearing suffering from the breakdown, thereby passing through the copper loop, the *measurable current i_{bL} is strongly influenced* by C_{rf}. With the value of C_{rf} rising three decades from 0.153 nF to 152.9 nF and the other parameters according to data set (7.59), the ratio $\hat{i}_{bL}/\hat{i}_b$ increases by almost one decade from 0.15 to 1.21 (Table 7.11, Fig. 7.7).

R_{cu}, L_{cu}, C_b, C_{rf}, C_i and $\tilde{v}_b$ according to data set (7.59)	$R_b = 1\ \Omega$	$\hat{i}_{bL}/\hat{i}_b = 1.27\ \text{A}/15\ \text{A} = 0.09$
	$R_b = 10\ \Omega$	$\hat{i}_{bL}/\hat{i}_b = 0.96\ \text{A}/1.5\ \text{A} = 0.64$
	$R_b = 100\ \Omega$	$\hat{i}_{bL}/\hat{i}_b = 0.24\ \text{A}/0.15\ \text{A} = 1.60$

Table 7.9: Calculated influence of the *bearing resistance R_b* on $\hat{i}_{bL}$, $\hat{i}_b$ and the ratio $\hat{i}_{bL}/\hat{i}_b$, induction motor M11b, data set (7.59)

R_{cu}, L_{cu}, C_b, C_{rf}, C_i and R_b according to data set (7.59)	$\tilde{v}_b = 5$ V	$\hat{i}_{bL}/\hat{i}_b = 0.32\ \text{A}/0.5\ \text{A} = 0.64$
	$\tilde{v} = 10$ V	$\hat{i}_{bL}/\hat{i}_b = 0.64\ \text{A}/1.0\ \text{A} = 0.64$
	$\tilde{v} = 15$ V	$\hat{i}_{bL}/\hat{i}_b = 0.96\ \text{A}/1.5\ \text{A} = 0.64$
	$\tilde{v} = 20$ V	$\hat{i}_{bL}/\hat{i}_b = 1.27\ \text{A}/2.0\ \text{A} = 0.64$

Table 7.10: Calculated influence of the *bearing voltage at breakdown $\tilde{v}_b$* on $\hat{i}_{bL}$, $\hat{i}_b$ and the ratio $\hat{i}_{bL}/\hat{i}_b$, induction motor M11b, data set (7.59)

L_{cu}, R_{cu}, C_i, R_b and $\tilde{v}_b$ according to data set (7.59)	$C_b = 0.0047$ nF	$C_{rf} = 1.529$ nF	$\hat{i}_{bL}/\hat{i}_b = 0.95$ A/1.5 A $= 0.63$
	$C_b = 0.047$ nF		$\hat{i}_{bL}/\hat{i}_b = 0.96$ A/1.5 A $= 0.64$
	$C_b = 0.47$ nF		$\hat{i}_{bL}/\hat{i}_b = 1.01$ A/1.5 A $= 0.67$
	$C_b = 4.7$ nF		$\hat{i}_{bL}/\hat{i}_b = 1.17$ A/1.5 A $= 0.78$
	$C_b = 0.047$ nF	$C_{rf} = 0.153$ nF	$\hat{i}_{bL}/\hat{i}_b = 0.22$ A/1.5 A $= 0.15$
		$C_{rf} = 1.529$ nF	$\hat{i}_{bL}/\hat{i}_b = 0.96$ A/1.5 A $= 0.64$
		$C_{rf} = 15.29$ nF	$\hat{i}_{bL}/\hat{i}_b = 1.76$ A/1.5 A $= 1.17$
		$C_{rf} = 152.9$ nF	$\hat{i}_{bL}/\hat{i}_b = 1.81$ A/1.5 A $= 1.21$

Table 7.11: Calculated influence of *bearing capacitance* C_b and *rotor-to-frame capacitance* C_{rf} on the ratio $\hat{i}_{bL}/\hat{i}_L$, motor M11b, data set (7.59)

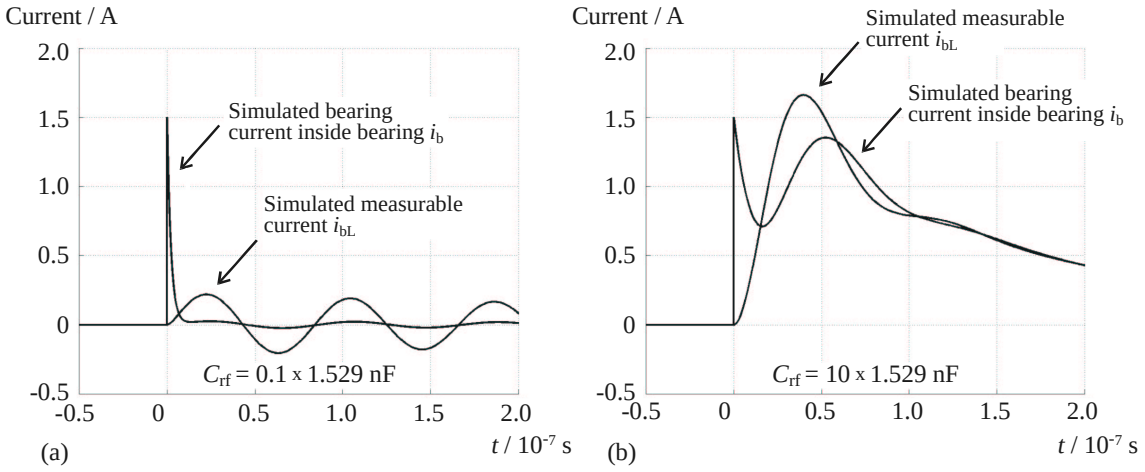

Figure 7.7: Calculated bearing current i_b and measurable current i_{bL} for *different values of the rotor-to-frame capacitance* C_{rf}, motor M11b, data set (7.59)

The - qualitative - difference between the measured bearing currents of motor M11a and M11b is also explained by the influence of the capacitance C_{rf}: Motor M11b has about a 30 % smaller value of C_{rf} than motor M11a, resulting in a 15 % larger amplitude of the calculated measurable current $\hat{i}_{bL}$. However, the amplitude of the measured bearing current of motor M11b is 30 % larger than of motor M11a, e.g., with the peak amplitude derived from the measured peak-to-peak value according to (4.1) (Section 4.11, p. 67), it is 0.6 A versus 0.4 A at motor speed $n = 1500$ /min and bearing temperature $\vartheta_b \approx 70°C$ (Table 7.12).

Motor	C_{rf}	C_b	$\hat{i}_{bL,measured}$	$\hat{i}_{bL,calculated}$
M11a	1.151 nF	0.040 nF	0.4 A	0.55 A
M11b	1.529 nF	0.047 nF	0.6 A	0.64 A

Table 7.12: Measured and calculated current amplitude in copper loop of induction motors M11a and M11b, bearing temperature $\vartheta_b \approx 70°C$, motor speed $n = 1500$ /min, bearing voltage at breakdown $\tilde{v}_b = 10$ V (measured), values of C_i, L_{cu}, R_{cu} and R_b according to data set (7.59)

♦ ***Discussion of the influence of different system parameters***:

The EDM-currents show *a maximum amplitude as function of the motor operational parameters "motor speed n" and "motor bearing temperature ϑ_b"*. Both parameters influence directly the thickness of the lubricating film and therefore the bearing breakdown voltage (→ Section 7.1). This effect can be explained by a trade-off between two opposite effects: On the one hand, the thickness of the lubricating film increases with increasing motor speed n. Therefore, the breakdown voltage and hence the discharge current increase also. On the other hand, the mean time between statistical passing of metallic wear, which is short-circuiting the film, decreases with rising speed. This results in more frequent discharges with lower amplitudes at lower bearing voltage and therefore a lower average value. The maximum bearing current amplitude is shifted to higher motor speed with rising bearing temperature ϑ_b, as the viscosity of the lubricating grease decreases with rising temperature, yielding a higher necessary circumferential bearing speed to establish a certain hydrodynamic film thickness.

For inverters with a dc-link voltage of 560 V, a value of the BVR as small as 2 % is sufficient to result in voltage buildup across the bearings beyond the bearing threshold voltage and resulting in discharge bearing currents. Furthermore, the stator winding has a smoothing effect on the shape of the common mode voltage pulses (→ Section 7.2). The EDM-bearing currents do not occur with the switching instant, but when the lubricating film has been loaded. Therefore, *the amplitudes of the EDM-bearing currents remain almost unaffected by the motor-inverter-combination.*

Neither cable length l_c, motor cable type (unshielded or shielded motor cable), nor filters that do not eliminate the common mode voltage, influence the peak common mode voltage over the bearing. Therefore, these parameters do not influence the amplitude of the EDM-bearing currents.

Only common mode *voltage* filters influence the EDM-bearing currents significantly, as they cancel the common mode voltage, which is the origin of these bearing currents, *thereby suppressing the currents.*

If an insulated bearing is used, the capacitance of the insulating coat C_{ins} (→ Section 7.7.4, p. 162) is in series with the rotor-to-frame capacitance C_{rf} (Fig. 7.8). The solutions of the measurable current and of the "real", not measurable bearing current inside the bearing with use of one insulated bearing, i_{bL}^* and i_b^*, are given by the solutions of i_{bL}

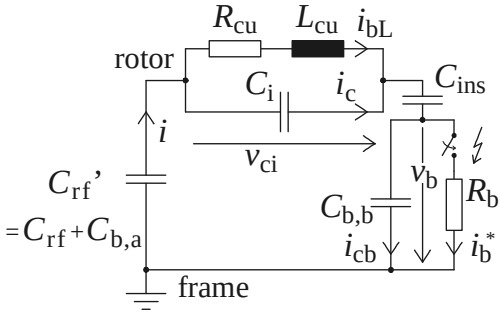

Figure 7.8: Equivalent circuit for representing the EDM-current measurement setup with use of an insulated bearing

(7.23) and i_b (7.27) with changed parameters. The parameter C_rf becomes C^*_rf (7.60), a_1 to a_3 become a^*_1 (7.61) to a^*_3 (7.63), and α, β, K_1, K_2 and K_3 change accordingly to α^*, β^*, K^*_1, K^*_2 and K^*_3.

If two insulated bearings are used, the capacitance of the insulating coat C_ins of the second bearing which does not suffer from the breakdown is in series to the capacity $C_\mathrm{b,a}$ of this bearing (Fig. 7.8). The parameter C_rf becomes C^{**}_rf (7.64), resulting also in changed parameters a^{**}_1 to a^{**}_3, α^{**}, β^{**}, K^{**}_1, K^{**}_2 and K^{**}_3 to obtain the solutions for the measurable current i^{**}_bL and the "real"bearing current i^{**}_b from the solutions of i_bL (7.23) and i_b (7.27).

$$C^*_\mathrm{rf} = \{\frac{1}{C'_\mathrm{rf}} + \frac{1}{C_\mathrm{ins}}\}^{-}1 = \{\frac{1}{C_\mathrm{rf} + C_\mathrm{b,a}} + \frac{1}{C_\mathrm{ins}}\}^{-}1 \tag{7.60}$$

$$\mathrm{a}^*_1 = R_\mathrm{cu}(C^*_\mathrm{rf} + C_\mathrm{i}) + R_\mathrm{b}(C^*_\mathrm{rf} + C_\mathrm{b}) \tag{7.61}$$

$$\mathrm{a}^*_2 = L_\mathrm{cu}(C^*_\mathrm{rf} + C_\mathrm{i}) + R_\mathrm{b}R_\mathrm{cu}C_\mathrm{i}(C^*_\mathrm{rf} + C_\mathrm{b}) \tag{7.62}$$

$$\mathrm{a}^*_3 = R_\mathrm{b}L_\mathrm{cu}(C^*_\mathrm{rf}C_\mathrm{i} + C_\mathrm{i}C_\mathrm{b} + C_\mathrm{b}C^*_\mathrm{rf}) \tag{7.63}$$

$$C^{**}_\mathrm{rf} = \{\frac{1}{C_\mathrm{rf} + C_\mathrm{b,a}C_\mathrm{rf}/(C_\mathrm{b,a} + C_\mathrm{rf})} + \frac{1}{C_\mathrm{ins}}\}^{-}1 \tag{7.64}$$

The values of the capacitances C^*_rf and C^{**}_rf are about the same. This is in line with (7.18) (p. 119), where it is stated that the capacitance of an insulated bearing has about the same value as the capacity of a conventional bearing.

The simulated peak amplitudes of the measurable currents i^*_bL and i^{**}_bL of motor M11b, using data set 7.59), $C_\mathrm{ins} = 2.7$ nF (→ Table 7.20, p. 163) and $\tilde{v} = 10$ V (bearing temperature $\vartheta_\mathrm{b} \approx 70°\mathrm{C}$, motor speed $n = 1500$ /min) value $\hat{i}^*_\mathrm{bL} = \hat{i}^{**}_\mathrm{bL} = 0.55$ A (Table 7.13). Hence, the reduction is down to 86 %, which is smaller than the measured reduction down to 67%, respectively 55%. Furthermore, in the measurements, the larger amplitude of the bearing current was measured at the side of the non-insulated bearing. *The equivalent circuit is only appropriate for a rough estimation of the influence of use of an insulated*

"Insulated bearing(s)?"	C_rf / C^*_rf / C^{**}_rf	$\hat{i}_\mathrm{bL}$, measured	$\hat{i}_\mathrm{bL}$, calculated	remaining bearing current	
				measured	calculated
No insulated, but two conventional bearings	$C_\mathrm{rf} = 1.529$ nF	0.60 A	0.64 A	100 %	100 %
$C_\mathrm{ins} = 2.7$ nF in series with $C_\mathrm{b,b}$	$C^*_\mathrm{rf} = 0.976$ nF	0.40 A	0.55 A	67 %	86 %
$C_\mathrm{ins} = 2.7$ nF in series with $C_\mathrm{b,a}$ and $C_\mathrm{b,b}$	$C^{**}_\mathrm{rf} = 0.995$ nF	0.33 A	0.55 A	55 %	86 %

Table 7.13: Measured and calculated current amplitude in copper loop of induction motor M11b, bearing temperature $\vartheta_\mathrm{b} \approx 70°\mathrm{C}$, motor speed $n = 1500$ /min, bearing voltage at breakdown $\tilde{v}_\mathrm{b} = 10$ V, values of C_i, L_cu, R_cu and R_b according to data set (7.59)

"Insulated bearing(s)?"	C_{rf} / C^{*}_{rf} / C^{**}_{rf}	
No insulated, but two conventional bearings	$C_{\mathrm{rf}} = 1.529$ nF	$\hat{i}_{\mathrm{bL}}/\hat{i}_{\mathrm{b}} = 0.64$ A/1.0 A $= 0.63$
$C_{\mathrm{ins}} = 2.7$ nF in series with $C_{\mathrm{b,b}}$	$C^{*}_{\mathrm{rf}} = 0.976$ nF	$\hat{i}_{\mathrm{bL}}/\hat{i}_{\mathrm{b}} = 0.55$ A/1.0 A $= 0.55$
$C_{\mathrm{ins}} = 2.7$ nF in series with $C_{\mathrm{b,a}}$ and $C_{\mathrm{b,b}}$	$C^{**}_{\mathrm{rf}} = 0.995$ nF	$\hat{i}_{\mathrm{bL}}/\hat{i}_{\mathrm{b}} = 0.55$ A/1.0 A $= 0.55$

Table 7.14: Calculated ratio $\hat{i}_{\mathrm{bL}}/\hat{i}_{\mathrm{L}}$ with use of *insulated bearings*, induction motor M11b, bearing temperature $\vartheta_{\mathrm{b}} \approx 70°\mathrm{C}$, motor speed $n = 1500$ /min, bearing voltage at breakdown $\tilde{v}_{\mathrm{b}} = 10$ V, values of C_{i}, L_{cu}, R_{cu} and R_{b} according to data set (7.59)

bearing. Furthermore, it has to be noted that the insulating coat does only reduce the amplitude of the measurable current, but not *the amplitude of the "real" bearing current inside the bearing.* The ratio $\hat{i}_{\mathrm{bL}}/\hat{i}_{\mathrm{b}}$ decreases from 0.64 to 0.55 (Table 7.14). In the model, a singular breakdown of the bearing voltage is considered. In the measurements average values of occurring bearing current pulses are observed. Therefore, a strongly reduced number of occurrence results in a smaller average value of the measured bearing current. In the measurements, with use of one insulated bearing, the reduced average bearing current amplitude was measured at both sides of the motor, with a smaller value occurring at the side non insulated bearing. This, as well as the measured further reduction with use of two insulated bearings is not explained by the model.

With hybrid bearings, the whole diameter of the ceramic balls (Si_3N_4) represents the length of the insulating gap. This distance is much larger than the thickness of the lubricating film. The respective breakdown voltage is much larger than the bearing voltage. Therefore, *no EDM-bearing currents occur due to a breakdown of the bearing voltage.*

The EDM-bearing current path and a copper loop bypassing the insulation of the bearing seat which is applied for measurement purposes, is described by an equivalent electrical circuit.
Since the bearing currents can only be measured indirectly, only a rough estimate of the real bearing current inside the bearing is feasible. However, because of the identical measurement technique for all investigated drive configurations, comparison among the different measurements is possible. Typical ratio of peak amplitude of measurable current in the loop $\hat{i}_{\mathrm{bL}}$*, which has to be taken as the bearing current, versus peak amplitude of the real bearing current* $\hat{i}_{\mathrm{b}}$ *is about 2/3. With additional bearing insulation, the ratio* $\hat{i}_{bL}/\hat{i}_{b}$ *is 0.55. The insulating coat does only reduce the amplitude of the measurable current, but* not *the amplitude of the "real" bearing current inside the bearing.*

7.5 Generation of High-Frequency Ground Currents

7.5.1 Lumped RLC-Circuit

The measured high frequency ground currents of inverter-supplied motors are almost sinusoidal, they are damped and have frequencies in the range of several 100 kHz. Waveforms of ground currents measured in the frame of the research project are summarized in Appendix F (p. 227). This motivates the use of a linear RLC-network to model the motor-cable configuration similar to what is done in [60] and [61]. In this model,

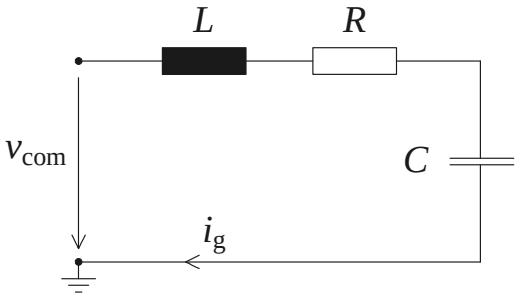

Figure 7.9: Lumped RLC circuit for modeling of high frequency ground currents [60], [61]

▷ L is related to the cable only,

▷ R is related to the motor only and

▷ C is also related to the motor only. C is identified as a capacitance between stator winding and frame, which may differ from the capacitance C_{wf} as defined above (→ Section 1.4, p. 8).

The model is used in [60], [61] to predict the reduction of the ground current when a common mode choke is used. It implies that i_g is not a conduction current, but a mere displacement current. Other authors (e.g. [46], [47]) model the motor as a single lumped capacitance, but those publications only offer a general approach to transient effects *outside* the motor and not to the ground current formation inside the motor (→ Section 7.2).

A relationship between the dv_{Lg}/dt of the line-to-earth voltage at the motor terminals v_{Lg} and the stator winding-to-frame capacitance C_{wf} is derived from such a model (7.65).

$$i_g = \frac{dv_{Lg}}{dt} C_{wf} \tag{7.65}$$

Fig. 7.10 shows the measured and calculated stator ground currents using (7.65) for both motors of the 11 kW, 110 kW and 500 kW power level and motor supply with 10 m unshielded cable and inverters I11a, I110a and I500 respectively. The *calculated and measured values are quite different* for motors M110b and M500a, whereas for the other motors the calculation results match quite well. When comparing the calculated results for the two motors of the 11 kW and 110 kW power level respectively, the motors with an equal or *smaller stator winding-to-frame capacitance* (→ Table 7.2, motors M11b and M110b) have a *larger* amplitude of the stator ground current although the dv_{Lg}/dt is equal or smaller (→ Appendix G, p. 229). At the 500 kW power level, the difference in the calculated ground currents is not the same as in the measured ones. Hence, (7.65) *is only reliable for a rough estimate of the stator ground current.*

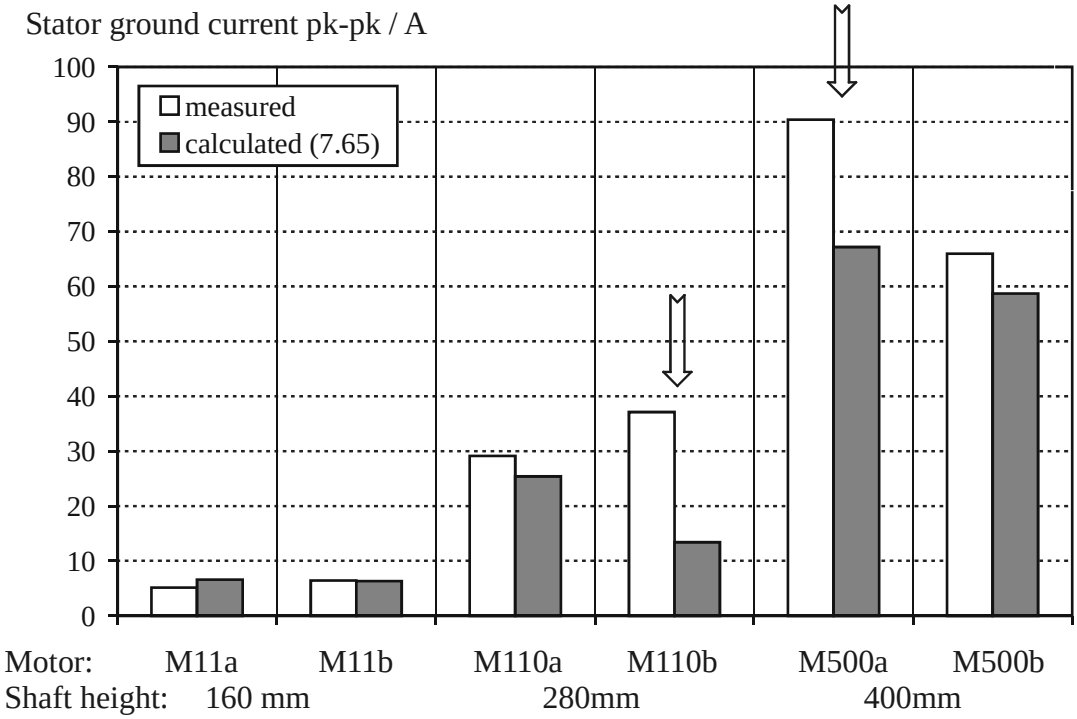

Figure 7.10: Comparison of measured and calculated stator ground currents for three different motor sizes, inverters I11a, I110a and I500 respectively, configuration $E1_{10}$ (l_c = 10 m, unshielded cable), n = 15 /min. Note that in this configuration the stator ground current equals the common mode current.

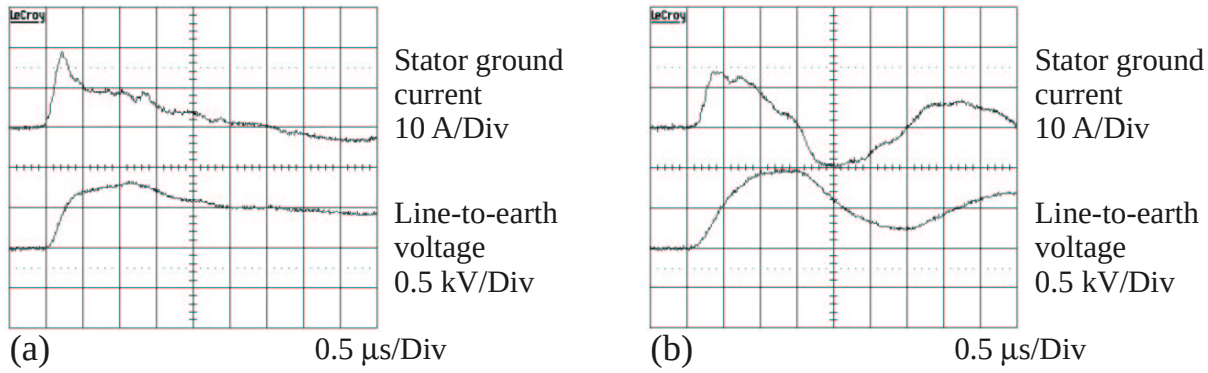

Figure 7.11: Measured stator ground current and line-to-earth voltage, inverter I110a, motor speed n = 1500 /min, configuration $E1^*_{80}$ (l_c = 80 m, shielded cable) (a) induction motor M110a, (b) induction motor M110b. Note that in this configuration the stator ground current equals the common mode current.

Fig. 7.11 shows two measured waveforms of the ground current i_g along with the line-to-earth voltage at the motor terminals v_{Lg} for the 110 kW power level. If i_g was a merely capacitive current, it would be about constant along the rise of v_{Lg}. However, i_g reaches its maximum value before v_{Lg} reaches its maximum value. This observation is also true for almost all the other investigated configurations. Therefore, *inductive elements in the path of the common mode current inside the machine cannot be neglected.*

7.5.2 Problem Formulation: Distributed Parameter Network

A distributed-parameter network is used to model the generation of high frequency ground currents based on the dv_{Lg}/dt of the line-to-earth voltage v_{Lg} at the motor terminals. The model is based on the design parameters of the machines under consideration and *does not require measurement of the motor impedance over a wide frequency range* (→ Section 7.2).

The superposition of ground currents resulting from two switching instants of the IGBT-inverters at different phases is not considered, as the time-lag T_{c} between two switching instants is larger than the characteristic time constant of the ground current. For example, if the time-lag T_{c} between the switching instants of the three phases is assumed to be the same, at switching frequency $f_{\mathrm{c}} = 3$ kHz the time-lag values $T_{\mathrm{c}} = (\frac{1}{3}\ \frac{1}{3 \cdot 10^3}\ \mathrm{s} =)$ 0.11 ms, whereas the characteristic time constant of the ground current is typically in the range of some 10 μs.

The definition of the common mode voltage (1.1) (p. 7) is used as a starting point for the description of the problem. The line-to-earth voltages v_{ug}, v_{vg} and v_{wg} in (1.1) (p. 7) are replaced by the product of the phase currents i_{u}, i_{v} and i_{w} and a phase impedance Z_{ph} to be determined. The phase impedance is assumed to be the same for all three phases (7.66). Hence, the common mode current can be computed from the line-to-earth voltage at the motor terminals (Fig. 7.12). Here, the *common mode current is the overall ground current*. If no other current paths exist except for the grounding connection of the stator exist, this current equals the stator ground current.

$$v_{\mathrm{com}} = \frac{v_{\mathrm{ug}} + v_{\mathrm{vg}} + v_{\mathrm{wg}}}{3} = \frac{i_{\mathrm{u}} Z_{\mathrm{ph}} + i_{\mathrm{v}} Z_{\mathrm{ph}} + i_{\mathrm{w}} Z_{\mathrm{ph}}}{3} = \frac{i_{\mathrm{com}}}{3}\ Z_{\mathrm{ph}} \tag{7.66}$$

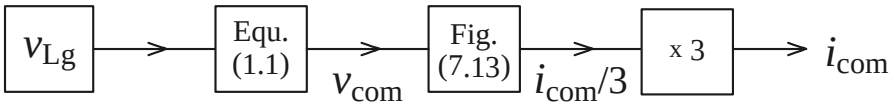

Figure 7.12: Flowchart of model for generation of high frequency ground currents

In order to determine the phase impedance Z_{ph}, first, the frequency range of the ground currents is considered. The ground currents are almost sinusoidal with oscillating frequencies in the range of several 100 kHz and a damping time constant of a few periods. However, the first rise is very steep, with rise times of typically (200...500) ns. Using (7.1) (p. 111), this corresponds to frequencies of $f = (\frac{1}{\pi 0.2 \mu \mathrm{s}} =)$ 1.6 MHz to $f = (\frac{1}{\pi 0.5 \mu \mathrm{s}} =)$ 640 kHz. Therefore, *the parameters of the model are identified for a frequency of 1 MHz.*

Each phase of a machine consists of $2p$ poles, each comprising q coils. The individual poles of one phase can be connected in series or parallel. Hence, the total number of coils in series q_{series} of one phase is given by (7.67).

$$q_{\text{series}} = q\frac{p}{a} \tag{7.67}$$

where:

q_{series} = number of coils in series per phase,
q = number of slots per pole and phase,
p = number of pole pairs,
a = number of parallel winding branches.

In the model, the *number of segments (a) in series equals the number of coils in series* q_{series} *of the modeled machine, where each segment (a) represents one coil.* The model is built from the distributed network of q_{series} segments, *a parts in parallel to consider the overall phase.* One segment of different type, *segment (b), is added to consider the parameters of the path of the common mode current that are not related to a specific coil* (Fig. 7.13). The segments are explained in detail in the following.

7.5.3 Coil Model

Two different circuits are used as segments for the distributed-parameter network (Fig. 7.14). The first circuit, resulting in segment (a), is used to represent an individual coil of the machine. The second circuit, giving segment (b), is associated to components of the path of the ground current that are not related to a specific coil.

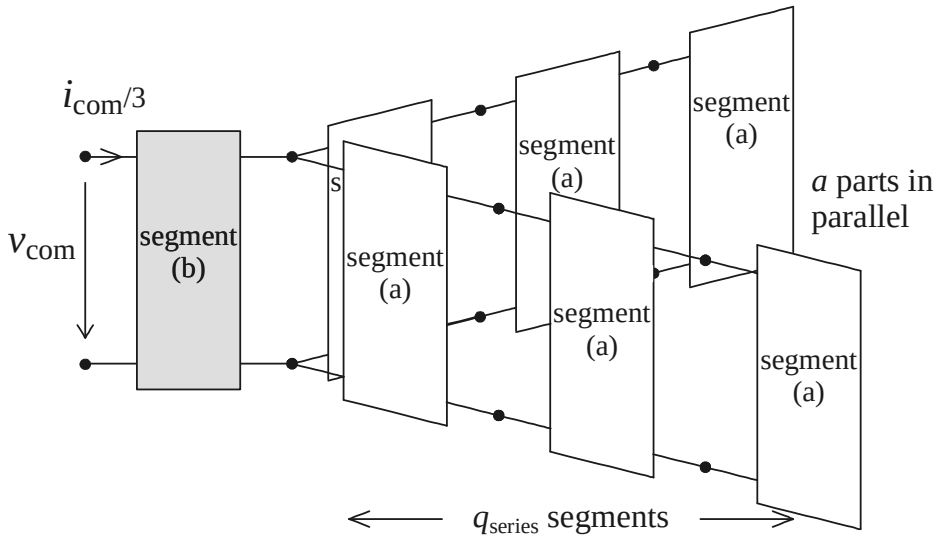

Figure 7.13: Sketch of distributed-parameter network for modeling of high frequency ground current generation

1. First, the elements of segment (a) that are associated to parameters of the coils of a machine are discussed.

▶ The ***case capacitance*** $\boldsymbol{C_c}$ and ***series capacitance*** $\boldsymbol{C_s}$ account for the capacitive behavior in the frequency range considered, where the current paths are not only determined by the conducting wires, but also by the capacitive coupling between the individual wires among each other and between the wires and the frame. The *case capacitance* C_c represents the stator winding-to-frame capacitance per coil, and the *series capacitance* C_s the mutual capacitance between the individual windings of one coil.

The *value of the case capacitance* C_c is derived from measurements, using the measured values of the stator winding-to-frame capacitance per phase C_{wf} and the number of stator slots per phase $Q_s/3$ (7.68).

The *value of the series capacitance* C_s is calculated using an equation proposed by [45] that considers the sum of the wire diameters per slot $N_c/q \cdot d_{wire}$, the length of a winding per turn l_{wire}/N_c and the length of a winding per coil l_{wire}/q, where l_{wire} is the total length of the winding of one phase (7.69).

$$C_c = 2\,\frac{C_{wf}}{Q_s/3} \tag{7.68}$$

$$C_s = 7.3 \cdot 10^{-3}\,\left(\frac{N_c/q \cdot d_{wire}}{\text{mm}} \cdot \frac{l_{wire}/N_c}{\text{m}}\right)^{1.25}\,\frac{1}{\frac{l_{wire}/q}{m}},\ C_s \text{ in nF} \tag{7.69}$$

where:

C_{wf} = measured stator winding-to-frame capacitance,
Q_s = number of stator slots,
N_c = number of turns per coil,
d_{wire} = wire diameter,
l_{wire} = length of winding per phase,
l_{wire}/N_c = length of winding per turn,
l_{wire}/q = length of winding per coil.

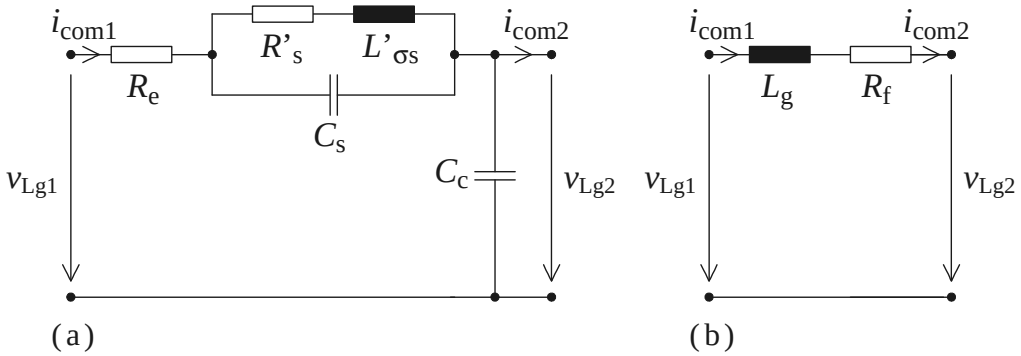

Figure 7.14: Segments of the distributed-parameter network representing (a) one coil of a machine, (b) part of the ground current path not related to an individual coil

▶ The **parameter $L'_{\sigma s}$** represents the inductance of the stator winding per coil that acts in parallel to the series capacitance C_s. This inductance corresponds to the (approximated) stator leakage inductance per coil at 1 MHz frequency. Only the stator leakage inductance is considered, as the high frequency flux is confined to the stator [50], [62]. This can be understood as follows:

For an induction machine, the slip s_ν of a current harmonic ν, where $\nu >> 1$, is about $s_\nu \approx 1$ (7.70). Hence, for the harmonic ν, the machine is at standstill and the magnetizing inductance is short-circuited by the rotor leakage inductance and the rotor resistance.

$$s_\nu = \frac{\nu\omega_s/p - \Omega_m}{\nu\omega_s/p} = 1 - \frac{1}{\nu}(1-s) \approx 1 \tag{7.70}$$

where:

s_ν = slip of fundamental wave, exited by current harmonic ν,
ω_s/p = synchronous speed,
Ω_m = rotational speed of the rotor.

Next, a simplified equivalent circuit of capacitances of a machine at high frequencies as described in Section 1.4 (p. 8) is considered. The capacitance in parallel to the stator winding-to-frame capacitance C_{wf} is given by the series connection of the stator winding-to-rotor capacitance C_{wr} and the sum of rotor-to-frame capacitance C_{rf} and bearing capacitance C_b (Fig. 7.15). Considering the ratios of the capacitances as identified in Section 7.3 (p. 112), *the contribution of the rotor to the generation of the high frequency ground current is negligible* (7.71).

$$\begin{aligned}
\frac{i_{1g}}{i_{2g}} &= \left(\frac{1}{C_{wr}} + \frac{1}{C_{rf} + 2\,C_b}\right) \Big/ \frac{1}{3\,C_{wf}} \\
&\approx \left(\frac{1}{C_{wr}} + \frac{1}{15\,C_{wr} + 2\,C_{wr}}\right) \Big/ \frac{1}{3\,C_{wf}} \approx \frac{0.94}{C_{wr}} \Big/ \frac{1}{3\,C_{wf}} \\
&= 2.8\,\frac{C_{wf}}{C_{wr}} < 2.8 \cdot 10 = 28
\end{aligned} \tag{7.71}$$

As a consequence, *only the stator leakage inductance $L_{\sigma s}$ is considered to model the generation of high frequency ground currents.*

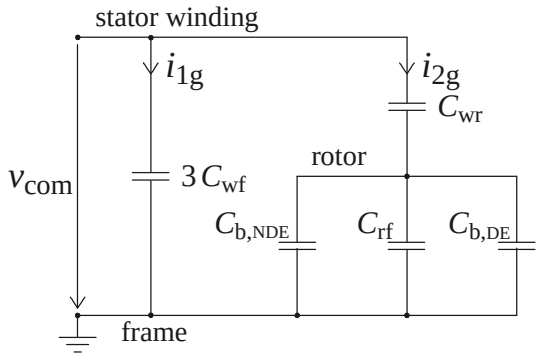

Figure 7.15: Parallel current paths in stator and rotor for generation of high frequency ground currents ($C_{b,NDE} = C_{b,DE} = C_b$)

The *value of the parameter* $L'_{\sigma s}$ *is derived as follows*: The stator leakage inductance $L_{\sigma s}$ as given in the equivalent circuit diagram for fundamental frequency comprises three components:

▷ $L_{\sigma s,sl}$: stator slot leakage inductance,

▷ $L_{\sigma s,ew}$: stator end-winding leakage inductance,

▷ $L_{\sigma s,k}$: stator harmonic leakage inductance.

The influence of frequency on the three components is discussed for each leakage inductance individually.

▷ $\boldsymbol{L_{\sigma s,sl}}$: The slot leakage inductance at 1 MHz frequency is calculated using formulas given in [63]. Considered are N_{sl} conductors one upon the other that all carry the same current. Here, several conductors arranged side by side in a slot can be considered as one conductor where $b_{s,cu}$ is the width of all conductors together.

The parameter α_s represents the inverse of the skin depth δ_s (7.72) that accounts for the slot aspect ratio (7.73). The height ratio of the winding β is defined using α_s and the height of one conductor $h_{s,cu}$ (7.74). The parameter k_x gives the decrease of the slot leakage inductance at ac-, as compared to dc-operation. It is a function of β and the number of conductors upon each other N_{sl} (7.75), where the functions $\varphi'(\beta)$ and $\psi'(\beta)$ are given by (7.76) and (7.77) respectively. For $\beta > 2$, (7.76) and (7.77) simplify to (7.77) and (7.78).

$$\delta_s = \sqrt{\frac{1}{\pi f \mu_0 \kappa}\frac{b_{s,cu}}{b_s}} \tag{7.72}$$

$$\alpha_s = \sqrt{\pi f \mu_0 \kappa \frac{b_{s,cu}}{b_s}} \tag{7.73}$$

$$\beta = \alpha_s h_{s,cu} \tag{7.74}$$

$$k_x = \frac{\varphi'(\beta) + \psi'(\beta)(N_{sl}^2 - 1)}{N_{sl}^2} \tag{7.75}$$

$$\varphi'(\beta) = \frac{3(\sinh(2\beta) - \sin(2\beta))}{2\beta(\cosh(2\beta) - \cos(2\beta))} \tag{7.76}$$

$$\psi'(\beta) = \frac{\sinh(\beta) + \sin(\beta)}{\beta(\cosh(\beta) + \cos(\beta))}$$

$$\beta > 2\text{: } \varphi'(\beta) \approx \frac{3}{2\beta} \tag{7.77}$$

$$\beta > 2\text{: } \psi'(\beta) \approx \frac{1}{\beta} \tag{7.78}$$

where:

δ_s = skin depth,

μ_0 = permeability of vacuum,

$b_{s,cu}$ = width of copper in stator slot,

b_s = stator slot width.

h_s = conductor height.

The values of the parameters discussed in (7.73) to (7.78) at 1 MHz frequency are calculated for the test motors of the 11 kW, 110 kW and 500 kW power level. As a result, *the value of k_x is below 0.001 for all motors. The slot leakage inductance at 1 MHz frequency is reduced to a negligible small value.*

▷ $\boldsymbol{L_{\sigma s,ew}}$: The value of the end-winding leakage of a machine depends on the form of the end-winding. Mostly, the value of the end-winding leakage used for calculations is deduced from experimentally obtained data. The exact calculation of the flux distribution in the end-winding is complicated, because the effect of the adjacent coils and phases on each other and the neighboring iron parts have to be considered. For the presented context, *it is assumed that the end-winding leakage flux does not change significantly with the frequency*, because the winding is not embedded in iron.

▷ $\boldsymbol{L_{\sigma s,k}}$: The harmonic leakage accounts for the voltage drop in the winding due to air-gap field space harmonics. The space harmonics result from the non-sinusoidal flux distribution along the circumference of the air gap that is due to the finite number of slots. At 1 MHz frequency, the flux is confined to the stator slot and does not cross the air gap. Therefore, no voltage drop due to harmonics resulting from the flux distribution in the air gap is considered. *This part of the stator leakage inductance is considered to be negligible at 1 MHz.*

As a result, the *stator leakage inductance at 1 MHz $L_{\sigma s}(1\text{ MHz})$ is approximated only by $L_{\sigma s,ew}$, which is about one third of the stator leakage inductance per phase at fundamental frequency $L_{\sigma s}$* (7.79). Therefore, the parameter $L'_{\sigma s}$, which is the inductance $L_{\sigma s}(1\text{ MHz})$ per coil, is given by (7.80).

$$L_{\sigma s}(1\text{ MHz}) = \frac{1}{3}\, L_{\sigma s} \tag{7.79}$$

$$L'_{\sigma s} = \frac{1}{3}\, \frac{L_{\sigma s}}{q_{\text{series}}} a \tag{7.80}$$

► The **parameter $\boldsymbol{R'_s}$** represents the resistance of the stator winding per coil at 1 MHz frequency. The increase of the resistance with frequency was calculated using again formulas given in [63]. Here, for the part of the winding that is embedded in the slot, a parameter k_r is introduced that gives the increase of the resistance of the stator winding at ac-, when compared to dc-operation, using the parameters α_s and β as defined in (7.73) and (7.74). The value of k_r is given in (7.81), where the functions $\varphi(\beta)$ and $\psi(\beta)$ are given by (7.82) and (7.83) respectively. For $\beta > 2$, (7.82) and (7.83) simplify to (7.83) and (7.84), hence (7.81) simplifies to (7.85).

$$k_\mathrm{r} = \varphi(\beta) + \psi(\beta)(\frac{N_\mathrm{sl}^2 - 1}{3}) \tag{7.81}$$

$$\varphi(\beta) = \beta \, \frac{\sinh(2\beta) + \sin(2\beta)}{\cosh(2\beta) - \cos(2\beta)} \tag{7.82}$$

$$\psi(\beta) = 2\beta \, \frac{\sinh(2\beta) - \sin(2\beta)}{\cosh(2\beta) + \cos(2\beta)}$$

$$\beta > 2\text{: } \varphi(\beta) \approx \beta \tag{7.83}$$

$$\beta > 2\text{: } \psi(\beta) \approx 2\beta \tag{7.84}$$

$$\beta > 2\text{: } k_\mathrm{r} \approx \beta\frac{2N_\mathrm{sl}^2 + 1}{3} \tag{7.85}$$

The increase of the resistance of the winding overhang is calculated according to (7.86), which is also given in [63].

$$k_\mathrm{rw} = 1 + 0.005 N_\mathrm{cu}(\frac{d_\mathrm{wire}}{cm})^4(\frac{f}{50})^2 \tag{7.86}$$

where:

N_cu = number of wires with diameter d_wire,

d_wire = diameter of winding.

As a result, the *stator resistance per coil at 1 MHz* R'_s *is about 500 times larger than the resistance at fundamental frequency per coil* $R_\mathrm{s}a/q_\mathrm{series}$ (7.87).

$$R'_\mathrm{s} = 500\frac{R_\mathrm{s}}{q_\mathrm{series}}a \tag{7.87}$$

▶ The **parameter R_e** is an auxiliary parameter that does not have a physical meaning. This external resistance is added to avoid infinite current following a voltage pulse with lim $dv/dt \to \infty$. The resistance R_e is set constant to a very small value of 1 mΩ. Thus, the resistance R_e is negligible when compared with the other elements of the equivalent circuit and does not affect the simulation results significantly.

2. Next, the parameters of segment (b) are explained. These parameters are associated with components of the path of the ground current and are not assigned to a specific coil.

▶ The **parameter R_f** signifies the damping of the ground current due to the motor frame resistance, including skin effect. Analytical calculation of the resistance of the path of the common mode current through the stator lamination is derived in Section 7.7.1 and is in the order of a 0.1Ω to a few Ω. However, the motor frame resistance is not calculated from design parameters, as calculation is not possible with rather simple means and exceeds the scope of the presented research. According to [61], this resistance

Motor	M11a	M11b	M110a	M110b	M500a	M500b
C_{wf}	1.9 nF	1.9 nF	12.1 nF	9.9 nF	28.0 nF	23.0 nF
p	4	4	4	4	6	2
a	1	2	1	2	3	1
C_{c}	0.238 nF	0.317 nF	1.008 nF	0.990 nF	2.333 nF	2.875 nF
C_{s}	1.107 nF	2.157 nF	3.051 nF	3.935 nF	7.523 nF	4.516 nF
$L_{\sigma\mathrm{s}}$	6.7 mH	9 mH	0.77 mH	0.82 mH	0.25 mH	0.82 mH
$R_{\mathrm{s}}(100°\mathrm{C})$	1.993 Ω	1.551 Ω	0.046 Ω	0.061 Ω	0.021 Ω	0.008 Ω
$L'_{\sigma\mathrm{s}}q_{\mathrm{series}}/a$ (7.80)	2.233 mH	3.0 mH	0.257 mH	0.273 mH	0.083 mH	0.273 mH
$R'_{\mathrm{s}}q_{\mathrm{series}}/a$ (7.87)	996.6 Ω	775.5 Ω	22.8 Ω	30.7 Ω	10.3 Ω	4.1 Ω
L_{g}(1 MHz) (7.105)	0.043 μH	0.042 μH	0.111 μH	0.116 μH	0.122 μH	0.231 μH
R_{f} (7.88)	20 Ω					

Table 7.15: Values of the parameters of the distributed-parameters network for the test motors of the 11 kW, 110 kW and 500 kW power level

values some tens Ω, which was obtained empirically. Therefore, the value of R_{f} is set constant (7.88).

$$R_{\mathrm{f}} = 20\ \Omega \tag{7.88}$$

▶ The **parameter $\boldsymbol{L_{\mathrm{g}}}$** represents the internal inductance of the path of the ground current through the stator lamination (7.105) (→ Section 7.6).

▶ ▶ ▶ Table 7.15 summarizes the values of the different parameters for the test motors of the 11 kW, 110 kW and 500 kW power level.

7.5.4 Simulated ground currents

The distributed-parameter model is implemented into the simulation program *MATLAB SIMULINK* (Fig. 7.12, Fig. 7.13, Fig. 7.14, Fig. 7.16). Measured waveforms of the dv_{Lg}/dt at the motor terminals are converted from the storage format of the scope for use as input to *MATLAB SIMULINK*.

Fig. 7.17 to Fig. 7.21 show simulation results for each of the two motors of the 11 kW, 110 kW and 500 kW power level. Generally, *the shape of the waveforms compare well with the measured ground currents* as they are also summarized in Appendix F (p. 227). Differences are supposed to be due to aspects that are not considered in the model, which are notably cross-coupling between the different phases and between the different coils in the winding overhang. Furthermore, the cable is not included, resulting in differences in the oscillating behavior of the ground current. In addition to this, the waveforms of the dv_{Lg}/dt at the motor terminals are subject to a certain variation. As voltage and current were not measured at the same time, voltage used for simulation and "real" voltage for measured current (→ Appendix F, p. 227) might have differed.

However, the simulation of the first current peak is achieved to a satisfying extent. Notable, *the model explains the difference of the amplitude of the ground current of the two motors of each power level. The motors with the larger ground current (motor* M11*b versus motor* M11*a, motor* M110*b versus motor* M110*a, motor* M500*a versus motor* M500*b) have a higher number of parallel winding branches a respectively* (Table 7.15). As the steep voltage rise at the motor terminals is attenuated as it travels through the coils, the more parallel winding branches the machine has, the larger part of the winding is submitted to the initial steep voltage rise.

The high-frequency ground current generation can be described by a distributed-parameter network that is based on design parameters of the machine.
For a given shaft height, the number of parallel winding branches has a strong influence on the amplitude of the ground current. As the steep voltage rise occurring at the motor terminals is attenuated as it travels through the winding, a larger part of the winding is submitted to the high frequency components of the voltage rise if the machine has more parallel winding branches.
Simulation of the oscillating behavior of the ground current requires consideration of the cable in the model.

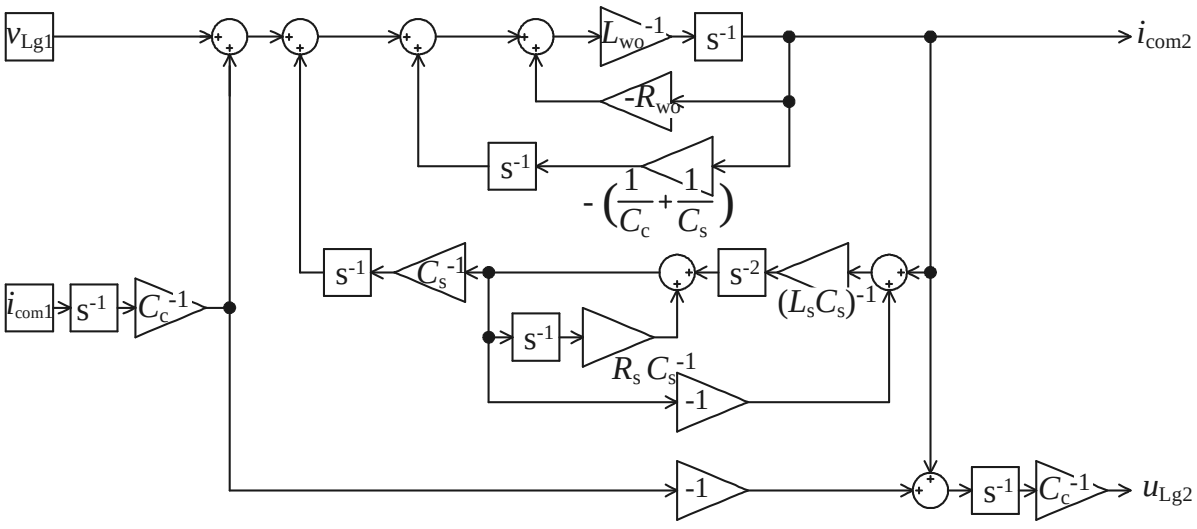

Figure 7.16: Simulation circuit in *MATLAB SIMULINK* for simulation of high frequency common mode ground current generation (segment (a))

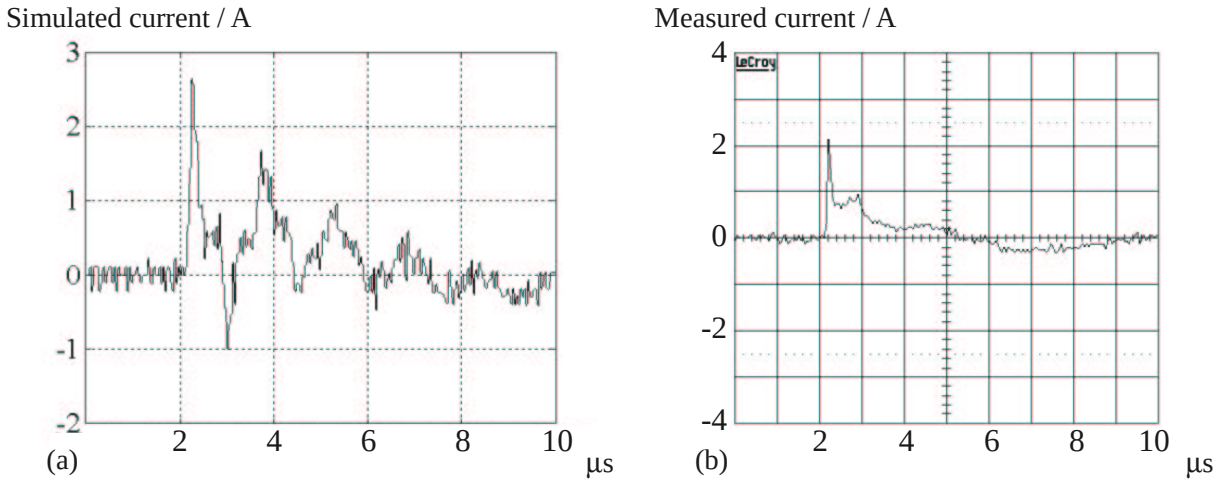

Figure 7.17: 11 kW power level, motor M11a - (a) simulated common mode current, (b) measured stator ground current, inverter I11a, E1*$_{50}$ (l_c = 50 m, shielded cable)

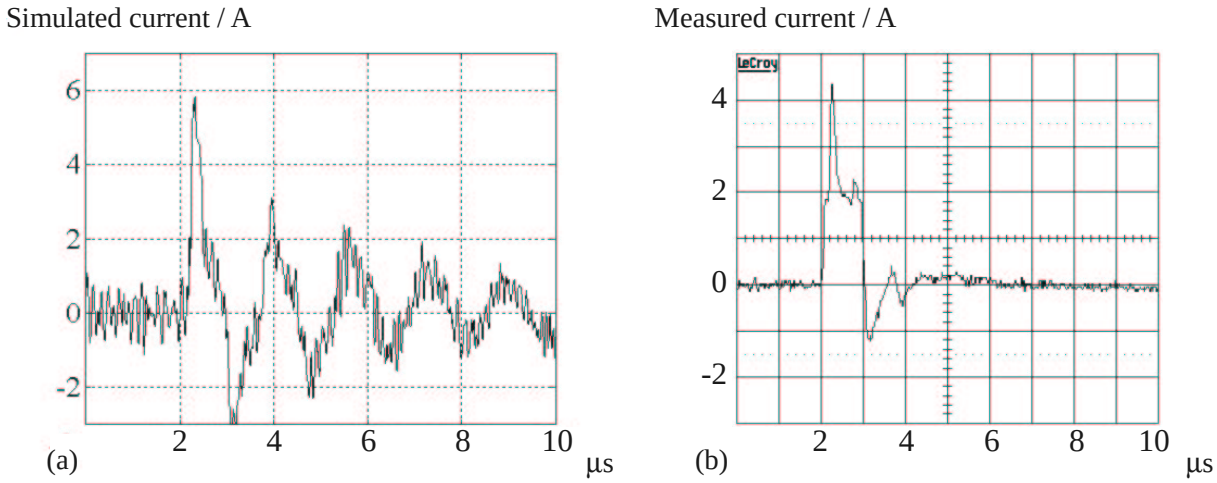

Figure 7.18: 11 kW power level, motor M11b - (a) simulated stator ground current, (b) measured stator ground current, inverter I11a, E1*$_{50}$ (l_c = 50 m, shielded cable)

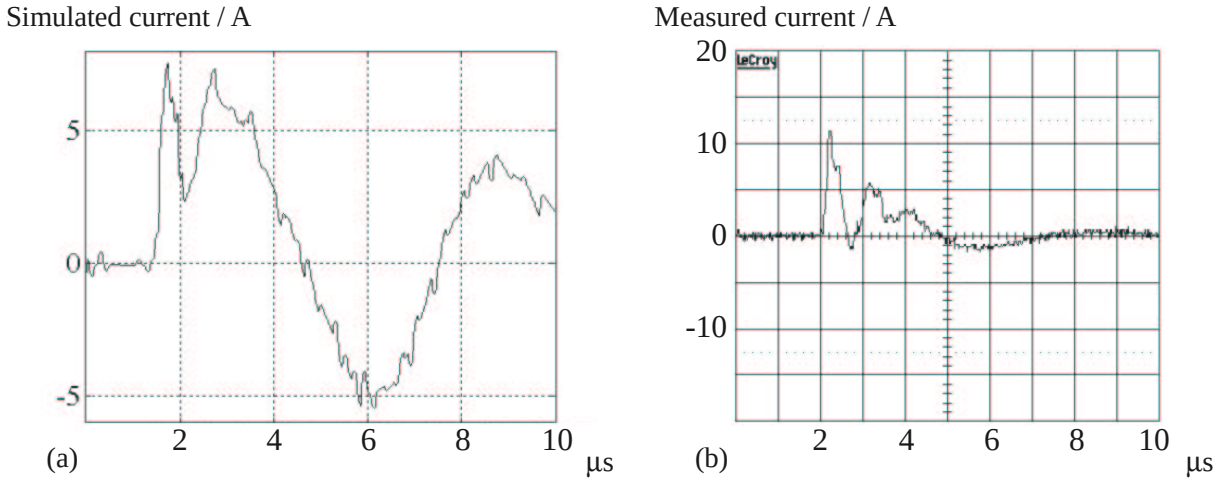

Figure 7.19: 110 kW power level, motor M110a - (a) simulated stator ground current, (b) measured stator ground current, inverter I110a, E1*$_{10}$ (l_c = 10 m, shielded cable)

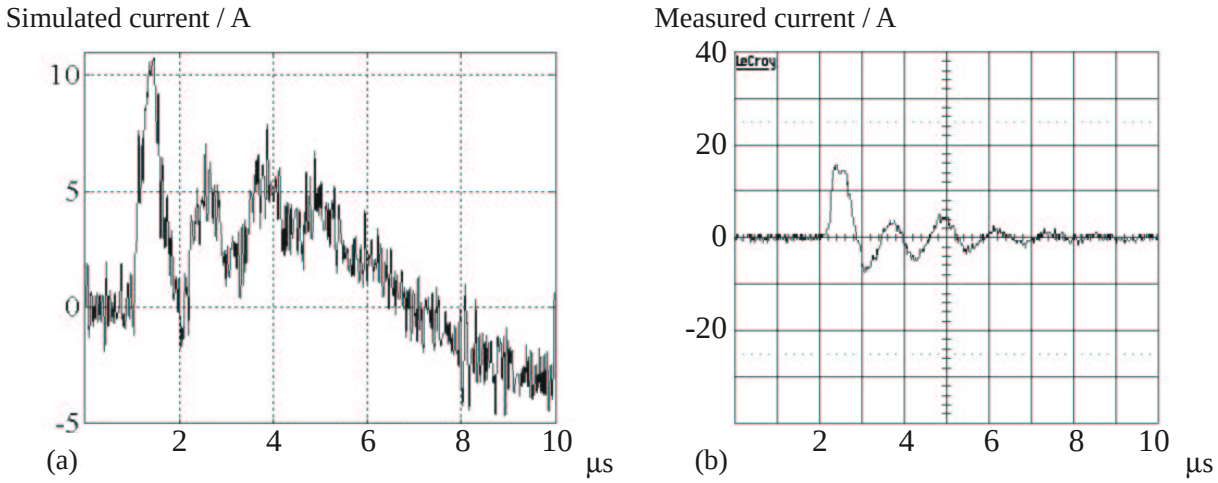

Figure 7.20: 110 kW power level, motor M110b - (a) simulated stator ground current, (b) measured stator ground current, inverter I110a, E1*$_{10}$ (l_c = 10 m, shielded cable)

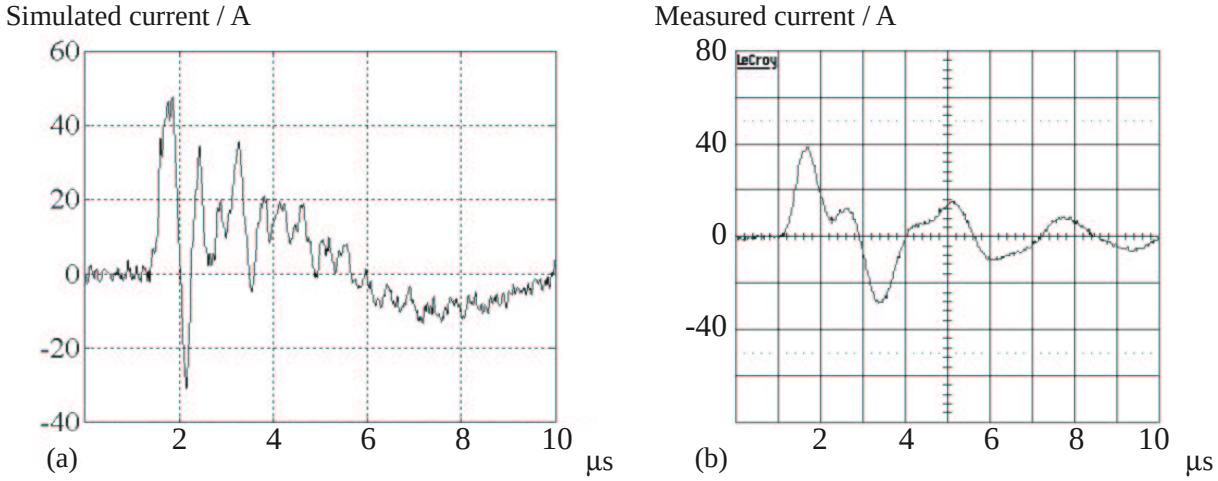

Figure 7.21: 500 kW power level, motor M500a - (a) simulated stator ground current, (b) measured stator ground current, inverter I500, E1*$_{10}$ (l_c = 10 m, shielded cable)

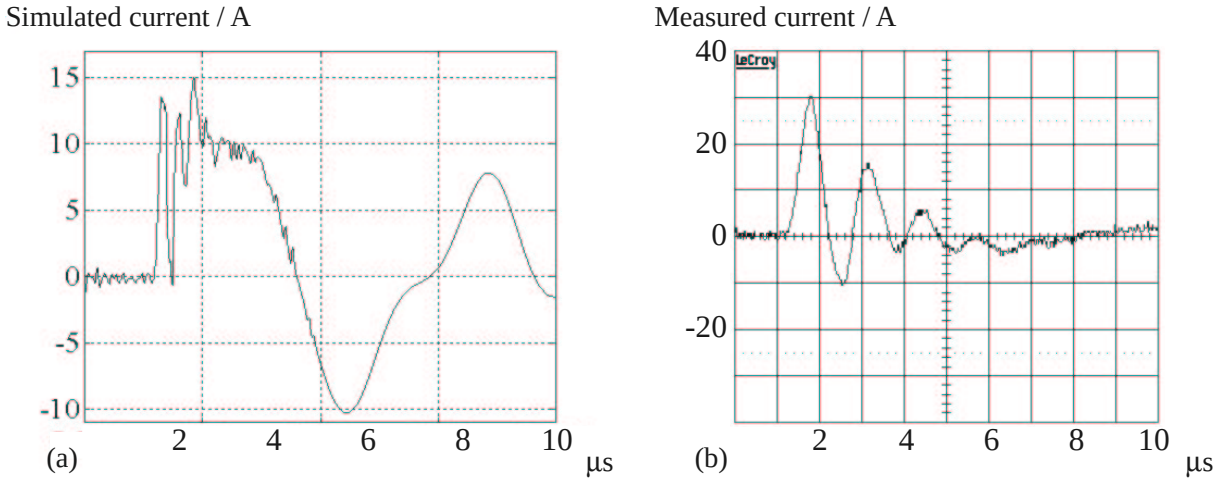

Figure 7.22: 500 kW power level, motor M500b - (a) simulated stator ground current, (b) measured stator ground current, inverter I500, E1*$_{10}$ (l_c = 10 m, shielded cable)

7.6 Calculation of Common Mode Ring Flux

7.6.1 Problem Formulation

The high frequency circulating bearing currents are induced by a circumferential flux ("ring flux"or "common mode flux") which is excited by the high frequency common mode current (→ Section 1.5, p. 10 and Fig. 1.10, p. 13). The common mode current enters the machine via the stator windings and leaves through the grounding connection(s) of the motor, thereby passing the stator stack lamination. Understanding of the generation of the common mode flux Φ_0 is essential for the comprehension of the circulating bearing current phenomenon. Important work in this field is reported in [64] and [65], and is used here as a starting point.

The current distribution in the stator lamination can be described by an eddy current model. In case of sinusoidal variation in time, the complex magnetic field strength $\underline{\vec{H}}$ can be computed from the complex, magnetodynamic partial differential equation (7.89).

$$\nabla \times \left(\frac{1}{\kappa} \nabla \times \underline{\vec{H}} \right) + j2\pi f \mu \underline{\vec{H}} = 0 \tag{7.89}$$

where:

$\underline{\vec{H}}$ = complex vector of magnetic field strength,
f = frequency,
μ = permeability,
κ = conductivity.

The stator lamination stack is represented by a 2D model with cylindrical symmetry, using the cylindrical coordinate system (r, φ, z). The common mode flux is supposed to flow in the azimuthal direction, i.e., $\underline{\vec{H}} = \big(0, \underline{H}_\varphi(r,z), 0\big)$. The current density has only an r- and a z-component, i.e., $\underline{\vec{J}} = (\underline{J}_r(r,z), 0, \underline{J}_z(r,z))$. Thanks to the cylindrical symmetry, derivatives with respect to the azimuthal direction vanish: $\frac{\partial}{\partial \varphi} = 0$. With these assumptions, (7.89) simplifies to (7.90).

$$-\frac{\partial}{\partial r}\left(\frac{1}{r}\frac{1}{\kappa}\frac{\partial \left(r\underline{H}_\varphi\right)}{\partial r} \right) - \frac{\partial}{\partial z}\left(\frac{1}{r}\frac{1}{\kappa}\frac{\partial \left(r\underline{H}_\varphi\right)}{\partial z} \right) + j2\pi f \mu \underline{H}_\varphi = 0 \tag{7.90}$$

The laminations of the stator stack are insulated from each other by a coating. It is assumed that the contact impedance between the laminations and the stator frame is very small and that the conductivity of the lamination sheets is significantly larger than the conductivity of the frame. Furthermore, it is supposed that the circumferential flux flows mainly in the cylindrical part of the stator lamination stack, the so-called stator iron back (or iron yoke). Therefore, *stator teeth and coil ends are excluded from the model.*

The eddy phenomenon can be simulated using *two models for an individual sheet, "model (a)", in which current enters from the stator slot and leaves through the stator housing* (Fig. 7.23a), and *"model (b)", for which the current enters the sheet on one side from the stator housing and leaves at the other side through the stator housing* (Fig. 7.23b). The models differ only in the excitations which are applied as different boundary conditions. The field solution in one sheet with current flowing both from the winding and the neighboring sheet is given by superposition of the two models.

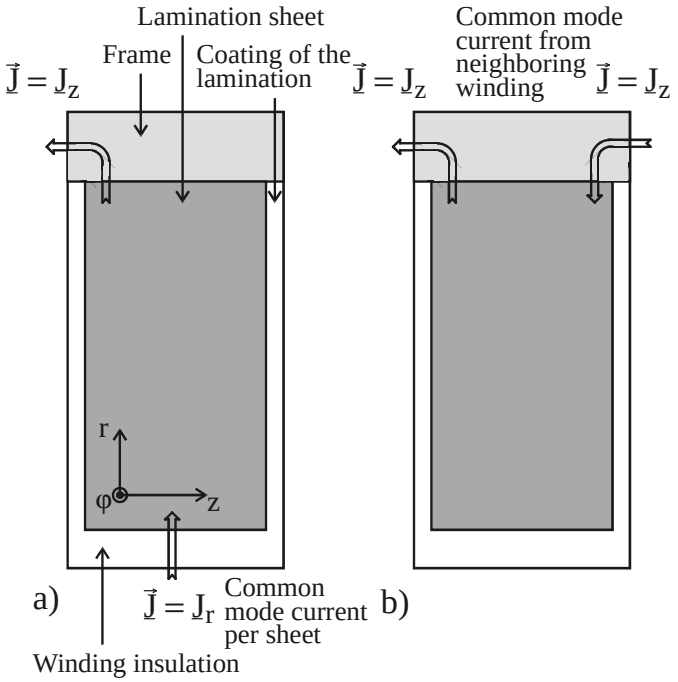

Figure 7.23: Sheet with (a) current flowing from the winding, and (b) current flowing from the neighboring sheet

The boundary of the model (Fig. 7.24) is divided into two types, insulated boundaries ("current walls") and boundaries where current leaves or enters the model ("current gates"). In the formulation (7.90), current gates correspond to homogeneous Neumann boundary conditions, i.e., $\frac{1}{\kappa}\frac{\partial \underline{H}_\varphi}{\partial n}$ where $\vec{n}$ is a vector normal to the boundary. Current walls correspond to Dirichlet boundary conditions where $2\pi r \underline{H}_\varphi$ is a constant. A prescribed current density $\underline{J}$ is applied at a current gate by assigning Dirichlet boundary conditions to the adjacent current walls such that the constants differ by the value of $\underline{I}$. To one of the current walls, a reference value of zero is assigned.

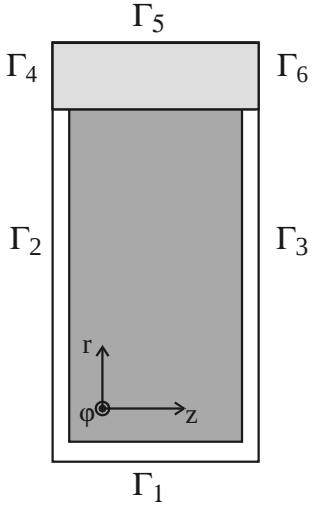

Figure 7.24: Boundaries for field solutions

The boundary conditions for model (a) are:

$$\begin{cases} \frac{1}{\kappa}\frac{\partial \underline{H}_\varphi}{\partial r} = 0 & \text{at } \Gamma_1 \cup \Gamma_4 \\ 2\pi r \underline{H}_\varphi = 0 & \text{at } \Gamma_3 \cup \Gamma_5 \cup \Gamma_6 \\ 2\pi r \underline{H}_\varphi = i_{\text{com,sheet}} & \text{at } \Gamma_2 \end{cases} \tag{7.91}$$

The boundary conditions applied to model (b) are:

$$\begin{cases} \frac{1}{\kappa}\frac{\partial \underline{H}_\varphi}{\partial r} = 0 & \text{at } \Gamma_4 \cup \Gamma_6 \\ 2\pi r \underline{H}_\varphi = 0 & \text{at } \Gamma_5 \\ 2\pi r \underline{H}_\varphi = i_{\text{com}} & \text{at } \Gamma_1 \cup \Gamma_2 \cup \Gamma_3 \end{cases} \tag{7.92}$$

The potential $2\pi r\underline{H}_\varphi$ is discretized by finite elements at the considered computational domain. Fig. 7.25[1] shows the numerical field solutions of the individual lamination by the different excitations and their superposition [64].

For further calculation, the density of the common mode current as it enters the stator lamination stack from the stator winding is assumed to be homogeneous along the length of the stack length l_{Fe}. In fact, the dv/dt decreases along the phase winding (Section 7.2). Therefore, the flow of common mode current across the stator winding insulation into the lamination is not constant along the winding. However, averaging over one phase at a given distance from the end of the lamination stack into axial (z-)direction results in an approximately constant distribution of the common mode current along the stack length l_{Fe} (Fig. 7.26). Fig. 7.27[2] shows the numerical field solution in three sheets of the stator lamination [65].

7.6.2 Analytical Solution

♦ ***Solution of model (a)***: For frequencies of several 100 kHz, the skin depth δ_{s} (7.93) is less than 50 μm and is much smaller than the thickness of a lamination sheet b_{Fe} of typically 0.5 mm. In this case, the lamination can be described by an analytical model for a conducting half-plane, and the solution for model (a) (Fig. 7.25a) is given by (7.94). The phase lag of the magnetic field relative to the current depends on the distance z. Based thereon, using (7.95), the total magnetic flux of one sheet, $\Phi_{0,(\mathrm{a})}$, is computed, resulting in (7.96). The phase of the total magnetic flux lags 45°relative to the common mode current.

$$\delta_{\mathrm{s}} = \sqrt{\frac{2}{2\pi f\mu\kappa}} \tag{7.93}$$

$$\underline{H}_\varphi(r,z) = \hat{H}_\varphi \frac{d_{\mathrm{se}}}{2r} e^{-(1+j)z/\delta_{\mathrm{s}}} \tag{7.94}$$

$$\hat{H}_\varphi = \frac{i_{\mathrm{com,sheet}}}{\pi d_{\mathrm{se}}} \tag{7.95}$$

$$\begin{aligned}
\Phi_{0,(\mathrm{a})} &= |\mu \int_{\frac{d_{\mathrm{si}}}{2}+h_{\mathrm{s}}}^{\frac{d_{\mathrm{se}}}{2}} \int_0^\infty \underline{H}_\varphi(r,z)\mathrm{d}r\mathrm{d}z| = |\mu \int_{\frac{d_{\mathrm{si}}}{2}+h_{\mathrm{s}}}^{\frac{d_{\mathrm{se}}}{2}} \int_0^\infty \hat{H}_\varphi \frac{d_{\mathrm{se}}/2}{r} e^{-(1+j)z/\delta_{\mathrm{s}}}\mathrm{d}r\mathrm{d}z| \\
&= |\mu\hat{H}_\varphi \frac{d_{\mathrm{se}}}{2} \ln(\frac{d_{\mathrm{se}}/2}{d_{\mathrm{si}}/2+h_{\mathrm{s}}}) \frac{\delta_{\mathrm{s}}}{(1+j)}| = |\mu \frac{i_{\mathrm{com,sheet}}}{\pi d_{\mathrm{se}}} \frac{d_{\mathrm{se}}}{2} \ln(\frac{d_{\mathrm{se}}/2}{d_{\mathrm{si}}/2+h_{\mathrm{s}}}) \frac{\delta_{\mathrm{s}}}{(1+j)}| \\
&= \mu \frac{i_{\mathrm{com,sheet}}}{2\pi} \ln(\frac{d_{\mathrm{se}}/2}{d_{\mathrm{si}}/2+h_{\mathrm{s}}}) \frac{\delta_{\mathrm{s}}}{\sqrt{2}}
\end{aligned} \tag{7.96}$$

[1] Fig. 7.25 was provided and allowed for publication by courtesy of P. Maeki-Ontto and Prof. J. Luomi of Helsinki University of Technology.

[2] Fig. 7.27 was also provided and allowed for publication by courtesy of P. Maeki-Ontto and Prof. J. Luomi of Helsinki University of Technology. The figure was published by the authors in [65].

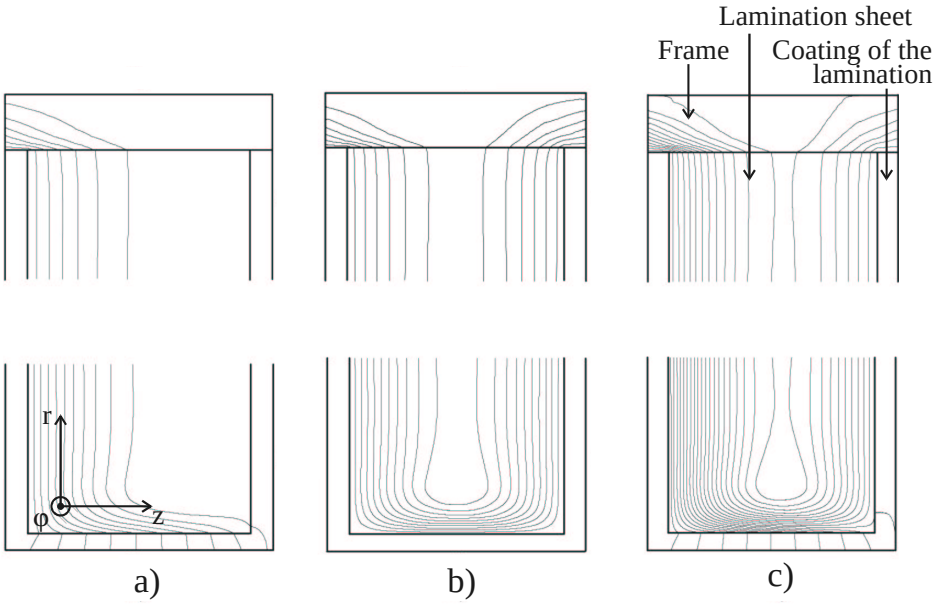

Figure 7.25: Numerical field solutions in a single sheet according to [64]: (a) current flow from the winding, (b) current flow from the neighboring sheet, (c) = (a) + (b) current flow from both the winding and the neighboring sheet. For clarity, only the upper and lower parts of the sheet are shown.

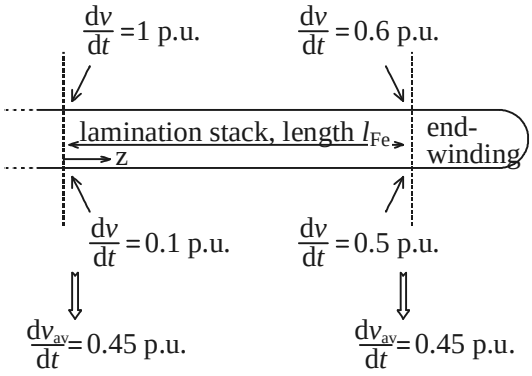

Figure 7.26: Sketch of one turn of stator winding and distribution of the dv/dt along the stack length

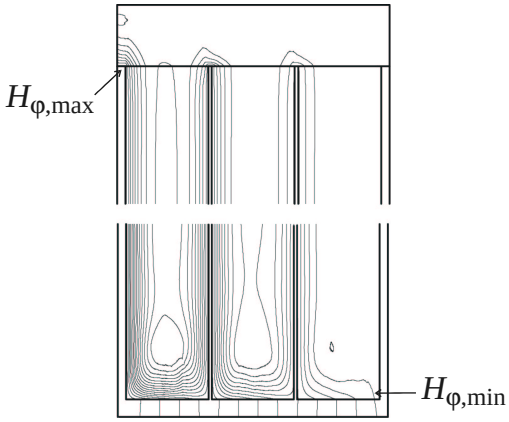

Figure 7.27: Computed current flow lines of absolute value of magnetic field strength $|\underline{\vec{H}}| = |\underline{H}_\varphi|$ in three sheets of the stator lamination for $f = 30$ kHz according to [65]. For clarity, only the upper and lower parts of the sheet are shown.

where:

d_{se}/d_{si} = stator lamination inner/outer diameter,

b_{Fe} = thickness of lamination sheet,

h_s = height of stator slot.

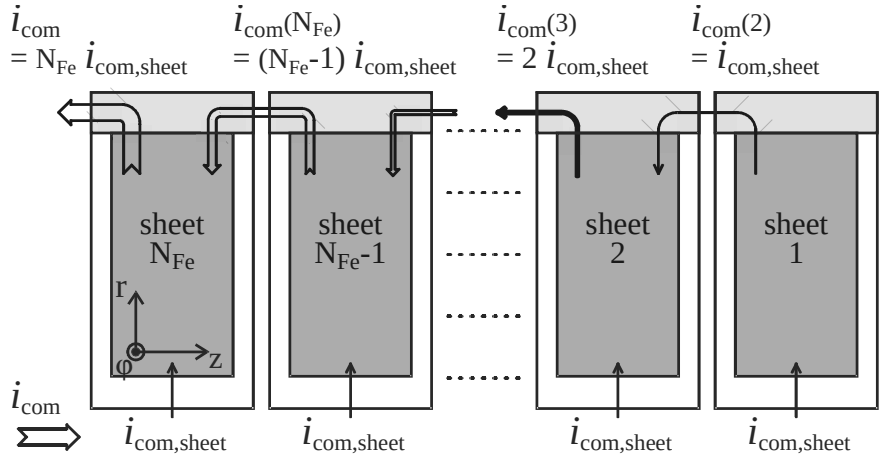

Figure 7.28: Common mode currents of individual sheets flowing from the stator winding (model (a)) and from the neighboring sheet (model (b))

♦ ***Solution of model (b)***: As the skin depth δ_s (7.93) is much smaller than the thickness of a lamination sheet b_{Fe}, the lamination can be described by an analytical model for two conducting half-planes in case of model (b). Therefore, for a single sheet, the solution of model (b) (Fig. 7.25b) is two times the solution of model (a) with the current $i_{com}(k)$ entering sheet k from the neighboring sheet $k-1$. Hence, the total magnetic flux of one sheet, $\Phi_{0,(b)}$, using (7.97), is given by (7.98).

$$\hat{H}_\varphi(k) = \frac{i_{com}(k)}{\pi d_{se}} \tag{7.97}$$

$$\Phi_{0,(b)} = \mu \frac{i_{com}(k)}{\pi} \ln\left(\frac{d_{se}/2}{d_{si}/2 + h_s}\right) \frac{\delta_s}{\sqrt{2}} \tag{7.98}$$

♦ The ***total common mode flux*** $\hat{\Phi}_0$ is the sum of the common mode flux of the individual sheets 1...k of models (a) and (b). The common mode current entering each sheet from the stator winding, $i_{com,sheet}$, is given by (7.99), the common mode current $i_{com}(k)$ entering sheet k from the neighboring sheet $k-1$ by (7.100) (Fig. 7.28), where N_{Fe} is the number of sheets of the stator lamination stack. The solutions of models (a) and (b) for all sheets (7.101) and (7.102) result in the solution for the total common mode flux (7.104), with N_{Fe} much larger than 1.

$$i_{com,sheet} = \frac{i_{com}}{N_{Fe}} \tag{7.99}$$

$$i_{com}(k) = (k-1)\frac{i_{com}}{N_{Fe}} \tag{7.100}$$

$$\Phi_{0,(a),sum} = \mu N_{Fe} \frac{i_{com,sheet}}{2\pi} \ln\left(\frac{d_{se}/2}{d_{si}/2 + h_s}\right) \frac{\delta_s}{\sqrt{2}} \tag{7.101}$$

$$\Phi_{0,(b),sum} = \mu \frac{\sum_{k=1}^{N_{Fe}} i_{com}(k)}{\pi} \ln\left(\frac{d_{se}/2}{d_{si}/2 + h_s}\right) \frac{\delta_s}{\sqrt{2}} \tag{7.102}$$

$$\begin{aligned}\sum_{k=1}^{N_{\mathrm{Fe}}} i_{\mathrm{com}}(k) &= \sum_{k=1}^{N_{\mathrm{Fe}}}(k-1)\frac{i_{\mathrm{com}}}{N_{\mathrm{Fe}}} = \frac{i_{\mathrm{com}}}{N_{\mathrm{Fe}}}\{\sum_{k=1}^{N_{\mathrm{Fe}}} k - \sum_{k=1}^{N_{\mathrm{Fe}}} 1\} \\ &= \frac{i_{\mathrm{com}}}{N_{\mathrm{Fe}}}\{\frac{N_{\mathrm{Fe}}(N_{\mathrm{Fe}}+1)}{2} - N_{\mathrm{Fe}}\} = \frac{i_{\mathrm{com}}}{N_{\mathrm{Fe}}}\{\frac{N_{\mathrm{Fe}}(N_{\mathrm{Fe}}-1)}{2}\} \qquad (7.103)\end{aligned}$$

$$\begin{aligned}\Phi_0 &= \mu N_{\mathrm{Fe}}\frac{i_{\mathrm{com}}/N_{\mathrm{Fe}}}{2\pi}\ln(\frac{d_{\mathrm{se}}/2}{d_{\mathrm{si}}/2+h_{\mathrm{s}}})\frac{\delta_{\mathrm{s}}}{\sqrt{2}} + \mu\frac{(N_{\mathrm{Fe}}-1)i_{\mathrm{com}}}{2\pi}\ln(\frac{d_{\mathrm{se}}/2}{d_{\mathrm{si}}/2+h_{\mathrm{s}}})\frac{\delta_{\mathrm{s}}}{\sqrt{2}} \\ &= \mu\frac{N_{\mathrm{Fe}}i_{\mathrm{com}}}{2\pi}\ln(\frac{d_{\mathrm{se}}/2}{d_{\mathrm{si}}/2+h_{\mathrm{s}}})\frac{\delta_{\mathrm{s}}}{\sqrt{2}} \qquad (7.104)\end{aligned}$$

7.6.3 Physical Properties of Common Mode Flux

As the common mode flux varies with time, it induces a voltage in the loop "stator frame - non drive end - shaft - drive end" (7.106) (Fig. 1.10, p. 13).

$$\frac{\hat{\Phi}_0}{\hat{i}_{\mathrm{com}}} = \mu_{\mathrm{r}}\mu_0\frac{N_{\mathrm{Fe}}}{2\pi}\ln(\frac{d_{\mathrm{se}}/2}{d_{\mathrm{si}}/2+h_{\mathrm{s}}})\frac{\delta_{\mathrm{s}}}{\sqrt{2}} \qquad (7.105)$$

$$\frac{\hat{v}}{\hat{i}_{\mathrm{com}}} = 2\pi f\frac{\Phi_0}{i_{\mathrm{com}}} = \mu_{\mathrm{r}}\mu_0 N_{\mathrm{Fe}} f\ln(\frac{d_{\mathrm{se}}/2}{d_{\mathrm{si}}/2+h_{\mathrm{s}}})\frac{\delta_{\mathrm{s}}}{\sqrt{2}} \qquad (7.106)$$

The number of sheets of the stator core stack N_{Fe} is proportional to the length of the stator core l_{Fe} that is proportional to the shaft height H of a machine (7.107). Furthermore, the stator winding-to-frame capacitance C_{wf} is proportional to the square of H (Section 7.3) and the common mode current is about proportional to C_{wf} (Section 7.5) (7.108).

$$N_{\mathrm{Fe}} \propto l_{\mathrm{Fe}} \propto H \qquad (7.107) \qquad i_{\mathrm{com}} \propto C_{\mathrm{wf}} \propto H^2 \qquad (7.108)$$

As $\delta_{\mathrm{s}} \propto 1/\sqrt{f\mu_{\mathrm{r}}}$, the common mode flux decreases with $1/\sqrt{f\mu_{\mathrm{r}}}$, resulting in (7.109) to (7.114):

$\Phi_0 \propto i_{\mathrm{com}} l_{\mathrm{Fe}} \propto H^3$	(7.109)	$v \propto i_{\mathrm{com}} l_{\mathrm{Fe}} \propto H^3$	(7.112)
$\Phi_0 \propto \sqrt{\frac{1}{f}}$	(7.110)	$v \propto \sqrt{f}$	(7.113)
$\Phi_0 \propto \sqrt{\mu_{\mathrm{r}}}$	(7.111)	$v \propto \sqrt{\mu_{\mathrm{r}}}$	(7.114)

Both common mode flux Φ_0 *and induced voltage* v increase with the *cube of the shaft height* H. The *frequency* f has an *inverse effect* on the two parameters: The *common mode flux decreases* and the *induced voltage increases* with the root of f. Both parameters increase with the root of the relative permeability μ_r.

Both shaft height H and frequency f can be measured, whereas the value of μ_r is determined by the large amplitude of the fundamental frequency field in the machine that varies with space and time. In [64] and [65] it is proposed to use an average value of μ_r to account for this biasing field ($\mu_\mathrm{r} = 100...1000$).

The following values were calculated for the test motors of the 11 kW, 110 kW and 500 kW power level (Table 7.16):

1. Ratio of amplitude of common mode flux $\hat{\Phi}_\mathbf{0}$ ***versus amplitude of common mode current*** $\hat{i}_\mathbf{com}$ ($\hat{\Phi}_0/\hat{i}_\mathrm{com}$),

2. Ratio of amplitude of induced voltage $\hat{v}$ ***versus amplitude of common mode current*** $\hat{i}_\mathrm{com}$ ($\hat{v}/\hat{i}_\mathrm{com}$),

3. Amplitude of the induced voltage $\hat{v}$ ***for a typical measured amplitude of common mode current*** $\hat{i}_\mathrm{com}$.

Three pairs of frequency f and relative permeability μ_r were chosen:

a) $f = 100$ kHz, $\mu_\mathrm{r} = 100$,

b) $f = 100$ kHz, $\mu_\mathrm{r} = 1000$,

c) $f = 1$ MHz, $\mu_\mathrm{r} = 1000$.

1. $\hat{\Phi}_0/\hat{i}_\mathrm{com} \propto \sqrt{\mu_\mathrm{r}/f}$:

The value of $\hat{\Phi}_0/\hat{i}_\mathrm{com}$ increases by the factor of $\sqrt{10} \approx 3.2$ from case a) to case b) according to $\sqrt{\mu_\mathrm{r,b)}/\mu_\mathrm{r,a)}} = \sqrt{10}$ and decreases accordingly by $\sqrt{\mu_\mathrm{r,c)}/\mu_\mathrm{r,b)}} = \sqrt{0.1} \approx 3.2^{-1}$ from case b) to case c).

Furthermore, the increase with motor size is noticeable. The two motors of the 11 kW and 110 kW power level have the same number of poles, therefore similar geometrical dimensions and about the same value of $\hat{\Phi}_0/\hat{i}_\mathrm{com}$. This is not the case for the two motors of the 500 kW power level: Motor M500a has six and motor M500b has two poles. Thus, the ratio of stator lamination outer and inner diameter d_se and d_si is larger for motor M500b than for motor Sie, resulting in a larger value of $\hat{\Phi}_0/\hat{i}_\mathrm{com}$.

2. $\hat{v}/\hat{i}_\mathrm{com} \propto \sqrt{\mu_\mathrm{r} f}$:

The ratio $\hat{v}/\hat{i}_\mathrm{com}$ increases by the factor of $\sqrt{10} \approx 3.2$ from case a) to case b), and case b) to case c), respectively. The influence of motor size and number of poles of the motors is the same as for the value of $\hat{\Phi}_0/\hat{i}_\mathrm{com}$ as discussed above.

Motor		M11a	M11b	M110a	M110b	M500a	M500b
$\hat{\Phi}_0/\hat{i}_{\mathrm{com}}$ ($f = 100$ kHz, $\mu_{\mathrm{r}} = 100$)	nWb/A	60.68	59.54	156.46	162.96	172.18	326.52
$\hat{\Phi}_0/\hat{i}_{\mathrm{com}}$ ($f = 100$ kHz, $\mu_{\mathrm{r}} = 1000$)	nWb/A	194.46	190.53	500.68	521.47	550.99	1044.86
$\hat{\Phi}_0/\hat{i}_{\mathrm{com}}$ ($f = 1$ MHz, $\mu_{\mathrm{r}} = 1000$)	nWb/A	60.68	59.54	156.46	162.96	172.18	326.52
$\hat{v}/\hat{i}_{\mathrm{com}}$ ($f = 100$ kHz, $\mu_{\mathrm{r}} = 100$)	V/A	0.0381	0.0374	0.0983	0.1024	0.1082	0.2052
$\hat{v}/\hat{i}_{\mathrm{com}}$ ($f = 100$ kHz, $\mu_{\mathrm{r}} = 1000$)	V/A	0.1220	0.1197	0.3146	0.3277	0.3462	0.6565
$\hat{v}/\hat{i}_{\mathrm{com}}$ ($f = 1$ MHz, $\mu_{\mathrm{r}} = 1000$)	V/A	0.3812	0.3741	0.9831	1.0239	1.0819	2.0516
$\hat{i}_{\mathrm{com}}$ (measured) (→ Chapter 4) p. 41)	A	3	4	19	24	60	40
$\hat{v}$ ($f = 100$ kHz, $\mu_{\mathrm{r}} = 100$)	V	0.11	0.15	1.87	2.46	6.49	8.21
$\hat{v}$ ($f = 100$ kHz, $\mu_{\mathrm{r}} = 1000$)	V	0.37	0.48	5.98	7.87	20.77	26.26
$\hat{v}$ ($f = 1$ MHz, $\mu_{\mathrm{r}} = 1000$)	V	1.14	1.50	18.68	24.57	64.91	82.06

Table 7.16: Calculated values of $\hat{\Phi}_0/\hat{i}_{\mathrm{com}}$, $\hat{v}/\hat{i}_{\mathrm{com}}$ and $\hat{v}$; $1/\kappa_{\mathrm{Fe}} = 25 \cdot 10^{-8}\ \Omega m$

3. $\hat{v} \propto \sqrt{\mu_{\mathrm{r}} f}\ \hat{i}_{\mathrm{com}}$:

As larger machines have larger common mode currents (7.108), the induced voltage increases with about the cube of the motor size (7.112). It has to be noticed that the *induced voltages* $\hat{v}$ of the two motors of the 500 kW power level are in *the same range*, even if the *values of* $\hat{\Phi}_{\mathrm{sh}}/\hat{i}_{\mathrm{g}}$ and $\hat{v}/\hat{i}_{\mathrm{g}}$ differ. As the ground current of motor M500a with the lower value of $\hat{v}/\hat{i}_{\mathrm{g}}$ is larger, the induced voltage is about the same as at motor M500b. Therefore, *no significant influence of the number of poles on the magnitude of the induced voltage is found.*

►►► ***The model explains the occurrence of circulating bearing currents for larger motors***: At the 11 kW power level, the calculated values of the induced voltage v are in the order of the threshold voltage $v_{\mathrm{b,th}}$ of the bearings. With an electric field strength of 15 V/μm [43] and minimum thickness of the lubricating film $h_{\mathrm{lb,min}}$ at low motor speed, $h_{\mathrm{lb,min}}(n = 15\ /\mathrm{min}) \leq\ 0.1\ \mu\mathrm{m}$, the value of $v_{\mathrm{b,th}}$ is $0.1\ \mu\mathrm{m} \cdot 15\ V/\mu\mathrm{m}\ =\ 1.5\ V$. At elevated motor speed, where the lubricating film is thicker, with $h_{\mathrm{lb,min}}(n = 3000\ /\mathrm{min}) \leq\ 1\ \mu\mathrm{m}$, the value of $v_{\mathrm{b,th}}$ is $1\ \mu\mathrm{m} \cdot 15\ V/\mu\mathrm{m}\ =\ 15\ V$.

This value is exceeded at the larger motors of the 110 kW and 500 kW power level. Therefore, the lubrication film does no longer have insulating properties and circulating bearing currents can flow in the loop "stator frame - non drive end - shaft - drive end".

The generation of the common mode flux can be described by an eddy current model. Both common mode flux and induced voltage increase with the cube of the motor size (shaft height). Therefore, circulating bearing currents dominate in case of large motors.

7.7 Circulating Bearing Currents

7.7.1 Mutual Inductance of Ground and Bearing Current Path

With the high-frequency ground current i_{g} causing the common mode flux Φ_0 that varies with time, thereby inducing a voltage v, and with the circulating bearing current flowing as a result of this voltage, the machine can be considered as a transformer. The ratio $\hat{i}_{\mathrm{b}}/\hat{i}_{\mathrm{g}}$ is given by the *compensation of the magnetomotive force of the two circuits*. Therefore, in a first step, *the mutual inductance L_{g} of the two circuits is calculated*.

Using (7.94) to (7.96) and the common mode flux that varies with time, the induced voltage $\underline{V}_{(\mathrm{a})}$ per sheet for model (a) is given by (7.115). Based on (7.115), a resistance due to eddy current distribution $R_{(\mathrm{a})}$ (7.116) and inductance $L_{(\mathrm{a})}$ (7.117) for model (a) can be defined.

$$\begin{aligned}
\underline{V}_{(\mathrm{a})} &= j\omega\underline{\Phi}_{0,(\mathrm{a})} \\
&= j\omega\mu\frac{\underline{I}_{\mathrm{com,sheet}}}{2\pi}\ln(\frac{d_{\mathrm{se}}/2}{d_{\mathrm{si}}/2+h_{\mathrm{s}}})\frac{\delta_{\mathrm{s}}}{2}(1-j) \\
&= \{\frac{\omega\mu}{2\pi}\ln(\frac{d_{\mathrm{se}}/2}{d_{\mathrm{si}}/2+h_{\mathrm{s}}})\frac{\delta_{\mathrm{s}}}{2} + j\frac{\omega\mu}{2\pi}\ln(\frac{d_{\mathrm{se}}/2}{d_{\mathrm{si}}/2+h_{\mathrm{s}}})\frac{\delta_{\mathrm{s}}}{2}\}\underline{I}_{\mathrm{com,sheet}} \\
&= \{R_{(\mathrm{a})} + j\omega L_{(\mathrm{a})}\}\underline{I}_{\mathrm{com,sheet}} \qquad (7.115)
\end{aligned}$$

$$R_{(\mathrm{a})} = \frac{\omega\mu}{2\pi}\ln(\frac{d_{\mathrm{se}}/2}{d_{\mathrm{si}}/2+h_{\mathrm{s}}})\frac{\delta_{\mathrm{s}}}{2} \qquad (7.116) \qquad\qquad L_{(\mathrm{a})} = \frac{\mu}{2\pi}\ln(\frac{d_{\mathrm{se}}/2}{d_{\mathrm{si}}/2+h_{\mathrm{s}}})\frac{\delta_{\mathrm{s}}}{2} \qquad (7.117)$$

In the same way, induced voltage $\underline{V}_{(\mathrm{b})}$ (7.118), resistance $R_{(\mathrm{b})}$ (7.119) and inductance

$L_{(b)}$ (7.120) per sheet for model (b) are derived from the flux of one sheet $\underline{\Phi}_{0,(b)}$ (7.98).

$$\begin{aligned}\underline{V}_{(b)} &= j\omega\underline{\Phi}_{0,(b)} \\ &= \{\frac{\omega\mu}{\pi}\ln(\frac{d_{se}/2}{d_{si}/2+h_s})\frac{\delta_s}{2} + j\frac{\omega\mu}{\pi}\ln(\frac{d_{se}/2}{d_{si}/2+h_s})\frac{\delta_s}{2})\}\underline{I}_{com}(k) \\ &= \{R_{(b)} + j\omega L_{(b)}\}\underline{I}_{com}(k) \end{aligned} \quad (7.118)$$

$$R_{(b)} = \frac{\omega\mu}{\pi}\ln(\frac{d_{se}/2}{d_{si}/2+h_s})\frac{\delta_s}{2} \quad (7.119) \qquad L_{(b)} = \frac{\mu}{\pi}\ln(\frac{d_{se}/2}{d_{si}/2+h_s})\frac{\delta_s}{2} \quad (7.120)$$

The *total inductance of the ground current path through the stator lamination* L_g is given by the sum of the individual inductances of model (a) $L_{(a),sum}$ (7.121) and model (b) $L_{(b),sum}$ (7.122), considering the current distribution in the stack (7.99 and 7.100). The loop of the circulating bearing current includes the path through the stator and the circulating bearing current and the ground current share this path. Therefore, *the mutual inductance is given by* L_g (7.123).

$$L_{(a),sum} = \frac{1}{i_{com}}\{N_{Fe}i_{com,\,sheet}\frac{\mu}{2\pi}\ln(\frac{d_{se}/2}{d_{si}/2+h_s})\frac{\delta_s}{2}\} = \frac{\mu}{2\pi}\ln(\frac{d_{se}/2}{d_{si}/2+h_s})\frac{\delta_s}{2} \quad (7.121)$$

$$\begin{aligned}L_{(b),sum} &= \frac{1}{i_{com}}\{\sum_{k=1}^{N_{Fe}} i_{com}(k)\frac{\mu}{\pi}\ln(\frac{d_{se}/2}{d_{si}/2+h_s})\frac{\delta_s}{2}\} \\ &= \frac{(N_{Fe}-1)}{2}\frac{\mu}{\pi}\ln(\frac{d_{se}/2}{d_{si}/2+h_s})\frac{\delta_s}{2} \end{aligned} \quad (7.122)$$

$$L_g = L_{(a),sum} + L_{(b),sum} = \frac{N_{Fe}}{2}\frac{\mu}{\pi}\ln(\frac{d_{se}/2}{d_{si}/2+h_s})\frac{\delta_s}{2} \quad (7.123)$$

7.7.2 Impedance of Bearing Current Path

The circulating bearing current is coupled with the ground current by the mutual inductance L_g and the bearing current amplitude is determined by the impedance of the bearing current path.

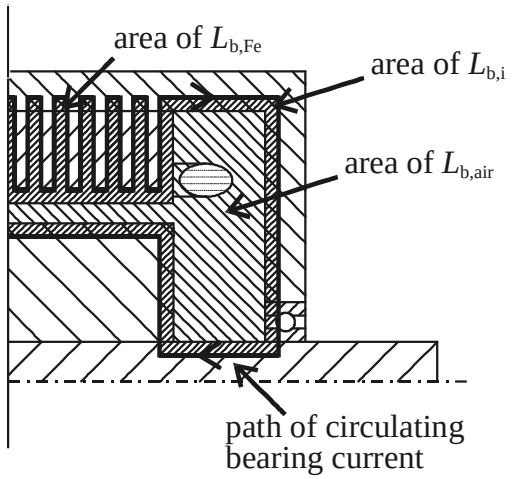

Figure 7.29: Inductances of the path of the circulating bearing currents. For clarity, only half of a machine is shown.

♦ ***First, the inductances along the path are considered. Three different parts may be distinguished (Fig. 7.29):***

1. Internal inductance of path through stator lamination stack (inductance $L_{b,Fe}$),

2. Self-inductance of area enclosed by the circulating bearing current that is given by the air gap and the end-winding cavity (inductance $L_{b,air}$),

3. Internal inductance of bearing current path outside stator lamination (inductance $L_{\mathrm{b,i}}$).

The rotor is supposed to be resurfaced by skimming. then a thin conducting layer bridges the rotor lamination and the rotor surface. The rotor bars are not insulated from the lamination. Therefore, it is assumed that the bearing current flows along the surface of the rotor stack.

The inductances are calculated as follows:

1. Internal inductance $L_{\mathrm{b,Fe}}$ of path through stator lamination stack: The path of the circulating bearing current through the stator lamination stack is the same as the path of the common mode current. However, the *total bearing current* i_{b} enters the stack on one side and leaves it on the other side. *No* current flows from the stator winding into the lamination. Therefore, the solution is given by the total inductance of all sheets resulting from model (b) (7.122), where the bearing current $i_{\mathrm{b}}(k)$ per sheet k equals the total bearing current i_{b} (7.124). The inductance $L_{\mathrm{b,Fe}}$ is given by (7.125). It is twice the internal inductance L_{g} (7.105).

$$i_{\mathrm{b}}(k) = i_{\mathrm{b}} \tag{7.124}$$

$$L_{\mathrm{b,Fe}} = \mu \frac{N_{\mathrm{Fe}}}{\pi} \ln\left(\frac{d_{\mathrm{se}}/2}{d_{\mathrm{si}}/2 + h_{\mathrm{s}}}\right)\frac{\delta_{\mathrm{s}}}{2} = 2L_{\mathrm{g}} \tag{7.125}$$

2. The ***self-inductance $L_{\mathrm{b,air}}$*** is calculated as the inductance of a coaxial cable. With the part of the air gap (7.126) and the part of the end-winding cavity (7.127), the inductance $L_{\mathrm{b,air}}$ is given by (7.128).

$$L_{\mathrm{b,air,gap}} = \frac{\mu_0}{2\pi}\ln\left(\frac{d_{\mathrm{si}}}{d_{\mathrm{re}}}\right)l_{\mathrm{Fe}} \tag{7.126}$$

$$L_{\mathrm{b,air,ew}} = \frac{\mu_0}{2\pi}\ln\left(\frac{d_{\mathrm{se}}}{d_{\mathrm{ri}}}\right)(l_{\mathrm{b}} - l_{\mathrm{Fe}}) \tag{7.127}$$

$$L_{\mathrm{b,air}} = L_{\mathrm{b,air,gap}} + L_{\mathrm{b,air,ew}} = \frac{\mu_0}{2\pi}\left\{\ln\left(\frac{d_{\mathrm{si}}}{d_{\mathrm{re}}}\right)l_{\mathrm{Fe}} + \left(\frac{d_{\mathrm{se}}}{d_{\mathrm{ri}}}\right)(l_{\mathrm{b}} - l_{\mathrm{Fe}})\right\} \tag{7.128}$$

where:

d_{re} = rotor lamination outer diameter,

d_{ri} = rotor lamination inner diameter,

l_{b} = distance between bearing seats.

3. Internal inductance of path outside stator lamination $L_{\mathrm{b,i}}$: Five parts contribute to the internal inductance of the path of the circulating bearing current outside the stator lamination stack (Fig. 7.30): a) frame outside stack ($L_{\mathrm{b,ia}}$), b) end-shield on drive end and non-drive end ($L_{\mathrm{b,ib}}$), c) shaft outside the rotor lamination stack ($L_{\mathrm{b,ic}}$), d) end sheet on drive end and non-drive end of the rotor lamination stack ($L_{\mathrm{b,id}}$) and resurfaced rotor lamination stack ($L_{\mathrm{b,ie}}$) (7.129).

The inductances $L_{\mathrm{b,ia}}$, $L_{\mathrm{b,ic}}$ and $L_{\mathrm{b,ie}}$ are calculated using the formula for an internal inductance of a circular conductor with radius r at high frequency L_{i} (7.130), inductances $L_{\mathrm{b,ib}}$ and $L_{\mathrm{b,id}}$ correspond to the solution of the single sheet of model (a) (7.101). Hence, the solutions of the individual inductances and of $L_{\mathrm{b,i}}$ are given by (7.131) to (7.135) and $L_{\mathrm{b,i}}$ (7.136), where δ_{s}^* is the skin depth of the material. For simplification, the frame, end-shields and shaft are assumed to have the same relative permeability μ_{r}^*.

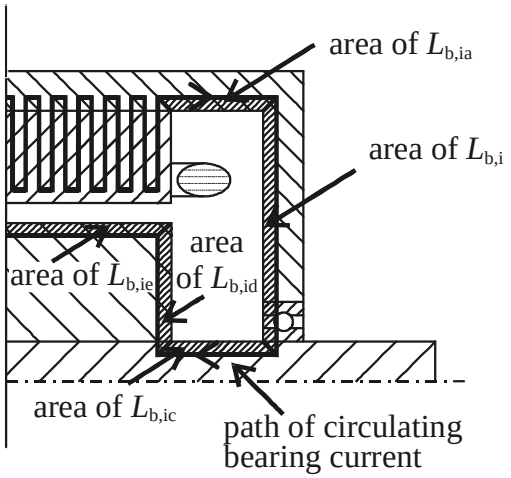

Figure 7.30: Parts of the internal inductance $L_{\mathrm{b,i}}$ of the path of the circulating bearing currents. For clarity, only half of a machine is shown.

$$L_{\mathrm{b,i}} = L_{\mathrm{b,ia}} + L_{\mathrm{b,ib}} + L_{\mathrm{b,ic}} + L_{\mathrm{b,id}} + L_{\mathrm{b,ie}} \tag{7.129}$$

$$L_{\mathrm{i}} = \frac{1}{2\pi r}\frac{1}{\omega\kappa\delta_{\mathrm{s}}^*}l = \frac{\mu}{4\pi}\frac{\delta_{\mathrm{s}}^*}{r}l \tag{7.130}$$

where:
r and l = radius and length of conductor

$$L_{\mathrm{b,ia}} = \frac{\mu^*}{4\pi}\frac{\delta_{\mathrm{s}}^*}{d_{\mathrm{se}}/2}(l_{\mathrm{b}} - l_{\mathrm{Fe}}) \tag{7.131}$$

$$L_{\mathrm{b,ib}} = 2\frac{\mu^*}{2\pi}\ln(\frac{d_{\mathrm{se}}}{d_{\mathrm{ri}}})\frac{\delta_{\mathrm{s}}^*}{2} \tag{7.132}$$

$$L_{\mathrm{b,ic}} = \frac{\mu^*}{4\pi}\frac{\delta_{\mathrm{s}}^*}{d_{\mathrm{ri}}/2}(l_{\mathrm{b}} - l_{\mathrm{Fe}}) \tag{7.133}$$

$$L_{\mathrm{b,id}} = 2\frac{\mu^*}{2\pi}\ln(\frac{d_{\mathrm{re}}}{d_{\mathrm{ri}}})\frac{\delta_{\mathrm{s}}^*}{2} \tag{7.134}$$

$$L_{\mathrm{b,ie}} = \frac{\mu}{4\pi}\frac{\delta_{\mathrm{s}}}{d_{\mathrm{re}}/2}l_{\mathrm{Fe}} \tag{7.135}$$

$$L_{\mathrm{b,i}} = \frac{\mu\delta_{\mathrm{s}}^*}{4\pi}\{\frac{l_{\mathrm{b}} - l_{\mathrm{Fe}}}{d_{\mathrm{se}}/2} + 2\ln(\frac{d_{\mathrm{se}}/2}{d_{\mathrm{ri}}/2}) + \frac{l_{\mathrm{b}} - l_{\mathrm{Fe}}}{d_{\mathrm{ri}}/2} + 2\ln(\frac{d_{\mathrm{re}}/2}{d_{\mathrm{ri}}/2})\} + \frac{\mu\delta_{\mathrm{s}}}{4\pi}\frac{l_{\mathrm{Fe}}}{d_{\mathrm{re}}/2} \tag{7.136}$$

The value of μ_{r}^* is about 100. It is an order of magnitude smaller than μ_{r} of the lamination which reaches values up to several 1000. Here, it is assumed that both relative permeabilities have the same value, $\mu_{\mathrm{r}}^* = \mu_{\mathrm{r}}$, therefore, the skin depths are the same, $\delta_{\mathrm{s}}^* = \delta_{\mathrm{s}}$. The internal inductance $L_{\mathrm{b,i}}$ is calculated too large, because of this assumption. This is accepted, because *it is shown that the internal inductance* $L_{\mathrm{b,i}}$ *is negligible* when compared with the inductances $L_{\mathrm{b,Fe}}$ and $L_{\mathrm{b,air}}$: The value of the parameter k_{Lb} as defined by (7.137) is larger that the value of the parameter $\tilde{k}_{\mathrm{Lb}}$ (7.138). With minimum

and maximum values of diverse ratios of the geometrical parameters of the investigated machines (7.139) to (7.146), *the minimum value of* $\tilde{k}_{\mathrm{Lb}}$ *is 8* (7.147).

$$k_{\mathrm{Lb}} = \frac{L_{\mathrm{b,Fe}} + L_{\mathrm{b,air}}}{L_{\mathrm{b,i}}} \qquad (7.137) \qquad\qquad k_{\mathrm{Lb}} > \tilde{k}_{\mathrm{Lb}} = \frac{L_{\mathrm{b,Fe}}}{L_{\mathrm{b,i}}} \qquad (7.138)$$

$$\begin{aligned} \tilde{k}_{\mathrm{Lb}} &= \frac{\mu N_{\mathrm{Fe}} \delta_{\mathrm{s}})/\pi}{\mu^* \delta_{\mathrm{s}}^*/(4\pi)} \\ &\times \frac{\ln(d_{\mathrm{se}}/d_{\mathrm{si}})}{(l_{\mathrm{b}} - l_{\mathrm{Fe}})/(d_{\mathrm{se}}/2) + 2\ln(d_{\mathrm{se}}/d_{\mathrm{ri}}) + (l_{\mathrm{b}} - l_{\mathrm{Fe}})/(d_{\mathrm{ri}}/2) + 2\ln(d_{\mathrm{re}}/d_{\mathrm{ri}}) + l_{\mathrm{Fe}}/(d_{\mathrm{re}}/2)} \\ &= \frac{4 N_{\mathrm{Fe}} \ln(d_{\mathrm{se}}/d_{\mathrm{si}})}{2\{(l_{\mathrm{b}} - l_{\mathrm{Fe}})/d_{\mathrm{se}} + 4\ln(d_{\mathrm{se}}/d_{\mathrm{ri}}) + (l_{\mathrm{b}} - l_{\mathrm{Fe}})/d_{\mathrm{ri}} + 4\ln(d_{\mathrm{re}}/d_{\mathrm{ri}}) + l_{\mathrm{Fe}}/d_{\mathrm{re}}\}} \end{aligned} \qquad (7.139)$$

$$\min\{\ln(d_{\mathrm{se}}/d_{\mathrm{si}})\} = 0.3 \qquad (7.140)$$

$$\min\{N_{\mathrm{Fe}}\} = 270 \qquad (7.141)$$

$$\max\{\frac{l_{\mathrm{b}} - l_{\mathrm{Fe}}}{d_{\mathrm{se}}}\} = 1.3 \qquad (7.142)$$

$$\max\{\ln(d_{\mathrm{se}}/d_{\mathrm{ri}})\} = 1.6 \qquad (7.143)$$

$$\max\{\frac{l_{\mathrm{b}} - l_{\mathrm{Fe}}}{d_{\mathrm{ri}}}\} = 6 \qquad (7.144)$$

$$\max\{\ln(d_{\mathrm{re}}/d_{\mathrm{ri}})\} = 1.3 \qquad (7.145)$$

$$\max\{\frac{l_{\mathrm{Fe}}}{d_{\mathrm{re}}}\} = 1.4 \qquad (7.146)$$

$$\min\{\tilde{k}_{\mathrm{Lb}}\} = \frac{2 \cdot 270 \cdot 0.3}{1.3 + 4 \cdot 1.6 + 4 \cdot 1.3 + 6 + 1.4} = 8 \qquad (7.147)$$

►►► The calculated values of the four inductances L_{g}, $L_{\mathrm{b,Fe}}$, $L_{\mathrm{b,air}}$ and $L_{\mathrm{b,i}}$ of the circulating bearing current path for the three pairs of frequency f and relative permeability μ_{r} considered in Section 7.6.3,

a) $f = 100$ kHz, $\mu_{\mathrm{r}} = 100$,

b) $f = 100$ kHz, $\mu_{\mathrm{r}} = 1000$,

c) $f = 1$ MHz, $\mu_{\mathrm{r}} = 1000$,

are shown in Table 7.17. *The values confirm that the inductance* $L_{\mathrm{b,i}}$ *is negligible* (7.148).

$$L_{\mathrm{b}} = L_{\mathrm{b,Fe}} + L_{\mathrm{b,air}} + L_{\mathrm{b,i}} \qquad (7.148)$$

Motor	M11a	M11b	M110a	M110b	M500a	M500b
L_{g} ($f = 100$ kHz, $\mu_{\mathrm{r}} = 100$) and ($f = 1$ MHz, $\mu_{\mathrm{r}} = 1000$)	0.043 μH	0.042 μH	0.111 μH	0.116 μH	0.122 μH	0.231 μH
L_{g} ($f = 100$ kHz, $\mu_{\mathrm{r}} = 1000$)	0.141 μH	0.133 μH	0.350 μH	0.365 μH	0.685 μH	0.730 μH
$L_{\mathrm{b,Fe}} = 2L_{\mathrm{g}}$ ($f = 100$ kHz, $\mu_{\mathrm{r}} = 100$) and ($f = 1$ MHz, $\mu_{\mathrm{r}} = 1000$)	0.086 μH	0.084 μH	0.221 μH	0.231 μH	0.244 μH	0.462 μH
$L_{\mathrm{b,Fe}} = 2L_{\mathrm{g}}$ ($f = 100$ kHz, $\mu_{\mathrm{r}} = 1000$)	0.281 μH	0.266 μH	0.699 μH	0.729 μH	0.770 μH	1.460 μH
$L_{\mathrm{b,air}}$	0.073 μH	0.048 μH	0.065 μH	0.097 μH	0.191 μH	0.277 μH
$L_{\mathrm{b,i}}$ ($f = 100$ kHz, $\mu_{\mathrm{r}} = 100$) and ($f = 1$ MHz, $\mu_{\mathrm{r}} = 1000$)	0.012 μH	0.011 μH	0.012 μH	0.011 μH	0.014 μH	0.016 μH
$L_{\mathrm{b,i}}$ ($f = 100$ kHz, $\mu_{\mathrm{r}} = 1000$)	0.039 μH	0.034 μH	0.038 μH	0.033 μH	0.044 μH	0.048 μH
L_{b} ($f = 100$ kHz, $\mu_{\mathrm{r}} = 100$) and ($f = 1$ MHz, $\mu_{\mathrm{r}} = 1000$)	0.171 μH	0.143 μH	0.298 μH	0.339 μH	0.449 μH	0.755 μH
L_{b} ($f = 100$ kHz, $\mu_{\mathrm{r}} = 1000$)	0.393 μH	0.348 μH	0.802 μH	0.859 μH	1.005 μH	1.785 μH

Table 7.17: Calculated values of $L_{\mathrm{g}}, L_{\mathrm{b,Fe}}, L_{\mathrm{b,air}}, L_{\mathrm{b,i}}$ and L_{b}

♦ ***Next, the resistances along the path are considered:***

Three resistances are distinguished:

1. Resistance of path through stator lamination (resistance $R_{\mathrm{b,Fe}}$),

2. Bearing resistance (resistance R_{b}),

3. Resistance of path outside stator lamination except for the bearing resistance (resistance $R_{\mathrm{b,i}}$).

The resistances are calculated as follows:

1. The ***resistance $R_{\mathrm{b,Fe}}$ of the path through the stator lamination*** is calculated according to the approach presented in Section 7.7.1. As the bearing current $\hat{i}_{\mathrm{b}}(k)$ per sheet k equals the total bearing current $\hat{i}_{\mathrm{b}}$ (7.124), the value of $R_{\mathrm{b,Fe}}$ is given by (7.149), which is N_{Fe} times the resistance of a single sheet of model (b) (7.119).

$$R_{\mathrm{b,Fe}} = N_{\mathrm{Fe}} \frac{\omega\mu}{\pi} \ln\left(\frac{d_{\mathrm{se}}/2}{d_{\mathrm{si}}/2 + h_{\mathrm{s}}}\right) \frac{\delta_{\mathrm{s}}}{2} \tag{7.149}$$

The resistance $R_{\mathrm{b,Fe}}$ and the inductance $L_{\mathrm{b,Fe}}$ are related by the factor ω (7.150) and the resistive and the reactive parts of the impedance by the factor 1 (7.151).

$$\frac{L_{\mathrm{b,Fe}}}{R_{\mathrm{b,Fe}}} = \left(N_{\mathrm{Fe}} \frac{\mu}{\pi} \ln\left(\frac{d_{\mathrm{se}}/2}{d_{\mathrm{si}}/2 + h_{\mathrm{s}}}\right) \frac{\delta_{\mathrm{s}}}{2}\right) / \left(N_{\mathrm{Fe}} \frac{\omega\mu}{\pi} \ln\left(\frac{d_{\mathrm{se}}/2}{d_{\mathrm{si}}/2 + h_{\mathrm{s}}}\right) \frac{\delta_{\mathrm{s}}}{2}\right) = \frac{1}{\omega} \tag{7.150}$$

$$\frac{X_{\mathrm{b,Fe}}}{R_{\mathrm{b,Fe}}} = \frac{\omega L_{\mathrm{b,Fe}}}{R_{\mathrm{b,Fe}}} = 1 \tag{7.151}$$

The calculated values of the resistance $R_{\mathrm{b,Fe}}$ for the three pairs of frequency f and relative permeability μ_{r} considered above (a) $f = 100$ kHz, $\mu_{\mathrm{r}} = 100$, b) $f = 100$ kHz, $\mu_{\mathrm{r}} = 1000$, c) $f = 1$ MHz, $\mu_{\mathrm{r}} = 1000$) are given in Table 7.18. In the same way as the inductances $L_{\mathrm{b,Fe}}$, $R_{\mathrm{b,Fe}}$ increases with increasing motor size. For $\mu_{\mathrm{r}} = 100$ and $f = 100$ kHz the values range between 50 mΩ and almost 300 mΩ. As the skin depths δ_{s} decreases with the root of frequency and μ_{r}, the values are ten times larger for $\mu_{\mathrm{r}} = 1000$ and 1 MHz, ranging from 500 mΩ to almost 3 Ω.

Motor	M11a	M11b	M110a	M110b	M500a	M500b
$R_{\mathrm{b,Fe}}$ ($f = 100$ kHz, $\mu_{\mathrm{r}} = 100$)	53.9 mΩ	52.9 mΩ	139.0 mΩ	144.8 mΩ	154.0 mΩ	290.1 mΩ
$R_{\mathrm{b,Fe}}$ ($f = 100$ kHz, $\mu_{\mathrm{r}} = 1000$)	170.5 mΩ	167.3 mΩ	439.7 mΩ	457.9 mΩ	483.8 mΩ	917.5 mΩ
$R_{\mathrm{b,Fe}}$ ($f = 1$ MHz, $\mu_{\mathrm{r}} = 1000$)	539.2 mΩ	529.1 mΩ	1390.3 mΩ	1448.0 mΩ	1540.0 mΩ	2901.4 mΩ

Table 7.18: Calculated values of $R_{\mathrm{b,Fe}}$

2. The ***bearing resistance R_{b}*** is estimated according to the approach explained in Section 7.1. The circulating bearing currents have peak amplitudes of several A. As a result, numerous current conducting bridges are built up and the bearing resistance is assumed to value less than 10 mΩ. Therefore, *it is negligible when compared with the resistance* $R_{\mathrm{b,Fe}}$.

3. In the same way as the inductance $L_{\mathrm{b,i}}$, the ***resistance $R_{\mathrm{b,i}}$ of the path through the stator lamination*** comprises five parts $R_{\mathrm{b,ia}}$, $R_{\mathrm{b,ib}}$, $R_{\mathrm{b,ic}}$, $R_{\mathrm{b,id}}$ and $R_{\mathrm{b,ie}}$, corresponding respectively to the parts that give the internal inductances $L_{\mathrm{b,ia}}$ to $L_{\mathrm{b,ie}}$ (Fig. 7.30). The resistances $R_{\mathrm{b,ib}}$ and $R_{\mathrm{b,id}}$ equal the impedance $X_{\mathrm{b,ib}}$ and $X_{\mathrm{b,id}}$, as the solutions are given by the single sheet model (a). The resistances $R_{\mathrm{b,ia}}$, $R_{\mathrm{b,ic}}$ and $R_{\mathrm{b,id}}$ are calculated using the formula for a resistance of a circular conductor at high frequency. Hence, the values of $R_{\mathrm{b,ia}}$, $R_{\mathrm{b,ic}}$, $R_{\mathrm{b,id}}$ and of $X_{\mathrm{b,ia}}$, $X_{\mathrm{b,ic}}$, $X_{\mathrm{b,id}}$ are related by a factor of 1 respectively (7.152).

$$R_{\mathrm{i}} = \frac{1}{2\pi r}\frac{1}{\kappa\delta_{\mathrm{s}}^{*}}l = \frac{\mu}{4\pi}\frac{\omega\delta_{\mathrm{s}}^{*}}{r}l = \omega L_{\mathrm{i}} = X_{\mathrm{i}} \tag{7.152}$$

Therefore, in the same way as the inductance $L_{\mathrm{b,i}}$ is negligible when compared with $L_{\mathrm{b,Fe}}$ (p. 157), the *resistance $R_{\mathrm{b,i}}$ is negligible when compared with $R_{\mathrm{b,Fe}}$.*

7.7.3 Ratio of Circulating Bearing Current and Ground Current

The circulating bearing current and the common mode current path are coupled via the common mode flux. The transformation ratio is given by the ratio of the respective impedances (7.153) (Fig. 7.31).

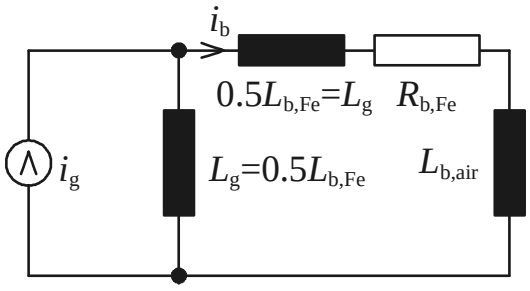

Figure 7.31: Equivalent circuit for calculation of circulating bearing currents

$$\begin{aligned}
\left|\frac{\hat{I}_{\mathrm{b}}}{\hat{I}_{\mathrm{g}}}\right| &= \left|\frac{j\omega L_{\mathrm{g}}}{R_{\mathrm{b,Fe}} + j\omega L_{\mathrm{b,Fe}} + j\omega L_{\mathrm{b,air}}}\right| \\
&= \left|\frac{X_{\mathrm{g}}}{X_{\mathrm{b,Fe}} + X_{\mathrm{b,air}} - jR_{\mathrm{b,Fe}}}\right| \\
&= \left|\frac{X_{\mathrm{g}}}{X_{\mathrm{b,Fe}}(1 + X_{\mathrm{b,air}}/X_{\mathrm{b,Fe}} - jR_{\mathrm{b,Fe}}/X_{\mathrm{b,Fe}})}\right| = 0.5\left|\frac{1}{1 + X_{\mathrm{b,air}}/X_{\mathrm{b,Fe}} - j}\right| \\
&= 0.5\sqrt{\frac{1}{(1 + X_{\mathrm{b,air}}/X_{\mathrm{b,Fe}})^2 + 1}}
\end{aligned} \tag{7.153}$$

The calculated values of $|\hat{I}_{\mathrm{b}}/\hat{I}_{\mathrm{g}}|$ for the three pairs of frequency f and relative permeability μ_{r} considered above (a) $f = 100$ kHz, $\mu_{\mathrm{r}} = 100$, b) $f = 100$ kHz, $\mu_{\mathrm{r}} = 1000$, c) $f = 1$ MHz, $\mu_{\mathrm{r}} = 1000$) for the test motors of the 11 kW, 110 kW and 500 kW power level are given in Table 7.19. As L_{g} and hence $L_{\mathrm{b,Fe}}$ depend on f and μ_{r} (Section 7.6.3), whereas $L_{\mathrm{b,air}}$ is independent of these parameters, the ratio $|\hat{I}_{\mathrm{b}}/\hat{I}_{\mathrm{g}}|$ *increases with increasing relative permeability and decreases with increasing frequency.*

MOTOR	M11a	M11b	M110a	M110b	M500a	M500b
$\lvert\hat{I}_\mathrm{b}/\hat{I}_\mathrm{g}\rvert$ (f = 100 kHz, μ_r = 100) and (f = 1 MHz, μ_r = 1000)	0.24	0.27	0.29	0.29	0.24	0.27
$\lvert\hat{I}_\mathrm{b}/\hat{I}_\mathrm{g}\rvert$ (f = 100 kHz, μ_r = 1000)	0.31	0.32	0.33	0.33	0.31	0.32
$\lvert\hat{I}_\mathrm{bL}/\hat{I}_\mathrm{g}\rvert$ (f = 100 kHz, μ_r = 100) and (f = 1 MHz, μ_r = 1000)	0.11	0.12	0.19	0.20	0.18	0.22
$\lvert\hat{I}_\mathrm{bL}/\hat{I}_\mathrm{g}\rvert$ (f = 100 kHz, μ_r = 1000)	0.22	0.23	0.29	0.29	0.28	0.30
$(\hat{I}_\mathrm{bL}-\hat{I}_\mathrm{b})/\hat{I}_\mathrm{b}$ (f = 100 kHz, μ_r = 100) and (f = 1 MHz, μ_r = 1000)	-51 %	-54 %	-38 %	-30 %	-27 %	-17 %
$(\hat{I}_\mathrm{bL}-\hat{I}_\mathrm{b})/\hat{I}_\mathrm{b}$ (f = 100 kHz, μ_r = 1000)	-28 %	-29 %	-13 %	-13 %	-12 %	-7 %

Table 7.19: Calculated values of $|\hat{I}_\mathrm{b}/\hat{I}_\mathrm{g}|$ (without copper loop), $|\hat{I}_\mathrm{bL}/\hat{I}_\mathrm{g}|$ (with copper loop) and $(\hat{I}_\mathrm{bL}-\hat{I}_\mathrm{b})/\hat{I}_\mathrm{g}$

♦ Based on this approach, the *influence of the copper loop which is applied for the bearing current measurement* is derived. The measured value of the inductance of the copper is L_cu = 0.1 μH. The capacitance of the insulating layer C_i (→ Section 3.3.1, p. 30) that is bridged by the copper loop is in the order of (1...5) nF. For frequencies of several 100 kHz, the parallel capacitive impedance $X_\mathrm{i} = 1/(\omega C_\mathrm{i})$ given by the insulating layer is much larger than the inductive impedance of the copper loop $X_\mathrm{cu} = \omega L_\mathrm{cu}$ ($f_0 = (2\pi\sqrt{C_\mathrm{i}L_\mathrm{cu}})^{-1} = (2\pi\sqrt{10^{-9}10^{-7}})^{-1}...(2\pi\sqrt{5\cdot10^{-9}10^{-7}})^{-1}$ = (16...7.1) MHz). Therefore, it is neglected. Using (7.153) as starting point, the *ratio* $|\hat{I}_\mathrm{bL}/\hat{I}_\mathrm{g}|$, where $\hat{I}_\mathrm{bL}$ is the bearing current amplitude with consideration of the copper loop, is given by (7.154) (Table 7.19).

$$|\frac{\hat{I}_\mathrm{bL}}{\hat{I}_\mathrm{g}}| = 0.5\ \sqrt{\frac{1}{(1+X_\mathrm{b,air}/X_\mathrm{b,Fe}+2X_\mathrm{cu}/X_\mathrm{b,Fe})^2+1}} \tag{7.154}$$

Depending on the value of the frequency f and the relative permeability μ_r, the copper loop for measurement of the bearing currents reduces the circulating bearing currents at the 110 kW power level by 13 % to 38 % and at the 500 kW power level by 7 % to 27 % . For the motors of the 11 kW power level, these calculations are not of importance, as no circulating bearing current flow occurs.

♦ *The measured ratios* $|\hat{i}_\mathrm{b}/\hat{i}_\mathrm{g}|_\mathrm{measured}$ (7.155) (→ Chapter 4, p. 41) *and the calculated ratios* $|\hat{I}_\mathrm{bL}/\hat{I}_\mathrm{g}|$ (Table 7.19) *are in line*, thereby validating the model.

$$|\frac{\hat{i}_\mathrm{b}}{\hat{i}_\mathrm{g}}|_\mathrm{measured} = 0.2 \ldots 0.3 \tag{7.155}$$

♦ As a result of the presented approach, ***the maximum ratio of circulating bearing current and ground current is 0.354*** (7.156).

$$\max\Big\{|\frac{\hat{I}_\mathrm{b}}{\hat{I}_\mathrm{g}}|\Big\} = \lim_{X_\mathrm{b,air}\to 0}\{0.5\sqrt{\frac{1}{(1+X_\mathrm{b,air}/X_\mathrm{b,Fe})^2+1}}\} = 0.5\sqrt{\frac{1}{1+1}} = 0.354 \tag{7.156}$$

7.7.4 Influence of Insulated Bearings and Insulated Inner Bearing Seats

♦ Insulated ("coated") bearings are conventional bearings that have an additional insulating coat of typically (50...250) μm thickness at the outer bearing race (→ Chapter 2, p. 15). Alternatively, an insulating coat - e.g of 500 μm thickness - can be applied at the motor shaft where the bearing bore is placed [66].

The capacitance of a coated bearing or shaft is calculated as the capacitance of a cylindric capacitor (7.157 and 7.158).

$$C_\mathrm{ins}^{(1)} = \frac{\varepsilon_\mathrm{r}\varepsilon_0 B D_\mathrm{b}\pi}{d_\mathrm{ins}} \tag{7.157}$$

$$C_\mathrm{ins}^{(2)} = \frac{\varepsilon_\mathrm{r}\varepsilon_0 B d_\mathrm{bi}\pi}{d_\mathrm{ins}} \tag{7.158}$$

where:

$\varepsilon_\mathrm{r} = 3$,
B = width of bearing,
D_b = bearing outer diameter,
d_ins = thickness of insulating layer,
d_bi = bearing bore inner diameter.

The capacitances $C_\mathrm{ins}^{(1)}$ and $C_\mathrm{ins}^{(2)}$ are calculated for the three types of insulated bearings, bearings type 6209, 6316 and 6317, and bearing bores of the motors considered here (Tables 7.20 and 7.21). For 100 kHz, the impedance of the insulating coat is in the order of 10 MΩ at the motor shaft and between 150 Ω and 10 MΩ at the bearing outer race, depending on the thickness of the coat (Fig. 7.33, Fig. 7.34).

Type of bearing	Bearing outer diameter D_b	Width B	$C_{ins}^{(1)}$ $d_{ins} = 50\ \mu$m	$C_{ins}^{(1)}$ $d_{ins} = 100\ \mu$m	$C_{ins}^{(1)}$ $d_{ins} = 250\ \mu$m
6209	85 mm	19 mm	2.70 nF	1.35 nF	0.54 nF
6316	170 mm	39 mm	11.07 nF	5.53 nF	2.21 nF
6317	180 mm	41 mm	12.32 nF	6.16 nF	2.46 nF

Table 7.20: Calculated capacitances of insulated bearings for different insulation thicknesses

Motor size (Shaft height)	Bearing bore d_b	Width B	$C_{ins}^{(2)}$ $d_{ins} = 500\ \mu$m
160 mm	45 mm	19 mm	45 pF
280 mm	80 mm	39 mm	166 pF
280 mm	85 mm	39 mm	176 pF
400 mm	85 mm	41 mm	185 pF
400 mm	120 mm	40 mm	254 pF

Table 7.21: Calculated capacitances of coated motor shaft

♦ The equivalent electric circuit of the circulating bearing current with use of two conventional bearings (Fig. 7.31) is extended for the case of one or two insulated instead of conventional bearings (Fig. 7.32). The induced circulating bearing current i_b^* is described by (7.159). With a sinusoidal ground current (7.160), the general solution of (7.159) is given by (7.161).

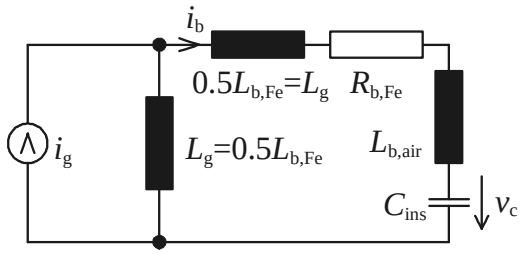

Figure 7.32: Equivalent circuit for calculation of circulating bearing currents

$$\frac{L_g}{L_{b,Fe}+L_{air}}\frac{d^2 i_g}{dt^2} = \frac{d^2 i_b^*}{dt^2} + \frac{R_g}{L_{b,Fe}+L_{air}}\frac{di_b^*}{dt} + \frac{1}{L_{ins}(L_{b,Fe}+L_{air})} i_b^* \qquad (7.159)$$

$$i_g = \hat{i}_g \sin(\omega t) \qquad (7.160)$$

$$\begin{aligned} i_b^* &= i_{b,h}^* + i_{b,p}^* \\ &= K_1 e^{-\alpha^* t}\sin(\beta^* t) + K_2 e^{-\alpha^* t}\cos(\beta^* t) \\ &+ K_3 \sin(\omega t) + K_4 \cos(\omega t) \end{aligned} \qquad (7.161)$$

where:

$$\alpha^* = \frac{R_{b,Fe}}{2(L_{b,Fe}+L_{b,air})} \qquad (7.162)$$

$$\beta^* = \sqrt{\omega^{*2} - \alpha^{*2}} \qquad (7.163)$$

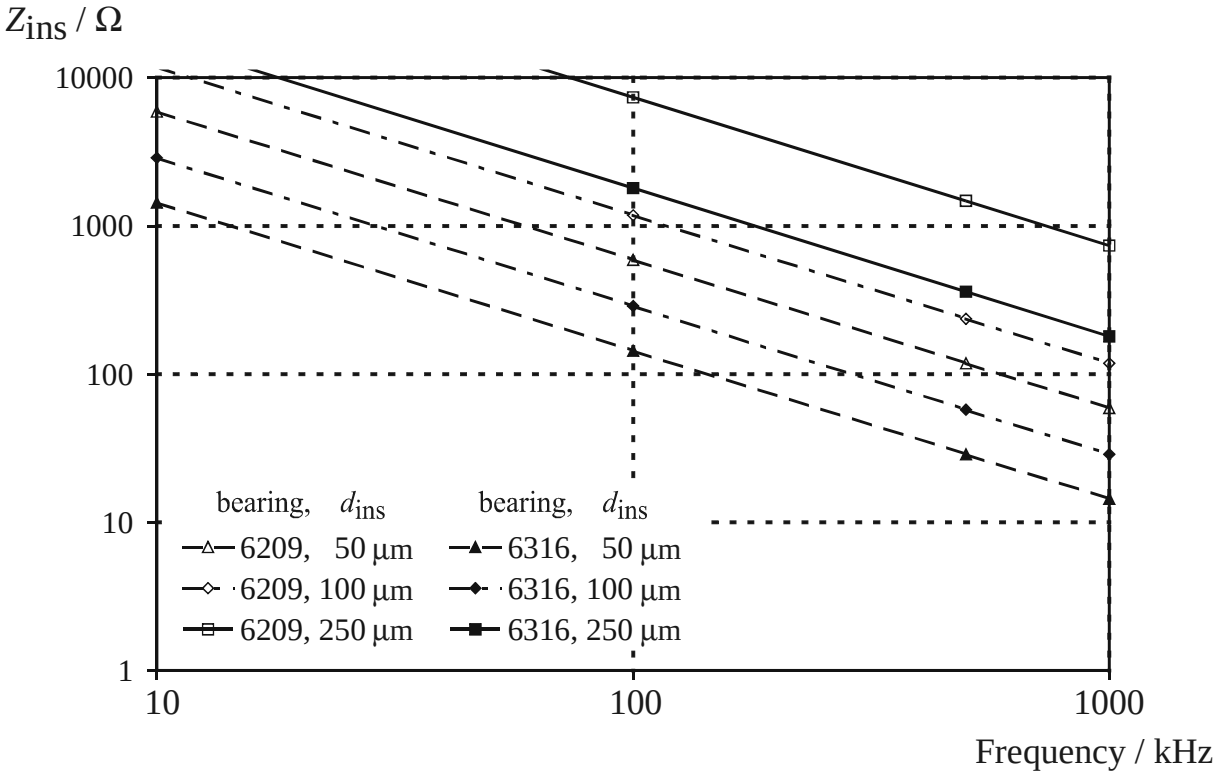

Figure 7.33: Calculated impedance of bearing insulation as function of insulation thickness and frequency

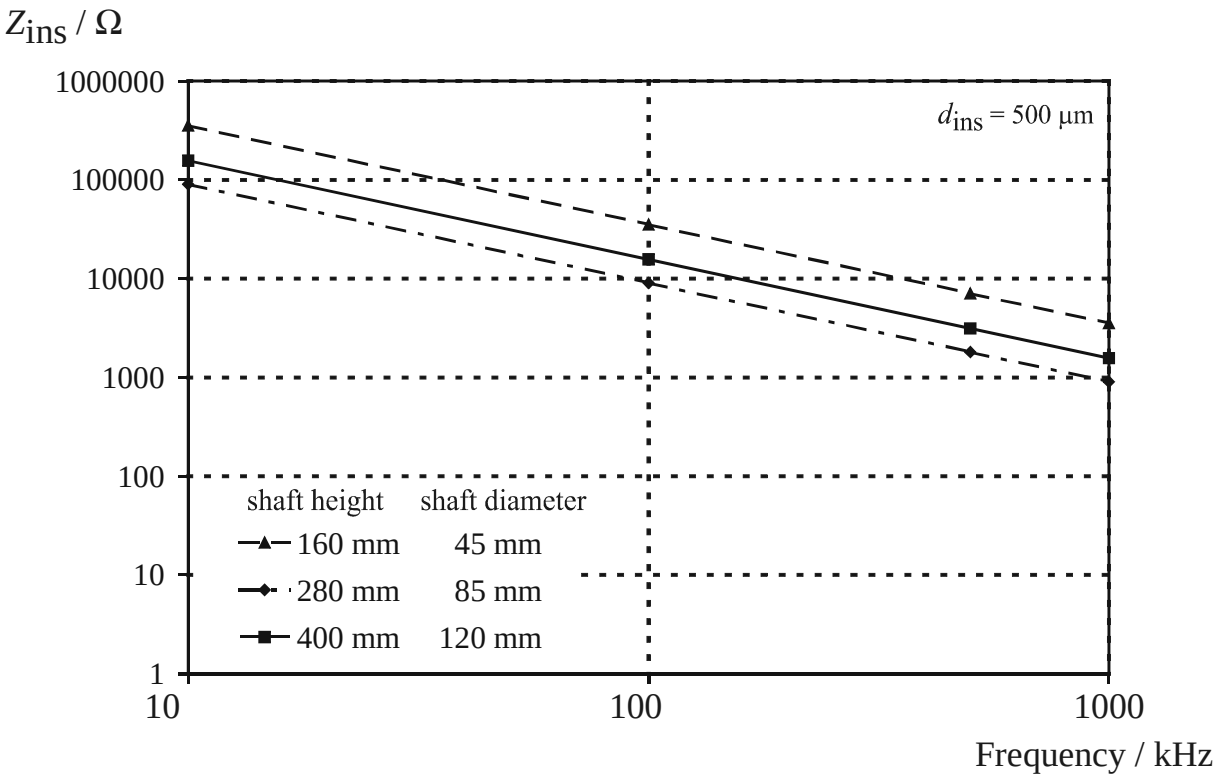

Figure 7.34: Calculated impedance of shaft insulation as function of frequency

K_1 to K_4 are constants to be determined from the particular solution and the initial conditions (7.164).

$$\begin{cases} i_{\mathrm{b}}(t=0) &= 0 \\ v_{\mathrm{c}}(t=0) &= 0 \end{cases} \tag{7.164}$$

The solution for (7.159) to (7.164) is given by (7.165).

$$\begin{aligned} i_{\mathrm{b}}^* &= \frac{\mathrm{C}^*}{\mathrm{D}^*}\Big\{\{\frac{\alpha^*}{\beta^*}\sin(\gamma^*) - \frac{\omega}{\beta^*}\cos(\gamma^*) - \frac{\mathrm{D}^*}{\omega\beta^*}\}e^{-\alpha^* t}\sin(\beta^* t) \\ &+ \sin(\gamma^*)e^{-\alpha^* t}\cos(\beta^* t) + \sin(\omega t - \gamma^*)\Big\} \end{aligned} \tag{7.165}$$

where:

$$\omega^{*2} = \frac{1}{\mathrm{C}_{\mathrm{ins}}(L_{\mathrm{b,Fe}} + L_{\mathrm{b,air}})} \tag{7.166}$$

$$\gamma^* = \tan^{-1}(\frac{-2\alpha^*\omega}{\omega^{*2} - \omega^2}) \tag{7.167}$$

$$\mathrm{C}^* = -\omega^2 \hat{i}_{\mathrm{g}} \frac{L_{\mathrm{g}}}{L_{\mathrm{b,Fe}} + L_{\mathrm{b,air}}} \tag{7.168}$$

$$\mathrm{D}^* = \sqrt{(2\alpha^*)^2 + (\omega^{*2} - \omega^2)^2} \tag{7.169}$$

With the orders of magnitudes of the investigated motors, (7.163) and (7.169) simplify to (7.170) and (7.171). Furthermore, one term for i_{b}^* dominates in (7.165), and (7.165) simplifies to (7.172). The maximum amplitude of the circulating bearing current occurs at the time $\tilde{t}^*$ (7.173) and (7.174).

$$\beta^* \approx \omega^* \tag{7.170}$$

$$\mathrm{D}^* \approx \omega^{*2} \tag{7.171}$$

$$i_{\mathrm{b}}^*(t) \approx -\frac{\mathrm{C}^*}{\mathrm{D}^*}\frac{\mathrm{D}^*}{\omega\beta^*}e^{-\alpha^* t}\sin(\beta^* t) \approx \hat{i}_{\mathrm{g}}\frac{\omega}{\omega^*}\frac{L_{\mathrm{g}}}{L_{\mathrm{b,Fe}} + L_{\mathrm{b,air}}}e^{-\alpha^* t}\sin(\omega^* t) \tag{7.172}$$

$$\max\{|i_{\mathrm{b}}^*|\} = i_{\mathrm{b}}^*(\tilde{t}^*) \tag{7.173}$$

$$\tilde{t}^* = \frac{1}{\omega^*}\tan^{-1}(\frac{\omega^*}{\alpha^*}) \tag{7.174}$$

♦ With consideration of the copper loops which are applied for the bearing current measurement (7.162) and (7.170) to (7.174) become (7.175) to (7.180).

$$\alpha_{\mathrm{L}}^{*} = \frac{R_{\mathrm{b,Fe}}}{2(L_{\mathrm{b,Fe}} + L_{\mathrm{b,air}} + 2L_{\mathrm{cu}})} \tag{7.175}$$

$$\sqrt{\mathrm{D}_{\mathrm{L}}^{*}} \approx \beta_{\mathrm{L}}^{*} \approx \omega_{\mathrm{L}}^{*} = \frac{1}{\mathrm{C}_{\mathrm{ins}}(L_{\mathrm{b,Fe}} + L_{\mathrm{b,air}} + 2L_{\mathrm{cu}})} \tag{7.176}$$

$$i_{\mathrm{bL}}^{*}(t) \approx \hat{i}_{\mathrm{g}} \frac{\omega}{\omega_{\mathrm{L}}^{*}} \frac{L_{\mathrm{g}}}{L_{\mathrm{b,Fe}} + L_{\mathrm{b,air}} + 2L_{\mathrm{cu}}} e^{-\alpha_{\mathrm{L}}^{*} t} \sin(\omega_{\mathrm{L}}^{*} t) \tag{7.177}$$

(7.178)

$$\max\{|i_{\mathrm{bL}}^{*}|\} = i_{\mathrm{bL}}^{*}(\tilde{t}_{\mathrm{L}}^{*}) \tag{7.179}$$

$$\tilde{t}_{\mathrm{L}}^{*} = \frac{1}{\omega_{\mathrm{L}}^{*}} \tan^{-1}\left(\frac{\omega_{\mathrm{L}}^{*}}{\alpha_{\mathrm{L}}^{*}}\right) \tag{7.180}$$

♦ This approach is used to calculate the maximum amplitude of the circulating bearing current for the two motors that showed circulating bearing currents and that were used for the investigations of insulated bearings, motor M110b of the 110 kW power level and motor M500b of the 500 kW power level (7.181 and 7.182) (Circuit parameters for $f = 1$ MHz, $\mu_{\mathrm{r}} = 1000$). Motor $\mathrm{M110b_1/M110b_2}$, $\mathrm{M500b_1/M500b_2}$ and $\mathrm{M110b_{1L}/M110b_{2L}}$, $\mathrm{M500b_{1L}/M500b_{2L}}$ denote use of one/two insulated bearing and - in the case of subscript $_{\mathrm{L}}$ - consideration of the inductivity of copper loops for bearing current measurement for motor M110b and motor M500b respectively. Assuming $\hat{I}_{\mathrm{g}} = \hat{i}_{\mathrm{g}}$, the calculated maximum amplitude $\hat{i}_{\mathrm{b}}^{*}$, respectively $\hat{i}_{\mathrm{bL}}^{*}$, is compared with the results $|\hat{I}_{\mathrm{b}}/\hat{I}_{\mathrm{g}}|/|\hat{I}_{\mathrm{bL}}/\hat{I}_{\mathrm{g}}|$ of Table 7.19 to calculated the reduction achieved by the use of the insulated bearing(s).

Calculation of bearing current with bearing insulation *without* copper loop:

$$\begin{cases} \text{motor M110b}_1 & \hat{i}_{\mathrm{b}}^{*} = 0.06\ \hat{i}_{\mathrm{g}} = 0.20\ |\hat{I}_{\mathrm{b}}/\hat{I}_{\mathrm{g}}|\ \hat{i}_{\mathrm{g}} \\ \text{motor M110b}_2 & \hat{i}_{\mathrm{b}}^{*} = 0.05\ \hat{i}_{\mathrm{g}} = 0.14\ |\hat{I}_{\mathrm{b}}/\hat{I}_{\mathrm{g}}|\ \hat{i}_{\mathrm{g}} \\ \text{motor M500b}_1 & \hat{i}_{\mathrm{b}}^{*} = 0.07\ \hat{i}_{\mathrm{g}} = 0.26\ |\hat{I}_{\mathrm{b}}/\hat{I}_{\mathrm{g}}|\ \hat{i}_{\mathrm{g}} \\ \text{motor M500b}_2 & \hat{i}_{\mathrm{b}}^{*} = 0.05\ \hat{i}_{\mathrm{g}} = 0.20\ |\hat{I}_{\mathrm{b}}/\hat{I}_{\mathrm{g}}|\ \hat{i}_{\mathrm{g}} \end{cases} \tag{7.181}$$

With use of copper loops for bearing current measurement calculated currents are:

$$\begin{cases} \text{motor M110b}_{1\mathrm{L}} & \hat{i}_{\mathrm{bL}}^{*} = 0.07\ \hat{i}_{\mathrm{g}} = 0.37\ |\hat{I}_{\mathrm{bL}}/\hat{I}_{\mathrm{g}}|\ \hat{i}_{\mathrm{g}} \\ \text{motor M110b}_{2\mathrm{L}} & \hat{i}_{\mathrm{bL}}^{*} = 0.05\ \hat{i}_{\mathrm{g}} = 0.27\ |\hat{I}_{\mathrm{bL}}/\hat{I}_{\mathrm{g}}|\ \hat{i}_{\mathrm{g}} \\ \text{motor M500b}_{1\mathrm{L}} & \hat{i}_{\mathrm{bL}}^{*} = 0.09\ \hat{i}_{\mathrm{g}} = 0.38\ |\hat{I}_{\mathrm{bL}}/\hat{I}_{\mathrm{g}}|\ \hat{i}_{\mathrm{g}} \\ \text{motor M500b}_{2\mathrm{L}} & \hat{i}_{\mathrm{bL}}^{*} = 0.05\ \hat{i}_{\mathrm{g}} = 0.25\ |\hat{I}_{\mathrm{bL}}/\hat{I}_{\mathrm{g}}|\ \hat{i}_{\mathrm{g}} \end{cases} \tag{7.182}$$

The calculated reduction of the circulating bearing current with insulated bearings down to (20...40) % compares well with the measured reduction down to (20...40) % (→ Section 5.4, p. 86).

Without copper loops applied for bearing current measurement, what is the real case of operation in the field, the reduction of the circulating bearing currents is larger, it is down to (14...26) %.

♦ The reduction of the circulating bearing current with use of one insulated bearing was also calculated for different thicknesses of the insulating coat and for use of an insulated motor shaft for motor M110b and motor M500b (Table 7.22). The thickness of the insulating coat has to be at least $d_{\mathrm{ins}} = 250\ \mu$m to reduce the circulating bearing currents down to less than 30 %.

Motor	$C_{\mathrm{ins}}^{(1)}$ $d_{\mathrm{ins}} = 50\ \mu$m	$C_{\mathrm{ins}}^{(1)}$ $d_{\mathrm{ins}} = 100\ \mu$m	$C_{\mathrm{ins}}^{(1)}$ $d_{\mathrm{ins}} = 250\ \mu$m	$C_{\mathrm{ins}}^{(2)}$ $d_{\mathrm{ins}} = 500\ \mu$m
$\mathrm{M110b_1}$	$\hat{i}_{\mathrm{b}}^{*} = 0.12\hat{i}_{\mathrm{g}}$	$\hat{i}_{\mathrm{b}}^{*} = 0.09\hat{i}_{\mathrm{g}}$	$\hat{i}_{\mathrm{b}}^{*} = 0.06\hat{i}_{\mathrm{g}}$	$\hat{i}_{\mathrm{b}}^{*} = 0.02\hat{i}_{\mathrm{g}}$
$\mathrm{M110b_1}$	$\hat{i}_{\mathrm{b}}^{*} = 0.41\ \lvert\hat{I}_{\mathrm{b}}/\hat{I}_{\mathrm{g}}\rvert\hat{i}_{\mathrm{g}}$	$\hat{i}_{\mathrm{b}}^{*} = 0.30\ \lvert\hat{I}_{\mathrm{b}}/\hat{I}_{\mathrm{g}}\rvert\hat{i}_{\mathrm{g}}$	$\hat{i}_{\mathrm{b}}^{*} = 0.20\ \lvert\hat{I}_{\mathrm{b}}/\hat{I}_{\mathrm{g}}\rvert\hat{i}_{\mathrm{g}}$	$\hat{i}_{\mathrm{b}}^{*} = 0.06\ \lvert\hat{I}_{\mathrm{b}}/\hat{I}_{\mathrm{g}}\rvert\hat{i}_{\mathrm{g}}$
$\mathrm{M500b_1}$	$\hat{i}_{\mathrm{b}}^{*} = 0.14\hat{i}_{\mathrm{g}}$	$\hat{i}_{\mathrm{b}}^{*} = 0.11\hat{i}_{\mathrm{g}}$	$\hat{i}_{\mathrm{b}}^{*} = 0.07\hat{i}_{\mathrm{g}}$	$\hat{i}_{\mathrm{b}}^{*} = 0.02\hat{i}_{\mathrm{g}}$
$\mathrm{M500b_1}$	$\hat{i}_{\mathrm{b}}^{*} = 0.53\ \lvert\hat{I}_{\mathrm{b}}/\hat{I}_{\mathrm{g}}\rvert\hat{i}_{\mathrm{g}}$	$\hat{i}_{\mathrm{b}}^{*} = 0.40\ \lvert\hat{I}_{\mathrm{b}}/\hat{I}_{\mathrm{g}}\rvert\hat{i}_{\mathrm{g}}$	$\hat{i}_{\mathrm{b}}^{*} = 0.27\ \lvert\hat{I}_{\mathrm{b}}/\hat{I}_{\mathrm{g}}\rvert\hat{i}_{\mathrm{g}}$	$\hat{i}_{\mathrm{b}}^{*} = 0.08\ \lvert\hat{I}_{\mathrm{b}}/\hat{I}_{\mathrm{g}}\rvert\hat{i}_{\mathrm{g}}$

Table 7.22: Calculated bearing currents of insulated bearings for different insulation thicknesses

The induction of circulating bearing currents can be described by an eddy current model and parameters of an equivalent electric circuit derived from the model.
The maximum ratio of the amplitude of the circulating bearing current and the common mode current is 0.354.
The copper loops for measurement of bearing currents decrease the circulating bearing currents at the 110 kW and 500 kW power level by 13 % to 38 %, depending on the frequency of the current and the relative permeability of the stator lamination stack.
The influence of insulated bearings can also be calculated based on the electric circuit. If no copper loops are used, the reduction of the circulating bearing currents is about twice as large as with the loops.
A minimum thickness of the insulating coat of 250 µm is required to reduce the circulating bearing currents down to less than 30 %.

Chapter 8

Practical Rules for Bearing Current Assessment

In practical applications in the field, many parameters may be unknown. Therefore, a flowchart is proposed that might serve as a tool to estimate the endangerment of a drive due to inverter-induced bearing currents and summarizes possible means to prevent damage. The flowchart is *based on the results obtained from the measurements done here*. It is therefore limited to the frame of the research program (Fig. 8.1).

It has to be pointed out that the *assessment of danger* to the bearings due to inverter-induced bearing currents is *based upon experience*. The mechanism of damage to the bearing is not understood to a satisfying extent. Nevertheless, the experience from dc- and low frequency ac-currents, that bearing current densities $J_\mathrm{b} \leq 0.1$ A/mm^2 are not harmful to the bearing, was not falsified by the measurements. Therefore, this limit is suggested as a reasonable limit to work with, until further knowledge is available.

The research project confirmed that *the interaction of several parameters and not a single parameter of the system* causes flow of inverter-induced bearing currents and eventually may lead to bearing damage.

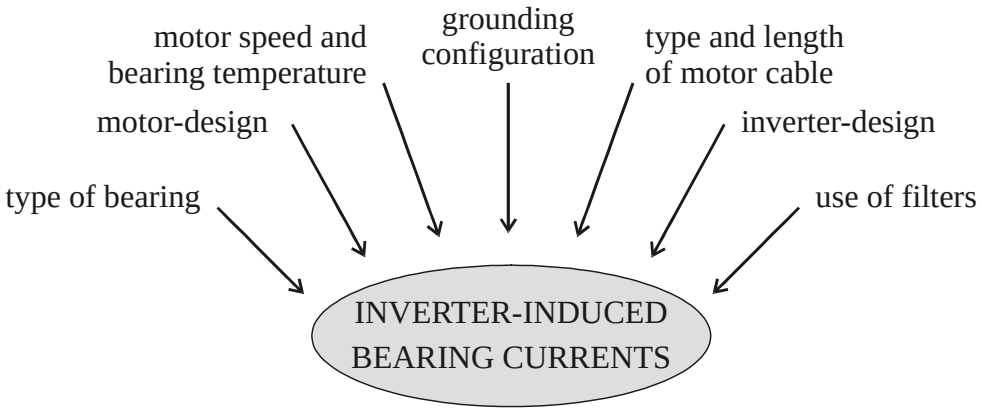

Figure 8.1: Investigated parameters of a variable speed drive system

The *flowchart is based on the strong influence of (a) grounding configuration of the rotor and (b) motor size on the type of bearing current that might occur.* As the different phenomena of inverter-induced bearing currents have different cause-and-effect chains, mitigation techniques have to be used selectively. A *properly meshed grounding system* is *pre-condition* for this flowchart.

♦ ***Rotor grounding configuration*** (Step ①) (Fig. 8.2): The rotor grounding configuration is the first parameter of influence considered, because it *determines if harmful rotor ground currents can flow.*

If the rotor is not grounded, the flowchart has to be continued at step 2. Otherwise, the type of motor cable - shielded or unshielded motor cable - is of importance. If a shielded motor cable is used and properly connected at both motor- and inverter-side with a 360°-connection, the impedance of the stator housing is generally low enough that hardly any rotor ground current flows.

If the grounding connection of the rotor cannot be eliminated, and shielded motor cable cannot be used, or, if the shielded motor cable is several hundred meters long, mitigation techniques for rotor ground currents should be applied. Otherwise, the flowchart can be continued at step 2.

♦ ***Influence of motor size*** (Step ②) (Fig. 8.3): The size of the motor determines strongly the type of bearing currents occurring. If no rotor ground currents flow, for small motors *below* about shaft height 100 mm, only *EDM-bearing currents* occur. With large motors *above* about shaft height 280 mm, *circulating bearing currents* dominate, with the largest amplitudes at low motor speed. Both types of bearing currents may occur at motors with shaft height between 100 mm and 280 mm, but the general tendency is for circulating bearing currents with increasing shaft height, notably when short, shielded motor cables are used.

The amplitude of the circulating bearing currents can be estimated from the ground current of the motor. This is done in step 3 of the flowchart.

The situation is different for the case of EDM-currents, where further calculations require knowledge of many parameters of the drive. Generally, the endangerment of the bearings is likely to increase with the reduction of the motor size because of the decrease of the contact area in the bearings. No further estimations are possible at this point, and it has to be decided wether mitigation techniques (Fig. 8.6) should be applied or not.

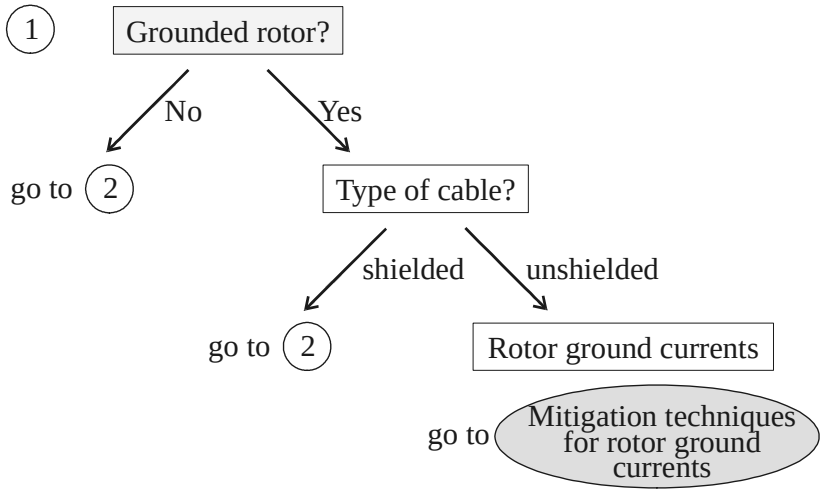

Figure 8.2: Flowchart concerning: ***Rotor grounding configuration*** (Step ①)

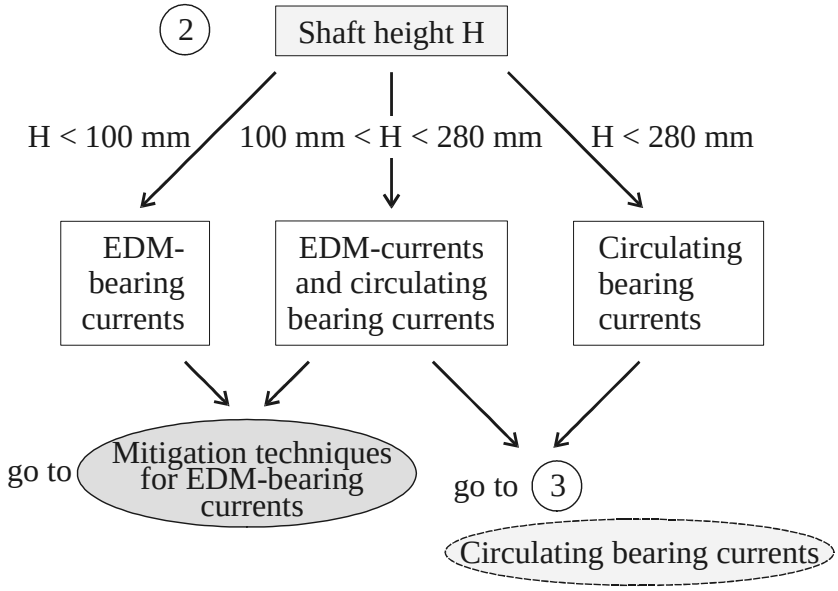

Figure 8.3: Flowchart concerning: ***Influence of motor size*** (Step ②)

♦ ***Estimation of the amplitude of the circulating bearing current*** (Step ③) (Fig. 8.4): The amplitude of the bearing current $\hat{i}_\mathrm{b}$ can be estimated from the amplitude of the ground current $\hat{i}_\mathrm{g}$ using (8.1) to (8.4):

▷ two conventional bearings:

$$\hat{i}_b \;\leq\; 0.4\;\hat{i}_g \qquad (8.1)$$

▷ one insulated, one conventional bearing:

$$\hat{i}_b \;\leq\; 0.2\;\hat{i}_g \qquad (8.2)$$

▷ two insulated bearings:

$$\hat{i}_b \;\leq\; 0.1\;\hat{i}_g \qquad (8.3)$$

▷ one or two hybrid bearings:

$$\hat{i}_b \;\approx\; 0 \qquad (8.4)$$

It has to be noted that these relationships are upper limits. The ratios $\hat{i}_\mathrm{b}/\hat{i}_\mathrm{g}$ are often

smaller. The apparent bearing current density J_b can be computed from the estimated bearing current amplitude and the *Hertz*'ian contact areas A_H of the bearings. However, calculation of A_H is complex.

If the amplitude of the ground current $\hat{i}_g$ is not known, it has to be measured by experts or estimated, otherwise use of mitigation techniques for circulating bearing currents have to be considered.

♦ ***Estimation of the amplitude of the ground current*** (Fig. 8.5): The amplitude of the ground current $\hat{i}_g$ depends strongly on the stator winding-to-frame capacitance C_{wf} and the dv_{Lg}/dt of the line-to-earth voltage v_{Lg} at the motor terminals. The value of C_{wf} can either be measured (Section 3.5, p. 37), or estimated using (8.5).

$$C_{wf} \;=\; 0.00024 \cdot H^2 - 0.039 \cdot H + 2.2 \tag{8.5}$$

where:

C_{wf} in nF,
H: shaft height in mm

If the value of dv_{Lg}/dt of the line-to-earth voltage v_{Lg} is not known, it needs to be measured or estimated. In case of $dv_{Lg}/dt > 0.5$ kV/μs, it has to be distinguished between electrical long and short motor cable. A cable is considered as electrically long, if the cable lengths l_c is equal or larger than the critical cable length $l_{c,crit}$, $l_c \geq l_{c,crit}$. It is considered as electrically short, if $l_c > l_{c,crit}$. The critical cable length l_c is given by the velocity of electromagnetic waves in the cable (cable velocity) v_{cable} and the rise time of the voltage pulse t_r (8.6).

$$l_c \;=\; v_{cable}\frac{t_r}{2} \tag{8.6}$$

where:

v_{cable} = cable velocity $\approx 150 \cdot 10^6$ m/s.

The amplitude of the ground current $\hat{i}_g$ can then be estimated using (8.7) to (8.9).

▷ $dv_{Lg}/dt > 0.5$ kV/μs:

∗ electrically long motor cable:

$$\hat{i}_g \;\leq\; 1.5\ 2/3\ dv_{Lg}/dt\ C_{wf} \tag{8.7}$$

∗ electrically short motor cable:

$$\hat{i}_g \;\leq\; 1.5\ dv_{Lg}/dt\ C_{wf} \tag{8.8}$$

▷ $dv_{Lg}/dt \leq 0.5$ kV/μs:

$$\hat{i}_g \;\leq\; dv/dt_{Lg}\ 2\ C_{wf} \tag{8.9}$$

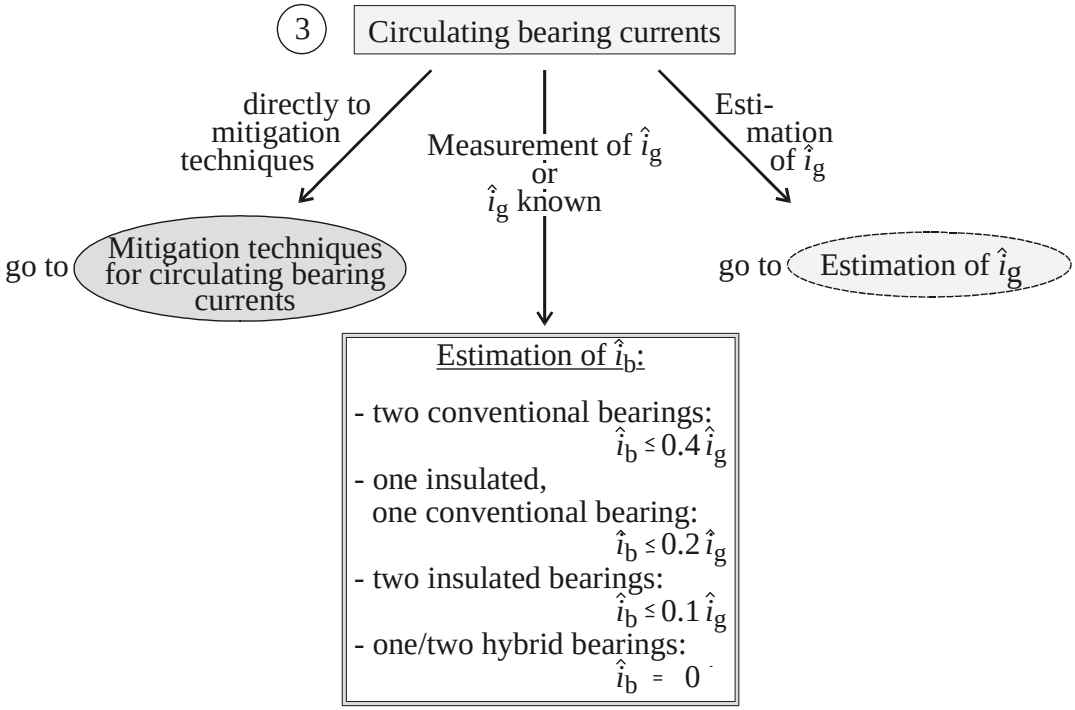

Figure 8.4: Flowchart concerning: ***Estimation of the amplitude of the circulating bearing current*** (Step ③)

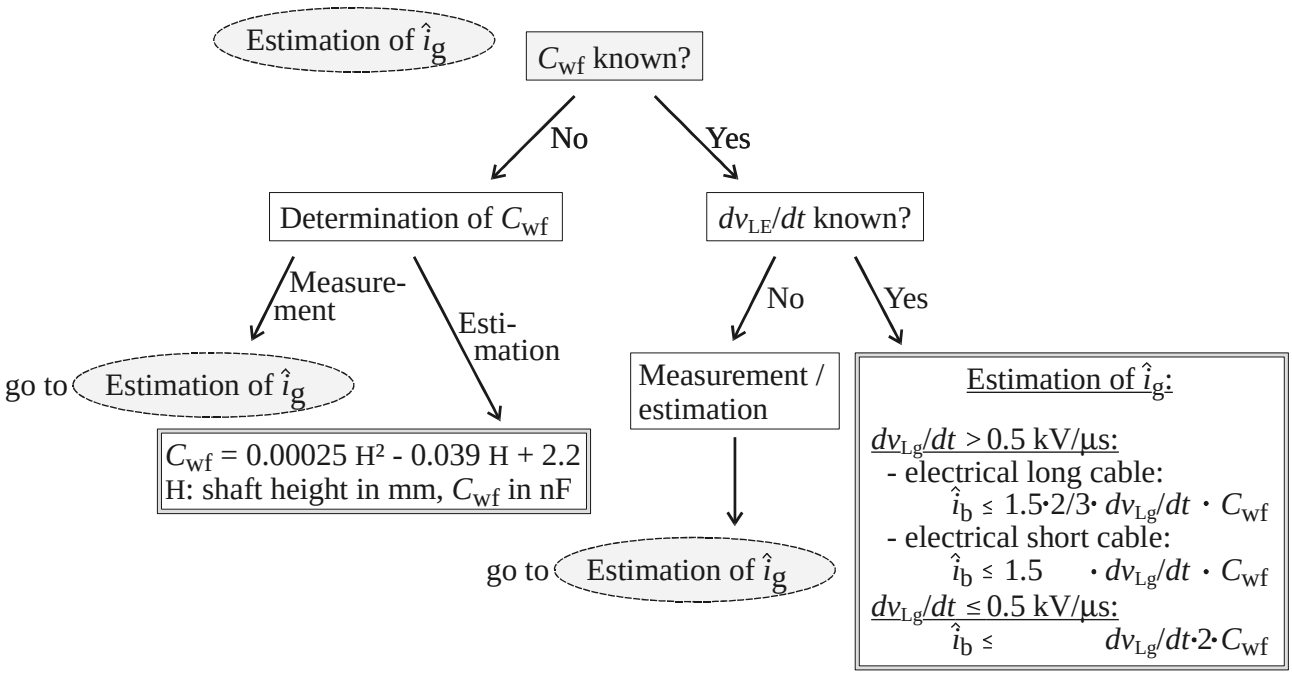

Figure 8.5: Flowchart concerning: ***Estimation of the amplitude of the ground current***

♦ ***Mitigation techniques for different types of inverter-induced bearing currents*** (Fig. 8.6): The common source of all inverter-induced bearing currents is the common mode voltage of the inverter. As the causal chain of the different bearing current phenomena is different, mitigation techniques have to be chosen according to the type of bearing current that shall be reduced or eliminated. Fig. 8.6 summarizes different mitigation techniques for different types of inverter-induced bearing currents. The mitigation techniques may be chosen according to the possibilities shown in Table 5.1.

The proposed flowchart might serve as a tool to assess the endangerment of bearings due to inverter-induced bearing currents where many parameters of a drive are unknown. First, the grounding configuration of the rotor is classified. Then, the size of the motor is considered to determine the type of possibly occurring bearing current. This is followed by instructions to estimate the amplitude of the circulating bearing currents. The chart also summarizes possible means to prevent bearing damage.

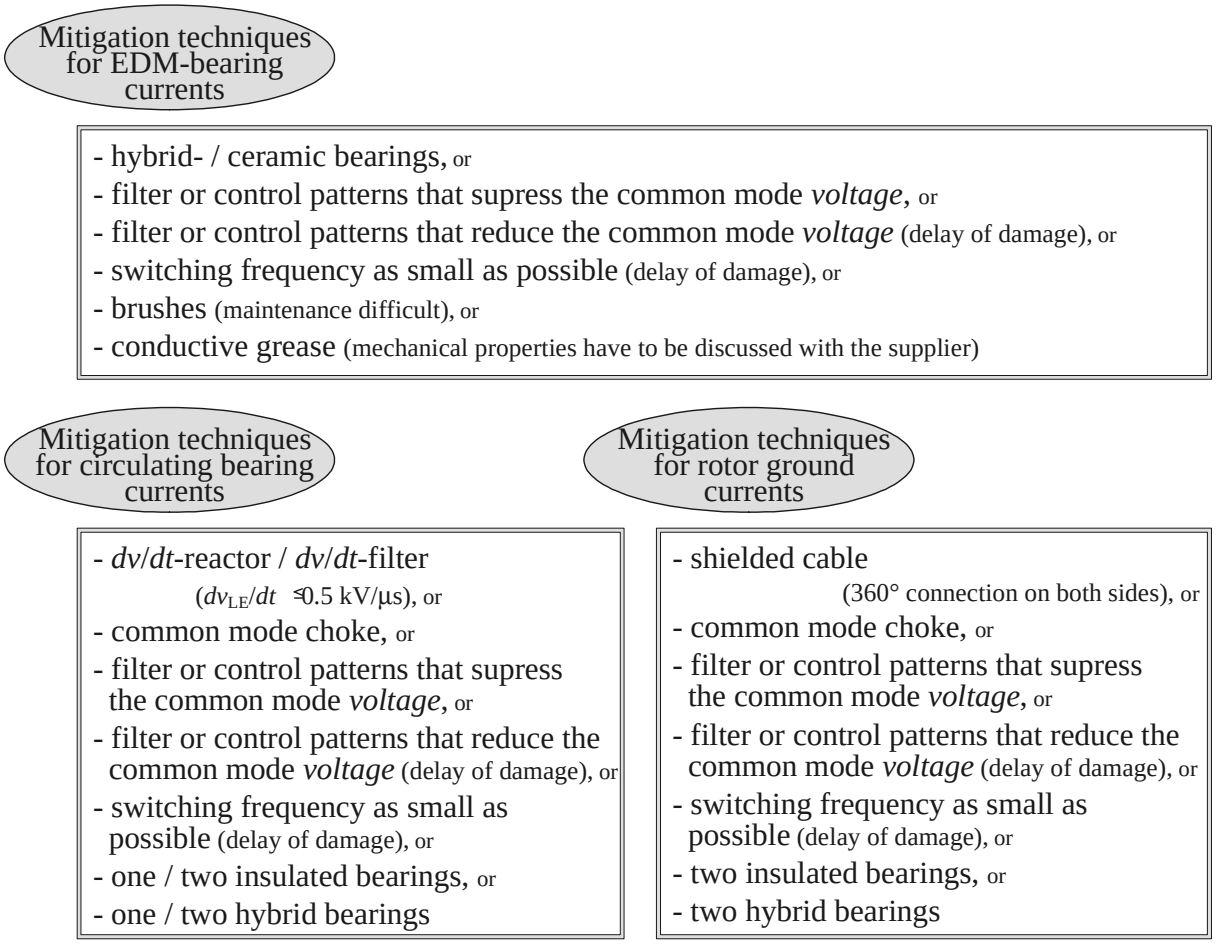

Figure 8.6: ***Mitigation techniques for different types of inverter-induced bearing currents***

Chapter 9

Conclusions

The reason for existence of inverter-induced bearing currents is the inverter-output common mode voltage. These bearing currents are:

► ***Capacitive bearing currents***: The v_b/dt of the bearing voltage causes along with the bearing capacity small, capacitive bearing currents that are, according to the present standard of knowledge, not harmful to the bearing. Therefore, this type of bearing current is not discussed any further.

► ***EDM-bearing currents*** (*E*lectric *D*ischarge *M*achining): The common mode source charges the bearings via a capacitive voltage divider resulting in a discharge current pulse, when the threshold voltage of the bearings is surpassed.

► ***Circulating bearings currents***: The high dv_{Lg}/dt of the line-to-earth voltage at the motor terminals generates a considerable high-frequency ground current. This current excites a circular magnetic flux which induces a high-frequency shaft voltage that may cause circulating bearing currents.

► ***Rotor ground currents***: In some configurations, the rotor may be connected to earth potential with a significantly lower impedance path than the grounding of the stator housing (e.g. via the driven load). In these cases, the ground current generated by the high dv_{Lg}/dt of the line-to-earth voltage at the motor terminals flows partly as rotor ground current via the bearings of the motor.

A research program for systematic investigation of the influence of selected parameters of an adjustable drive system on the bearing current phenomena had been set up as an industrially financed AiF-Project (*A*rbeitsgemeinschaft *I*ndustrieller *F*orschungsvereinigungen "Otto von Guericke" e.V.), initiated and accompanied by the ZVEI (*Z*entral *V*erband *E*lektrotechnik- und Elektronik*I*ndustrie e.V.). The investigations included a survey of different selected mitigation techniques to evaluate the effectiveness of these techniques for different types of bearing currents. All measurements were done under the same conditions, using identical measurement techniques for all configurations.

The influence of the following parameters was analyzed:

1. inverter-design (switching frequency, control method),

2. motor-inverter-connection (motor cable length and motor cable type, grounding configuration, use of filters)

3. motor operating parameters (motor speed, bearing temperature)

4. motor design (motor size, bearing voltage ratio (BVR), type of ball bearing insulation).

5. motor-inverter-combination.

►►► Table 9.1 summarizes the influence of the investigated parameters of an adjustable speed drive system on the different types of inverter-induced bearing currents.

1. Influence of inverter switching frequency and control method: Switching frequency and control method (common mode voltage not eliminated) do not influence the magnitude of the bearing currents significantly, but the occurrence rate increases about linearly with switching frequency.

2. Motor-Inverter-Connection:

Influence of motor cable length: The EDM-bearing currents remain unaffected by the length of the motor cable. The influence on the circulating bearing currents is not significant. If unshielded cable is used and the rotor is grounded, rotor ground currents increase with longer motor cable.

Influence of shielded versus unshielded motor cable: Use of shielded motor cable, if properly connected with a 360°-connection on both motor and inverter side, usually eliminates rotor ground currents. EDM-bearing currents remain unaffected, and circulating bearing currents increase only slightly.

Influence of rotor grounding configuration: Rotor ground currents of considerable magnitude due to a parasitic current path e.g. via grounded rotor may destroy bearings within a few months of operation time and have to be eliminated by a low impedance grounding connection of the stator housing.

3. Influence of motor operating parameters "motor speed" and "bearing temperature": The operational parameters "motor speed" and "motor bearing temperature" influence the thickness of the lubrication film, thus the electrical properties of the bearing and type and magnitude of the occurring bearing currents.

EDM-bearing currents show a maximum amplitude as function of motor speed and bearing temperature.

Circulating bearing currents and rotor ground currents increase with decreasing motor speed and increasing bearing temperature. Hence, the largest circulating bearing currents and rotor ground currents occur at low motor speed and elevated bearing temperature.

Influencing parameter	Type of bearing current occurring		
	EDM bearing current	Circulating bearing current	Rotor ground current
1. Inverter			
Switching frequency	little influence on amplitude, but on the frequency of occurrence		
Control method (v_{com} not eliminated)	little influence on amplitude, but on the frequency of occurrence		
2. Motor-Inverter-Connection			
Motor cable length	no influence	little influence	little influence
Use of shielded instead of unshielded motor cable	no influence	influence	significant influence
Grounded motor shaft	no influence	no influence	significant influence, if unshielded motor cable is used
Filters that reduce the dv_{Lg}/dt but that do *not* eliminate the common mode voltage	no influence	significant influence	significant influence
Filters that *do* eliminate the common mode voltage	significant influence	significant influence	significant influence
3. Motor Operating Parameters			
Motor speed	influence		
Bearing temperature	influence		
4. Motor Design			
Motor size	little influence	significant influence	significant influence
Bearing Voltage Ratio (BVR)	little influence	no influence	no influence
Number of parallel winding branches	no influence	influence for motors of same size (shaft height)	
Type of ball bearing insulation (conventional bearing/ insulated bearing/ hybrid bearing)	significant influence	significant influence	significant influence
5. Motor-Inverter-Combination			
	little influence		

Table 9.1: Influence of investigated system parameters on the different types of inverter-induced bearing currents (single row, deep grove ball bearings)

4. Influence of motor design parameter "motor size" (shaft height): If no rotor ground currents exist, EDM-bearing currents dominate at small motors, whereas circulating bearing currents dominate at large motors. The amplitude of the circulating bearing currents increases with increasing motor size.

Influence of bearing voltage ratio (BVR): The BVR is generally low for standard squirrel-cage induction motors. At bearing temperature typical for load operation, the bearing voltage is no longer determined by the common mode voltage, as the lubrication film discharges frequently before reaching maximum possible bearing voltage.

Influence of attenuation factor of stator winding: When comparing motors of the same size, the attenuation factor of the winding influences the magnitude of the ground current. Yet, this parameter is much less important than the motor size in general.

5. Motor-inverter-combination: At each power level, two motors and up to three inverters of different manufacturers were investigated. For a given power level, no significant difference between the endangerment of the bearings, evaluated by the calculated apparent bearing current density, was found between the different motor-inverter-combinations.

Mitigation Techniques for Inverter-Induced Bearing Currents

Mitigation techniques have to be chosen as function of the type of bearing current occurring. They can be separated into ***(a)*** *mitigation techniques on inverter side* and ***(b)*** *counter-measures within the motor.* The following techniques were investigated: ***(a)*** *dv/dt-filter, dv/dt-reactors, sinusoidal filters, common mode chokes, common mode voltage filters*, ***(b)*** *use of one or two insulated bearings, use of hybrid bearings.*

(a) Influence of filters: Filters that do not eliminate the common mode voltage do not affect the amplitude of EDM-bearing currents. Circulating bearing currents and rotor ground currents are reduced with decreasing dv_{Lg}/dt of the line-to-earth voltage at the motor terminals. The degree of reduction depends on the filter.

Filters that do cancel the common mode voltage at the motor terminals eliminate all types of bearing currents, as they remove the source of these currents.

(b) Influence of bearing insulation: Use of one insulated bearing reduces circulating bearing currents down to at least less than 40 %, use of two insulated bearings to at least less than 20 %. According to the present understanding, insulated bearings do *not* reduce the "real" bearing currents occurring inside the bearing.

Use of **two hybrid bearings** eliminates EDM-bearing currents, circulating bearing currents and rotor ground currents.

Tests for Bearing Damage Assessment

A series of tests for bearing damage assessment was carried out to obtain better understanding of the mechanism of damage and allow prediction of the endangerment of the bearings due to inverter-induced bearing currents. The influence of bearing current amplitude, bearing current density, inverter switching frequency, inverter control method, motor time of operation and type of bearing current (EDM-bearing current / rotor ground current) on the bearing damage was studied with 44 ball bearings comprising 22 bearings type 6209 C3, 11 bearings type 6308 C3 and 11 bearings type 6309 C3. Analysis was done by industrial partners, using visual inspection, light-optical microscopy, scanning electron microscopy and infrared spectroscopy of the evaporated grease.

Results: The mean diameter of pitting holes due to EDM-current pulses values about 0.5 μm. The generation of fluting cannot be explained on the basis of the performed investigation. The parameter ***electrical bearing stress*** **"W"**, which is proportional to an energy, was introduced:

$$\boldsymbol{W = \text{apparent bearing current density } J_\mathrm{b} \times \text{time of operation } t_\mathrm{op} \times \text{inverter switching frequency } f_\mathrm{c}}$$

The deterioration of the grease, shown by the indicator parameter "reduction of the carboxylic acid" rises in a first order approach linearly with W. The "grade of melting of the bearing race" also increases with W.

Modeling of Bearing and Ground Currents

▶ The ***bearing*** is a non-linear electrical impedance. It is mainly capacitive when the motor speed is high enough (typically above 100 /min) to result in buildup of an insulating film from the lubricating grease. After electrical breakdown of the insulating film, the bearing acts mainly ohmic.

▶ The amplitude of the ***EDM-bearing currents*** depends on the breakdown voltage of the bearing that is strongly determined by motor speed and bearing temperature and on the inverter dc-link voltage. The waveform of the current is also strongly influenced by the magnitude of the capacitance between stator winding and rotor. The amplitude of the "real", not measurable bearing current is assumed to value 2/3 of the measured current amplitude.

▶ The maximum amplitude of ***circulating bearing currents*** is about 0.4 times the amplitude of the ground current. Circulating bearing currents increase with the cube of the motor size and do not occur at small motors (typically below shaft height 100 mm), because the shaft voltage is not large enough to lead to puncturing of the lubricating film. The occurring bearing currents are about 13 % to 38 % larger if no copper loop is applied for bearing current measurement.

► ***Ground currents*** are generated by the interaction between high dv_{Lg}/dt of the line-to-earth voltage at the motor terminals and the motor winding to frame capacitance. Ground currents increase with the cube of the motor size. When comparing motors of the same size, the number of parallel winding branches has an influence on the magnitude of the ground current. However, this influence is much smaller than the one of the motor size (shaft height) in general.

Endangerment due to Inverter-Induced Bearing Currents

The *assessment of the endangerment of bearings due to inverter-induced bearing currents is still based upon experience.* The limit of apparent bearing current density of $J_b \leq 0.1$ A/mm^2, which is the considered limit for dc- and low frequency ac-bearing currents not to be harmful, was not disapproved. It is therefore suggested to work with this limit until deeper understanding has been obtained.

► ***Small motors with small bearings*** and therefore small *Hertz*'ian contact area have elevated bearing current densities. Hence, they are sensitive to ***bearing damage due to EDM-bearing currents***.

► ***Large*** motors are sensitive to ***bearing damage due to large circulating bearing currents***.

► ***All*** motors are sensitive to ***bearing damage due to rotor ground currents***, if the rotor is grounded.

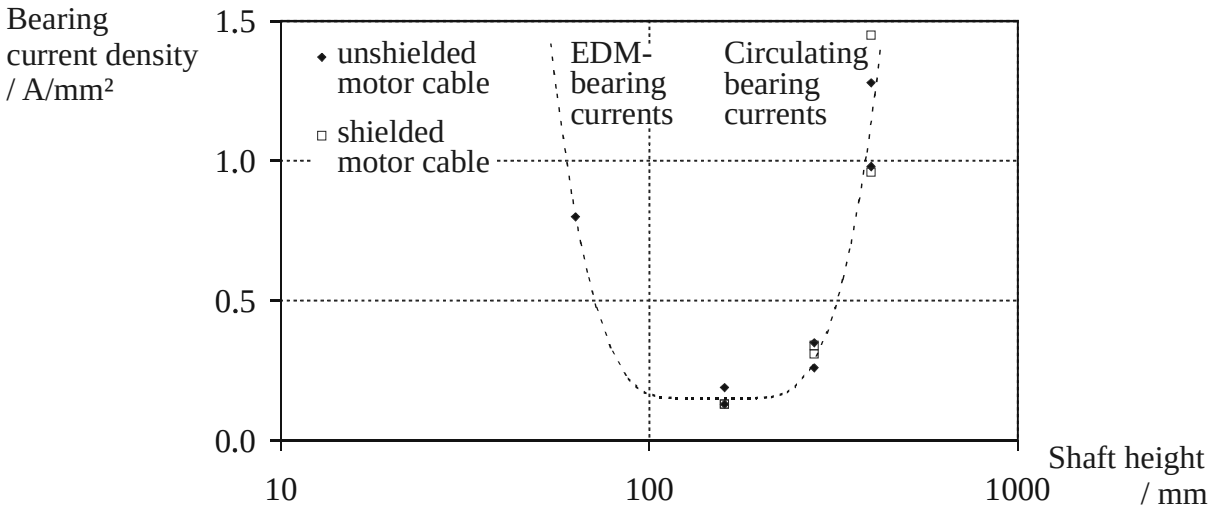

Figure 9.1: Apparent bearing current density as function of motor size (shaft height), values based on measured bearing currents and calculated *Hertz*'ian contact areas, main drive configuration E1, motor cable lengths l_c: 1 kW power level: $l_c = 1$ m, 11 kW power level: $l_c = 50$ m, 110 kW and 500 kW power level: $l_c = 10$ m, bearing temperature $\vartheta_b \approx 70°C$

A thorough analysis of the qualitative and quantitative influence of different parameters on the different bearing current phenomena was carried out on motors from less than 1 kW up to 500 kW rated power. All measurements were done under the same conditions, using identical measurement techniques for all configurations. The results show that the size of the motor is important to determine the type of possibly occurring bearing currents, and the grounding configuration of the rotor defines if rotor ground currents may flow. The effectiveness of mitigation techniques for inverter-induced bearing currents depends on the type of bearing current to be reduced or eliminated. Therefore, mitigation techniques have to be chosen for different drive systems selectively.

A series of tests for bearing damage assessment was carried out. Despite manifold investigations, the phenomena of the generation of corrugation cannot be explained with today's understanding. However, the deterioration of the bearing grease was found to correlate with the stress on the bearings. A parameter "W" that is proportional to an energy was introduced to quantify the stress.

Models that are based on the design parameters were proposed. The models give physical explanations for the measured correlations. Notably, they show that the circulating bearing currents increase with the cube of the shaft height and do not occur at small motors, and that the theoretical maximum amplitude values about 0.4 times the amplitude of the ground current. They allow calculation of the ground current and give reasons for the increase of the amplitude of the ground current with an increased number of parallel winding branches.

Symbols and Abbreviations

Symbols

Symbol	Unit	Name
a	-	number of parallel winding branches
A_{H}	m^2	*Hertz*'ian contact area
$A_{\mathrm{crater,av}}$	m^2	average crater area
A_{rf}	m^2	area between rotor and frame with assumption of closed stator slots
b_{o}	m	width of slot opening
b_{s}	m	stator slot width
$b_{\mathrm{s,cu}}$	m	width of copper in stator slot
b_{Fe}	m	thickness of lamination sheet
B	m	width of bearing
B_δ	T	average magnetic field density in the air gap along circumference
$\hat{B}_\delta$	T	maximum magnetic field density in the air gap
C	F	capacitance
C_{b}	F	bearing capacitance
C_{b}^*	F	bearing capacitance of insulated or hybrid bearing
C_{b1}	F	capacitance between bearing balls and outer bearing ring
C_{b2}	F	capacitance between bearing balls and inner bearing ring
$C_{\mathrm{b,a}}$	F	bearing capacitance of bearing opposite to bearing with occurring EDM-current pulse
$C_{\mathrm{b,b}}$	F	bearing capacitance of bearing with occurring EDM-current pulse
$C_{\mathrm{b,DE}}$	F	bearing capacitance on DE
$C_{\mathrm{b,NDE}}$	F	bearing capacitance on NDE
C_{c}	F	case capacitance of a stator coil
C_{cable}	F	cable capacitance
C_{i}	F	capacitance of insulating layer of end-shield
$C_{\mathrm{i,DE}}$	F	capacitance of insulating layer of end-shield on DE
$C_{\mathrm{i,NDE}}$	F	capacitance of insulating layer of end-shield on NDE

Symbol	Unit	Name
C_{ins}	F	capacitance of insulating coat
$C_{\mathrm{ins}}^{(1)}$	F	capacitance of insulating coat at bearing outer ring
$C_{\mathrm{ins}}^{(2)}$	F	capacitance of insulating coat at motor shaft
C_{Lg}	F	line-to-earth capacitance of sinusoidal filter
C_{LL}	F	line-to-line capacitance of sinusoidal filter
C_{m1}	F	measured capacitance 1, measurement of C_{wf} and C_{ph}
C_{m2}	F	measured capacitance 2, measurement of C_{wf} and C_{ph}
C_{m3}	F	measured capacitance 3, measurement of C_{wf} and C_{ph}
C_{m4}	F	measured capacitance 4, measurement of C_{rf}
C_{s}	F	series capacitance of a stator coil
C_{ph}	F	phase-to-phase capacitance
C_{rf}	F	rotor-to-frame capacitance
C'_{rf}	F	equivalent rotor-to-frame capacitance, $C_{\mathrm{rf}} + C_{\mathrm{b,a}}$
C^{*}_{rf}	F	equivalent rotor-to-frame capacitance with use of insulated bearing, (7.60)
C^{**}_{rf}	F	equivalent rotor-to-frame capacitance with use of two insulated bearings, (7.64)
C_{wf}	F	stator winding-to-frame capacitance
C_{wr}	F	stator winding-to-rotor capacitance
C_{wr0}	F	part of air gap and slot opening of C_{wr}
C_{wr1}	F	part of slot wedge and slot lining of C_{wr}
d_{b}	m	mean bearing diameter
d_{bi}	m	bearing bore inner diameter
$d_{\mathrm{crater,av}}$	m	average crater diameter
d_{slot}	m	thickness of slot lining (insulation)
d_{ins}	m	thickness of insulating layer
d_{wire}	m	diameter of wire
d_{re}	m	rotor lamination outer diameter
d_{ri}	m	rotor lamination inner diameter
d_{se}	m	stator lamination outer diameter
d_{si}	m	stator lamination inner diameter
D_{b}	m	bearing outer diameter
D_{rf}	$\mathrm{As/m^2}$	average electric flux density between rotor and frame along circumference
E	$\mathrm{N/m^2}$	*Young's* modulus of elasticity
E'	$\mathrm{N/m^2}$	effective modulus of elasticity
E_{rf}	V/m	average electric field strength between rotor and frame along circumference

Symbol	Unit	Name
f	Hz	frequency
f_0	Hz	resonance frequency of filter
f_a	Hz	limiting frequency for uniform voltage distribution
f_b	Hz	limiting frequency for possibility of wave propagation
f_c	Hz	inverter switching (chopping) frequency
$f_\mathrm{cut\text{-}off}$	Hz	cut-off frequency
f_s	Hz	fundamental frequency of motor
f_sr	Hz	rated motor frequency
F_A	N	axial bearing force
F_c	-	form factor for curly surface of random-wound winding
F_R	N	radial bearing force
G	-	material parameter
$h_\mathrm{lb,min}$	m	minimum thickness of lubrication film
h_o	m	height of slot opening
$h_\mathrm{wedge+ins}$	m	thickness of slot wedge + thickness of slot lining
h_s	m	height of slot
$h_\mathrm{s,cu}$	m	height of one conductor
H	m	shaft height
$\underline{\vec{H}}$	A/m	complex vector of magnetic field strength
H_cir	A/m	circular magnetic field strength
$\underline{H}_\mathrm{r}$	A/m	complex magnetic field strength in radial (r-)direction
$\underline{H}_\mathrm{z}$	A/m	complex magnetic field strength in axial (z-)direction
$\underline{H}_\varphi$	A/m	complex magnetic field strength in azimuthal (φ-)direction
i_1	A	current from frame to rotor
i_1g	A	current contribution from stator winding to frame
i_2	A	current contribution from rotor to frame
i_2g	A	ground current contribution from rotor
i_b	A	bearing current
$\hat{i}_\mathrm{b}$	A	bearing current, peak value
i_b^*	A	bearing current with use of insulated bearing(s),
$\hat{i}_\mathrm{b}^*$	A	bearing current with use of insulated bearing(s), peak value
$i_\mathrm{b,cap}$	A	capacitive bearing current
$i_\mathrm{b,EDM}$	A	EDM bearing current
i_bL	A	measurable current in copper loop
i_bL^*	A	measurable current in copper loop with use of one insulated bearing

Symbol	Unit	Name
i_{bL}^{**}	A	measurable current in copper loop with use of two insulated bearings
$\hat{i}_{\mathrm{bL}}$	A	measurable current in copper loop, peak value
$\hat{i}_{\mathrm{bL}}^{*}$	A	measurable current in copper loop with use of one insulated bearing, peak value
$\hat{i}_{\mathrm{bL}}^{**}$	A	measurable current in copper loop with use of two insulated bearings, peak value
$i_{\mathrm{c,cap}}$	A	capacitive cable current
i_{com}	A	common mode current
$i_{\mathrm{com,sheet}}$	A	common mode current per sheet
i_{u}	A	phase current, phase U
i_{v}	A	phase current, phase V
i_{w}	A	phase current, phase W
i_{g}	A	stator ground current
i_{rg}	A	rotor ground current
I_1	A	current at brake-off
I_{arc}	A	arc current
$\underline{I}_{\mathrm{b}}$	A	complex bearing current
$\underline{I}_{\mathrm{b}}^{*}$	A	complex bearing current with use of one insulated bearing
$\underline{I}_{\mathrm{bL}}$	A	complex measurable current in copper loop
$\underline{I}_{\mathrm{bL}}^{*}$	A	complex measurable current in copper loop with use of one insulated bearing
$\underline{I}_{\mathrm{com}}$	A	complex common mode current
$\underline{I}_{\mathrm{g}}$	A	complex stator ground current
I_{r}	A	rated motor current, rms-value
$I_{\mathrm{r,output}}$	A	rated inverter output current, rms-value
J	$\mathrm{A/m^2}$	local current density
J_{arc}	$\mathrm{A/m^2}$	bearing current density of current arc
J_{b}	$\mathrm{A/m^2}$	apparent bearing current density
k	-	sheet number
k_{c}	-	*Carter*-factor
k_{f}	-	slot fill factor
k_{r}	-	increase of resistance of winding part embedded in slot at ac-, as compared to dc-operation
k_{rw}	-	increase of resistance of winding overhang at ac-, as compared to dc-operation

Symbol	Unit	Name
k_{x}	-	decrease of slot leakage inductance at ac-, as compared to dc-operation
K	-	ratio of semi axes of (*Hertz*'ian) contact area
l_{b}	m	distance between bearing seats
l_{c}	m	cable length
$l_{\mathrm{c,crit}}$	m	critical cable length
l_{Fe}	m	length of stator lamination stack
l_{wire}	m	length of winding per phase
L	H	inductance
$L_{(\mathrm{a})}$	H	inductance of one lamination sheet of model (a)
$L_{(\mathrm{a}),\mathrm{sum}}$	H	inductance of lamination stack of model (a)
$L_{(\mathrm{b})}$	H	inductance of one lamination sheet of model (b)
$L_{(\mathrm{b}),\mathrm{sum}}$	H	inductance of lamination stack of model (b)
$L_{\mathrm{b,air}}$	H	inductance of area enclosed by circulating bearing current given by air gap and the end-winding cavity
$L_{\mathrm{b,air,ew}}$	H	$L_{\mathrm{b,air}}$, part of end-winding cavity
$L_{\mathrm{b,air,gap}}$	H	$L_{\mathrm{b,air}}$, part of air gap
$L_{\mathrm{b,Fe}}$	H	internal inductance of bearing current path through stator lamination stack
$L_{\mathrm{b,i}}$	H	internal inductance of bearing current path outside stator lamination stack
$L_{\mathrm{b,ia}}$	H	$L_{\mathrm{b,i}}$, part of frame outside stack
$L_{\mathrm{b,ib}}$	H	$L_{\mathrm{b,i}}$, part of end-shield on DE and NDE
$L_{\mathrm{b,ic}}$	H	$L_{\mathrm{b,i}}$, part of shaft outside rotor lamination stack
$L_{\mathrm{b,id}}$	H	$L_{\mathrm{b,i}}$, part of end sheet on DE and NDE of rotor lamination stack
$L_{\mathrm{b,ie}}$	H	$L_{\mathrm{b,i}}$, part of resurfaced rotor lamination stack
L_{com}	H	zero sequence inductance
L_{cu}	H	inductance of copper loop applied for bearing current measurement
L_{Fe}	H	internal inductance of common ground current path through stator lamination
L_{g}	H	internal inductance of the path of the ground current through the stator lamination
L_{ph}	H	inductance of phase reactor
L_{r}	m	effective length of rolling element
$L_{\sigma\mathrm{s}}$	H	stator leakage inductance per phase
$L'_{\sigma\mathrm{s}}$	H	stator leakage inductance per coil at $\approx$ 1MHz

Symbol	Unit	Name
$L_{\sigma s,sl}$	H	stator slot leakage inductance per phase
$L_{\sigma s,ew}$	H	stator end-winding leakage inductance per phase
$L_{\sigma s,k}$	H	stator harmonic leakage inductance per phase
n	1/min	motor speed
n_{arc}	1/min	maximum motor speed
n_b	1/min	rotational speed of bearing balls
n_c	1/min	cage speed
n_r	1/min	rated speed
n_s	1/min	synchronous speed
N_{arc}	-	number of arcs
N_b	-	number of rolling elements of a roller bearing
N_c	-	number of turns per coil
N_{cu}	-	number of wires with diameter d_{cu}
N_{Fe}	-	number of sheets of stator lamination stack
N_s	-	sampling size
N_{sl}	-	number of conductors upon each other
p	-	number of pole pairs
P	W	power
P_r	W	rated power
q	-	number of slots per pole and phase
q_{series}	-	number of coils in series per phase
Q	N	load on rolling element
Q_{rf}	C	electric charge on rotor and frame
Q_r	-	number of rotor slots
Q_s	-	number of stator slots
r	m	radius
R	Ω	resistance
$R_{(a)}$	Ω	resistance due to eddy current distribution of one lamination sheet of model (a)
$R_{(a),sum}$	Ω	resistance due to eddy current distribution of lamination stack of model (a)
$R_{(b)}$	Ω	resistance due to eddy current distribution of one lamination sheet of model (b)
$R_{(b),sum}$	Ω	resistance due to eddy current distribution of lamination stack of model (b)
R_b	Ω	bearing resistance
$R_{b,Fe}$	Ω	resistance due to eddy current distribution of circulating bearing current path through stator lamination stack

Symbol	Unit	Name
$R_{\mathrm{b,i}}$	Ω	resistance due to eddy current distribution of circulating bearing current path outside stator lamination except for R_{b}
$R_{\mathrm{b,ia}}$	Ω	$R_{\mathrm{b,i}}$, part of frame outside stack
$R_{\mathrm{b,ib}}$	Ω	$R_{\mathrm{b,i}}$, part of end-shield on DE and NDE
$R_{\mathrm{b,ic}}$	Ω	$R_{\mathrm{b,i}}$, part of shaft outside rotor lamination stack
$R_{\mathrm{b,id}}$	Ω	$R_{\mathrm{b,i}}$, part of end sheet on DE and NDE of rotor lamination stack
$R_{\mathrm{b,ie}}$	H	$R_{\mathrm{b,i}}$, part of resurfaced rotor lamination stack
R_{cu}	Ω	resistance of copper loop applied for bearing current measurement
R_{e}	Ω	auxiliary parameter for modeling of high-frequency ground currents
R_{f}	Ω	parameter to consider damping of the ground current due to the motor frame resistance including skin effect
R_{i}	Ω	resistance of a circular conductor at high frequency
R_{ph}	Ω	resistance of dv/dt-filter per phase
R_{r}	m	reduced radius of race curvature
R_{s}	Ω	stator winding resistance per phase
R'_{s}	Ω	stator winding resistance per coil at ≈ 1MHz
s	-	slip
s_ν	-	slip of fundamental wave exited by current harmonic ν
S_{r}	VA	rated apparent power, rms-value
$S_{\mathrm{r,output}}$	VA	rated inverter output power, rms-value
t	s	time
$\tilde{t}^\star$	s	time of occurrence of maximum bearing current amplitude
t_{arc}	s	duration of current flow
t_{op}	s	time of operation
t_{s}	s	sampling time
t_{r}	s	rise time
T	s	period time
T	s	time constant
T_{l}	Nm	breakaway torque
T_{b}	Nm	breakdown torque
T_{c}	s	time-lag between two switching instants
T_{r}	Nm	rated torque
U	-	speed parameter
U_{inv}	-	inverter terminal connection, phase U
U_{motor}	-	motor terminal connection, phase U

Symbol	Unit	Name
U_{slot}	m	circumference of stator slot
v	V	voltage
$\hat{v}$	V	final value of voltage rise
v_1	m/s	velocity of rolling element
v_2	m/s	surface velocity at contact point or line
v_{b}	V	bearing voltage
$\hat{v}_{\mathrm{b}}$	V	bearing voltage, peak value
$v_{\mathrm{b,th}}$	V	threshold voltage of bearing
$v_{\mathrm{b,DE}}$	V	bearing voltage at DE
$v_{\mathrm{b,NDE}}$	V	bearing voltage at NDE
$\tilde{v}_{\mathrm{b}}$	V	bearing voltage at break down
v_{cable}	m/s	cable velocity
v_{c}	V	voltage at capacitance
v_{ci}	V	voltage at insulating layer of end-shield
v_{com}	V	common mode voltage
v_{dc}	V	dc-voltage
v_{k}	-	rated voltage drop at reactor
v_{Lg}	V	line-to-earth voltage ("line-to-ground" voltage)
v_{LL}	V	line-to-line voltage
v_{LY}	V	line-to-neutral voltage
v_{m}	m/s	mean velocity in direction of rolling
v_{r}	V	voltage at resistance
v_{sh}	V	shaft voltage
$\hat{v}_{\mathrm{sh}}$	V	shaft voltage, peak value
$v_{\mathrm{sh,rms}}$	V	shaft voltage, rms-value
$v_{\mathrm{steady\text{-}state}}$	V	voltage, steady-state value
v_{ug}	V	line-to-earth voltage, phase U
v_{uv}	V	line-to-line voltage between phases U and V
v_{uY}	V	line-to-neutral voltage, phase U
v_{vg}	V	line-to-earth voltage, phase V
v_{vw}	V	line-to-line voltage between phases V and W
v_{vY}	V	line-to-neutral voltage, phase V
v_{wg}	V	line-to-earth voltage, phase W
v_{wu}	V	line-to-line voltage between phases W and U
v_{wY}	V	line-to-neutral voltage, phase W
v_{Y}	V	stator winding common mode voltage
V	m^3	volume
$\underline{V}_{(\mathrm{a})}$	V	induced voltage per sheet for model (a)

Symbol	Unit	Name
$\underline{V}_{(b)}$	V	induced voltage per sheet for model (b)
V_{arc}	V	arc voltage
V_{dc}	V	dc-link voltage
V_{inv}	-	inverter terminal connection, phase V
V_k	V	voltage drop at reactor, rms-value
V_{max}	V	maximum voltage of voltage step
V_{motor}	-	motor terminal connection, phase V
V_s	V	motor voltage, rms-value
V_{sr}	V	rated motor voltage, rms-value
V_{rf}	V	voltage between rotor and frame
w	-	load parameter at point contact
w'	-	load parameter at line contact
W	A/mm^2	degree of electrical bearing stress
W_{arc}	VAs	local energy input for melting metallic surface per arc
$W_{b,arc}$	VAs	total energy dissipated in bearing
W_{inv}	-	inverter terminal connection, phase W
W_{motor}	-	motor terminal connection, phase W
$X_{b,air}$	Ω	$\omega L_{b,air}$
$X_{b,Fe}$	Ω	$\omega L_{b,Fe}$
$X_{cu,loop}$	Ω	$\omega L_{cu,loop}$
$X_{cu,loop}$	Ω	$(\omega C_i)^{-1}$
Z_{ph}	Ω	phase impendance
Y	-	wye-connection
α	m^2/N	pressure-viscosity coefficient of lubricant
α_s	1/m	inverse of skin depth
β	-	height ratio of the winding
δ	m	mechanical air gap
δ_e	m	equivalent air gap including effect of slotting $\delta_e = \delta k_c$
δ_s	m	skin depth
Δ	-	delta-connection
Δ	m	distance between bearing cover and shaft
Δ_R	m	radial bearing play
ε_0	As/(Vm)	permittivity of vacuum, $8.8542 \cdot 10^{-12}$ As/(Vm)
ε_r	-	relative permittivity
η	-	efficiency
η_0	Ns/mm^2	lubricant viscosity at atmospheric pressure
Φ_0	Wb	total common mode flux
$\Phi_{0,(a)}$	Wb	total magnetic flux per sheet of model (a)

Symbol	Unit	Name
$\Phi_{0,(b)}$	Wb	total magnetic flux per sheet of model (b)
$\Phi_{0,(a),sum}$	Wb	total common mode flux of model (a)
$\Phi_{0,(b),sum}$	Wb	total common mode flux of model (b)
Φ_{circ}	Wb	circular magnetic flux
κ	1/(Ωm)	electrical conductivity
μ_0	Vs/(Am)	permeability of vacuum, $4\pi 10^{-7}$ Vs/(Am)
μ_r	-	relative permeability
ω_s	1/rad	synchronous speed
Ω_m	1/rad	rotational speed of rotor
ρ	kg/m^3	mass density
ϑ_b	°C	bearing temperature

Abbreviations

Abbreviation	Name
ac	*a*lternating *c*urrent
AC-IM	*A*luminum *C*age *I*nduction *M*otor
av.	average
bear.	bearing
BVR	*B*earing *V*oltage *R*atio
CMC	common mode choke
CMF	common mode filter
conf.	configuration
dc	*d*irect *c*urrent
DE	*D*rive *E*nd
DV	*dv*/*dt*-reactor
DVF	*dv*/*dt*-filter
E1	grounding configuration E1
E2	grounding configuration E2
E3	grounding configuration E3
E4	grounding configuration E4
$E1_{01}$	l_c = 1 m, unshielded motor cable, configuration E1
$E1_{02}$	l_c = 2 m, unshielded motor cable, configuration E1
$E1_{10}$	l_c = 10 m, unshielded motor cable, configuration E1
$E1^*_{10}$	l_c = 10 m, shielded motor cable, configuration E1
$E1_{50}$	l_c = 50 m, unshielded motor cable, configuration E1
$E1^*_{50}$	l_c = 50 m, shielded motor cable, configuration E1

Abbreviation	Name
E1*$_{80}$	l_c = 80 m, shielded motor cable, configuration E1
EC	*E*lectronically *C*ommutated
EDM	*E*lectric *D*ischarge *M*achining
EHL	*E*lasto-*H*ydrodynamic *L*ubrication
EMI	*E*lectro-*M*agnetic *I*nterference
hyb.	hybrid
I	*I*nverter
IC	*I*nternational *C*ooling class
IGBT	*I*nsulated *G*ate *B*ipolar *T*ransistor
IP	*I*nternational *P*rotection class
ins.	insulation
insul.	insulating
LTHF	*L*ong *T*ime *H*igh *F*requency
LTMF	*L*ong *T*ime *M*edium *F*requency
M	*M*otor
mat.	material
NDE	*N*on *D*rive *E*nd
op.	operation
PE	*P*rotective *E*arth
pk-to-pk	peak-to-peak
PM-ECM	*P*ermanent *M*agnet *E*lectronically *C*ommutated *M*otor
PWM	*P*ulse *W*idth *M*odulation
SF	sinusoidal filter
sh.	shielded
STHF	*S*hort *T*ime *H*igh *F*requency
STMF	*S*hort *T*ime *M*edium *F*requency
unsh.	unshielded

Appendix A

Test Objects

A.1 Three-phase Motors with Random-Wound Winding

A.1.1 1 kW Power Level

Permanent Magnet Synchronous Motors M1a and M1b,
electronically commutated
Inner stator, outer rotor motors,
Shaft height 63 mm,
400 V, 50 Hz, 4 poles,
Thermal classification F, IC 00, IP 54,
No. of stator slots $Q_\mathrm{s} = 24$,
Outer diameter of stator core $d_\mathrm{se} = 230$ mm,
Inner diameter of stator core $d_\mathrm{si} = 95$ mm,
Outer diameter of rotor core $d_\mathrm{re} = 299$ mm,
Inner diameter of rotor core $d_\mathrm{ri} = 231$ mm,
Iron length $l_\mathrm{Fe} = 35$ mm

P_r	n_r	η
kW	rpm	%
0.8 kW	2150	85.5

A.1.2 11 kW Power Level

Squirrel-cage Induction Motors M11a and M11c
Inner rotor (aluminum-cage), outer stator motors,
Shaft height 160 mm,
690 V Y / 400 V Δ, 50 Hz, 4 poles,
Thermal classification B, IC 44, IP 55,
No. of stator slots $Q_s = 48$, no. of rotor slots $Q_r = 40$,
Outer diameter of stator core $d_{se} = 240$ mm, inner diameter of stator core $d_{si} = 158$ mm,
Outer diameter of rotor core $d_{re} = 156.9$ mm inner diameter of rotor core $d_{ri} = 55$ mm,
Iron length $l_{Fe} = 145$ mm

P_r	n_r	η	$cos\varphi$	I_r(400 V)	I_1/I_r	T_1/T_r	T_b/T_r
kW	rpm	%	–	A	–	–	–
11	1465	87.5	0.87	21	6.9	2.0	2.7

Squirrel-cage Induction Motors M11b and M11c
Inner rotor (aluminum-cage), outer stator motors,
Shaft height 160 mm,
400 V Y / 230 V Δ, 50 Hz, 4 poles,
Thermal classification B, IC 41, IP 55,
No. of stator slots $Q_s = 36$, no. of rotor slots $Q_r = 28$,
Outer diameter of stator core $d_{se} = 235$ mm, inner diameter of stator core $d_{si} = 150$ mm,
Outer diameter of rotor core $d_{re} = 149.24$ mm, inner diameter of rotor core $d_{ri} = 56$ mm,
Iron length $l_{Fe} = 140$ mm

P_r	n_r	η	$cos\varphi$	I_r(400 V)	I_1/I_r	T_1/T_r	T_b/T_r
kW	rpm	%	–	A	–	–	–
11	1460	91.0	0.82	22	6.9	2.3	2.9

Squirrel-cage Induction Motors M11e and M11f
Inner rotor (aluminum-cage), outer stator motors,
Shaft height 160 mm,
690 V Y / 400 V Δ, 50 Hz, 4 poles,
Thermal classification B, IC 41, IP 55,
No. of stator slots $Q_s = 48$, no. of rotor slots $Q_r = 40$,
Outer diameter of stator core $d_{se} = 206$ mm, inner diameter of stator core $d_{si} = 128$ mm,
Outer diameter of rotor core $d_{re} = 127$ mm, inner diameter of rotor core $d_{ri} = 52$ mm,
Iron length $l_{Fe} = 194$ mm

P_r	n_r	η	$cos\varphi$	I_r(400 V)	I_1/I_r	T_1/T_r	T_b/T_r
kW	rpm	%	–	A	–	–	–
11	1450	86.0	0.85	21.5	6.8	2.2	3.3

A.1.3 110 kW Power Level

Squirrel-cage Induction Motor M110a
Inner rotor (aluminum-cage), outer stator motor,
Shaft height 280 mm,
690 V Y / 400 V Δ, 50 Hz, 4 poles,
Thermal classification B, IC 41, IP 55,
No. of stator slots $Q_s = 72$, no. of rotor slots $Q_r = 56$,
Outer diameter of stator core $d_{se} = 460$ mm, inner diameter of stator core $d_{si} = 295$ mm,
Outer diameter of rotor core $d_{re} = 293$ mm, inner diameter of rotor core $d_{ri} = 100$ mm,
Iron length $l_{Fe} = 310$ mm

P_r	n_r	η	$cos\varphi$	I_r(400 V)	I_1/I_r	T_1/T_r	T_b/T_r
kW	rpm	%	–	A	–	–	–
110	1484	95.6	0.87	194	7.7	3.0	3.0

Squirrel-cage Induction Motor M110b
Inner rotor (aluminum-cage), outer stator motor,
Shaft height 315 mm, but active parts could also be housed within shaft height 280 mm,
690 V Y / 400 V Δ, 50 Hz, 4 poles,
Thermal classification B, IC 41, IP 55,
No. of stator slots $Q_s = 60$, no. of rotor slots $Q_r = 50$,
Outer diameter of stator core $d_{se} = 465$ mm, inner diameter of stator core $d_{si} = 295$ mm,
Outer diameter of rotor core $d_{re} = 293$ mm, inner diameter of rotor core $d_{ri} = 115$ mm,
Iron length $l_{Fe} = 345$ mm

P_r	n_r	η	$cos\varphi$	I_r(400 V)	I_1/I_r	T_1/T_r	T_b/T_r
kW	rpm	%	–	A	–	–	–
110	1485	95.1	0.86	194	7.5	1.8	2.2

A.1.4 500 kW Power Level

Squirrel-cage Induction Motor M500a
Inner rotor (aluminum-cage), outer stator motor,
Shaft height 400 mm,
690 V Y / 400 V Δ, 50 Hz, 6 poles,
Thermal classification B, IC 41, IP 55,
No. of stator slots $Q_s = 72$, no. of rotor slots $Q_r = 54$,
Outer diameter of stator core $d_{se} = 700$ mm, inner diameter of stator core $d_{si} = 500$ mm,
Outer diameter of rotor core $d_{re} = 497$ mm, inner diameter of rotor core $d_{ri} = 140$ mm,
Iron length $l_{Fe} = 530$ mm

P_r	n_r	η	$cos\varphi$	I_r(690 V)	I_1/I_r	T_1/T_r	T_b/T_r
kW	rpm	%	–	A	–	–	–
435	993	96.4	0.85	445	7.0	2.1	2.8

Squirrel-cage Induction Motor M500b
Inner rotor (aluminum-cage), outer stator motor,
Shaft height 400 mm,
690 V Δ, 50 Hz, 2 poles,
Thermal classification B, IC 411, IP 55,
No. of stator slots $Q_s = 48$, no. of rotor slots $Q_r = 40$,
Outer diameter of stator core $d_{se} = 680$ mm, inner diameter of stator core $d_{si} = 360$ mm,
Outer diameter of rotor core $d_{re} = 353$ mm, inner diameter of rotor core $d_{ri} = 150$ mm,
Iron length $l_{Fe} = 490$ mm

P_r	n_r	η	$cos\varphi$	I_r(690 V)	I_1/I_r	T_1/T_r	T_b/T_r
kW	rpm	%	–	A	–	–	–
560	2983	97.0	0.91	530	6.2	0.85	2.7

Rem: The motor is operated at 400 V Δ, 30 Hz.

A.2 Inverters

A.2.1 1 kW Power Level

Inverter EC1
System voltage 1 x 230 V,
Switching frequency 9.0 kHz, asynchronous PWM,
IP 54

$S_{r,output}$ (230 V)	$I_{r,output}$
kVA	A
1.2	1

A.2.2 11 kW Power Level

INVERTER I11a
System voltage 3 x (380...500) V,
Switching frequency (3.0...14.0) kHz, asynchronous PWM,
IP 20

$S_{\mathrm{r,output}}$ (380...440 V)	$I_{\mathrm{r,output}}$
kVA	A
18.3	24

INVERTER I11b
System voltage 3 x (380...415) V,
Switching frequency average (2.0...3.0) kHz, direct torque control,
IP 22

$S_{\mathrm{r,output}}$ (400 V)	$I_{\mathrm{r,output}}$
kVA	A
30	47

Although inverter is rated for 30 kVA, the same inverter is also labeled for 16 kVA, and is therefore used at the 11 kW power level.

INVERTER I11c
System voltage 3 x (200...415) V,
Switching frequency average (4.5...7.5) kHz,
Space vector control with predictive control algorithm to obtain sinusoidal current, optimized for minimum switching operations,
Alternatively operated with / without dv/dt-filter at inverter output ($dv/dt \leq 0.5\,\mathrm{kV}/\mu\mathrm{s}$),
IP 20

$S_{\mathrm{r,output}}$ (400 V)	$I_{\mathrm{r,output}}$
kVA	A
20	29

INVERTER I11d
System voltage 3 x (380...500) V,
Switching frequency (3.0...10.0) kHz, asynchronous PWM,
IP 20

$S_{\mathrm{r,output}}$ ((380...440) V)	$I_{\mathrm{r,output}}$
kVA	A
33.5	44

A.2.3 110 kW Power Level

Inverter I110a
System voltage 3 x (380...500) V,
Switching frequency (3.0...4.5) kHz, asynchronous PWM,
IP 20

$S_{\mathrm{r,output}}$ ((380...440) V)	$I_{\mathrm{r,output}}$
kVA	A
147	212

Inverter I110b
System voltage 3 x (380...415) V,
Switching frequency average 3.0 kHz, direct torque control,
IP 22

$S_{\mathrm{r,output}}$ (400 V)	$I_{\mathrm{r,output}}$
kVA	A
114	164

Inverter I110c
System voltage 3 x (200...415) V,
Switching frequency average (3.0...4.5) kHz,
Space vector control with predictive control algorithm to obtain sinusoidal current, optimized for minimum switching operations,
Alternatively operated with / without dv/dt-filter at inverter output ($dv/dt \leq 0.5\,\mathrm{kV}/\mu\mathrm{s}$),
IP 20

$S_{\mathrm{r,output}}$ (400 V)	$I_{\mathrm{r,output}}$
kVA	A
118	170

A.2.4 500 kW Power Level

Inverter I500
System voltage 3 x 660 V-15%...690 V+ 15%,
Switching frequency (1.7...2.5) kHz, asynchronous PWM,
IP 00 (chassis device, to be built into cubicle)

$S_{\mathrm{r,output}}$ (690 V)	$I_{\mathrm{r,output}}$
kVA	A
540	452

The inverter is operated as a 400 V device through modification of the voltage divider unit of the voltage measurement system.

A.3 Motor Cables

A.3.1 1 kW Power Level

Cable C1

Rated voltage 0.3/0.5 kV,

Current carrying capacity at three loaded strands (ϑ_{amb}=30°C) 3 A/strand

Type	Cross sectional area	
Y-JZ	4 x 0.5 mm^2	unshielded

Cable length l_c = 1 m

A.3.2 11 kW Power Level

Cable C11a

Rated voltage 0.3/0.5 kV,

Current carrying capacity at three loaded strands (ϑ_{amb}=30°C) 26 A/strand

Type	Cross sectional area	
Y-JZ	4 x 2.5 mm^2	unshielded

Cable lengths l_c = 2 / 10 / 50 m

Cable C11b

Rated voltage 0.6/1.0 kV,

Current carrying capacity at three loaded strands (ϑ_{amb}=30°C) 26 A/strand

Type	Cross sectional area	
NY-CY	3 x 2.5 mm^2	shielded , coax. PE

Cable length l_c = 50 m

A.3.3 110 kW Power Level

Cable C110a

Rated voltage 0.6/1.0 kV,

Current carrying capacity at three loaded strands (ϑ_{amb}=30°C) 207 A/strand

Type	Cross sectional area	
NYY-J	4 x 70 mm^2	unshielded

Cable lengths l_c = 10 / 50 m

Cable C110b

Rated voltage 0.6/1.0 kV,

Current carrying capacity at three loaded strands (ϑ_{amb}=30°C) 207 A/strand

Type	Cross sectional area	
2YSLCY-J	4 x 70 mm^2	shielded

Cable lengths l_c = 10 / 50 / 80 m

A.3.4 500 kW Power Level

Cable C500a

Rated voltage 0.6/1.0 kV,

Current carrying capacity at three loaded strands (ϑ_{amb}=30°C) 335 A/strand

Type	Cross sectional area	
NYY-J	3 x 150 mm^2 + 1 x 70 mm^2	unshielded

Two cables in parallel, cable length l_c = 10 m

Cable C500b

Rated voltage 0.6/1.0 kV,

Current carrying capacity at three loaded strands (ϑ_{amb}=30°C) 335 A/strand

Type	Cross sectional area	
2YSLCY-J	3 x 150 mm^2 + 3 x 25 mm^2	shielded

Two cables in parallel, cable length l_c = 2 / 10 m

A.4 Inverter-Output Filters

A.4.1 11 kW Power Level

Sinusoidal filter SF11a

System voltage 3 x (380...500) V,

IP 20

Type	Power	I_r(400 V)	Switching frequency	max. frequency
	kVA	A	kHz	Hz
sinusoidal filter	22	32	4.5	60

L_{ph} = 1 mH, C_{Lg} = 4 μF (Y-connection) (C_{LL}(Δ-connection) = 3·4 μ F = 12 μF),
$f_0 = (2\pi\sqrt{1\text{ mH } 3 \cdot 4\mu\text{F}})^{-1}$ = 2517 Hz

SINUSOIDAL FILTER SF11b

System voltage max. 3 x 400 V,

IP 20

Type	Power	I_r	Switching frequency	max. frequency
	kVA	A	kHz	Hz
sinusoidal filter	22	32	4...16	60

L_{ph} = 2 mH, C_{Lg} = 2 μF (Y-connection) ($C_{LL(\Delta\text{-connection})}$ = 3·2 μF = 6 μF),
$f_0 = (2\pi\sqrt{2 \text{ mH } 3 \cdot 2\mu\text{F}})^{-1}$ = 2517 Hz

dv/dt-FILTER DVF11a

System voltage max. 3 x 500 V,

Motor power max. 11 kW (3 x 400 V),

IP 20

Type	Power	I_r	Switching frequency	max. frequency
	kVA	A	kHz	Hz
dv/dt-filter	16.6	24	max. 16 (l_c = 80 m)	400

The name *dv/dt*-filter DVF11a designates a *dv/dt*-filter type FN 510-24-33 of Schaffner EMV GmbH. It is used as a black box.

dv/dt-FILTER DVF11b

System voltage max. 3 x 500 V,

IP 20

Type	Power	I_r	Switching frequency	Frequency
	kVA	A	kHz	Hz
dv/dt-filter, integrated common mode choke	17.3	25	max. 8 (l_c = 50 m)	60

The name *dv/dt*-filter DVF11b designates a *dv/dt*-filter type FS 3889-25-29 of Schaffner EMV GmbH. It is used as a black box.

dv/dt-FILTER DVF11c

Filter already integrated in inverter housing of I11c,

System voltage 3 x (0...415) V,

Motor power max. 11 kW (3 x 400 V),

IP 20 (corresponding to the IP of inverter I11c)

Type	Power	I_r	Switching frequency	max. frequency
	kVA	A	kHz	Hz
dv/dt-filter	20	29	max. 7.5	650

This filter is a standard filter of manufacturer G. It is used as a black box.

Common mode choke CMC11a
Ferrite core,
System voltage max. 3 x 600 V,
IP 00

Type	Power	I_r	Switching frequency	max. frequency
	kVA	A	kHz	Hz
common mode choke	17.3	25	max. 16	400

Inductivity measured with all three phases in parallel $L = 2.5$ mH.

Common mode choke CMC11b
Laminated low-loss iron core,
System voltage max. 3 x 480 V,
IP 00

Type	Power	I_r	Switching frequency	Frequency
	kVA	A	kHz	Hz
common mode choke	55	80	max. 8	50

Inductivity measured with all three phases in parallel $L = 5.0$ mH.

Common mode filter CMF11
System voltage max. 3 x 500 V,
IP 20

Type	Power	I_r	Switching frequency	max. frequency
	kVA	A	kHz	Hz
common mode filter	8.3	12	6...20	200

The name common mode choke CMF11 designates a common mode choke type FN 530 of Schaffner EMV GmbH. It is used as a black box. The principal design of the filter is shown in Fig. 5.4 (p. 77).

A.4.2 110 kW Power Level

Sinusoidal filter SF110
Rated voltage 3 x 400 V,
IP 00

Type	Power	I_r	Switching frequency	max. frequency
	kVA	A	kHz	Hz
sinusoidal filter	118	170	mind. 4.5	60

$L_{ph} = 0.5$ mH, $C_{LL} = 35$ μF (Δ-connection) ($C_{Lg(\text{Y-connection})} = 35$ μF$/3 = 11.7$ μF$/3$),
$f_0 = (2\pi\sqrt{0.5 \text{ mH } 35\mu\text{F}/3})^{-1} = 2084$ Hz

dv/dt-Reactor DV110a

System voltage 3 x (400...690) V,

Motor power max. 11 kW (3 x 400 V),

IP 00

Type	Power	I_r(400 V)	Switching frequency	max. frequency
	kVA	A	kHz	Hz
dv/dt-reactor	114	164	max. 3	120

$L_{ph} = 0.092$ mH

dv/dt-Reactor DV110b

Rated voltage 3 x 400 V,

IP 00

Type	Power	I_r	Switching frequency	Frequency
	kVA	A	kHz	Hz
dv/dt-reactor	118	170	max. 7.5	50

DV110b consists of the three inductors of sinusoidal filter SF110 ($L_{ph} = 0.5$ mH)

dv/dt-Filter DVF110c

Filter already integrated in inverter housing of I110c,

System voltage 3 x (0...415) V,

IP 20 (corresponding to the IP of inverter I110c)

Type	Power	I_r	Switching frequency	max. frequency
	kVA	A	kHz	Hz
dv/dt-filter	118	170	max. 4.5	650

This filter is a standard filter of manufacturer G. It is used as a black box.

Common mode choke CMC110

System voltage 3 x (400...500) V,

IP 00

Type	Power	I_r	Switching frequency	max. frequency
	kVA	A	kHz	Hz
common mode choke	139	200	max. 20	1000

Inductivity measured with all three phases in parallel $L = 0.073$ mH.

A.4.3 500 kW Power Level

Sinusoidal filter SF500

System voltage 3 x 400 V,

IP 00

Type	Power	I_r	Switching frequency	max. frequency
	kVA	A	kHz	Hz
sinusoidal filter	423	610	2...6	60

SF500 is built from the inductors of dv/dt-reactor DV500 and additional capacitors. $L_{ph} = 0.05$ mH, $C_{LL} = 24$ μF (Δ-connection) ($C_{Lg(\text{Y-connection})} = 24$ μF$/3 = 8$ μF$/3$), $f_0 = (2\pi\sqrt{0.05 \text{ mH } 24\mu\text{F}/3})^{-1} = 7958$ Hz

dv/dt-Reactor DV500

System voltage 3 x 500 V,

IP 00

Type	Power	I_r	Switching frequency	max. frequency
	kVA	A	kHz	Hz
dv/dt-reactor	312	450	2...6	60

$L_{ph} = 0.05$ mH

Common mode choke CMC500

System voltage 3 x 500 V,

IP 00

Type	Power	I_r(400 V)	Switching frequency	max. frequency
	kVA	A	kHz	Hz
common mode choke	159	230	2...6	60

Inductivity measured with all three phases in parallel $L = 0.62$ mH.

A.5 Grease

The bearings of the motors of the 1 kW power level were lubricated with the standard high impedance grease *Asonic* GHY72 with the following data:

Colour	beige
Temperature range	(-40...180)°C
Maximum continuous temperature	180°C
Maximum value $n \times d_\mathrm{b}$	700 000 mm/min
Maximum value $n \times d_\mathrm{b}$	300 000 mm/min
Thickening agent	polyurea
Main oil	ester oil
Viscosity of main oil at 40°C	70 $\mathrm{mm^2/s}$
Viscosity of main oil at 100°C	9.4 $\mathrm{mm^2/s}$
Melting temperature	> 250°C

The bearings of the motors of the 11 kW, 110 kW and 500 kW power level were lubricated with the high impedance bearing grease *Norlith* STM3 with the following data:

Colour	yellowish
Temperature range	(-30...140)°C
Maximum continuous temperature	75°C
Maximum speed ball $n \times d_\mathrm{b}$	500 000 mm/min
Maximum speed roll $n \times d_\mathrm{b}$	250 000 mm/min
Thickening agent	lithium
Main oil	mineral oil
Viscosity of main oil at 40°C	80 $\mathrm{mm^2/s}$
Viscosity of main oil at 100°C	8 $\mathrm{mm^2/s}$
Melting temperature	190°C

Appendix B

Measuring Instruments

Measured parameter	Measuring instrument	Measuring range
Bearing temperature ϑ_b	Fe-CuNi thermocouple (type J) and thermocouple indicator	(-200...+900)°C (-190...+745)°C (for type J)
Bearing current i_b	Current probes *LEM* PR-50	(0...30) A(rms), 50 A(peak), (0...50) MHz
Bearing current i_b	Current probes *Tektronix* A6303 and corresponding amplifying system	(0...100) A(peak), (0...15) MHz (0...100) MHz
Stator ground current i_g	Current probes *Tektronix* A6303 and corresponding amplifying system	(0...100) A(peak), (0...15) MHz (0...100) MHz
Rotor ground current i_{rg}	Current probes *LEM* PR-50	(0...30) A(rms), 50 A(peak), (0...50) MHz
Rotor ground current i_{rg}	Current probes *Tektronix* A6303 and corresponding amplifying system	(0...100) A(peak), (0...15) MHz (0...100) MHz
Phase current	a) Inverter display	not specified
	b) Current probes *Tektronix* A6303 and corresponding amplifying system	(0...100) A(peak), (0...15) MHz (0...100) MHz

Measured parameter	Measuring instrument	Measuring range
Bearing voltage v_b	Differential voltage probes *Tektronix* SI-9000	(0...1000) V, 1:20 and 1:200, (0...25) MHz
Shaft voltage v_{sh} (at line-operation)	Voltage probes *Gould* PB 12	(0...600) V, 1:1, (0...10) MHz and 1:10, (0...100) MHz
	and differential amplifier *Le Croy* DT 9010	(0...1000) V, 1:10 (0...80) MHz
Line-to-line voltage v_{LL}, Line-to-earth voltage v_{Lg}	Voltage probes *Le Croy* PPE100XDIF	(0...4000) V, 1:100, (0...400) MHz
	and differential amplifier *Le Croy* DT 9010	(0...1000) V, 1:10, (0...80) MHz
Time function of voltages and currents, statistical evaluation	Scope *Le Croy* LT 364L	(0...500) MHz, sample rate 1 GS/s, memory depth 2Mpoints
Time function of voltages and currents	Scope *Tektronix* TDS 420 A	(0...200) MHz, sample rate 100 MS/s memory depth 120 kpoints

Appendix C

Calculated *Hertz*'ian Contact Areas

This chapter summarizes the basics of the formulas of Hertz and explains the calculation of the Hertz'ian contact areas A_{H} of the investigated motors. These calculations have been done by Mr. Ortegel, FAG Schweinfurt, in order to evaluate the endangerment of the bearings through bearing currents via the "apparent bearing current density" $J_b = i_b/A_H$ (→ Section 1.5.1, p. 14).

If under mechanical pressure, ***two bodies in punctual or linear contact*** are subject to elastic deformation. Under the following conditions, the ***formulas of Hertz can be applied to calculate these values*** [32], [33]:

(i) Homogeneous and isotropic material,
(ii) Plain area of deformation, axes of this elliptic area are small when compared with the radius of bearing ring at the point of deformation; only transmission of normal pressure, not of shear stress,
(iii) Bearing pressure is within the limits of linear elasticity of bearing material, no irreversible deformation.

When considering the bearing application, these conditions are not exactly met:
(i) Metallic materials are not homogeneous, the modulus of elasticity (*Young*'s modulus E) gives only the average value of the behavior of the numerous individual crystals.
(ii) The contact area in bearings may be bent at high load, depending on the osculation of the bearing race.
(iii) Small plastic deformations occur at the bearings and races at high load, hence, the limits of linear elasticity of the materials are exceeded.

In spite of these restraints, the calculated areas A_{H}, using the formulas of *Hertz*, do not differ much from those experimentally determined (extensive literature is given in [32]). Therefore, this method is generally taken to calculate the minimum area of contact in the bearing.

The ***Hertz'ian contact areas of the investigated motors*** were calculated using the formulas of *Hertz*, in order to derive the apparent bearing current densities J_b. Practical advice and strong support was given by FAG, Schweinfurt, Dr. Hering and Mr. Ortegel. The calculations were done at FAG with a special in-house calculation tool.

For these calculations, numerous variations of radial force F_R, axial force F_A and radial play Δ_R were done, notably at the 110 kW power level. At first, the average values of the calculated *Hertz*'ian contact areas A_H of the investigated motors are summarized in Table C.1. For the 1 kW, 11 kW and 110 kW power level, where the test motors have all the same number of four poles, the *Hertz*'ian contact areas increase with increasing motor size. At the 500 kW power level, due to the different numbers of poles, which is six poles for motor M500a and two poles for motor M500b, the *Hertz*'ian contact area of motor M500b is even a little smaller than the *Hertz*'ian contact areas of the motors of the 110 kW power level.

The details on bearing type and the performed variations of the radial force F_R, axial force F_A and radial play Δ_R of the test motors of each of the investigated power levels are given in Tables C.2, C.3, C.4 and C.5. Furthermore, the calculations on the bearings of the motors of the tests for assessment bearing damage have already been given in Table 6.1 of Chapter 6 (p. 93).

The variations done at the 1 kW and 110 kW power level (Tables C.2 and C.4) show the interaction of the radial and axial load on the *Hertz*'ian contact area A_H: If *no axial load* exists ($F_A = 0$), the value of A_H is *substantially smaller than with existence of axial load* ($F_A \neq 0$) for the *same radial load* F_R.

The value A_H *is about constant*, if bearing load and radial play vary within the range typical for motor operation. Notably, A_H is *about the same for both motors per power level* at the 11 kW and 110 kW power level, where the motors have the *same number of poles* and therefore similar geometric properties.

The situation is different at the 500 kW power level: Due to the different number of poles of the motors with similar rated power, the 6-pole rotor of motor M500a is much bigger than the 2-pole rotor of motor M500b. Hence, the load of the bearing is larger and so is the *Hertz*'ian contact area A_H. As, for a given grounding configuration, the stator ground current i_g increases in general with the number of poles (→ Section 7.5, p. 132), the circulating bearing current is also larger. The *bearing current density* in the bearings of the motors is therefore *about the same*.

	Average value of calculated *Hertz*'ian contact area A_H
Motors M1a and M1b	0.25 mm^2
Motors M11a and M11c	3.0 mm^2
Motors M11b and M11d	3.5 mm^2
Motors M11e and M11f, DE-bearing	2.4 mm^2
Motors M11e and M11f, NDE-bearing	2.2 mm^2
Motor M110a	10 mm^2
Motor M110b	10 mm^2
Motor M500a	20 mm^2
Motor M500b	8 mm^2

Table C.1: Average values of calculated *Hertz*'ian contact areas of the investigated motors

	Motors M1a and M1b		
Bearing	DE and NDE 6002		
Radial force $F_R = 0.0285$ kN, calculation of 9 combinations of axial force F_A and radial play Δ_R			
	$\Delta_R = 0$ μm	$\Delta_R = 5$ μm	$\Delta_R = 10$ μm
$F_A = 0$ kN	$A_H = 0.09$ mm^2	$A_H = 0.06$ mm^2	$A_H = 0.06$ mm^2
$F_A = 0.03$ kN	$A_H = 0.32$ mm^2	$A_H = 0.26$ mm^2	$A_H = 0.23$ mm^2
$F_A = 0.06$ kN	$A_H = 0.46$ mm^2	$A_H = 0.39$ mm^2	$A_H = 0.35$ mm^2
Average value of *Hertz*'ian contact area A_H:			
	$\boxed{A_H(\text{M1a, M1b}) \approx 0.25 \text{ mm}^2}$		

Table C.2: 1 kW power level - Calculated *Hertz*'ian contact areas for different bearing parameters

	Motor M11a		Motor M11b	
Bearing	DE 6209 C3	NDE 6209 C3	DE 6209 C3	NDE 6209 C3
Radial force F_R	396 N	396 N	295 N	255 N
Axial force F_A	458 N	458 N	736 N	736 N
Average values of *Hertz*'ian contact area A_H:				
	$\boxed{A_H(\text{M11a}) \approx 3 \text{ mm}^2}$		$\boxed{A_H(\text{M11b}) \approx 3.5 \text{ mm}^2}$	

Table C.3: 11 kW power level - Calculated *Hertz*'ian contact areas for different bearing parameters

	Motor M110a		Motor M110b	
Bearing	DE 6316 C3	NDE 6316 C3	DE 6317 C3	NDE 6316 C3
6316 C3, calculation of 12 combinations of radial force F_R, axial force F_A and radial play Δ_R radial force F_R = 1.7 / 2.5 kN, axial force F_A = 1.0 / 1.3 kN radial play Δ_R = 5 / 15 / 25 μm $A_{H,min}$ = 8.81 mm^2 (F_R = 1.7 kNm, F_A = 1.0 kNm, Δ_R = 25 μm) $A_{H,max}$ = 11.71 mm^2 (F_R = 2.5 kNm, F_A = 1.3 kNm, Δ_R = 5 μm)				
6317 C3: A_H(6317 C3) $\approx$ A_H(6316 C3) (The difference between the calculated values for bearing 6317 C3 and 6316 C3 is less than 2 % (100 % = A_H(6316 C3)).				
Large influence of the axial force F_A: If F_A = 0, a much larger value of the radial force F_R is required to obtain about the same A_H as above of $A_H \approx$ 10 mm^2 (e.g. bearing 6316 C3 with radial play Δ_R = 10 μm): F_R = 2 kNm, F_A = 0: A_H = 3.7 mm^2 F_R = 4 kNm, F_A = 0: A_H = 5.9 mm^2 F_R = 8 kNm, F_A = 0: A_H = 9.5 mm^2				
Average values of *Hertz*'ian contact area A_H:				
	$\boxed{A_H(\text{M110a}) \approx 10 \text{ mm}^2}$		$\boxed{A_H(\text{M110b}) \approx 10 \text{ mm}^2}$	

Table C.4: 110 kW power level - Calculated *Hertz*'ian contact areas for different bearing parameters

	Motor M500a		Motor M500b	
Bearing	DE 6224 C3 + NU224e	NDE NU224e	DE 6317 C3	NDE 6317 C3
Radial force F_R	12.13 kN	7.35 kN	2.50 kN	3.56 kN
Axial force F_A	3.57 kN	0 kN	0.85 kN	0.85 kN
	6224 C3, radial play Δ_R = 25 μm		radial play Δ_R = 5 μm	
	A_H = 20.3 mm^2	no axial load	A_H = 9.3 mm^2	A_H = 8.8 mm^2
	NU224e, radial play Δ_R = 40 μm		radial play Δ_R = 10 μm	
	A_H = 25.2 mm^2	A_H = 19.4 mm^2	A_H = 8.3 mm^2	A_H = 7.7 mm^2
	NU224e, radial play Δ_R = 80 μm		radial play Δ_R = 15 μm	
	A_H = 24.7 mm^2	A_H = 18.5 mm^2	A_H = 7.6 mm^2	A_H = 7.1 mm^2
Average values of *Hertz*'ian contact area A_H:				
	$\boxed{A_H(\text{M500a}) \approx 20 \text{ mm}^2}$		$\boxed{A_H(\text{M500b}) \approx 8 \text{ mm}^2}$	

Table C.5: 500 kW power level - Calculated *Hertz*'ian contact areas for different bearing parameters

Appendix D

Calculated Minimum Thicknesses of the Lubrication Films

This chapter summarizes the results of the calculations of the minimum thicknesses of the lubrication films of the bearings of the investigated motors. The calculations were done by strong support by FAG, Schweinfurt, Dr. Hering and Mr. Ortegel.

The lubrication film between balls and rolling surfaces of the bearings can be described by means of the *theory of "elastohydrodynamic lubrication"* (EHL). The minimum thicknesses of the lubrication film $h_{\mathrm{lb,min}}$ were calculated for a large amount of operation points using two different models: the equation for point contact of *Hamrock and Dowson* (D.1) [32], [67] and the equation for line contact of *Dowson* (D.2) [32], [68], [69] (D.1).

$$h_{\mathrm{lb,min}} = 3.63 U^{0.68} G^{0.49} w^{-0.073} (1 - e^{-0.68K}) R_{\mathrm{r}} \tag{D.1}$$

$$h_{\mathrm{lb,min}} = 2.65 U^{0.7} G^{0.54} w'^{-0.13} R_{\mathrm{r}} \tag{D.2}$$

where:

$$U = \frac{\eta_0 v_{\mathrm{m}}}{E' R_{\mathrm{r}}} \tag{D.3}$$

$$G = \alpha E' \tag{D.4}$$

$$w = \frac{Q}{E' R_{\mathrm{r}}^2} \tag{D.5}$$

$$w' = \frac{Q}{E' R_{\mathrm{r}} L_{\mathrm{r}}} \tag{D.6}$$

U = speed parameter,
G = material parameter,
w = load parameter at point contact,
w' = load parameter at line contact,
K = ratio of semi axes of (*Hertz*'ian) contact area,
α = pressure-viscosity coefficient of lubricant,
η_0 = lubricant viscosity at atmospheric pressure,
$v_{\mathrm{m}} = (v_1 + v_2)/2$ = mean velocity in direction of rolling,
v_1 = velocity of rolling element,
v_2 = surface velocity at contact point or line,
E' = effective modulus of elasticity,

R_r = reduced radius of race curvature,
Q = load on rolling element,
L_r = effective length of rolling element (length of gap).

The thickness $h_{lb,min}$ was determined for the inner and the outer bearing race, different loads of the bearings and various motor speeds n and bearing temperatures ϑ_b. The load distribution inside the bearings was obtained from the calculations of the *Hertz*'ian contact areas A_H. These results were used to choose prominent bearing loads for the calculations of $h_{lb,min}$. Calculations were done with both the model of point and of line contact at the bottom. The model of point contact respects the drain of the grease at the sides of the small gap.

Rolling speed and *temperature* of the bearing have a *significant influence* on the minimum thickness of the lubrication film $h_{lb,min}$, whereas to the bearing load has only a small influence on $h_{lb,min}$.

Fig. D.1, Fig. D.2 and Fig. D.3 show the minimum thicknesses of the lubrication film $h_{lb,min}$ as function of motor speed n and bearing temperature ϑ_b for the 11 kW, 110 kW and 500 kW power level respectively. The values given are the average of the results obtained with both the models of point and of line contact for inner and outer bearing race and different bearing loads for each point of operation with a given motor speed n and bearing temperature ϑ_b.

The strong influence of bearing temperature ϑ_b and motor speed n on the minimum thickness of the lubrication film $h_{lb,min}$ is obvious in these figures. The thicknesses $h_{lb,min}$ range from $h_{lb,min} < 0.1$ μm for motor speed $n = 15$ /min and bearing temperature $\vartheta_b \approx 70°C$, to some μm at motor speed n of several 1000 /min and bearing temperature $\vartheta_b \approx 20°C$. The values of the thickness $h_{lb,min}$ of the two motors of the 500 kW power level differ, because of the large difference in the bearing load of these motors that results from the different weight of the rotors (→ Appendix C, p. 211).

Fig. D.4 summarizes the minimum thickness of the lubrication film $h_{lb,min}$ as function of motor speed n of the 11 kW, 110 kW and 500 kW power level at bearing temperature typical for load operation, $\vartheta_b \approx 70°C$. At this bearing temperature ϑ_b and motor speed $n \leq 3000$ /min, the thickness $h_{lb,min}$ is *always smaller than 1 μm.*

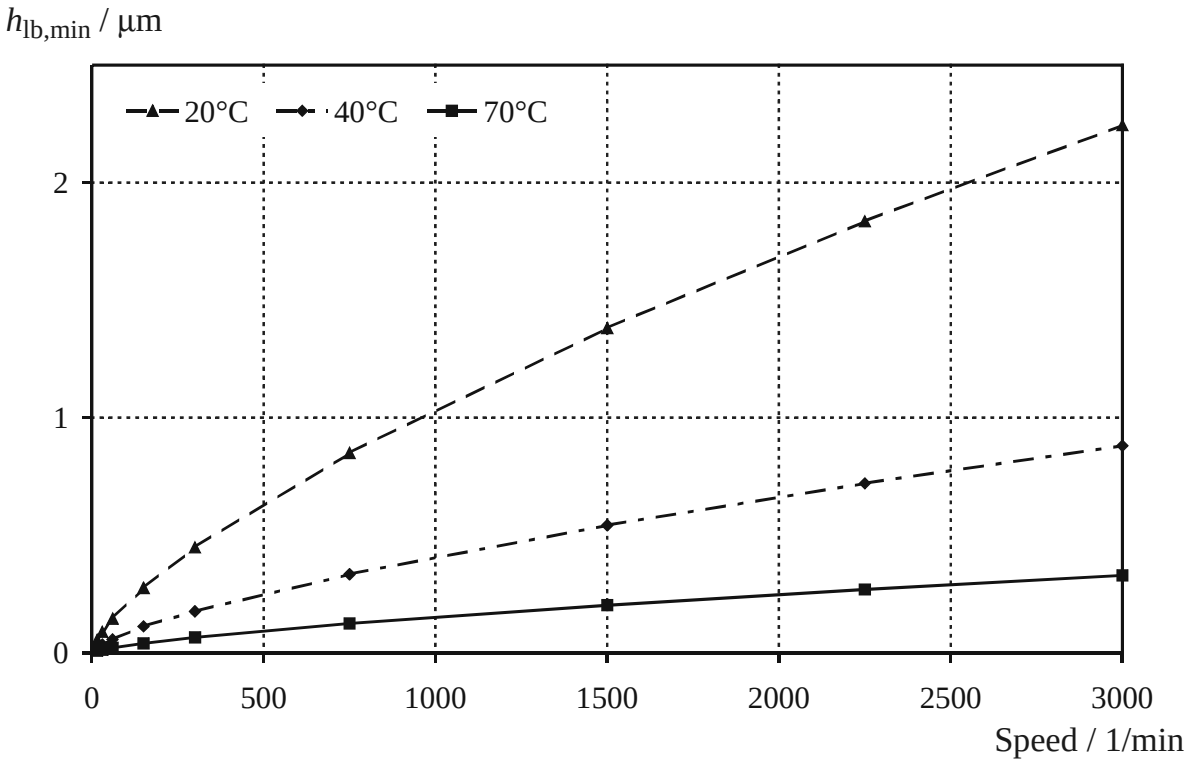

Figure D.1: 11 kW power level - Calculated minimum thickness of lubricating film as function of motor speed and bearing temperature

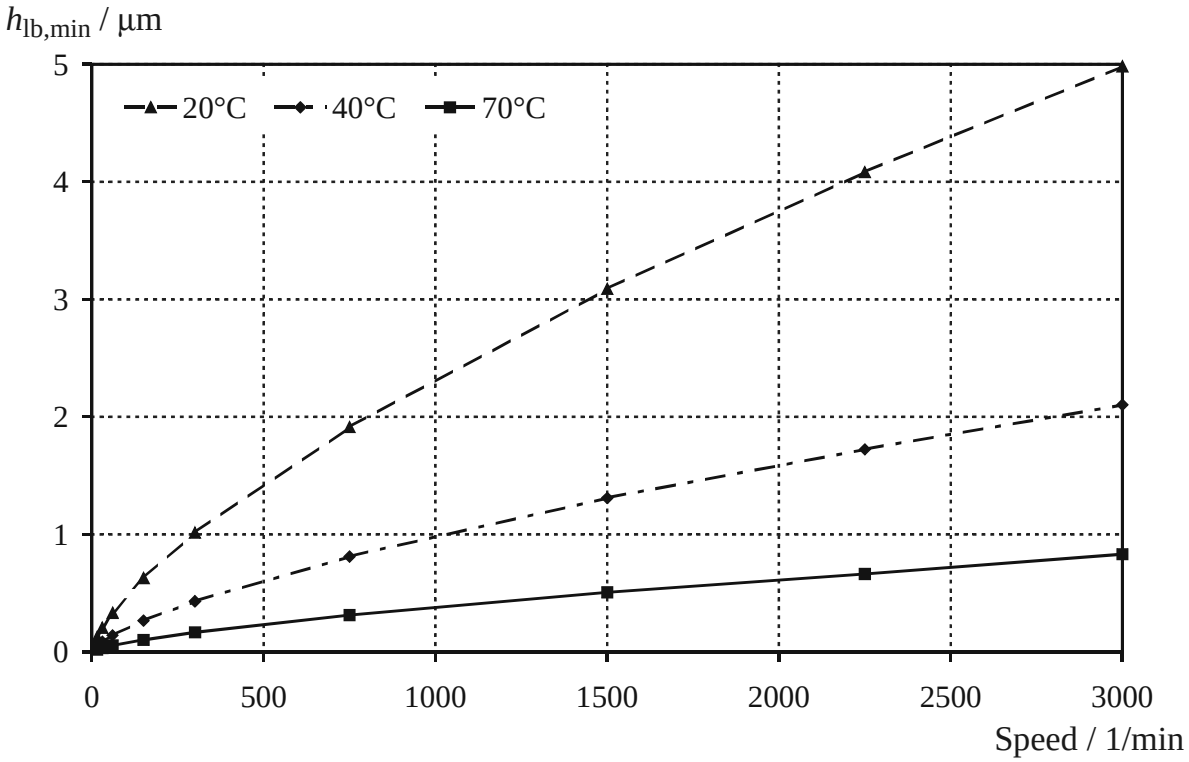

Figure D.2: 110 kW power level - Calculated minimum thickness of lubricating film as function of motor speed and bearing temperature

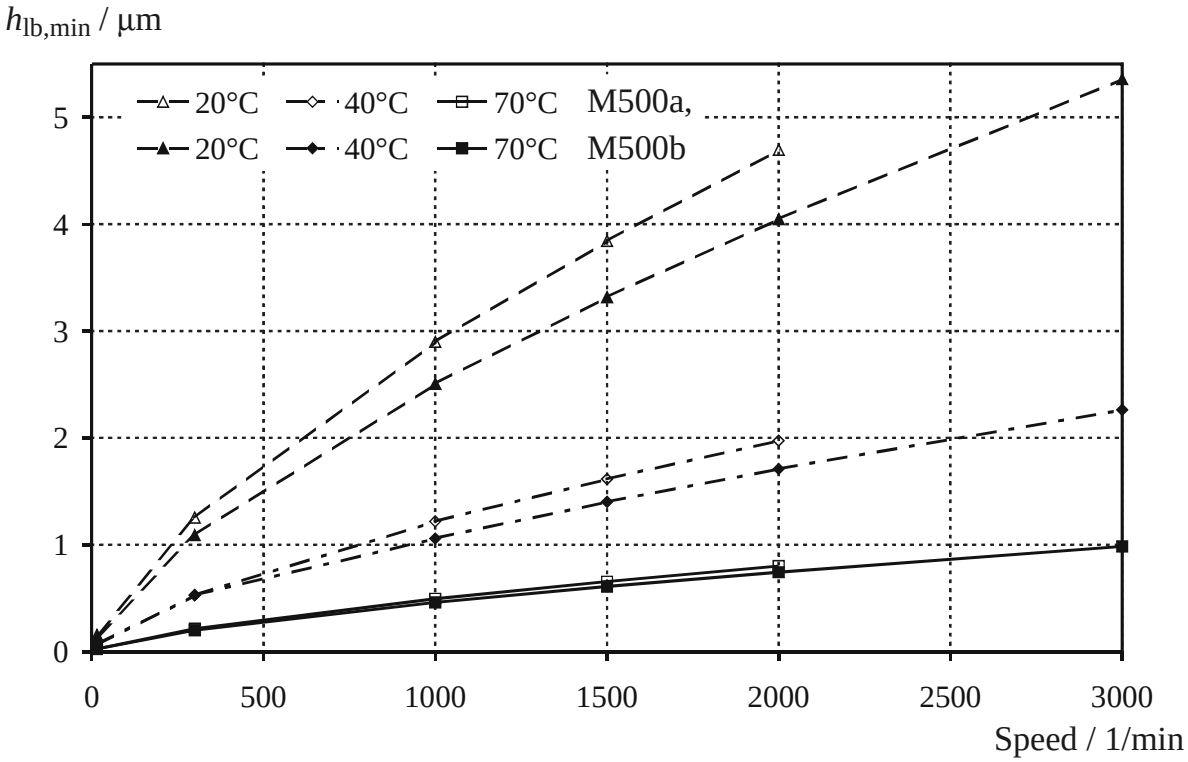

Figure D.3: 500 kW power level - Calculated minimum thickness of lubricating film as function of motor speed and bearing temperature

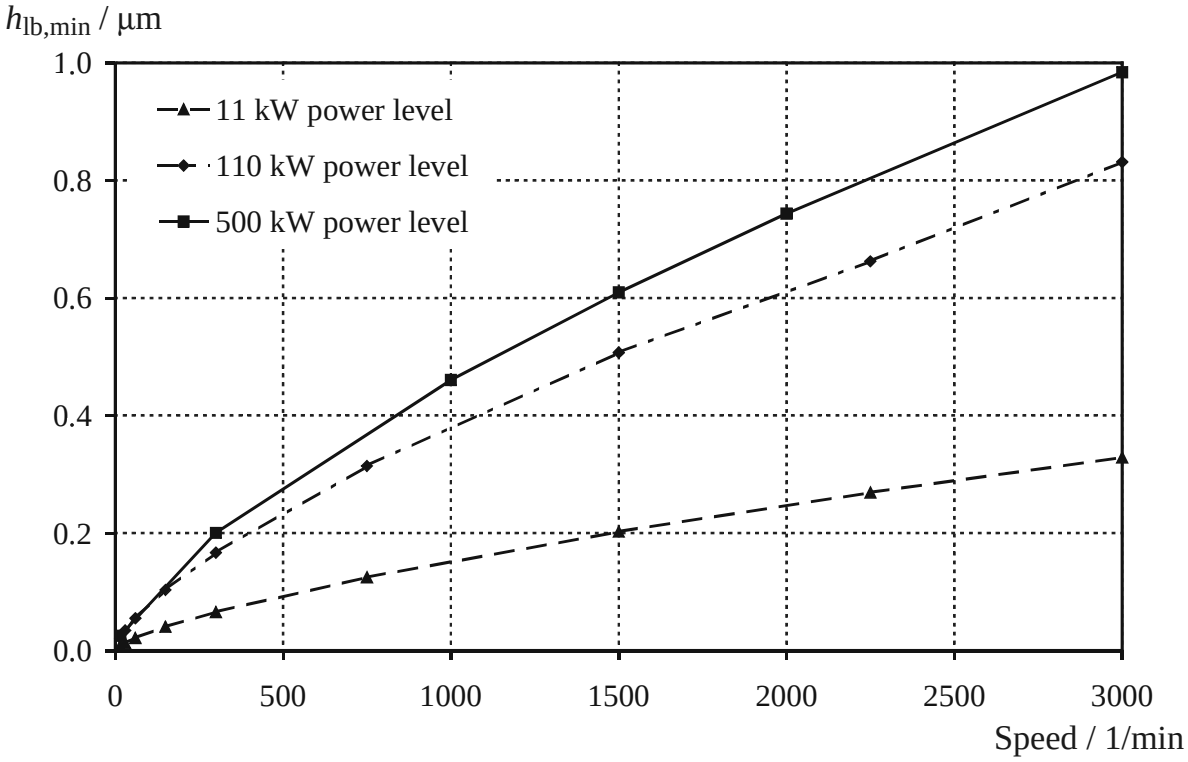

Figure D.4: Comparison of the three investigated power levels - Calculated minimum thickness of lubricating film as function of motor speed at bearing temperature $\vartheta_b \approx 70°C$ (500 kW power level: motor M500b)

Appendix E

Measured Waveforms of Stator Winding Common Mode and Bearing Voltages

This chapter summarizes the measured waveforms and dv/dt of stator winding common mode voltage v_Y and bearing voltage v_b for the different investigated drive configurations.

The stator winding common mode voltage v_Y and the bearing voltage v_b were measured for many different drive configurations as described in Section 3.5 (p. 37). Measurements were done on all investigated motors. The BVR could not be measured on motor M500a, because the occurring circulating bearing currents prevented any buildup of an insulating lubricating film in the bearing. The influence of the following parameters was analyzed:

- ▷ motor speed,
- ▷ motor-inverter-combination,
- ▷ motor cable length l_c and
- ▷ motor cable type (shielded/unshielded),
- ▷ use of one and of two insulated bearings and
- ▷ use of hybrid bearings.

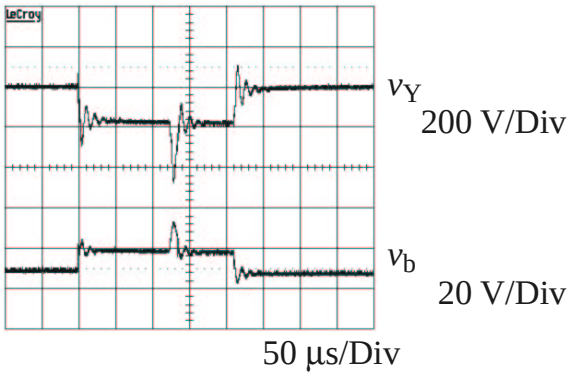

Figure E.1: 500 kW power level - Measured stator winding common mode and bearing voltages v_Y and u_b of induction motor M500b and inverter I500, configuration E1*$_{10}$ (l_c = 10 m, shielded motor cable), V_s = 400 V Y, f_s = 17 Hz / motor speed n = 1020 /min (→ Table E.3)

No remarkable difference between the measured bearing voltage v_b on *drive-end and on non-drive end* was found.

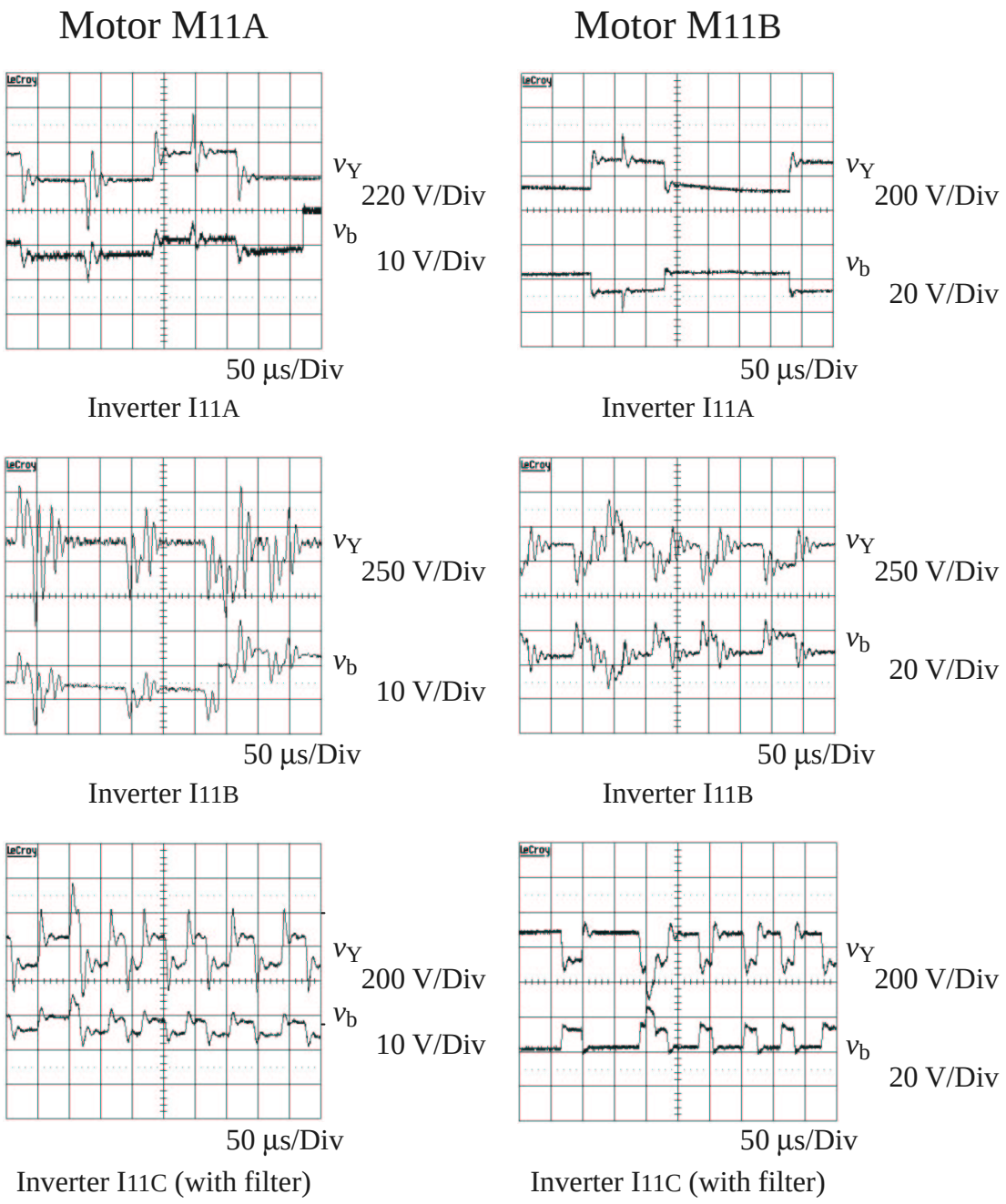

Figure E.2: 11 kW power level - Measured stator winding common mode and bearing voltages v_Y and u_b of *different motor-inverter-combinations*, configuration $E1_{50}$ ($l_c = 50$ m, unshielded motor cable), conventional bearings, $V_s = 400$ V Y, induction motor M11a: $f_s = 30$ Hz / motor speed $n = 900$ /min, induction motor M11b: $f_s = 50$ Hz / motor speed $n = 1500$ /min (→ Table E.1)

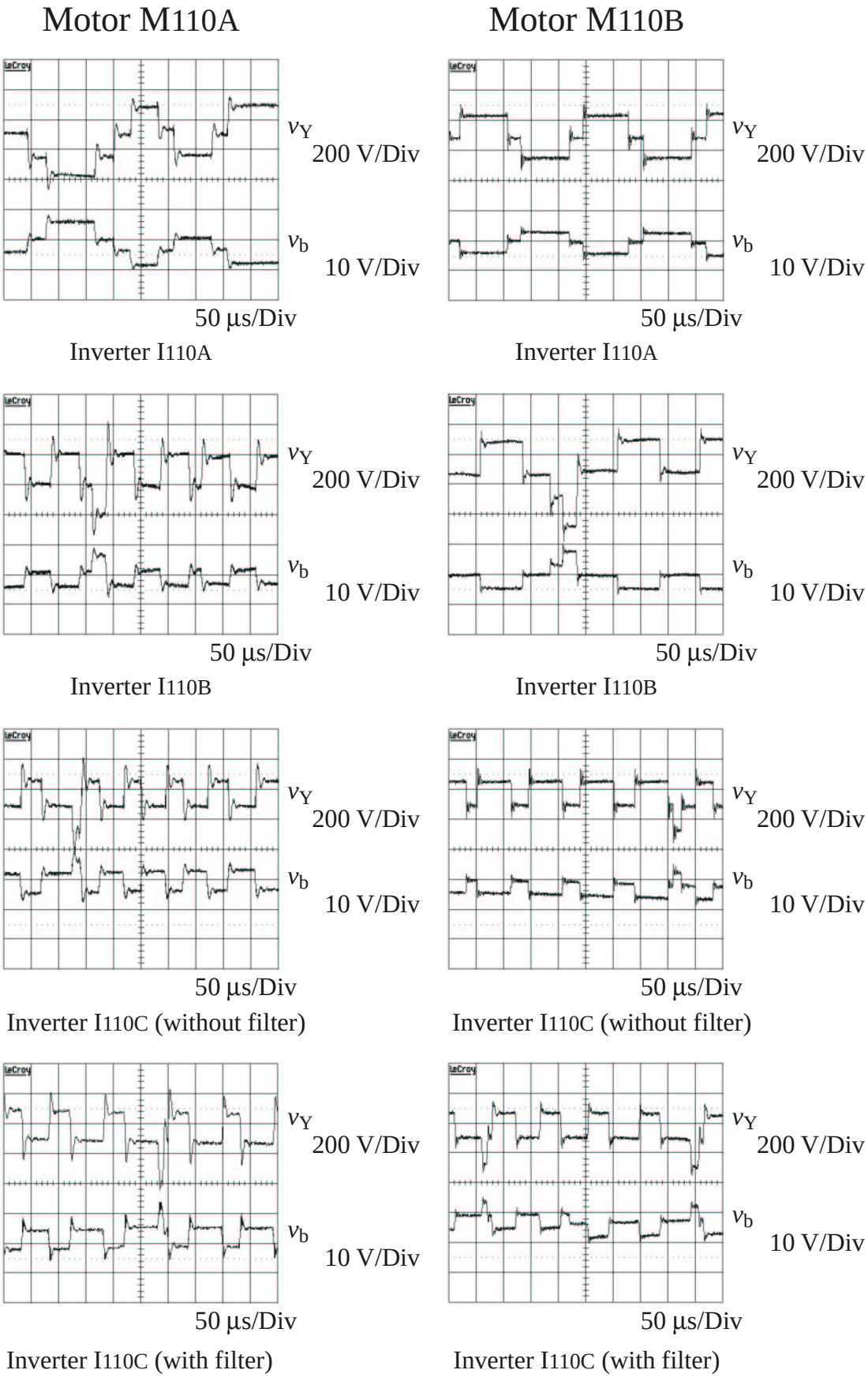

Figure E.3: 110 kW power level - Measured stator winding common mode and bearing voltages v_Y and u_b of *different motor-inverter-combinations*, configuration $E1_{50}$ ($l_c = 50$ m, unshielded motor cable), conventional bearings, $V_s = 400$ V Y, $f_s = 30$ Hz / motor speed $n = 900$ /min (→ Table E.2)

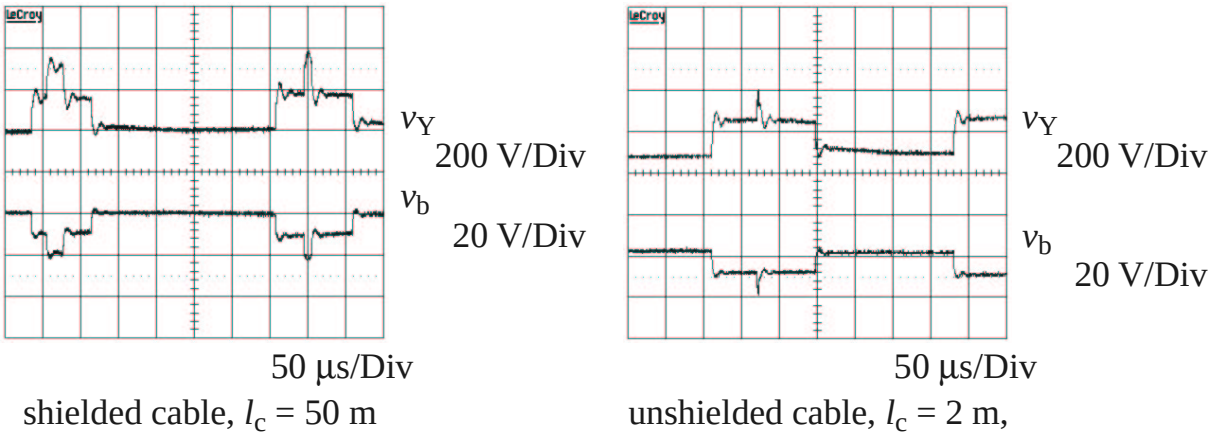

Figure E.4: 11 kW power level - Measured stator winding common mode and bearing voltages v_Y and u_b for use of *shielded motor cables with different lengths*, induction motor M11b and inverter I11a, conventional bearings, V_s = 400 V Y, f_s = 50 Hz / motor speed n = 1500 /min

The motors were Y-connected in order to measure the stator winding common mode voltage v_Y between star point and grounding connection of the motor. Only motor M11b is designed for 400 V Y / 50 Hz. On this motor, measurements were done at f_s = 50 Hz /n = 1500 /min and f_s = 30 Hz / n = 900 /min. *No remarkable influence* on the bearing voltage v_b of this *change of motor speed* was found. The motors M11a, M110b and M110a were operated at V_s = 400 V Y, f_s = 30 Hz / n = 900 /min, motor M500b at V_s = 400 V Y, f_s = 17 Hz / n = 1020 /min for measurements at operation with rated flux. Additional measurements with weakened flux were done with V_s = 400 V Y, f_s = 50 Hz / n = 1500 /min (motors M11a, M110b, M110a) / n = 3000 /min (motor M500b). Again, *no significant influence* on v_Y and v_b was found.

Stator winding common mode and bearing voltages v_Y and v_b were also determined for all the different *motor-inverter-combinations* investigated. *No significant influence* of the combination on BVR and dv/dt was found. The waveforms are different, as are the waveforms of the voltage at the motor terminals (→ Appendix G, p. 229). However, the dv/dt is about the same for a given motor and in the same order for all motors as can be seen from Fig. E.1, Fig. E.2 and Fig. E.3 as well as Tables E.1, E.2 and E.3.

In the same way, *neither cable length nor type* do influence the BVR, nor dv/dt of v_Y and u_b, as can be seen from Fig. E.4 and Table E.4.

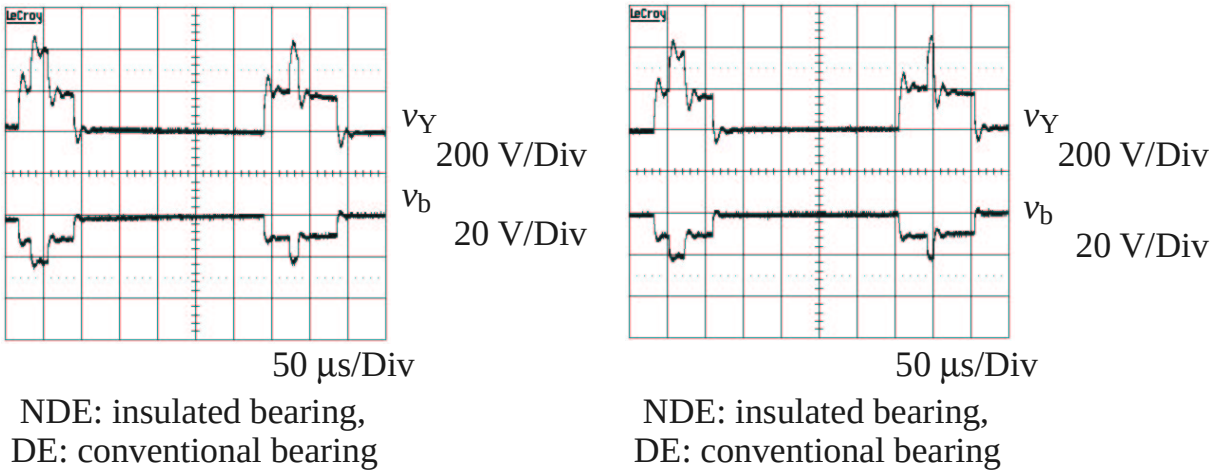

Figure E.5: 11 kW power level - Measured stator winding common mode and bearing voltages v_Y and u_b for use of *one insulated and one conventional bearing* and use of *two insulated bearings*, induction motor M11b and inverter I11a, configuration $E1_{02}$ ($l_c = 2$ m, unshielded motor cable), $V_s = 400$ V Y, $f_s = 50$ Hz / motor speed $n = 1500$ /min (→ Table E.5)

Furthermore, a *change of the type of bearing* does *not* result in a *measurable change* of the BVR, nor of dv/dt of v_Y and u_b. Fig. E.5 shows the measured waveforms for operation of motor M11b with one and with two insulated bearings and Fig. E.6 with two hybrid bearings. Table E.5 summarizes the corresponding dv/dt.

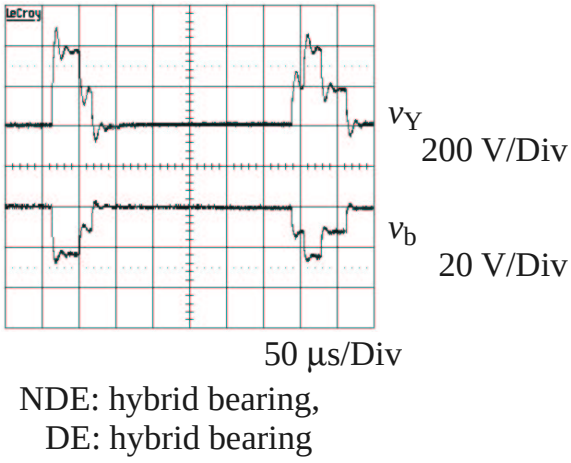

Figure E.6: 11 kW power level - Measured stator winding common mode and bearing voltages v_Y and u_b for *use of hybrid bearings*, induction motor M11b and inverter I11a, configuration $E1_{02}$ (l_c= 2 m, unshielded motor cable), $V_s = 400$ V Y, $f_s = 50$ Hz / motor speed $n = 1500$ /min (→ Table E.5)

	Voltage gradient		Voltage over-shoot	
	Motor M11a	Motor M11b	Motor M11a	Motor M11b
Inverter I11a				
v_Y	0.08 kV/μs	0.06 kV/μs max. grad. $\leq$ 0.2 kV/μs	80 %	35 %
v_b	(1...2) V/μs	4 V/μs max. grad. $\leq$ 18 kV/μs	90 %	25 %
Inverter I11b				
v_Y	0.08 kV/μs	0.05 kV/μs	(130...170) %	80 %
v_b	(1...2) V/μs	4 V/μs	(110...180) %	85 %
Inverter I11c				
v_Y	0.07 kV/μs	0.06 kV/μs	85 %	35 %
v_b	(1...2) V/μs	4 V/μs	60 %	35 %

Table E.1: 11 kW power level - Measured dv/dt and voltage over-shoot of stator winding common mode and bearing voltage v_Y and v_b of *different motor-inverter-combinations*, configuration $E1_{50}$ ($l_c = 50$ m, unshielded motor cable), conventional bearings, $V_s = 400$ V Y, induction motor M11a: $f_s = 30$ Hz / motor speed $n = 900$ /min, induction motor M11b: $f_s = 50$ Hz / motor speed $n = 1500$ /min (→ Fig. E.2)

	Voltage gradient		Voltage over-shoot	
	Motor M110a	Motor M110b	Motor M110a	Motor M110b
Inverter I110a				
v_Y	0.08 kV/μs	0.14 kV/μs	50 %	55 %
v_b	(2...3) V/μs	4 V/μs	40 %	60 %
Inverter I110b				
v_Y	0.14 kV/μs	0.14 kV/μs	50 %	50 %
v_b	(2...3) V/μs	3 V/μs	50 %	50 %
Inverter I110c (without filter)				
v_Y	0.14 kV/μs	0.19 kV/μs	65 %	45 %
v_b	(2...3) V/μs	4 V/μs	50 %	45 %
Inverter I110c (with filter)				
v_Y	0.08 kV/μs	0.08 kV/μs	70 %	30 %
v_b	(2...3) V/μs	(2...3) V/μs	70 %	30 %

Table E.2: 110 kW power level - Measured dv/dt and voltage over-shoot of stator winding common mode and bearing voltage v_Y and v_b for *different motor-inverter-combinations*, configuration $E1_{50}$ ($l_c = 50$ m, unshielded motor cable), conventional bearings, $V_s = 400$ V Y, $f_s = 30$ Hz / motor speed $n = 900$ /min (→ Fig. E.3)

	Voltage gradient		Voltage over-shoot	
	Motor M500a	Motor M500b	Motor M500a	Motor M500b
v_Y	0.07 kV/μs	0.06 kV/μs	60 %	70 %
v_b	not measured	3 V/μs	not measured	75 %

Table E.3: 500 kW power level - Measured dv/dt and voltage over-shoot of stator winding common mode and bearing voltage v_Y and v_b for *different motor-inverter-combinations*, inverter I500, configuration $E1_{10}$ ($l_c = 10$ m, unshielded motor cable), conventional bearings, $V_s = 400$ V Y, induction motor M500a: $f_s = 17$ Hz / motor speed $n = 1020$ /min, induction motor M500a: $f_s = 30$ Hz / motor speed $n = 900$ /min (→ Fig. E.1)

	Voltage gradient		Voltage over-shoot	
	Motor M11a	Motor M11b	Motor M11a	Motor M11b
Shielded motor cable, $l_c = 50$ m				
v_Y	0.07 kV/μs	0.05 kV/μs max. grad. $\leq$ 0.2 kV/μs	75 %	30 %
v_b	(1...2) V/μs	4 V/μs max. grad. $\leq$ 20 kV/μs	50 %	20 %
Unshielded motor cable, $l_c = 50$ m				
v_Y	0.08 kV/μs	0.06 kV/μs max. grad. $\leq$ 0.2 kV/μs	80 %	35 %
v_b	(1...2) V/μs	4 V/μs max. grad. $\leq$ 18 kV/μs	90 %	25 %
Unshielded motor cable, $l_c = 10$ m				
v_Y	0.08 kV/μs	0.05 kV/μs max. grad. $\leq$ 0.3 kV/μs	80 %	30 %
v_b	(1...2) V/μs	4 V/μs max. grad. $\leq$ 20 kV/μs	(35...85) %	25 %
Unshielded motor cable, $l_c = 2$ m				
v_Y	0.07 kV/μs	0.05 kV/μs max. grad. $\leq$0.3 kV/μs	80 %	30 %
v_b	(1...2) V/μs	3 V/μs max. grad. $\leq$ 20 kV/μs	60 %	20 %

Table E.4: 11 kW power level - Measured dv/dt and voltage over-shoot of stator winding common mode and bearing voltage v_Y and v_b when fed with *different motor cables*, inverter I11a, configuration E1, conventional bearings, $V_s = 400$ V Y, induction motor M11a: $f_s = 30$ Hz / motor speed $n = 900$ /min, induction motor M11b: $f_s = 50$ Hz / motor speed $n = 1500$ /min (→ Fig. E.4)

Voltage gradient		Voltage over-shoot	
stator winding common mode voltage v_Y	bearing voltage v_b	stator winding common mode voltage v_Y	bearing voltage v_b
DE & NDE: conventional bearings			
0.05 kV/μs max. grad. $\leq$ 0.3 kV/μs	3 V/μs max. grad. $\leq$ 20 kV/μs	30 %	20 %
DE: insulated bearing, NDE: conventional bearing			
0.05 kV/μs max. grad. $\leq$ 0.3 kV/μs	3 V/μs max. grad. $\leq$ 21 kV/μs	35 %	25 %
DE & NDE: insulated bearings			
0.05 kV/μs max. grad. $\leq$ 0.3 kV/μs	3 V/μs max. grad. $\leq$ 20 kV/μs	35 %	20 %
DE & NDE: hybrid bearings			
0.06 kV/μs max. grad. $\leq$ 0.4 kV/μs	4 V/μs max. grad. $\leq$ 23 kV/μs	35 %	20 %

Table E.5: 11 kW power level - Measured dv/dt and voltage over-shoot of stator winding common mode and bearing voltage v_Y and v_b when operated with *different types of bearings*, induction motor M11b, inverter I11a, configuration $E1_{02}$ ($l_c = 02$ m, unshielded motor cable) $V_s = 400$ V Y, $f_s = 50$ Hz / motor speed $n = 1500$ /min (→ Fig. E.6)

Appendix F

Measured Waveforms of Ground Currents

This chapter summarizes measured waveforms of the stator ground currents for different investigated drive configurations of the three power levels 11 kW, 110 kW and 500 kW.

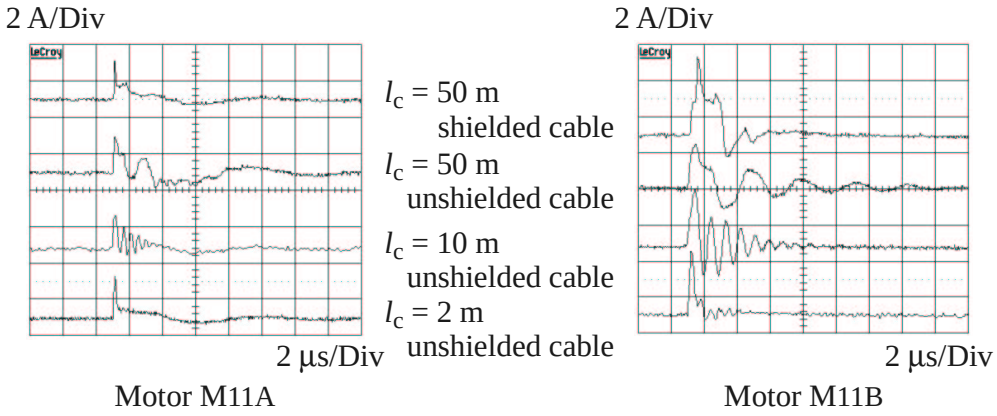

Figure F.1: 11 kW power level - Measured ground current for use of *different motor cables*, inverter I11a, configurations $E1^*_{50}$, $E1_{50}$, $E1_{10}$ and $E1_{02}$, $f_s = 50$ Hz

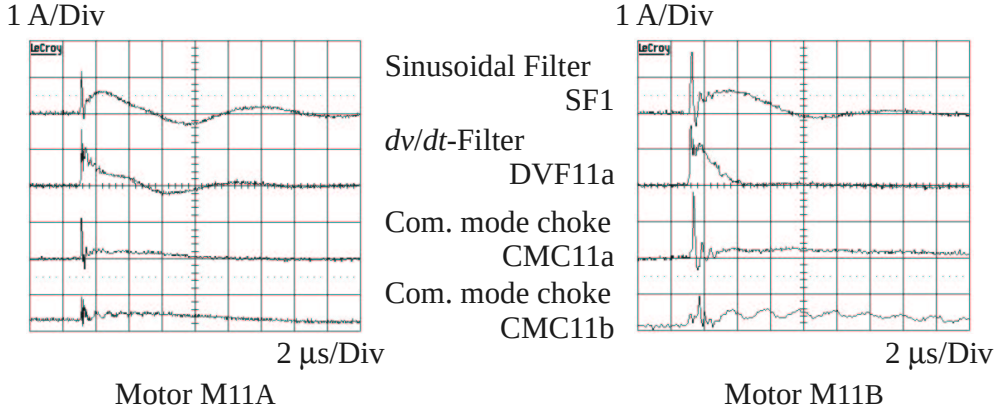

Figure F.2: 11 kW power level - Measured ground current for use of *different filters*, inverter I11a, configuration $E1_{02}$ ($l_c = 2$ m, unshielded motor cable), $f_s = 50$ Hz

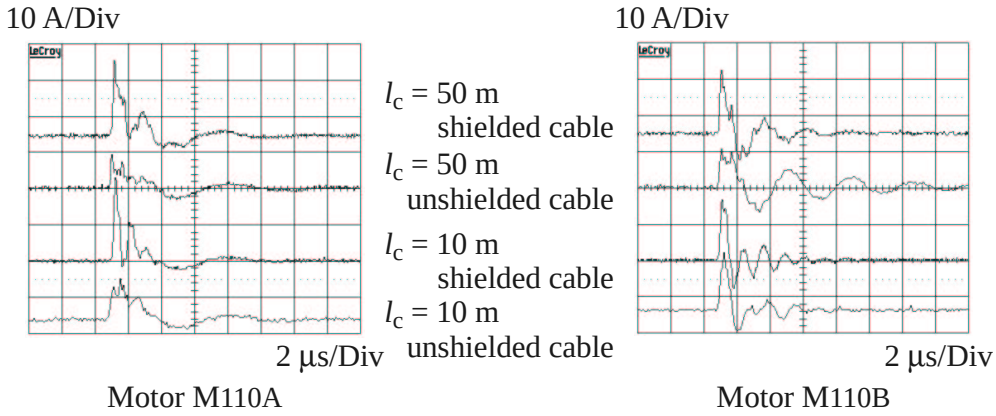

Figure F.3: 110 kW power level - Measured ground current for use of *different motor cables*, inverter I110a, configurations E1*$_{50}$, E1$_{50}$, E1$_{10}$ and E1*$_{10}$, f_s = 50 Hz

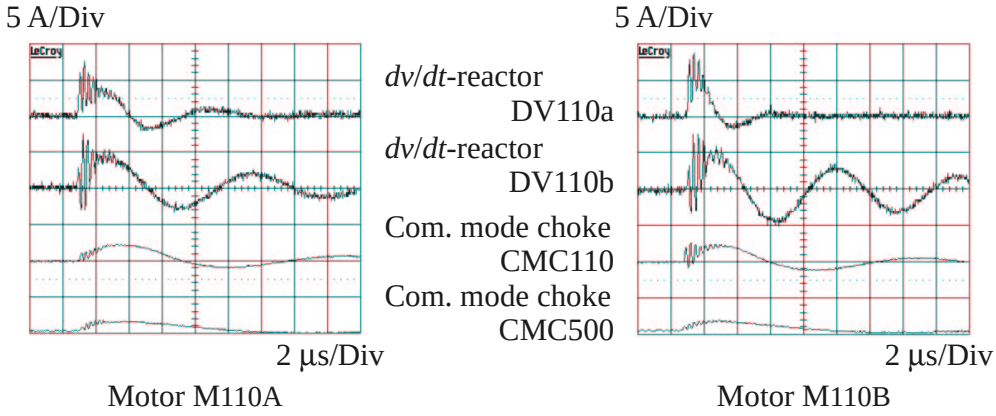

Figure F.4: 110 kW power level - Measured ground current for use of *different filters*, inverter I110a, configuration E1*$_{10}$ (l_c = 10 m, shielded motor cable), f_s = 50 Hz

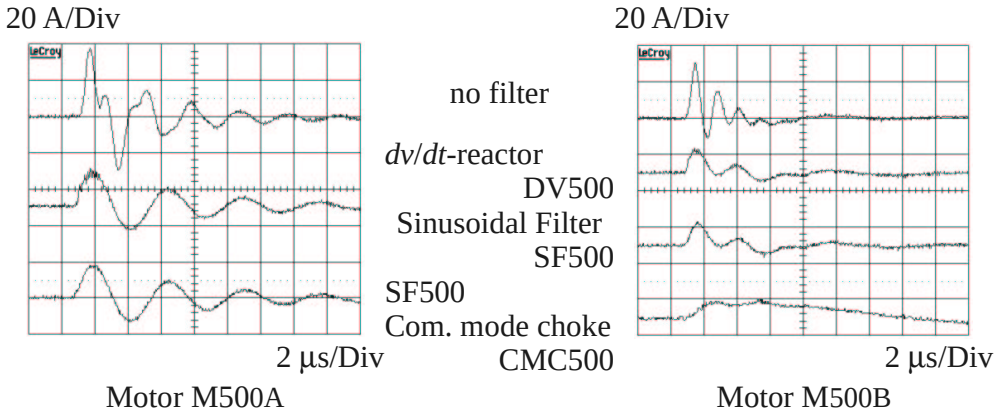

Figure F.5: 500 kW power level - Measured ground current for use of *different filters*, inverter I500, configuration E1*s_{10} (l_c = 10 m, shielded motor cable), f_s = 50 Hz, (exception: induction motor M500b and sinusoidal filter SF500: f_s = 17 Hz)

Appendix G

Measured Waveforms of Line-to-line and Line-to-earth Voltages

This chapter summarizes the measured dv/dt, voltage over-shoot and waveforms of line-to-line and line-to-earth voltages for the different configurations studied.

Generally, the dv/dt is in the order of $dv/dt = (1...3)$ kV/μs, with higher values for the smaller than for the larger motors, and for the line-to-line voltages v_{LL} when compared with the line-to-earth voltages v_{Lg}. The voltage pulses do not rise constantly, but the gradients decrease with increasing voltage. Therefore, the measured dv/dt is an average value. This is obvious notably at inverters I11a and I110a.

Due to a positive reflection coefficient, the dv/dt at the motor terminals is larger than at the output of the inverter, where the reflection coefficient is negative. With an increase of the cable length, two factors have opposite effect on the dv/dt at the motor terminals: With increased cable length, the critical cable length (8.6) (p. 172) is surpassed, and voltage over-shoot at the motor terminals rises up to maximal $2V_{\mathrm{dc}}$. As with rising cable length, attenuation due to cable resistance increases linear, whereas voltage reflection is limited to twice the dc-link voltage, the dv/dt at the motor terminals is reduced at long cable lengths.

The influence of the type of cable on the dv/dt of the voltages at the motor terminals is negligible. The dv/dt with filter operation is an order of magnitude smaller than without use of a filter, because of the increase of the rise time t_{r} (→ Section 5.2, p. 74).

Voltage gradient				
	Inverter output	Open end of cable, no motor connected	Motor M11a	Motor M11b
Inverter I11a				
v_{LL}	(2.2...5.5) kV/μs max. grad. $\leq$ 9.6 kV/μs	3.2 kV/μs max. grad. $\leq$ 7.8 kV/μs	(1.9...3.6) kV/μs max. grad. $\leq$ 6.0 kV/μs	(1.2...2.5) kV/μs max. grad. $\leq$ 3.7 kV/μs
v_{Lg}	0.5 kV/μs max. grad. $\leq$ 2.1 kV/μs	1.6. kV/μs max. grad. $\leq$ 3.2 kV/μs	1.5 kV/μs max. grad. $\leq$ 2.8 kV/μs	1.2 kV/μs max. grad. $\leq$ 2.0 kV/μs
Inverter I11b				
v_{LL}	1.3 kV/μs max. grad. $\leq$ 2.8 kV/μs	2.7 kV/μs max. grad. $\leq$ 4.9 kV/μs	2.9 kV/μs max. grad. $\leq$ 4.9 kV/μs	1.5 kV/μs max. grad. $\leq$ 3.2 kV/μs
v_{Lg}	0.1 kV/μs max. grad. $\leq$ 1.4 kV/μs	1.4 kV/μs max. grad. $\leq$ 2.6 kV/μs	0.1 kV/μs max. grad. $\leq$ 2.8 kV/μs	0.1 kV/μs max. grad. $\leq$ 2.1 kV/μs
Inverter I11c (with filter)				
v_{LL}	0.1 kV/μs	0.1 kV/μs	0.1 kV/μs max. grad. $\leq$ 0.2 kV/μs	0.1 kV/μs max. grad. $\leq$ 0.2 kV/μs
v_{Lg}	0.2 kV/μs	0.2 kV/μs	0.2 kV/μs	0.2 kV/μs
Voltage over-shoot				
	Inverter output	Open end of cable, no motor connected	Motor M11a	Motor M11b
Inverter I11a				
v_{LL}	15 %	90 %	90 %	85 %
v_{Lg}	5 %	60 %	50 %	60 %
Inverter I11b				
v_{LL}	5 %	85 %	85 %	80 %
v_{Lg}	30 %	40 %	35 %	35 %
Inverter I11c (with filter)				
v_{LL}	20 %	20 %	20 %	20 %
v_{Lg}	10 %	10 %	10 %	15 %

Table G.1: 11 kW power level - Measured voltage dv/dt and voltage over-shoot of line-to-line and line-to-earth voltage v_{LL} and v_{Lg} at inverter output and motor terminals at *different motor-inverter-combinations*, configuration $E1_{50}$ (l_c = 50 m, unshielded motor cable) (→ Fig. G.1)

Voltage gradient				
	Inverter output	Open end of cable, no motor connected	Motor M110a	Motor M110b
Inverter I110a				
v_{LL}	0.4 kV/μs max. grad. $\leq$ 1.8 kV/μs	0.8 kV/μs max. grad. $\leq$ 2.8 kV/μs	0.6 kV/μs max. grad. $\leq$ 1.5 kV/μs	0.4 kV/μs max. grad. $\leq$ 0.9 kV/μs
v_{Lg}	0.4 kV/μs max. grad. $\leq$ 1.5 kV/μs	1.5 kV/μs max. grad. $\leq$ 2.2 kV/μs	0.8 kV/μs max. grad. $\leq$ 1.6 kV/μs	0.5 kV/μs max. grad. $\leq$ 0.9 kV/μs
Inverter I110b				
v_{LL}	2.1 kV/μs max. grad. $\leq$ 4.1 kV/μs	3.1 kV/μs max. grad. $\leq$ 3.9 kV/μs	2.5 kV/μs max. grad. $\leq$ 3.6 kV/μs	1.4 kV/μs max. grad. $\leq$ 1.9 kV/μs
v_{Lg}	0.8 kV/μs max. grad. $\leq$ 2.1 kV/μs	2.0 kV/μs max. grad. $\leq$ 3.5 kV/μs	1.6 kV/μs max. grad. $\leq$ 2.6 kV/μs	1.0 kV/μs max. grad. $\leq$ 1.5 kV/μs
Inverter I110c (without filter)				
v_{LL}	1.2 kV/μs max. grad. $\leq$ 2.0 kV/μs	2.7 kV/μs max. grad. $\leq$ 4.1 kV/μs	1.8 kV/μs max. grad. $\leq$ 2.8 kV/μs	1.2 kV/μs max. grad. $\leq$ 1.8 kV/μs
v_{Lg}	1.0 kV/μs max. grad. $\leq$ 1.6 kV/μs	2.3 kV/μs max. grad. $\leq$ 3.3 kV/μs	1.4 kV/μs max. grad. $\leq$ 2.6 kV/μs	1.0 kV/μs max. grad. $\leq$ 1.3 kV/μs
Inverter I110c (with filter)				
v_{LL}	0.2 kV/μs	0.2 kV/μs	0.2 kV/μs	0.2 kV/μs
v_{Lg}	0.2 kV/μs	0.2 kV/μs	0.2 kV/μs	0.2 kV/μs
Voltage over-shoot				
	Inverter output	Open end of cable, no motor connected	Motor M110a	Motor M110b
Inverter I110a				
v_{LL}	35 %	45 %	45 %	35 %
v_{Lg}	20 %	45 %	50 %	40 %
Inverter I110b				
v_{LL}	10 %	90 %	80 %	85 %
v_{Lg}	5 %	85 %	60 %	60 %
Inverter I110c (without filter)				
v_{LL}	10 %	100 %	80 %	80 %
v_{Lg}	10 %	90 %	60 %	55 %
Inverter I110c (with filter)				
v_{LL}	20 %	20 %	20 %	20 %
v_{Lg}	10 %	10 %	20 %	20 %

Table G.2: 110 kW power level - Measured voltage dv/dt and voltage over-shoot of line-to-line and line-to-earth voltage v_{LL} and v_{Lg} at inverter output and motor terminals at *different motor-inverter-combinations*, configuration $E1_{50}$ (l_c = 50 m, unshielded motor cable) (→ Fig. E.5 and Fig. G.2)

Voltage gradient			
	Inverter output	Motor M11a	Motor M11b
Shielded motor cable, $l_c = 50$ m			
v_{LL}	(1.8...5.1) kV/μs max. grad. $\leq$ 10 kV/μs	3.0 kV/μs max. grad. $\leq$ 5.4 kV/μs	3.1 kV/μs max. grad. $\leq$ 5.5 kV/μs
v_{Lg}	0.5 kV/μs max. grad. $\leq$ 2.7 kV/μs	1.5 kV/μs max. grad. $\leq$ 3.0 kV/μs	1.8 kV/μs max. grad. $\leq$ 2.8 kV/μs
Unshielded motor cable, $l_c = 50$ m			
v_{LL}	(2.2...5.5) kV/μs max. grad. $\leq$ 9.6 kV/μs	(1.9...3.6) kV/μs max. grad. $\leq$ 6.0 kV/μs	(1.2...2.5) kV/μs max. grad. $\leq$ 3.7 kV/μs
v_{Lg}	0.5 kV/μs max. grad. $\leq$ 2.1 kV/μs	1.5 kV/μs max. grad. $\leq$ 2.8 kV/μs	1.2 kV/μs max. grad. $\leq$ 2.0 kV/μs
Unshielded motor cable, $l_c = 10$ m			
v_{LL}	3.4 kV/μs max. grad. $\leq$ 4.8 kV/μs	(3.2...6.2) kV/μs max. grad. $\leq$ 8.1 kV/μs	3.0 kV/μs max. grad. $\leq$ 4.2 kV/μs
v_{Lg}	1.3 kV/μs max. grad. $\leq$ 2.7 kV/μs	2.3 kV/μs max. grad. $\leq$ 2.2 kV/μs	3.0 kV/μs max. grad. $\leq$ 3.1 kV/μs
Unshielded motor cable, $l_c = 2$ m			
v_{LL}	(2.4...5.5) kV/μs	(3.6...10.4) kV/μs	(3.1...8.5) kV/μs
v_{Lg}	1.8 kV/μs max. grad. $\leq$ 3.7 kV/μs	1.6 kV/μs max. grad. $\leq$ 3.1 kV/μs	1.5 kV/μs max. grad. $\leq$ 2.9 kV/μs
Voltage over-shoot			
	Inverter output	Motor M11a	Motor M11b
Shielded motor cable, $l_c = 50$ m			
v_{LL}	10 %	90 %	90 %
v_{Lg}	5 %	60 %	65 %
Unshielded motor cable, $l_c = 50$ m			
v_{LL}	15 %	90 %	85 %
v_{Lg}	5 %	50 %	60 %
Unshielded motor cable, $l_c = 10$ m			
v_{LL}	25 %	80 %	50 %
v_{Lg}	5 %	20 %	30 %
Unshielded motor cable, $l_c = 2$ m			
v_{LL}	30 %	55 %	15 / 50 %
v_{Lg}	10 %	0 %	10 %

Table G.3: 11 kW power level - Measured voltage dv/dt and voltage over-shoot of line-to-line and line-to-earth voltage v_{LL} and v_{Lg} at inverter output and motor terminals at motor-operation with *different motor cables*, inverter I11a, configuration E1 (→ Fig. G.1)

Voltage gradient			
	Inverter output	Motor M110a	Motor M110b
Shielded motor cable, $l_c = 80$ m			
v_{LL}	0.4 kV/μs max. grad. $\leq$ 0.8 kV/μs	0.6 kV/μs max. grad. $\leq$ 1.2 kV/μs	0.5 kV/μs
v_{Lg}	0.4 kV/μs max. grad. $\leq$ 1.3 kV/μs	0.7 kV/μs max. grad. $\leq$ 1.5 kV/μs	0.6 kV/μs max. grad. $\leq$ 1.2 kV/μs
Shielded motor cable, $l_c = 50$ m			
v_{LL}	0.4 kV/μs max. grad. $\leq$ 0.9 kV/μs	0.7 kV/μs max. grad. $\leq$ 1.0 kV/μs	0.5 kV/μs max. grad. $\leq$ 0.9 kV/μs
v_{Lg}	0.4 kV/μs max. grad. $\leq$ 1.4 kV/μs	0.8 kV/μs max. grad. $\leq$ 1.6 kV/μs	0.7 kV/μs max. grad. $\leq$ 1.1 kV/μs
Unshielded motor cable, $l_c = 50$ m			
v_{LL}	0.4 kV/μs max. grad. $\leq$ 1.8 kV/μs	0.6 kV/μs max. grad. $\leq$ 1.5 kV/μs	0.4 kV/μs max. grad. $\leq$ 0.9 kV/μs
v_{Lg}	0.4 kV/μs max. grad. $\leq$ 1.5 kV/μs	0.8 kV/μs max. grad. $\leq$ 1.6 kV/μs	0.5 kV/μs max. grad. $\leq$ 0.9 kV/μs
Shielded motor cable, $l_c = 10$ m			
v_{LL}	0.9 kV/μs	1.1 kV/μs	0.5 kV/μs max. grad. $\leq$ 0.8 kV/μs
v_{Lg}	1.0 kV/μs	1.5 kV/μs	1.0 kV/μs
Unshielded motor cable, $l_c = 10$ m			
v_{LL}	1.0 kV/μs max. grad. $\leq$ 1.3 kV/μs	1.2 kV/μs max. grad. $\leq$ 2.4 kV/μs	0.7 kV/μs max. grad. $\leq$ 1.5 kV/μs
v_{Lg}	1.0 kV/μs max. grad. $\leq$ 2.1 kV/μs	1.4 kV/μs max. grad. $\leq$ 2.8 kV/μs	0.9 kV/μs max. grad. $\leq$ 1.6 kV/μs
Voltage over-shoot			
	Inverter output	Motor M110a	Motor M110b
Shielded motor cable, $l_c = 80$ m			
v_{LL}	40 %	45 %	45 %
v_{Lg}	30 %	35 %	40 %
Shielded motor cable, $l_c = 50$ m			
v_{LL}	30 %	40 %	40 %
v_{Lg}	20 %	35 %	30 %
Unshielded motor cable, $l_c = 50$ m			
v_{LL}	35 %	45 %	35 %
v_{Lg}	20 %	50 %	40 %
Shielded motor cable, $l_c = 10$ m			
v_{LL}	20 %	25 %	30 %
v_{Lg}	15 %	30 %	20 %
Unshielded motor cable, $l_c = 10$ m			
v_{LL}	20 %	30 %	30 %
v_{Lg}	20 %	35 %	35 %

Table G.4: 110 kW power level - Measured voltage dv/dt and voltage over-shoot of line-to-line and line-to-earth voltage v_{LL} and v_{Lg} at inverter output and motor terminals at motor-operation with *different motor cables*, inverter I110a, configuration E1 ($\rightarrow$ Fig. G.2)

Voltage gradient			
	Inverter output	Motor M500a	Motor M500b
Unshielded motor cable, $l_c = 10$ m			
v_{LL}	2.7 kV/μs max. grad. $\leq$ 4.1 kV/μs	3.4 kV/μs	3.3 kV/μs
v_{Lg}	1.1 kV/μs max. grad. $\leq$ 2.7 kV/μs	1.6 kV/μs max. grad. $\leq$ 3.2 kV/μs	1.7 kV/μs max. grad. $\leq$ 3.2 kV/μs
Shielded motor cable, $l_c = 10$ m			
v_{LL}	not measured	2.6 kV/μs	2.9 kV/μs max. grad. $\leq$ 3.3 kV/μs
v_{Lg}	not measured	1.7 kV/μs	1.8 kV/μs
Shielded motor cable, $l_c = 2$ m			
v_{LL}	not measured	2.6 kV/μs max. grad. $\leq$ 4.6 kV/μs	2.6 kV/μs max. grad. $\leq$ 3.6 kV/μs
v_{Lg}	not measured	2.2 kV/μs	2.2 kV/μs

Voltage over-shoot			
	Inverter output	Motor M500a	Motor M500b
Unshielded motor cable, $l_c = 10$ m			
v_{LL}	20...35 %	65 %	60 %
v_{Lg}	10 %	35 %	40 %
Shielded motor cable, $l_c = 10$ m			
v_{LL}	not measured	65 %	65 %
v_{Lg}	not measured	35 %	40 %
Shielded motor cable, $l_c = 2$ m			
v_{LL}	not measured	40 %	30 %
v_{Lg}	not measured	30 %	30 %

Table G.5: 500 kW power level - Measured voltage dv/dt and voltage over-shoot of line-to-line and line-to-earth voltage v_{LL} and v_{Lg} at inverter output and motor terminals at motor-operation with *different motor cables*, inverter I500, configuration E1 (→ Fig. G.3)

	Voltage gradient		Voltage over-shoot	
	Motor M11a	Motor M11b	Motor M11a	Motor M11b
No filter				
v_{LL}	(3.6...10.4) kV/μs	(3.1...8.5) kV/μs	resp.55 %	15 resp. 50 %
v_{Lg}	1.6 kV/μs max. grad. $\leq$ 3.1	1.5 V/μs max. grad. $\leq$ 2.9	10 %	10 %
dv/dt-filter DVF11a				
v_{LL}	0.5 kV/μs	0.4 kV/μs	45 %	50 %
v_{Lg}	0.5 kV/μs	0.4 kV/μs	50 %	30 %
dv/dt-filter DVF11b				
v_{LL}	0.5 kV/μs	0.5 kV/μs	50 %	60 %
v_{Lg}	$<$ 0.1 kV/μs max. grad. $\leq$ 0.4	$<$ 0.1 kV/μs max. grad. $\leq$ 0.4	25 %	15 %
Sinusoidal filter SF11a				
v_{LL}	$\approx$ 0.1 V/μs	$\approx$ 0.1 V/μs	$\approx$ 0.1 V/μs	$\approx$ 0.1 V/μs
v_{Lg}	0.1 kV/μs	0.1 V/μs	20 %	45 %
Sinusoidal filter SF11b				
v_{LL}	$\approx$ 0.1 V/μs	$\approx$ 0.1 V/μs	$\approx$ 0.1 V/μs	$\approx$ 0.1 V/μs
v_{Lg}	0.1 kV/μs	0.1 V/μs	25 %	50 %
Common mode choke CMC11a				
v_{LL}	not measured	0.5 kV/μs	not measured	60 %
v_{Lg}	0.3 kV/μs max. grad. $\leq$ 0.6	0.3 kV/μs max. grad. $\leq$ 0.4	10 %	10 %
Common mode choke CMC11b				
v_{LL}	3.1 kV/μs	2.5 kV/μs	80 %	95 %
v_{Lg}	2.4 kV/μs	1.4 kV/μs	35 %	20 %

Table G.6: 11 kW power level - Measured voltage dv/dt and voltage over-shoot of line-to-line and line-to-earth voltage v_{LL} and v_{Lg} at inverter output and motor terminals with use of *different inverter-output filters*, inverter I11a, configuration $E1_{02}$ (l_c = 2 m, unshielded motor cable), f_s = 50 Hz ($\rightarrow$ Fig. G.4)

	Voltage gradient		Voltage over-shoot	
	Motor M110a	Motor M110b	Motor M110a	Motor M110b
No filter				
v_{LL}	1.1 kV/μs	0.5 kV/μs max. grad. $\leq$ 0.8 kV/μs	25 %	30 %
v_{Lg}	1.5 kV/μs	1.0 kV/μs	30 %	20 %
dv/dt-reactor DV110a				
v_{LL}	0.6 kV/μs	0.3 kV/μs max. grad. $\leq$ 0.7 kV/μs	25 %	25 %
v_{Lg}	0.7 kV/μs	0.4 V/μs max. grad. $\leq$ 0.5 kV/μs	15 %	25 %
dv/dt-reactor DV110b				
v_{LL}	0.1 kV/μs max. grad. $\leq$ 0.2 kV/μs	0.1 kV/μs	20 %	15 %
v_{Lg}	$<$ 0.2 kV/μs	$<$ 0.2 kV/μs	25 %	20 %
Sinusoidal filter SF110				
v_{LL}	$\approx$ 0.1 V/μs	$\approx$ 0.1 V/μs	$\approx$ 0.1 V/μs	$\approx$ 0.1 V/μs
v_{Lg}	0.1 kV/μs	0.1 kV/μs	40 %	70 %
Common mode choke CMC110				
v_{LL}	1.3 kV/μs	0.7 kV/μs max. grad. $\leq$ 0.9 kV/μs	25 %	35 %
v_{Lg}	0.2 kV/μs max. grad. $\leq$ 1.1 kV/μs	0.2 kV/μs max. grad. $\leq$ 0.6 kV/μs	25 %	25 %
Common mode choke CMC500				
v_{LL}	0.9 kV/μs max. grad. $\leq$ 1.1 kV/μs	0.3 kV/μs	35 %	35 %
v_{Lg}	0.1 kV/μs max. grad. $\leq$ 0.4 kV/μs	0.2 V/μs max. grad. $\leq$ 0.3 kV/μs	20 %	15 %

Table G.7: 110 kW power level - Measured voltage dv/dt and voltage over-shoot of line-to-line and line-to-earth voltage v_{LL} and v_{Lg} at inverter output and motor terminals with use of *different inverter-output filters*, inverter I110a, configuration E1*$_{10}$ (l_c = 10 m, shielded motor cable), f_s = 50 Hz ($\rightarrow$ Fig. G.5)

	Voltage gradient		Voltage over-shoot	
	Motor M500a	Motor M500b	Motor M500a	Motor M500b
No filter				
v_{LL}	2.6 kV/μs	2.9 kV/μs max. grad. $\leq$ 3.3 kV/μs	65 %	65 %
v_{Lg}	1.7 kV/μs	1.8 V/μs	35 %	40 %
dv/dt-reactor DV500				
v_{LL}	0.3 kV/μs	0.3 kV/μs max. grad. $\leq$ 0.4 kV/μs	35 %	45 %
v_{Lg}	0.4 kV/μs	0.5 V/μs	40 %	30 %
Sinusoidal filter SF500				
v_{LL}	$\approx$ 0.1 V/μs	$\approx$ 0.1 V/μs	$\approx$ 0.1 V/μs	$\approx$ 0.1 V/μs
v_{Lg}	0.2 kV/μs	0.3 V/μs	70 %	55 %
Common mode choke CMC500				
v_{LL}	not measured	0.2 kV/μs max. grad. $\leq$ 0.3 kV/μs	not measured	70 %
v_{Lg}	not measured	0.1 V/μs max. grad. $\leq$ 0.3 kV/μs	not measured	30 %

Table G.8: 500 kW power level - Measured voltage dv/dt and voltage over-shoot of line-to-line and line-to-earth voltage v_{LL} and v_{Lg} at inverter output and motor terminals with use of *different inverter-output filters*, inverter I500, configuration E1*$_{10}$ (l_c = 10 m, shielded motor cable), f_s = 50 Hz (→ Fig. G.6)

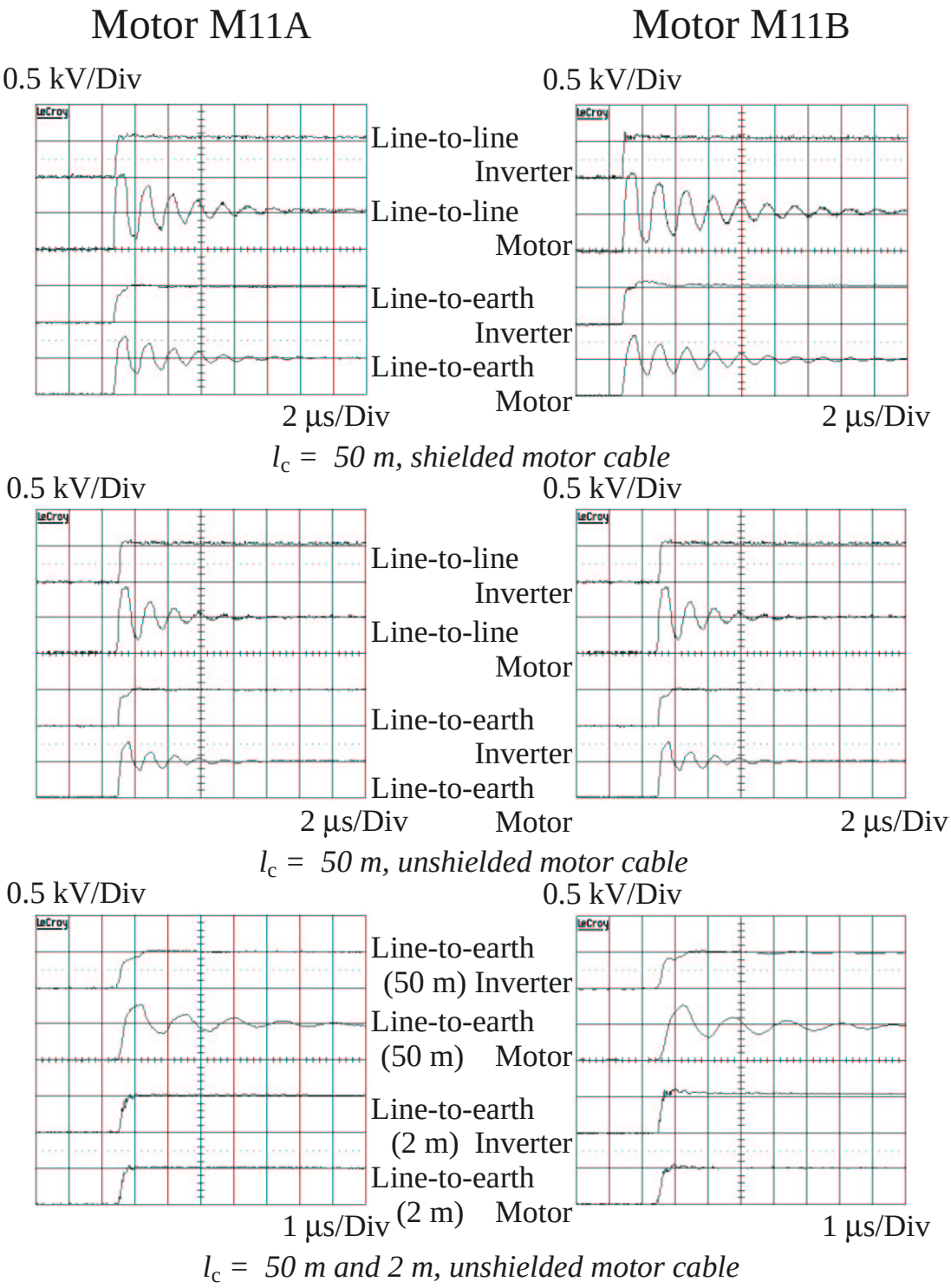

Figure G.1: 11 kW power level - Measured line-to-line and line-to-earth voltages v_{LL} and v_{Lg} at operation with *different cables*, inverter I11a, configuration E1 (→ Table G.1 and Table G.3)

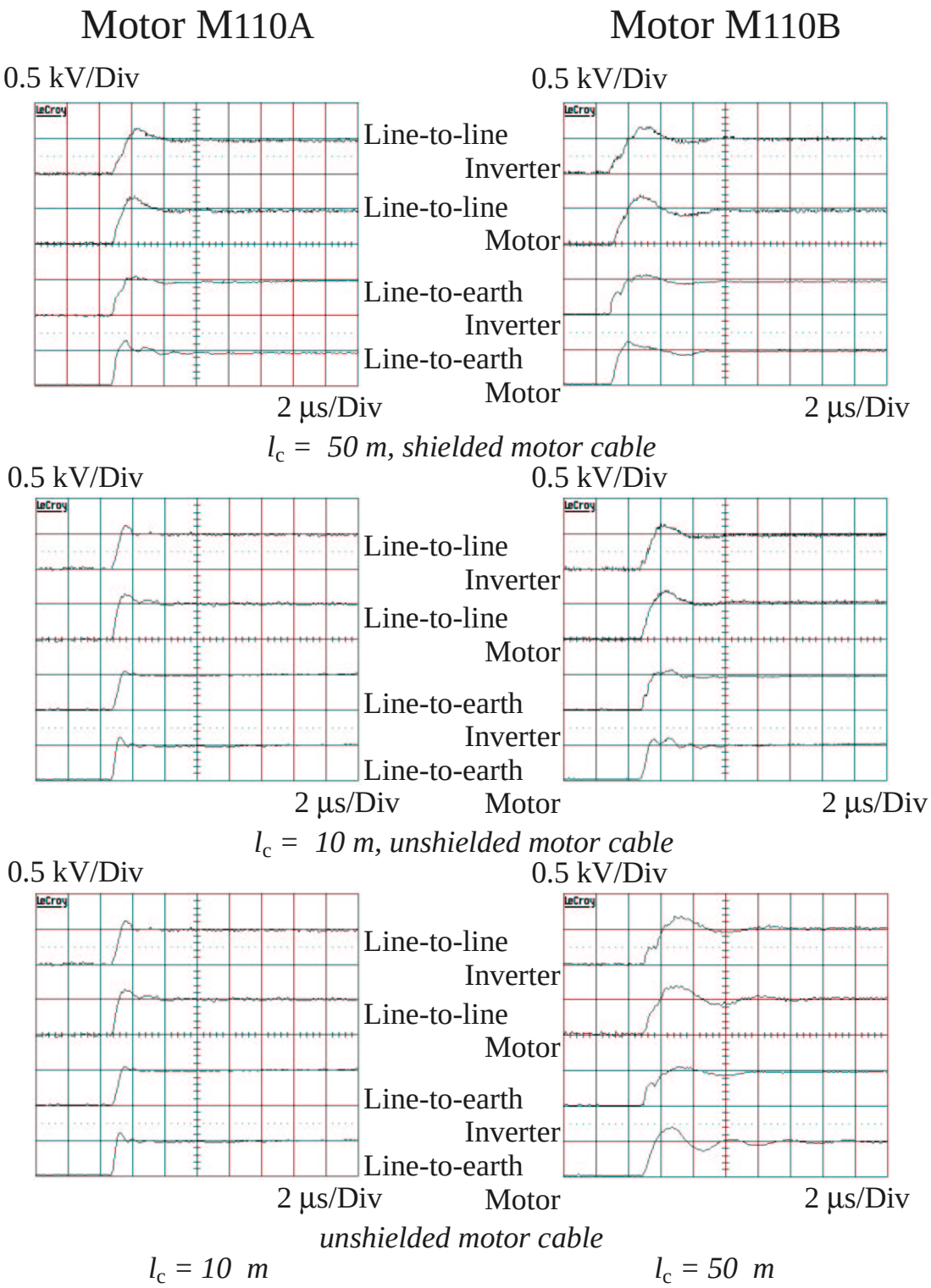

Figure G.2: 110 kW power level - Measured line-to-line and line-to-earth voltages v_{LL} and v_{Lg} at operation with *different motor cables*, inverter I110a, configuration E1 (→ Table G.2 and Table G.4)

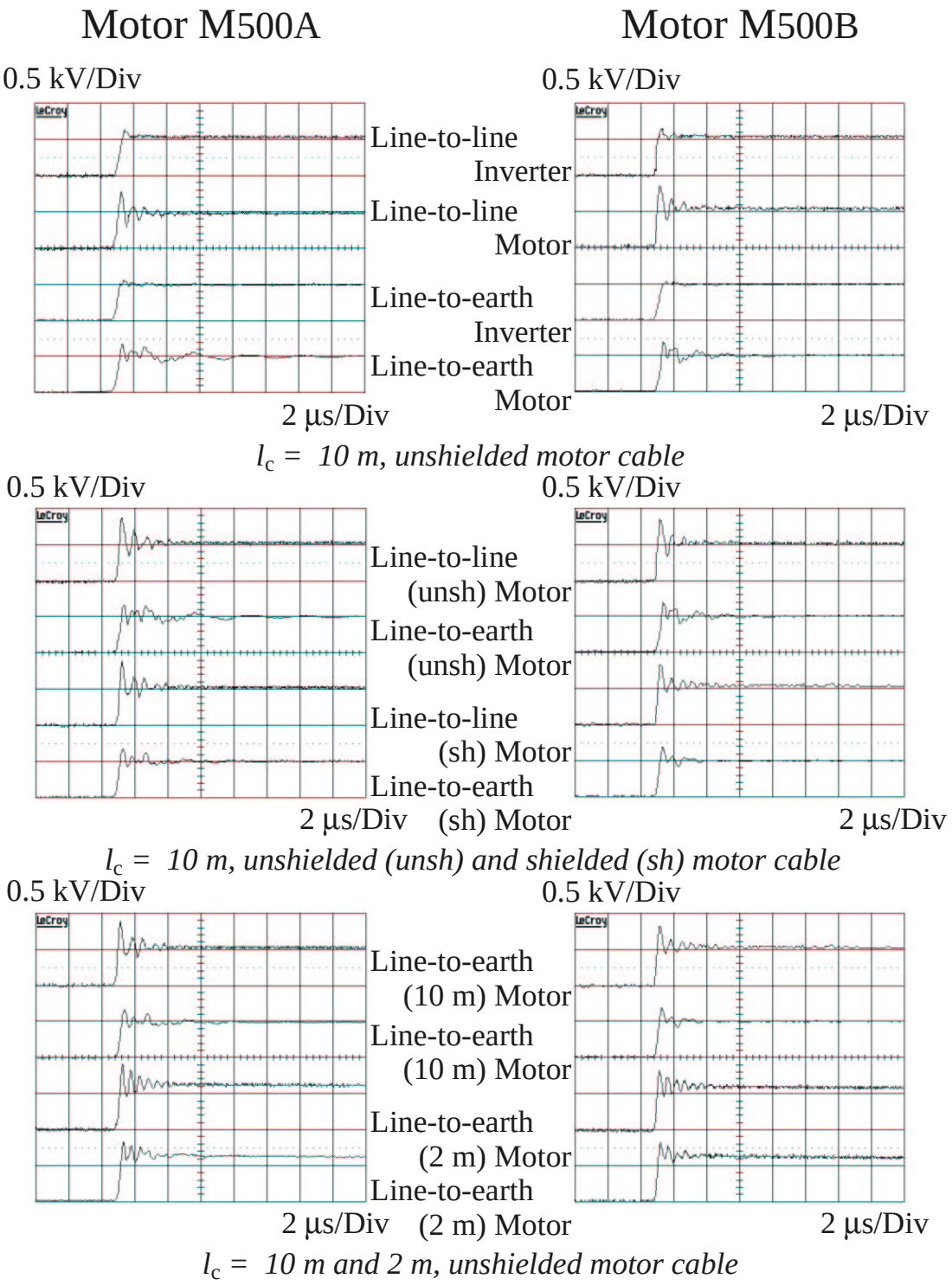

Figure G.3: 500 kW power level - Measured line-to-line and line-to-earth voltages v_{LL} and v_{Lg} at operation with *different motor cables*, inverter I500, configuration E1 (→ Table G.5)

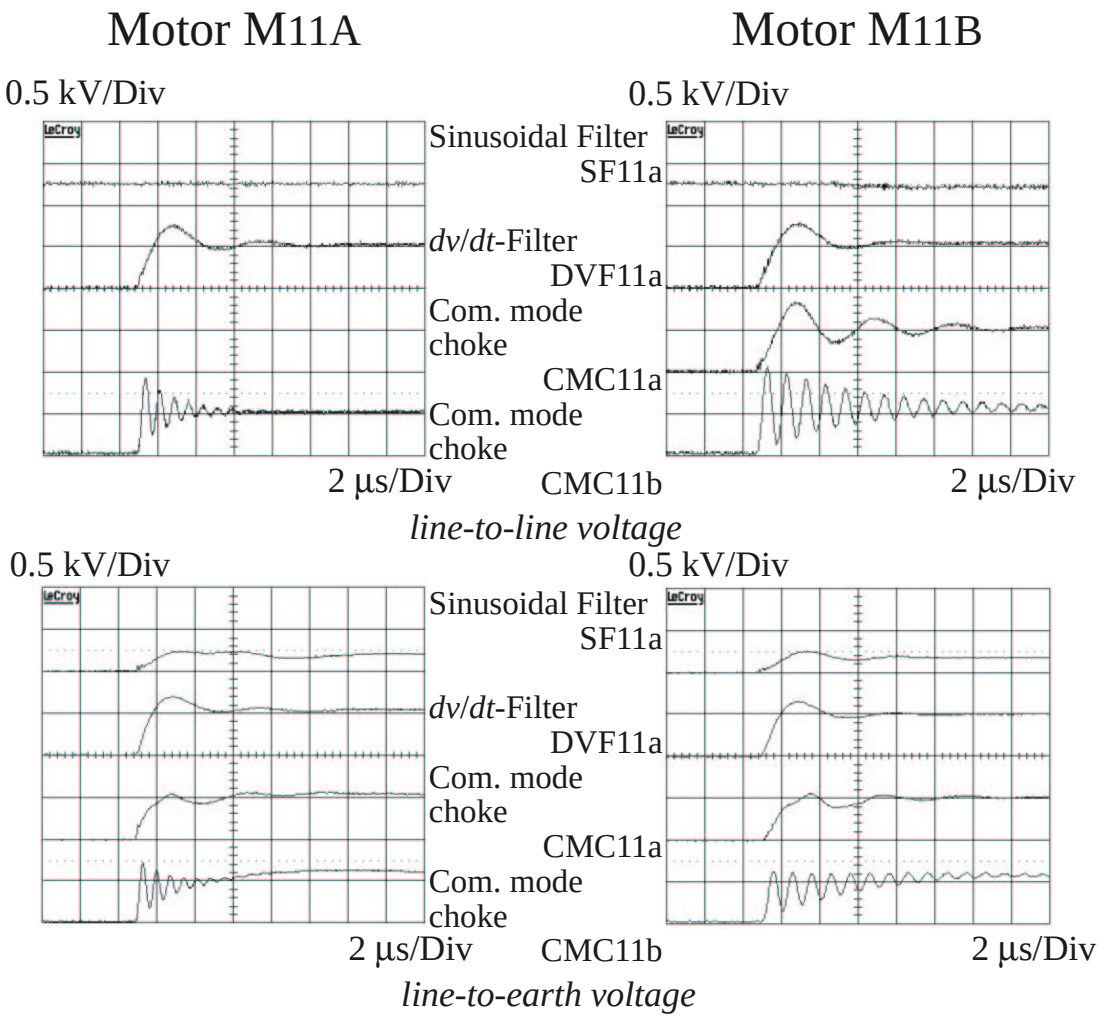

Figure G.4: 11 kW power level - Measured line-to-line and line-to-earth voltages v_{LL} and v_{Lg} at use of *different inverter-output filters*, inverter I11a, configuration $\mathrm{E1}_{02}$ ($l_{\mathrm{c}} = 2$ m, unshielded motor cable) (→ Table G.6)

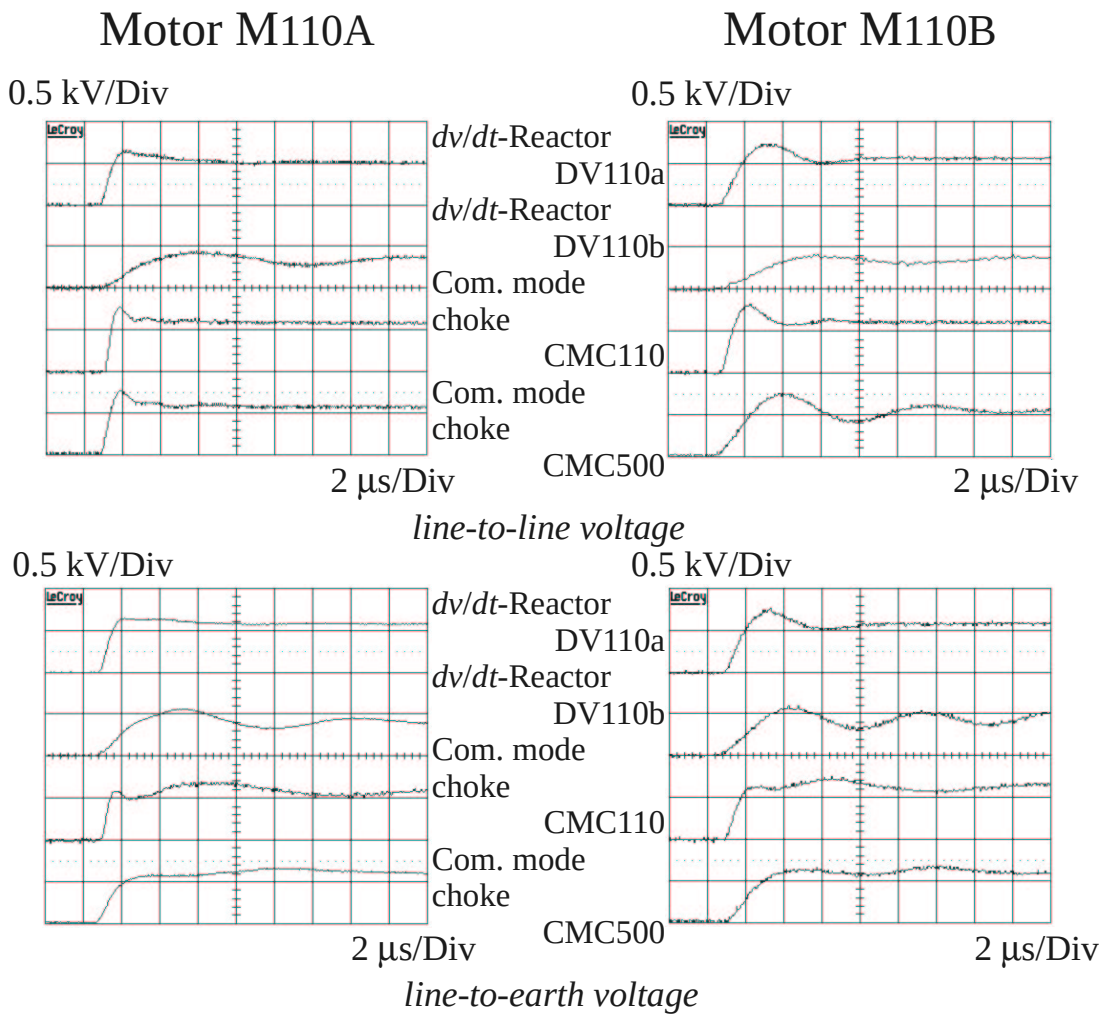

Figure G.5: 110 kW power level - Measured line-to-line and line-to-earth voltages v_{LL} and v_{Lg} at use of *different inverter-output filters*, inverter I110a, configuration E1*$_{10}$ ($l_{\mathrm{c}} = 10$ m, shielded motor cable) (→ Table G.7)

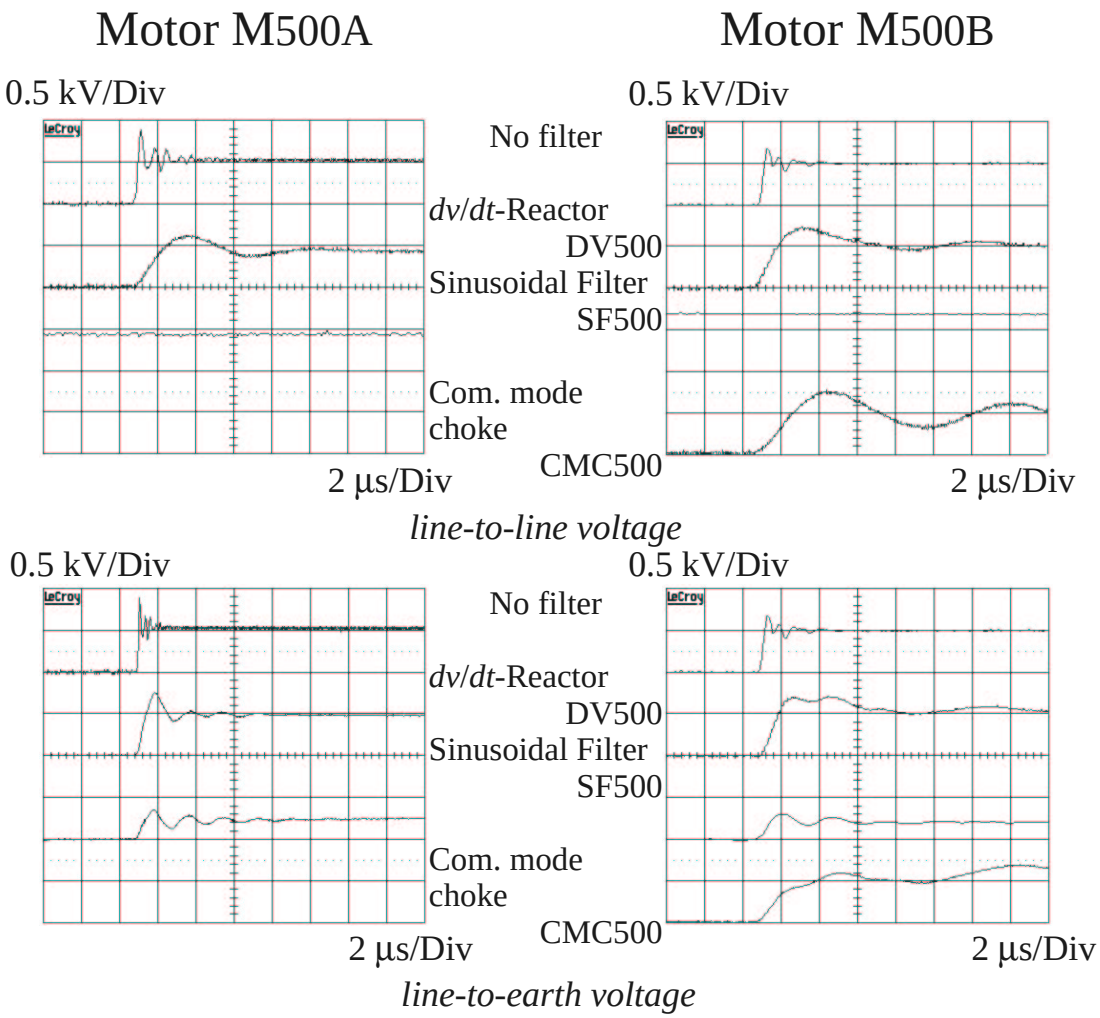

Figure G.6: 500 kW power level - Measured line-to-line and line-to-earth voltages v_{LL} and v_{Lg} for use of *different inverter-output filters*, inverter I500, configuration E1*$_{10}$ ($l_{\mathrm{c}} = 10$ m, shielded motor cable) (→ Table G.8)

Bibliography

[1] S. Chen, T.A. Lipo, and D. Fitzgerald, "Modeling of bearing currents in PWM inverter drives", Orlando, 1995, IEEE Industry Applications Conference, pp. 388-393.

[2] S. Chen, *Bearing current, EMI and soft switching in induction motor drives*, PhD thesis, UMI's Dissertation Services, Michigan, 1996.

[3] V. Hausberg and H.O. Seinsch, "Kapazitive Lagerspannungen und -stroeme bei umrichtergespeisten Induktionsmaschinen", *Electrical Engineering*, vol. 82, pp. 153–162, 2000.

[4] V. Hausberg and H.O. Seinsch, "Wellenspannungen und zirkulierende Lagerstroeme bei umrichtergespeisten Induktionsmaschinen", *Electrical Engineering*, vol. 82, pp. 313–326, 2000.

[5] V. Hausberg and H.O. Seinsch, "Schutzmaßnahmen gegen Lagerschaeden umrichtergespeister Motoren", *Electrical Engineering*, vol. 82, pp. 339–345, 2000.

[6] S. Andreason, "Stromdurchgang durch Waelzlager", *Die Kugellagerzeitschrift (SKF)*, vol. 153, pp. 6–12, 1968.

[7] H. Pittroff, "Waelzlager im elektrischen Stromkreis", *Elektrische Bahnen*, vol. 39, pp. 54–61, 1968.

[8] SKF, *Waelzlager in elektrischen Maschinen und Geraeten*, SKF-Druckschrift, 3rd edition, Schweinfurt, 1966.

[9] FAG, *Waelzlager in Elektromaschinen und in der Buerotechnik*, FAG-Druckschrift, Schweinfurt, 1989.

[10] DIN Deutsches Institut fuer Normung e.V. und Verband der Elektrotechnik und Informationstechnik e.V., *VDE 0123 Stromfuehrung im Bereich von Radsatz-Waelzlagern in Schienenfahrzeugen*, VDE Verlag, Berlin, 1985.

[11] W. Freise and H. Jordan, "Die Ermittlung von Wellenspannungen und Lagerstrom in elektrischen Maschinen unter Beruecksichtigung der magnetischen Spannung im Eisen", *Elektrotechnik und Maschinenbau*, vol. 80, pp. 80–84, 1963.

[12] J. Boyd and H.N. Kaufman, "The causes and the control of electrical currents in bearings", *Journal of the Society of Lubrication Engineers*, pp. 28–34, 1959.

[13] O. Haus, "Wellenspannungen und Lagerstroeme, ihre Ursache, Wirkung und Abhilfemassnahmen", *ETZ-A*, vol. 85, pp. 106–112, 1964.

[14] H. Jordan and F. Taegen, "Wellenfluesse infolge von Schwankungen des Luftspaltleitwerts", *ETZ-A*, vol. 85, pp. 865–867, 1964.

[15] C. Ammann, K. Reichert, R. Joho, and Z. Posedel, "Shaft voltages in generators with static excitation systems - problems and solutions", *IEEE Transactions on Energy Conversion*, vol. 3, pp. 409–419, 1988.

[16] K. Brach, *Wellenspannungen bei Drehstrom-Induktionsmaschinen mit Kaefiglaeufer*, PhD thesis, Universitaet Hannover, VDI-Verlag, series 21, no. 63, 1990.

[17] H.J. Conraths, F. Giessler, and H.-D. Heining, "Shaft-voltages and bearing currents - new phenomena in inverter driven induction machines", Lausanne, 1999, 8th European Conference on Power Electronics and Applications (EPE), paper no. 165.

[18] International Electrotechnical Commission, *IEC 60034-17: Rotating electrical machines; Guide for the application of cage induction motors when fed from converters.*

[19] NEMA, *NEMA MG-1 Specification 31, section IV, 1993*, NEMA, 1993.

[20] A. Binder and A. Schrepfer, "Bearing currents in induction machines due tu inverter supply", Istanbul, 1998, 13th International Conference on Electrical Machines and Drives (ICEM), pp. 586-591.

[21] A. Binder, R.P. Aust, and A. Schrepfer, "Bearing currents - a danger to inverter-fed induction motors?", *Iron and Steel Engineer*, vol. 76, pp. 47–52, July 1999.

[22] S. Chen, T.A. Lipo, and D.W. Novotny, "Circulating type motor bearing current in inverter drives", San Diego, 1996, IEEE Industry Applications Conference, pp. 162-167.

[23] J. Erdman, R. Kerkman, D. Schlegel, and G. Skibinski, "Effect of PWM inverters on AC motor bearing currents and shaft voltages", *IEEE Transactions on Industry Applications*, vol. 32, pp. 250–259, 1996.

[24] Z. Krzemien, "Bearing currents in induction motors supplied with power from PWM inverters", Istanbul, 1998, 13th International Conference on Electrical Machines and Drives (ICEM), pp. 592-596.

[25] J. Ollila, T. Hammar, J. Iisakkala, and H. Tuusa, "A new reason for bearing current damages in variable speed drives", Trondheim, 1997, 7th European Conference on Power Electronics and Applications (EPE), pp. 2539-2543.

[26] G. Kure and W. Palmetshofer, "Stromisolierte Waelzlager", *Evolution*, vol. 3, pp. 22–24, 1996.

[27] D. Busse, J. Erdman, R. Kerkman, D. Schlegel, and G. Skibinski, "System electrical parameters and their effect on bearing currents", *IEEE Transactions on Industry Applications*, vol. 33, pp. 577–584, 1997.

[28] N. Mohan, T.M. Undeland, and W.P. Robbins, *Power Electronics: Converters, Applications and Design*, John Wiley & Sons Inc., 3rd ed., 2003.

[29] D.W. Novotny and T.A. Lipo, *Vector Control and Dynamics of AC Drives*, Oxford University Press Inc., New York, 1996.

[30] FAG, *Hydraulikverfahren zum Ein- und Ausbau von Waelzlagern*, FAG-Druckschrift WL82 102/6 DA, Schweinfurt, 1996.

[31] SKF, *Der SKF Druckoel-Pressverband*, SKF-Produktinformation 303/I, Schweinfurt, 1990.

[32] J. Braendlein, P. Eschmann, L. Hasbargen, and K. Weigand, *Die Waelzlagerpraxis*, Vereinigte Fachverlage GmbH, Mainz, 1998.

[33] W. Beitz and K.-H. Kuettner (Editors), *Dubbel, Taschenbuch fuer den Maschinenbau*, Springer Verlag, Heidelberg, 1990.

[34] D. Busse, J.M. Erdman, R.J. Kerkman, D.W. Schlegel, and G.L. Skibinski, "An evaluation of the electrostatical shielded induction motor: A solution for shaft voltage buildup and bearing current", *IEEE Transactions on Industry Applications*, vol. 33, pp. 1563–1570, 1997.

[35] S. Bell, T.J. Cookson, S.A. Cope, R.A. Epperly, A. Fischer, D.W. Schlegel, and G.L. Skibinski, "Experience with variable-frequency drives and motor bearing reliability", *IEEE Transactions on Industry Applications*, vol. 37, pp. 1438–1446, 1998.

[36] P. Link, "Minimizing electric bearing currents in ASD systems", *IEEE Industry Applications Magazine*, vol. 5, pp. 55–66, 1999.

[37] International Electrotechnical Commission, *IEC 60034-25: Rotating electrical machines; Guide for the design and performance of cage induction motors for converter supply (Draft), document 2/1271/DTR.*

[38] A. Kohaut, "Riffelbildung in Waelzlagern infolge elektrischer Korrosion", *Zeitschrift fuer angewandte Physik*, vol. 1, pp. 197–211, 1948.

[39] J.I. Steinfeld, *Molecules and Radiation - an Introduction to Modern Molecular Spectroscopy*, MIT Press, 2nd edition, Cambridge, Massachusetts, 1989.

[40] G. Carlin, "Stromdurchgang durch die Rollenachsenlager von Reisezugwagen", *Die Kugellagerzeitschrift (SKF)*, vol. 158, pp. 25–34, 1968.

[41] P.A. Botö, "Stromdurchgang in einem Waelzkontakt", *Die Kugellagerzeitschrift (SKF)*, vol. 153, pp. 13–18, 1967.

[42] H. Prashad, "Effect of operating parameters on the threshold voltages and impedance response of non-insulated rolling element bearings under the action of electrical currents", *Wear*, vol. 117, pp. 223–239, 1987.

[43] D. Busse, J. Erdman, R. Kerkman, D. Schlegel, and G. Skibinski, "The effects of PWM voltage source inverters on the mechanical performance of rolling bearings", *IEEE Transactions on Industry Applications*, vol. 33, pp. 567–576, 1997.

[44] M. Kaufhold, *Elektrisches Verhalten der Windungsisolierung von Niederspannungsmaschinen bei Speisung durch Pulsumrichter*, PhD thesis, Technische Universitaet Dresden, VDI-Verlag, series 21, no. 172, 1994.

[45] M. Berth, *Elektrische Belastung der Wicklungsisolierung pulsumrichtergespeister Niederspannungsmotoren*, PhD thesis, Technische Universitaet Dresden, VDI-Verlag, series 21, no. 247, 1998.

[46] D. Potoradi, C. Hofmeier, R. Nuscheler, and W. Hutter, "Transient voltages caused by switching of high voltage asynchronous machines and their distribution in the stator windings", Vigo, 1996, 12th International Conference on Electrical Machines and Drives (ICEM), pp. 664-649.

[47] Z. Peroutka and V. Kus, "Investigation of phenomena in the system voltage inverter-cable - induction motor", Graz, 2001, 9th European Conference on Power Electronics and Applications (EPE), paper no. 372.

[48] H.W. Lorenzen and R. Nuscheler, "Experimental results of various asynchronous machines in the time and frequency range as basis for modelling fast transient as well as 50/60 Hz time behaviour", 12th Vigo, 1996, International Conference on Electrical Machines and Drives (ICEM), pp. 446-451.

[49] E. Zhong, T.A. Lipo, and S. Rossiter, "Transient modeling and analysis of motor terminal voltage on PWM inverter-fed AC Motor Drives", 1998, IEEE Industry Applications Society Annual Meeting, pp. 773-780.

[50] G. Skibinski, G. Kerkman, D. Leggate, J. Pankau, and D. Schlegel, "Reflected wave modeling techniques for PWM AC motor drives", 1998, Applied Power Electronics Conference and Exposition (APEC), pp. 1021-1029.

[51] S. Bhattacharya, L. Resta, D.M. Divan, and D.W. Novotny, "Experimental comparison of motor bearing currents with PWM hard- and soft-switched voltage-source inverters", *IEEE Transactions on Power Electronics*, vol. 14, pp. 552–562, 1999.

[52] G. Grandi, D. Casadei, and A. Massarini, "High frequency lumped parameter model for AC motor windings", Trondheim, 1997, 7th European Conference on Power Electronics and Applications (EPE), pp. 2578-2583.

[53] S. Chen, T.A. Lipo, and D. Fitzgerald, "Modeling of bearing currents in PWM inverter drives", *IEEE Transactions on Industry Applications*, vol. 32, pp. 21–32, 1996.

[54] G. Grandi, D. Casadei, and U. Reggiani, "Analysis of common- and differential mode HF current components in PWM inverter-fed AC motors", Fukuoka, 1998, IEEE Power Electronics Specialists Conference, pp. 1146-1151.

[55] L. Ran, S. Gokani, J. Clare, K.J. Bradley, and C. Christopoulos, "Conducted electromagnetic emissions in induction motor drive systems; part I: time domain analysis and identification of dominant modes", *IEEE Transactions on Industry Applications*, vol. 13, pp. 757–767, 1998.

[56] L. Ran, S. Gokani, J. Clare, K.J. Bradley, and C. Christopoulos, "Conducted electromagnetic emissions in induction motor drive systems; part II: frequency domain models", *IEEE Transactions on Industry Applications*, vol. 13, pp. 768–776, 1998.

[57] M. Cacciato, A. Consoli, G. Scarcella, and A. Testa, "Reduction of common-mode currents in PWM inverter motor drives", *IEEE Transactions on Industry Applications*, vol. 1, pp. 707–714, 1999.

[58] A. von Jouanne, H. Zhang, and A.K. Wallace, "An evaluation of mitigation techniques for bearing currents, EMI and overvoltages in ASD applications", *IEEE Transactions on Industry Applications*, vol. 34, pp. 1113–1122, 1998.

[59] S. Ogasawara, H. Ayano, and H. Akagi, "Measurement and reduction of EMI radiated by a PWM inverter-fed AC motor drive system", *IEEE Transactions on Industry Applications*, vol. 33, pp. 1019–1026, 1997.

[60] S. Ogasawara and H. Akagi, "Modeling and damping of high-frequency leakage currents in PWM inverter-fed AC motor drive systems", *IEEE Transactions on Industry Applications*, vol. 32, pp. 1105–1114, 1996.

[61] I. Boldea and S.A. Nasar, *Electric Drives*, CRC Press LLC, Florida, 1999.

[62] G. Suresh, H. A. Toliyat, D.A. Rendusara, and P.N. Enjeti, "Predicting the transient effects of pwm voltage waveform on the stator windings of random wound machines", *IEEE Transactions on Power Electronics*, vol. 14, pp. 23–29, 1999.

[63] K. Vogt, *Berechnung Elektrischer Maschinen*, VCH Verlagsgesellschaft mgH, Weinheim, 1996.

[64] P. Maeki-Ontto and J. Luomi, "Common mode flux calculation of AC machines", Bruges, 2002, 15th International Conference on Electrical Machines and Drives (ICEM), paper no. 549.

[65] P. Maeki-Ontto and J. Luomi, "Circumferential flux as a source of bearing current of converter-fed AC machines", Stockholm, 2002, Nordic Workshop on Power and Industrial Electronics (NORPIE), (CD-ROM).

[66] J. Wimmer and H. Stadler, "Lagerstroeme bei umrichtergespeisten Drehstrommaschinen", *antriebstechnik*, vol. 39, pp. 34–38, 2000.

[67] B.J. Hamrock and D. Dowson, *Ball Bearing Lubrication - The Elastohydrodynamics of Eliptical Contacts*, John Wiley and Sons, New York, 1981.

[68] D. Dowson, G. Higginson, and A. Whitaker, "Elastohhydrodynamic lubrication: a survey of isothermal solutions", *Journal Mechanical Engineering Science*, vol. 4, pp. 121–126, 1962.

[69] D. Dowson and A. Whitaker, "The isothermal lubrication of cylinders", *ASLE Transactions*, vol. 8, pp. 224–234, 1965.

List of Publications

[1] A. Muetze and A. Binder, "High frequency ground currents of inverter-fed squirrel-cage induction motors up to 500 kW", Toulouse, 2003, 10th European Power Electronics Conference (EPE), paper no. 027.

[2] A. Muetze and A. Binder, "Experimental evaluation of mitigation techniques for bearing currents in inverter-supplied drive-systems - investigations on induction motors up to 500 kW", Madison, WI, 2003, 4th International Electric Machines and Drives Conference (IEMDC), vol. 3, pp. 1859-1865.

[3] A. Muetze and A. Binder, "Influence of cable and filter configuration on bearing currents in inverter-fed induction motors 11 kW to 500 kW", Nuernberg, 2003, 46th International Conference on Power Electronics and Intelligent Motion Power Quality (PCIM), paper no. IM 2.2.

[4] A. Muetze, A.G. Jack, and B.C. Mecrow, "Alternate designs of brushless-dc motors using soft magnetic composites", Bruegge, 2002, 15th International Conference on Electrical Machines and Drives (ICEM), paper no. 237.

[5] A. Muetze and A. Binder, "Systematic approach to bearing current evaluation in variable speed drive systems", Bruegge, 2002, 15th International Conference on Electrical Machines and Drives (ICEM), paper no. 201.

[6] A. Muetze and A. Binder, "Influence of motor size on the nature of bearing currents - Investigations at 11 kW and 110 kW inverter-fed induction motors", Nuernberg, 2002, 45th International Conference on Power Electronics and Intelligent Motion Power Quality (PCIM), paper no. IM 3.1.

[7] A. Muetze, A.G. Jack, and B.C Mecrow, "Brushless-dc motor using soft magnetic composites as a direct drive in an electric bicycle", Graz, 2001, 9th European Power Electronics Conference (EPE), paper no. 350.

[8] A. Muetze, "Vergleich verschiedener Motorkonzepte unter Verwendung von SMC als Direktantrieb eines Fahrrads", Hannover, 2000, 14th ETG-Fachforum, Hannover 2000, pp. 79-83.

Curriculum Vitae

Annette Muetze
born February 2, 1974, in Singen/Hohentwiel

Education

Course of Studies

1993 - 1999 Technische Universitaet Darmstadt, Darmstadt, Germany,
"Diplom-Ingenieur" Electrical Engineering
Ecole Centrale de Lyon, Lyon, France,
"Ingénieur générale"
final project no 1: study in the area of high temperature fuel cells and their application in passenger cars (with BMW AG, Munich)
final project no 2: study in the field of electromagnetic efficiency of a switched reluctance drive

Internships

11/1998 - 03/1999 BMW AG, Munich, Germany (final project no 1)
06/1997 - 10/1997 ABB Power T&D, Athens, GA, US,
transformer design, fault recognition and correction
07/1996 - 08/1996 Jeumont Schneider Transformateurs, Lyon, France,
dielectric laboratory
06/1993 - 10/1993 Behringwerke Marburg, Germany, mechanical worker

College

1985 - 1993 Elisabeth Schule, Marburg, Germany,
"Abitur" (German High School Diploma)

Experience

as of 05/2004 Assistant Professor
University of Wisconsin-Madison, WI, US,
Department of Electrical and Computer Engineering
2000 - 2003 Research and Teaching Assistant
Technische Universitaet Darmstadt, Germany
Department of Electrical Energy Conversion
1999 - 2000 Research initiated by "Herbert-Kind-Preis 2000"
(Research award of ETG, electrotechnical society within VDE)
University Newcastle upon Tyne, UK,
Power Electronics, Drives and Machines Group